Leg 208 Preliminary Report

Early Cenozoic Extreme Climates: The Walvis Ridge Transect

6 March–6 May 2003

Shipboard Scientific Party

Ocean Drilling Program
Texas A&M University
1000 Discovery Drive
College Station TX 77845-9547
USA

August 2003

PUBLISHER'S NOTES

This report was prepared from shipboard files by scientists who participated in the cruise. The report was assembled under time constraints and does not contain all works and findings that will appear in the *Initial Reports* of the ODP *Proceedings*. Reference to the whole or to part of this report should be made as follows:

Shipboard Scientific Party, 2003. Leg 208 Preliminary Report. *ODP Prelim. Rpt.,* 108 [Online]. Available from World Wide Web: <http://www-odp.tamu.edu/publications/prelim/208_prel/208PREL.PDF>. [Cited YYYY-MM-DD]

Distribution: Electronic copies of this series may be obtained from the Ocean Drilling Program's World Wide Web site at http://www-odp.tamu.edu/publications.

This publication was prepared by the Ocean Drilling Program, Texas A&M University, as an account of work performed under the international Ocean Drilling Program, which is managed by Joint Oceanographic Institutions, Inc., under contract with the National Science Foundation. Funding for the program is provided by the following agencies:

Australia/Canada/Chinese Taipei/Korea Consortium for Ocean Drilling
Deutsche Forschungsgemeinschaft (Federal Republic of Germany)
Institut National des Sciences de l'Univers–Centre National de la Recherche Scientifique (INSU-CNRS; France)
Ocean Research Institute of the University of Tokyo (Japan)
National Science Foundation (United States)
Natural Environment Research Council (United Kingdom)
European Science Foundation Consortium for Ocean Drilling (Belgium, Denmark, Finland, Iceland, Ireland, Italy, The Netherlands, Norway, Portugal, Spain, Sweden, and Switzerland)
Marine High-Technology Bureau of the State Science and Technology Commission of the People's Republic of China

DISCLAIMER

The following scientists and participants were aboard the *JOIDES Resolution* for Leg 208 of the Ocean Drilling Program:

SHIPBOARD SCIENTIFIC PARTY

Dick Kroon
Co-Chief Scientist
Faculty of Earth and Life Sciences
Vrije Universiteit
De Boelelaan 1085
HV 1081 Amsterdam
The Netherlands
Work: (31) 204447261
Fax: (31) 206462457
kroo@geo.vu.nl

James C. Zachos
Co-Chief Scientist
Earth Sciences Department
University of California, Santa Cruz
Earth and Marine Sciences Building
Santa Cruz CA 95064
USA
Work: (831) 459-4644
Fax: (831) 459-3074
jzachos@emerald.ucsc.edu

Peter Blum
Staff Scientist
Ocean Drilling Program
Texas A&M University
1000 Discovery Drive
College Station TX 77845-9547
USA
Work: (979) 845-9299
Fax: (979) 845-0876
blum@odpemail.tamu.edu

Julie Bowles
Paleomagnetist
Scripps Institution of Oceanography
University of California, San Diego
9500 Gilman Drive
MC0208
La Jolla CA 92093
USA
Work: (858) 822-4879
Fax: (858) 534-0784
jbowles@ucsd.edu

Philippe Gaillot
Logging Staff Scientist
Laboratoire de Mesures en Forages, ISTEEM
Universite Montpellier II
Laboratorie de Tectonophysique
Place Eugene Bataillon
34095 Montpellier Cedex 5
France
Work: (33) 467 149 310
Fax: (33) 467 149 308
gaillot@dstu.univ-montp2.fr

Takashi Hasegawa
Organic Geochemist
Department of Earth Sciences, Faculty of Science
Kanazawa University
Kakuma-machi
Kanazawa, Ishikawa-Prefecture 920-1192
Japan
Work: (81) 76-264-5636
Fax: (81) 76-264-5746
jh7ujr@kenroku.kanazawa-u.ac.jp

Edmund C. Hathorne
Inorganic Geochemist
Department of Earth Sciences
The Open University
Walton Hall
Milton Keynes MK7 6AA
United Kingdom
Work: (44) 1908 653023
Fax: (44) 1908 655151
e.c.hathorne@open.ac.uk

David A. Hodell
Sedimentologist
Department of Geological Sciences
University of Florida
241 Williamson Hall
PO Box 112120
Gainesville FL 32611
USA
Work: (352) 392-6137
Fax: (352) 392-9294
dhodell@geology.ufl.edu

Daniel C. Kelly
Paleontologist (foraminifers)
Department of Geology and Geophysics
University of Wisconsin-Madison
1215 West Dayton Street
Madison WI 53706
USA
Work: (608) 262-1698
Fax: (608) 262-0693
ckelly@geology.wisc.edu

Ja-Hun Jung
Physical Properties Specialist
Department of Applied Geology
Pukyong National University
599-1 Daeyeon 3-dong, Nam-gu
Busan 608-737
Korea
Work: (82) 51-620-6233
Fax: (82) 51-623-5068
jh1206@mail1.pknu.ac.kr

Susan M. Keller
Sedimentologist
Earth Sciences Department
University of California, Santa Cruz
1156 High Street
Santa Cruz CA 95064
USA
Work: (831) 459-5088
Fax: (831) 459-3074
skeller@es.ucsc.edu

Youn Soo Lee
Paleomagnetist
Division of Geological Research
Korea Institute of Geoscience and Mineral Resources (KIGAM)
30 Grajeong-dong, Yuseong-gu
Daejeon 305-350
Korea
Work: (82) 42-868-3036
Fax: (82) 42-861-9714
lys0222@hotmail.com

Dirk C. Leuschner
Sedimentologist
Institut für Geophysik und Geologie
Universität Leipzig
Talstrasse 35
04103 Leipzig
Germany
Work: (49) 341-9732-909
Fax: (49) 341-9732-809
dcleu@rz.uni-leipzig.de

Zhifei Liu
Sedimentologist
School of Ocean and Earth Sciences
Tongji University
1239 Siping Road
Shanghai 200092
China
Work: (86) 21 6598 4877
Fax: (86) 21 6598 8808
lzhifei@online.sh.cn

Kyger C. Lohmann
Sedimentologist
Department of Geological Sciences
University of Michigan
425 East University
Ann Arbor MI 48109-1063
USA
Work: (734) 763-2298
Fax: (734) 763-4690
kacey@umich.edu

Lucas Lourens
Stratigraphic Correlator
Department of Geology
Faculty of Earth Sciences
Utrecht University
Budapestlaan 4
3584 CD Utrecht
The Netherlands
Work: (31) 30-253-5173
Fax: (31) 30-253-2648
llourens@geo.uu.nl

Simonetta Monechi
Paleontologist (nannofossils)
Dipartimento di Scienze della Terra
Università degli Studi di Firenze
Via La Pira 4
50121 Firenze
Italy
Work: (39) 0550275 7657
Fax: (39) 05521 8628
monechi@unifi.it

Micah Nicolo
Sedimentologist
Department of Earth Science
Rice University
6100 Main Street
MS-126
Houston TX 77005-1892
USA
Work: (713) 348-4159
Fax: (713) 348-5214
micahn@rice.edu

Isabella Raffi
Paleontologist (nannofossils)
Dipartimento di Scienze della Terra
Universitario "G. D'Annunzio"
Campus Universitario
Via dei Vestini 31
66013 Chieti Scalo
Italy
Work: (39) 871-355-6421
Fax: (39) 871-355-6454
raffi@unich.it

Christina Riesselman
Sedimentologist
Department of Geological and Environmental Sciences
Stanford University
450 Serra Mall
Braun Hall, Building 320
Stanford CA 94305-2115
USA
Work: (650) 725-6830
Fax: (650) 725-0979
criessel@pangea.stanford.edu

Ursula Röhl
Stratigraphic Correlator
Department of Geosciences
Universität Bremen
Postfach 33 04 40
Klagenfurter Strasse
28334 Bremen
Germany
Work: (49) 421-2182482
Fax: (49) 421-2183116
uroehl@allgeo.uni-bremen.de

Stephen A. Schellenberg
Sedimentologist
Department of Geological Sciences
San Diego State University
5500 Campanile Drive
San Diego CA 92182-1020
USA
Work: (619) 787-3217
Fax: (619) 594-4372
schellenberg@geology.sdsu.edu

Daniela Schmidt
Paleontologist (foraminifers)
Department of Geology
Royal Holloway University of London
Egham Hill
Egham, Surrey TW20 0EX
United Kingdom
Work: (44) 1784-443593
Fax: (44) 1784-471780
dschmidt@gl.rhul.ac.uk

Appy Sluijs
Student Trainee
Department of Geobiology
Utrecht University
Budapestlaan 4
3584 CD Utrecht
The Netherlands
Work: (31) 30-253-2629
Fax: (31) 30-253-5096
a.sluijs@students.uu.nl

Deborah Thomas
Inorganic Geochemist/Paleontologist (foraminifers)
Geological Sciences
University of North Carolina at Chapel Hill
CB 3315, Mitchell Hall
Chapel Hill NC 27599-3315
USA
Work: (919) 225-7463
Fax: (919) 966-4519
dthomas1@email.unc.edu

Wesleyan University
265 Church Street
Middletown CT 06459-0139
USA
Work: (860) 685-2238
Fax: (860) 685-3651
ethomas@wesleyan.edu

Henry Vallius
Physical Properties Specialist
Geological Survey of Finland
Espoo Unit
Betonimiehenkuja 4
PO Box 96
02151 Espoo
Finland
Work: (358) 20 550 2573
Fax: (358) 20 550 12
henry.vallius@gsf.fi

TRANSOCEAN OFFICIALS

Pete Mowat
Master of the Drilling Vessel
Overseas Drilling Ltd.
707 Texas Avenue South, Suite 213D
College Station TX 77840-1917
USA

Tim McCown
Drilling Superintendent
Overseas Drilling Ltd.
707 Texas Avenue South, Suite 213D
College Station TX 77840-1917
USA

ODP SHIPBOARD PERSONNEL

Christopher Bennight
Marine Laboratory Specialist (Chemistry)

Timothy Bronk
Assistant Laboratory Officer

John Davis
Marine Computer Specialist

Jason Deardorff
Marine Laboratory Specialist (X-Ray)

Peter Esmay
Marine Laboratory Specialist (Curation)

John Gill
Marine Laboratory Specialist (Core)

Ron Grout
Operations Manager

Burney Hamlin
Laboratory Officer

Jennifer Henderson
Marine Laboratory Specialist (Paleomagnetism)

Michael Hodge
Marine Computer Specialist

Shannon Houseley
Marine Laboratory Specialist (Photography)

Jessica Huckemeyer
Marine Laboratory Specialist (Downhole Tools/
Thin Sections)

Karen Johnston
Marine Laboratory Specialist (Core)

Steve Kittredge
Schlumberger Logging Engineer

Jurie Kotze
Marine Electronics Specialist

William Mefford
Marine Laboratory Specialist (Core)

Debbie Partain
Marine Laboratory Specialist (Yeoperson)

Pieter Pretorius
Marine Electronics Specialist

Patrick Riley
Marine Laboratory Specialist (Physical Properties)

Derryl Schroeder
Development Engineer

Johanna Suhonen
Marine Laboratory Specialist (Underway Geophysics)

Robert Wheatley
Marine Laboratory Specialist (Chemistry)

Yunyou Yao
Programmer

ABSTRACT

During Ocean Drilling Program (ODP) Leg 208, six sites were drilled at water depths between 2500 and 4770 m to recover lower Cenozoic sediments on the northeastern flank of Walvis Ridge. Previous drilling in this region (Deep Sea Drilling Project [DSDP] Leg 74) recovered pelagic oozes and chalk spanning the Cretaceous/Paleogene (K/P), Paleocene/Eocene, and Eocene/Oligocene boundaries. The objective of Leg 208 was to recover intact composite sequences of these "critical" transitions from a wide range of depths. Multichannel seismic data (*Meteor* Cruise M49/1) along with information from DSDP Leg 74 sites were used to identify sites where continuous sequences of lower Cenozoic sediment should be present. Double to triple advanced hydraulic piston coring, occasional extended core barrel coring to deepen the holes, and high-resolution physical property measurements were employed to construct "composite sections." The composite sections provide a detailed history of paleoceanographic variation associated with several prominent episodes of early Cenozoic climate change, including the K/P boundary, early Eocene Climatic Optimum, the Paleocene–Eocene Thermal Maximum (PETM), and the early Oligocene Glacial Maximum.

The PETM interval, the main focus of Leg 208, was recovered at five sites along a depth transect of 2.2 km. The sediment sequence is marked by a red clay layer, which varies in thickness from 20 to 50 cm from site to site, within a thick and uniform sequence of upper Paleocene and lower Eocene foraminifer-bearing nannofossil ooze. The basal color contact is relatively sharp, although magnetic susceptibility data show a more gradual, steplike transition at the deeper Sites 1262 and 1267. The carbonate content drops to 0 wt% at all sites except for Site 1265. The upper contact is gradational in the shallow sites and relatively sharp at the deeper sites. Overlying the clay layer is a sequence of nannofossil ooze, which is slightly richer in carbonate than the unit immediately underlying the clay layer.

The depth transect permits testing of the leading hypothesis for the cause of the PETM: the abrupt dissociation of as much as 2000 Gt of marine methane hydrate. Numerical modeling demonstrates that the injection of such a large mass of carbon to the ocean/atmosphere could have triggered a rapid (~10 k.y.) global shoaling of the calcite compensation depth (CCD) and lysocline, followed by a gradual recovery, and "overcompensation" with the CCD overshooting pre-excursion depths. Based on sediment cores recovered during Leg 208, the estimated magnitude of the shoaling of the CCD is >2 km, considerably more than predicted in present carbon cycle models of the event.

Leg 208 material also documents biotic responses to environmental changes as a result of the methane release and CCD shoaling (e.g., severe dissolution over such a large depth range may well have been an important factor in the benthic foraminiferal extinction event coincident with the base of the clay layer at every site, and nannofossils showed a short-term relative abundance response from *Fasciculithus* to *Zygrhablithus*). Planktonic foraminifers are heavily dissolved in the clay layer with only extremely rare specimens of acarinids and morozovellids remaining.

The Leg 208 transect complements a transect drilled on the southern Shatsky Rise during Leg 198, a deep latitudinal transect in the equatorial Pacific drilled during Leg 199, a shallow to bathyal transect drilled on Demarera Rise during Leg 207, and a depth transect proposed for future drilling in the western North Atlantic Ocean (J-Anomaly Ridge and Southeast Newfoundland Rise).

INTRODUCTION

The Paleogene represents a climatically dynamic period in Earth history. Stable isotope and other temperature proxy records reveal a complex history of warming and cooling, characterized by periods of both gradual and rapid change (Miller et al., 1987; Miller and Katz, 1987; Stott et al., 1990; Zachos et al., 2001, 1994). Major events include a 1-m.y.-long global warming trend that began in the late Paleocene and climaxed in the early Eocene in a 1- to 2-m.y.-long climatic optimum (early Eocene Climatic Optimum [EECO]) and a 12-m.y.-long stepped cooling trend that began in the early middle Eocene and culminated in the earliest Oligocene with the appearance of continental-scale ice sheets (Hambrey et al., 1991; Zachos et al., 1992). One of the more prominent events is a transient but extreme greenhouse interval known as the Paleocene–Eocene Thermal Maximum (PETM). This event occurred at ~55.0 Ma. Major changes in ocean chemistry as inferred from shifts in carbon isotope patterns and distribution and preservation patterns of terrigenous and biogenic sediments on the seafloor (e.g., Bralower et al., 1995; Kennett and Stott, 1991; Robert and Kennett, 1997) characterize the PETM. In addition, distinct shifts in the distribution of key groups of fauna and flora occurred in the oceans and on land (e.g., Kelly et al., 1998; Koch et al., 1995, 1992; Thomas and Shackleton, 1996; Thomas, 1998; Wing, 1998). Another notable event is the earliest Oligocene Glacial Maximum (EOGM, or Oi-1), a brief but extreme glacial interval that occurred at ~33.4 Ma and marks the transition to permanent glacial conditions on Antarctica (e.g., Miller et al., 1987, 1991; Zachos et al., 1996). This event, like the PETM, has caused large-scale perturbations in ocean chemistry and paleoecology (Barrera and Huber, 1993, 1991; Salamy and Zachos, 1999; Thomas and Gooday, 1996; Thunell and Corliss, 1986).

Multiple hypotheses exist to explain the large-scale, long-term changes in Paleogene climate, although none have yet gained universal acceptance. In general, among many factors, the role of ocean gateways (continental geography) and greenhouse gas levels are considered as key variables. Theoretical models have invoked either the absence of a circum-Antarctic current or higher greenhouse levels or some combination of both to account for the EECO (Barron, 1985; Bice et al., 2000; Sloan and Barron, 1992; Sloan and Rea, 1996; Sloan et al., 1995, 1992). Similarly, the Oligocene glaciation has been attributed to both the initiation of the Antarctic Circumpolar Current and a reduction in greenhouse levels and (e.g., Kennett and Shackleton, 1976; Mikolajewicz et al., 1993; Oglesby, 1991; Raymo et al., 1990; Rind and Chandler, 1991). Some of the more abrupt transient excursions are more likely to have been forced by rapid changes in greenhouse gas levels because they occur over short timescales (e.g., 10^3–10^4 yr) and, most importantly, are accompanied by geochemical and isotopic anomalies suggestive of major perturbations in the carbon and sulfur cycles (Dickens et al., 1997, 1995; Paytan et al., 1998; Pearson and Palmer, 2000; Schmitz et al., 1997; Stott et al., 1990; Zachos et al., 1993).

Progress in characterizing Paleogene oceanography and climate history, particularly the transient events, has been hampered by the lack of high-quality, high-resolution multicored sequences. Most sites cored prior to Leg 198 suffer from poor recovery and drilling disturbance, and few were multicored or drilled as part of depth transects. The few exceptions are sites recovered during recent Ocean Drilling Program (ODP) legs including Sites 865, 999, 1001, 1051, and Bass River (Bralower et al., 1997, 1995; Miller et al., 1998; Norris and Röhl, 1999; Röhl et al., 2000, 2001, 2003). High-resolution records produced from these sites yield a wealth of exciting, important evidence of climate change to be more fully explored with additional data.

The ODP extreme climate advisory panel (Program Planning Group [PPG]) recognized the dearth of high-resolution records across climate transients, and the panel formulated new questions concerning extreme climates (Kroon et al., 2000) and potential drilling targets among which was the Walvis Ridge area. The ODP Leg 208 proposal, which resulted from the PPG discussions, described as its major goal the acquisition of sediment archives necessary to characterize such short-term changes in ocean chemistry and circulation that theoretically should have accompanied these climatic extremes, as well as their effects on the oceanic biota. Acquisition of more complete records of these events at a higher temporal resolution is required for both formulating and testing hypotheses on the origin of these and similar events.

Walvis Ridge, located in the eastern South Atlantic Ocean (Fig. F1), is one of the few known locations where it is possible to recover Paleogene sediments, including the PETM and EOGM, over a broad range of depths, including depths exceeding 4.5 km. The ridge was the target of drilling by Deep Sea Drilling Project (DSDP) Leg 74, which occupied Sites 525–529 on the northern flank of the ridge between depths of 2.5 and 4.2 km (Moore, Rabinowitz, et al., 1984). Paleogene pelagic sediments characterized by moderate sedimentation rates (~6–15 m/m.y.) and good magnetic stratigraphy were recovered at each site. However, because of the poor recovery (~50%–75%) and coring disturbances, especially with the rotary core barrel in unlithified sediments, only short segments of the sequences were recovered fully intact, and none of the sequences were double cored. Technical problems, combined with the lack of high-resolution shipboard core logs, limited high-resolution cyclostratigraphic investigations to a few short segments of the Cretaceous (Herbert and D'Hondt, 1990). Nevertheless, subsequent shore-based studies of low-resolution samples collected from these cores were instrumental in adding to our understanding of long-term Maastrichtian and Paleogene paleoceanography of the South Atlantic Ocean (e.g., calcite compensation depth [CCD], carbon isotope stratigraphy, deep-sea temperature/ice volume) (e.g., Moore, Rabinowitz, et al., 1984; Hsü and Weissert, 1985, and papers within; Shackleton, 1987). Nearly complete PETM intervals were recovered at the shallowest and deepest Sites 525 and 527. Stable isotope analysis of foraminifers recovered from these sites have helped to constrain the magnitude of the deep Atlantic biogeochemical and environmental changes during this event (Thomas et al., 1999; Thomas and Shackleton, 1996). At the remaining sites, the PETM was not recovered because of core gaps (poor recovery).

During the winter of 2000, a seismic survey of the southeastern Walvis Ridge was undertaken by the *Meteor* (Cruise M49/1). The survey extended coverage of the Leg 74 sites to the north and northeast, where more continuous and slightly thicker sediment sequences were discovered (Fig. F2). The higher fidelity multichannel seismic data generated during the survey allowed identification of several areas where the PETM and other critical intervals could be recovered by advanced hydraulic piston corer/extended core barrel (APC/XCB) drilling. The Leg 208 sites cover a paleodepth range of 2.3 km, sufficient to constrain large and subtle changes in the chemistry of deep and intermediate waters. Advances in coring technology and drilling strategies (i.e., multiple hole composite sections) allowed for 100% recovery of sequences that were only partially recovered during Leg 74. In addition, recent advances in data acquisition and cyclostratigraphy enabled high-precision correlation and dating of these sediments.

Geologic Setting

Walvis Ridge is a northeast-southwest-trending aseismic ridge that divides the eastern South Atlantic Ocean into two basins, the Angola Basin to the north and the Cape Basin to the south (Figs. F1, F3). The ridge consists of a series of interconnected crustal blocks that slope gradually toward the northwest and more steeply toward the southeast. Magnetic and gravity anomalies indicate that Walvis Ridge was formed by hotspot volcanism near the spreading ridge as the Atlantic basin gradually widened (Rabinowitz and Simpson, 1984) and is subsequently assumed to have followed a simple thermal subsidence model with ~1.1 km of subsidence since the Maastrichtian (Moore, Rabinowitz, et al., 1984).

Pelagic sediments drape most of the ridge and generally increase in thickness toward the continental margin (Moore, Rabinowitz, et al., 1984). In the vicinity of the primary Leg 208 target area on the southeastern portion of the ridge, sediment thickness varies from ~300 m on the deep (>4.5 km) seafloor adjacent to the ridge to ~600 m near the summit (~2.5 km), a pattern that is clearly expressed by seismic sequences in the multichannel seismic profiles (Fig. F4). The sediments are primarily calcareous oozes and chalks that range in age from Campanian to Holocene. The Neogene sequences consist primarily of nannofossil and foraminifer nannofossil oozes with relatively high carbonate contents, often in excess of 90%, although much lower values were recorded in lower through middle Miocene sections. Turbidites and slumps are present in some intervals. The underlying Paleogene sediments are dominated by nannofossil and foraminifer-bearing nannofossil oozes to chalks. Carbonate contents are also high, generally in excess of 80% through most of the Paleocene, Eocene, and Oligocene with the exception of several short, carbonate-poor intervals at the deeper sites (e.g., Paleocene and upper Eocene of Site 527) that represent episodes of CCD shoaling. A few thin chert layers are present below the upper Paleocene of the shallowest Sites 525 and 528 and in the lower Eocene of Site 529. Slump deposits of various scales are present in the upper Paleocene at Site 529. In most sections, calcareous microfossil preservation varies from good to excellent. The natural remnant magnetism of the Walvis Ridge sediments appears to be strong and stable. As a result, the quality of the magnetic polarity records is excellent, particularly in the Upper Cretaceous and lower Paleocene intervals (Chave, 1984).

Stratigraphic Evolution

Sediment accumulation rates on Walvis Ridge have varied considerably with time. On average, the highest rates (~8–13 m/m.y.) occur in the Pleistocene, Paleocene, and Maastrichtian. Much lower sedimentation rates (1–5 m/m.y.) as well as unconformities are common at most sites in the Neogene. For example, most of the Pleistocene is absent at the shallowest sites (Sites 525 and 526) whereas the lower and middle Miocene is absent at several of the deeper sites. The Neogene unconformities appear to be predominantly erosional in nature although dissolution clearly affected deposition downslope of the ridge (i.e., lower–middle Miocene at Site 527). Unconformities are also present in the upper Eocene and Oligocene. In contrast, at middepths (Site 529), most of the Paleogene is present but the middle–upper Miocene is either condensed or absent. In the deepest section (Site 527), the middle–upper Eocene is relatively condensed and the Oligocene and Miocene are highly condensed and/or absent. Nevertheless, it appears that for most of the early Paleogene, deposition was more or less continuous over much of the ridge. This continuity in sediment accumulation is reflected to some extent in the similar patterns in the low-resolution carbon isotope stratigraphies for four of the Leg 74 sites (Shackleton and Hall, 1984; Shackleton, 1987).

Cyclical variations in sedimentation are evident in various lithologic and physical property indexes, particularly in the more expanded Maastrichtian and Paleocene sequences. Spectral analysis of sediment color banding reveals the presence of a strong precessional beat in upper Maastrichtian and lower Paleocene sediments at Sites 525 and 528 (Herbert and D'Hondt, 1990). Similar cycles, although more subtle, may be present in the upper Paleocene and lower Eocene.

Scientific Objectives

Leg 208 scientists recovered sediments from Walvis Ridge suitable for addressing a number of important questions concerning the regional and global response to critical climatic events in the Paleogene. In addition, the overlying sediments at several sites will be used to resolve various aspects of the regional response to Neogene climate transitions. Here we discuss the critical climatic events of interest.

Early Eocene Climatic Optimum

The EECO represents the most recent episode of sustained global warmth. For nearly 2 m.y. of the early Eocene, the global climate was warm and ice free. Paleontologic and isotopic proxies indicate that the high-latitude seas and bottom waters were as much as 8°C warmer than at present (Fig. F5) (Miller et al., 1987; Shackleton and Boersma, 1981; Zachos et al., 1994; Stott et al., 1990). The biogeographic ranges of subtropical to temperate terrestrial fauna and flora extended well into polar latitudes (Axelrod, 1984; Estes and Hutchison, 1980; Wolfe, 1980), and polar ice sheets were small or nonexistent.

Several critical issues concerning the EECO need to be addressed. The first concerns the nature of climate variability during this period. At present, not a single marine record details paleoceanographic or climatic variability of this interval on orbital timescales. As a result, the approximate duration of the EECO and climate stability during this period are unknown. The second issue concerns the origin of the EECO. Empirical and theoretical geochemical studies suggest that greenhouse gas levels were significantly higher, possibly six times that of preindustrial levels, at the peak of the EECO (Berner, 1991; Pearson and Palmer, 2000). These estimates are supported to some extent by climate modeling in which the observed EECO meridional thermal gradients could only be attained in simulations with greenhouse gas levels six to eight times those of the present (Sloan and Rea, 1996) and are further supported by a boron isotope record that indicates unusually low pH for the Eocene surface ocean, consistent with high pCO_2 (Fig. F6) (Pearson and Palmer, 2000). The third issue concerns the underlying mechanism for driving changes in greenhouse gas levels. Why did CO_2 levels increase in the early Eocene? Was the rate of mantle outgassing higher as suggested by geochemical models (Berner et al., 1983; Schrag, 2002)? If so, was the dissolved carbon content of the ocean higher than that of the present (Walker et al., 1981)? Constraints on the CCD and lysocline depths and their depth changes on orbital timescales might provide insight into this and related questions.

Paleocene–Eocene Thermal Maximum

In terms of rate and degree of warming, the PETM is unprecedented in Earth's history. Isotope records suggest that at 55 Ma the deep ocean and high-latitude surface waters warmed by 4° and 8°C, respectively, in a period of <40 k.y. (Fig. F7). This period of extreme warmth, which lasted <150 k.y., triggered profound changes in global precipitation and continental weathering patterns (e.g., Gibson et al., 1993; Kaiho et al., 1996; Robert and Kennett, 1994). The PETM also affected biota on a global scale, triggering rapid turnover of planktonic organisms in the ocean (Kelly et al., 1996; Bralower, 2002), the largest mass extinction of deep-sea benthic foraminifers of the last 90 m.y. (Thomas and Shackleton, 1996; Thomas, 1990), and the most rapid radiation of land mammals (Clyde and Gingerich, 1998; Koch et al., 1992; Rea et al., 1990).

Several forcing mechanisms have been proposed for the PETM, including massive outgassing associated with rifted margin volcanism (Eldholm and Thomas, 1993) and sudden dissociation of methane hydrates stored on continental shelves and slopes (Dickens et al., 1995, 1997). Both hypotheses were inspired, in part, by marine and terrestrial carbon isotope records that show an abrupt 3‰–4‰ decrease in the ocean/atmosphere inorganic carbon reservoirs in <2 k.y. (Röhl et al., 2000; Bralower et al., 1997, 1995; Kennett and Stott, 1991; Thomas and Shackleton, 1996; Koch et al., 1995, 1992). Such a large and rapid carbon isotope excursion requires input of a large volume of isotopically depleted carbon from and external reservoir into the ocean/atmosphere system. In terms of fluxes and isotopic mass balances, the hydrate dissociation model provides the most plausible solution. If estimates are correct, dissociation of only a fraction of the total reservoir of methane hydrate stored on continental margins is sufficient to generate the observed isotopic excursion. In principle, with warming of deep waters, shelf and slope hydrates could become unstable, triggering a catastrophic release of CH_4 and immediate greenhouse warming through positive feedback.

A massive methane dissociation event should have profound effects on ocean chemistry. Dickens et al. (1997) used a box model to simulate the effects of releasing ~1.1×10^3 Gt of methane (immediately oxidized to carbon dioxide) directly into the atmosphere on ocean carbonate chemistry (Fig. F8). The amount of carbon added to the system was determined from mass balance calculations assuming a $\delta^{13}C$ of –60‰ for bacterially produced methane. This exercise found several notable effects including a dramatic increase in weathering rates, a reduction in ocean pH, and a shoaling of the CCD and lysocline all within several thousand years (Fig F8). The effects on the ocean were greatest in areas proximal to deepwater formation where the excess CO_2 entered the deep ocean via convective processes. The CCD is eventually restored, although not to its original position, as the system appears to initially overcompensate before returning to a steady state. This predicted pattern is consistent with the PETM low carbonate or clay layers in many deep-sea PETM sites (Fig. F9).

The clathrate dissociation model can be tested with deep-sea drilling. A series of paleodepth transects in each of the major ocean basins would allow for characterization of the lysocline/CCD changes during this event. The initial shoaling should be expressed as a dissolution interval or hiatus in deeper sites coincident with the benthic foraminifer extinction and carbon isotope excursion. The model-predicted overshoot should be preserved as well. Existing PETM sequences show a reduction in carbonate content to varying degrees coincident with the excursion. However, without vertically offset sites, it is not yet possible to quantify the extent to which the reduction in carbonate content reflects changes in microfossil preservation or the depth range over which the carbonate changes are present. With a series of drill sites placed along vertical depth transects, it should be possible to separate effects of preservation from production. A Pacific Ocean depth transect was recently completed by ODP Leg 198 (Bralower, Premoli Silva, Malone, et al., 2002), and Walvis Ridge was targeted to provide a complementary Atlantic Ocean depth transect. Walvis Ridge is well suited for a depth transect, as rates of sedimentation are fairly high and continuous through the upper Paleocene–lower Eocene over most of the ridge. Leg 208 drilling on the ridge recovered the sequences needed to constrain how the deep-ocean carbonate chemistry changed during the important event.

An interesting new development is the emergence of evidence of additional biotic events and carbon isotope excursions. Faunal and isotope data from Sites 690 and 865 (Thomas and Zachos, 2000; Thomas et al., 2000) point toward other times with conditions potentially similar to, but not as extreme as, those of the PETM during the late Paleocene and early Eocene. If these lesser events have a similar origin as the PETM, we would expect lesser but similar scale responses in ocean carbonate chemistry. Drilling at Blake Nose shows similar repetition of the climatological/ sedimentological conditions of the Paleocene/Eocene (P/E) boundary. A long-term record of the gamma ray log (X-ray fluorescence [XRF] Fe data) (Röhl et al., 2003) of Site 1051 shows a series of major peaks that represent a reduction in the carbonate content and/ or increased terrigenous flux augmenting the clay content. Cyclicity of clay accumulation on the timescale of ~2 m.y. most likely reflects climate cycles, although the precise nature of the climatic changes is unknown. One of the gamma ray (or XRF Fe data) maxima coincides with the carbon isotope event and peaks again near the top of Chron C24r (Shipboard Scientific Party, 1998, Röhl et al., 2003). Similar cycles persist throughout the Eocene, indicating this warm greenhouse period was not stable (e.g., Wade and Kroon, 2002). The long-term periodicity in these records may reflect a long-period orbital cycle (~2 m.y.).

A continuous record, spanning at least 8 m.y. of the upper Paleocene and lower Eocene, is required to evaluate the possibility of Milankovitch-driven climate.

Middle Eocene to Early Oligocene Glaciation(s)

The primary transition from “greenhouse” to “ice-house” conditions occurred during the middle Eocene to early Oligocene. Although this interval encompasses 18 m.y., stable isotopic records reveal a steplike pattern, with much of the change occurring in just a few relatively brief steps in the earliest–middle Eocene (~52 Ma) and earliest Oligocene (Fig. F10) (EOGM; ~33.4 Ma) (e.g., Miller et al., 1987; Kennett and Stott, 1991; Zachos et al., 1996). The first event marks the onset of ephemeral glacial activity (Browning et al., 1996; Hambrey et al., 1991), whereas the second and larger of the two steps, the EOGM, represents the first appearance of permanent ice sheets on Antarctica (Barrera and Huber, 1991; Zachos et al., 1992). Furthermore, the highest-resolution deep-sea isotope records of this transition indicate that the final transition may have been modulated by orbital forcing (Diester-Haass and Zahn, 1996).

The climatic transition during the EOGM should have had a dramatic effect on oceanic/atmospheric circulation patterns and continental weathering rates and, hence, ocean chemistry. For example, reconstructions of bottom water isotope patterns hint at a brief pulse of a proto-North Atlantic Deep Water (NADW) coincident with the EOGM (Miller et al., 1991; Zachos et al., 1996). Also, carbonate sediment accumulation patterns suggest a significant deepening of the CCD at the Eocene/Oligocene (E/O) boundary (Peterson and Backman, 1990; van Andel, 1975; Lyle, Wilson, Janecek, et al., 2002). The latter is consistent with a sudden lowering of sea level and/or an increasing chemical weathering of continents, both of which would increase the flux of dissolved ions to the deep sea. However, the CCD on a regional or local scale is also sensitive to changes in the rates and patterns of carbonate production. A depth transect is required to separate the relative contributions of each process and to more robustly constrain rates of change.

Oceanic Recovery from the Cretaceous/Paleogene Mass Extinction

The Cretaceous/Paleogene (K/P) impact and mass extinction triggered a number of changes in oceanic properties, some long lasting. These changes include (1) a drastic decrease in the export production as indicated by decreased carbon isotopic gradients (Fig. F11) (Hsü et al., 1982; D’Hondt et al., 1998; Stott and Kennett, 1989; Zachos et al., 1989) and reduced barium accumulation rates, (2) a sharp decrease in deep-sea carbonate accumulation (D’Hondt and Keller, 1991; Zachos and Arthur, 1986), and (3) at least in the South Atlantic Ocean, enhanced 100-k.y. oscillations in deep-sea sedimentation (D’Hondt et al., 1996). Each of these changes was likely caused by the profound changes in pelagic ecosystems at the time of the K/P mass extinction and sustained for a half-million years or longer by the slow ecological recovery on evolutionary timescales. The final recovery from several of these changes is poorly constrained. For example, although we know that deep-sea carbonate accumulation did not recover for >2 m.y. after the mass extinction (Zachos and Arthur, 1986), the final recovery of deep-sea carbonate accumulation has only been identified at a single Caribbean site (ODP Site 1001) where carbonate accumulation rates did not recover until 4 m.y. into the Paleogene (D’Hondt et al., 1998). Poor core recovery has precluded successful identification of this final recovery in previously drilled South Atlantic Ocean sites. However, the improved recovery through modern ODP drilling techniques made it possible to acquire a complete APC-cored section in two holes at Site 1262.

The K/P mass extinction effectively changed the state of the global ecosystem, and documenting the timing of these recoveries and their relationships to other paleoceanographic properties will provide a critical test of the coupling between oceans, climate, and biota. There is little reason to believe that any physical consequences of the K/P impact could have lingered for more than a few thousand years. Consequently, the Maastrichtian through Paleocene record of deep-sea sediments provides an ideal opportunity for testing the sensitivity of the global environment to biological disaster. For example, the long-term decrease in deep-sea carbonate accumulation might have changed oceanic alkalinity and atmospheric CO_2 concentrations. If so, the interval of decreased carbonate accumulation should be marked by changes in various paleoceanographic proxies, such as increased foraminiferal preservation and migration of the lysocline or CCD. Similarly, the 100-k.y. oscillations in lower Paleocene deep-sea sediments may have resulted from a decreased ability of postextinction biota to buffer seasonal and Milankovitch-scale climate change (Herbert et al., 1995; Herbert and D'Hondt, 1990; D'Hondt et al., 1996). If so, these oscillations should correspond to similar oscillations in various paleoceanographic proxies, such as carbon isotopic differences between planktonic and benthic foraminifers.

Paleogene Deepwater Circulation and Chemical Gradients

Changes in either the meridional thermal gradient or precipitation patterns can dramatically alter the mode of ocean circulation, thermohaline or otherwise (Broecker, 1997). Warming of polar regions coupled with increased precipitation, for example, would tend to lower the density of high-latitude surface waters and thereby inhibit sinking. This, in turn, might be balanced by increased convection elsewhere, possibly in subtropical regions where high rates of evaporation raise seawater salinity and density. Given the extreme thermal gradients and precipitation patterns, it is likely that deep convection during the PETM, and possibly during the EECO, was affected at high latitudes. If true, there should be evidence for this in deepwater chemical gradients as inferred from stable carbon isotopes and the distribution of carbonates on the seafloor.

A shift in the source of waters bathing Walvis Ridge should be reflected in carbon isotope, carbonate dissolution, and benthic assemblage patterns, as well as in patterns of other isotopes with short residence times (i.e., Nd). Through much of the late Paleocene and early Eocene, the most negative deep-ocean carbon isotope values were consistently recorded by benthic foraminifers from the Pacific ocean (Kennett and Stott, 1990; Corfield, 1994; Corfield and Norris, 1996; Corfield and Cartlidge, 1992; Pak and Miller, 1992). Although this gradient is of the same sign as the modern one, it is much smaller, indicating that Pacific Ocean deep waters were only slightly older than Atlantic Ocean deep waters. As such, one would predict a similar CCD in the two basins. Low-resolution records of carbonate accumulation on Walvis Ridge for the Cenozoic suggest large-scale changes in the CCD at the P/E and E/O boundaries although these "events" are not well defined (Moore, Rabinowitz, et al., 1984).

Neogene Paleoceanography

Although the main focus for ODP Leg 208 was the recovery of Paleogene sediments, the younger part of the Walvis Ridge record is of considerable interest to paleoceanographers. The overlying Neogene sediments recovered during Leg 74 served to resolve several important paleoceanographic issues. For example, Shackleton et al. (1984) used oxygen isotopes to reveal long-term temperature trends of surface and deep waters for the Neogene in the Walvis Ridge area, and Moore, Rabinowitz, et al. (1984) used microfossil preservation to reconstruct carbonate saturation changes.

Today the lysocline depth is present at the boundary between NADW and Antarctic Bottom Water (AABW) between 4 and 4.8 km on the western side of the Mid-Atlantic Ridge. On the eastern side of the Mid-Atlantic Ridge, Walvis Ridge divides the South Atlantic Ocean into the northern Angola and southern

Cape Basin. This basinal topography blocks the AABW from directly entering the Angola Basin; instead, AABW enters through the Romanche Fracture Zone, where it mixes with NADW and forms a less defined NADW–AABW transition at ~5 km (Berger et al., 2002; Volbers and Henrich, 2002). Thus, the lysocline is deeper in the eastern Atlantic Ocean, although Schmiedl et al. (1997) argue that AABW is present at depths of ~4200 m to the north of Walvis Ridge.

Microfossil preservation improved markedly in the late Miocene (Moore, Rabinowitz, et al., 1984) at Walvis Ridge, suggesting the onset or intensification of NADW production and its increased influence within the Angola Basin. Another step of increased carbonate preservation occurs near the beginning of the Pliocene. However, detailed reconstruction from DSDP Leg 74 sites were hampered by poorly constrained age models and low recovery.

As part of ODP Leg 208, we intend to employ cyclostratigraphy to improve the accuracy of dating by tuning the sedimentary cycles to the astronomical cycles of Milankovitch as far back as possible. This technique has been used to improve the dating of the sedimentary record during several paleoceanographic legs. The astronomical timescale has been established back to the late Oligocene by using cyclostratigraphy in sediments of drill holes at Ceara Rise (Lourens et al., in press). The Walvis Ridge sediments show distinct cycles in certain intervals detected by visual means (Borella, 1984). However, sedimentary cycles were previously documented primarily in the Cretaceous and Paleogene parts of the geological record. High-resolution natural gamma radiation and magnetic susceptibility variability examinations on board the *JOIDES Resolution* during Leg 208, combined with multiple drill holes at every site, have revealed cycles throughout the Neogene.

Oxygen isotope records of carbonate microfossils will identify the long-term trends in the climate system and particularly the high-resolution structure of the mid-Miocene Climatic Optimum (MCO). High-resolution stable isotope records in an astronomically tuned time frame are expected to document small-scale ice expansions (so-called Mi events, e.g. Miller et al., 1991) and associated sea level changes during the Miocene. At present, the amplitude of the $\delta^{18}O$ profiles recording the intensity of these Mi events is poorly known.

The depth transect recovered during ODP Leg 208 is ideal for studying the vertical structure of the ocean throughout the Neogene. Carbon isotope records should establish deepwater characteristics of the waters bathing Walvis Ridge within the Angola Basin. Carbonate preservation profiles and benthic foraminiferal assemblages will be used to document the evolution of Neogene deepwater (e.g., presence and relative abundance of *Cibicidoides wuellerstorfi*). Identification of the timing of the intensification of NADW influence in the South Atlantic Ocean within the Miocene will be a primary focus of our study. Numerous microfossil datums will be calibrated employing the astronomically tuned Neogene timescale.

The eastern South Atlantic Ocean is characterized by intense upwelling in the Benguelan system. Although the ODP Leg 208 sites are located outside of the modern upwelling realm, stronger trade wind activity during glacials could have extended these upwelling filaments to Walvis Ridge (Little et al., 1997). ODP Leg 208 sediments may, therefore, hold clues on upwelling intensity during the Pliocene–Pleistocene period through planktonic foraminiferal assemblages that are sensitive to productivity changes. Moreover, benthic foraminiferal assemblages will provide information on seasonal variability in export productivity (e.g., relative abundance of *Epistominella exigua* and *Alabaminella weddellensis*).

Cenozoic Cyclostratigraphy

One of the main objectives for ODP Leg 208 drilling is to establish a cyclostratigraphy throughout the entire Cenozoic in order to construct an astronomical timescale for each of the sites. Establishment of such an astronomical timescale is critical for virtually all the objectives of ODP leg 208 drilling, especially for the upper Maastrichtian through lower Eocene, which currently lacks an orbitally tuned timescale. This lack of high-quality, high-resolution, and multicore sequences along a depth transect has slowed progress in reconstructing Paleogene paleoceanography and climate history. An orbitally tuned timescale is also essential for resolving rates of paleoceanographic change associated with the abrupt, short-lived events.

Drilling Objectives

To meet these scientific objectives, the primary drilling focus was to recover sediments representing each of the target intervals over a depth range of 2 km. Moreover, it was essential that these intervals be stratigraphically continuous and have sufficiently high sedimentation rates to resolve orbital cycles to at least the 41-k.y. periodicity. Reconstruction of the nature of the oceanic response to each of the target events further required that relatively unlithified sequences be recovered, from which well-preserved microfossils could be extracted for geochemical analysis. The preservation of these calcareous microfossils needed not to be perfect but sufficient to resolve relative differences in isotopic and elemental ratios of benthic and planktonic fauna reflective of changes in the oceanic thermal and chemical structure.

Overall, these objectives were achieved in material recovered at six sites at Walvis Ridge during ODP Leg 208. The K/P boundary interval was recovered at two sites, Sites 1262 and 1266. Three copies of the PETM were recovered at each of five sites over a depth range of 2300 m (Site 1263) to 4700 m (Site 1262). Two holes were drilled at Site 1264 to recover a nearly complete sequence for the Oligocene through Pleistocene. In addition, successful APC coring at all sites produced excellent and continuous recovery of most of the targeted intervals. Despite some condensed and unconformities, temporal coverage of the Paleogene through Neogene sedimentary sequences was excellent. The upper Maastrichtian interval was largely complete despite the necessary shift to XCB coring to recover chalky intervals at Site 1267.

Site Survey and Coring Strategy

During Leg 74 drilling in the Walvis Ridge area, the PETM and other critical intervals were not recovered at all sites, in part because of poor recovery and in part because of local unconformities. These unconformities, which appear erosional in nature, were most common in the Eocene and Oligocene sediments, particularly at shallow to middepth sites. These sites (DSDP Sites 525, 528, and 529) were located near gaps (channels) in the ridge that might explain the discontinuous nature of sedimentation. Based on seismic surveys, areas to the east of the existing sites appeared to provide more continuous sequences, which have a higher potential of recovering critical intervals. Thus, *Meteor* Cruise M49/1 (see report by Spieß et al., 2003) surveyed an area along the northeastern flank of Walvis Ridge that included the Leg 72 sites (Fig. F1). The main survey grid focused on a region to the north and east of the Leg 74 sites, away from a large channel that dissects the ridge to the southwest (Fig. F2). A seismic grid was established with several lines crossing existing sites in order to establish ages of key regional reflectors and sedimentary packages. Because of extensive upper Cenozoic downslope sediment transport throughout the region, the survey also targeted several isolated bathymetric highs where sediment transport might be minimal. The resultant M49/1 multichannel seismic profiles were then used, and existing DSDP site data were then used to locate stratigraphically continuous sequences of lower Cenozoic sediment at relatively shallow burial depths.

We designed a depth transect with 5 primary and 11 alternate sites (Fig. F2; Table T1). Based on the data, the unconformities encountered during Leg 74 appeared to be highly localized and more expanded, possibly continuous, sequences were identified. We maximized our potential to recover the P/E boundary and other key target intervals by selecting sites that had relatively thick Paleogene sequences and thin Neogene cover. In some instances, this approach required placing sites in channels where the Neogene was thinner but lower Paleogene horizons and bedding appeared uniform. A large number of alternate sites were identified for flexibility to move to a new site should a local unconformity be encountered at the P/E boundary.

The primary proposed sites for Leg 208, WALV-8A (Site 1264), -8E (Site 1263), -9B (Site 1265), -10F (Site 1266), -11B (Site 1267), and -12A (Site 1262), spanned a water depth range from 2507 to 4760 m. The stratigraphic targets for the two shallowest proposed sites, WALV-8E and WALV-9B (water depths of 2717 and 3059 m), included the PETM and EOGM in upper Paleocene to lower Oligocene chalks and oozes. We avoided areas near DSDP Site 525, where the upper Eocene and lower Oligocene are absent, and areas near Site 529, where several slumps were identified. Proposed Site WALV-10F (Site 1266), located to the south of Site 528 at an intermediate depth of 3811 m, appeared to contain a similar Paleogene sequence, but with much thinner Neogene cover. The deepest proposed site, WALV-12A (Site 1262), was located well north of DSDP Site 527 at 4770 m. Proposed Site WALV-11B was located near Site 527 but at a slightly shallower water depth of 4365 m.

A complete Paleogene sequence, including the PETM and EOGM excursions and the underlying K/P boundary, was the primary objective. Upper Paleocene sediments were drilled at five sites (Sites 1262 and 1264–1267), the upper Maastrichtian and lower Paleocene at two (Sites 1262 and 1267), and the Neogene at all six sites, including Site 1264 from which the lower Oligocene through Pleistocene was recovered. At least two APC and/or XCB cores were taken at each site to ensure recovery of a complete sequence, and cores were overlapped between holes to facilitate compilation of a composite section. During drilling composite sections were assembled using core log data (magnetic susceptibility, natural gamma radiation, and color reflectance) for correlation. In several cases, a third hole was cored to ensure recovery of at least two complete copies of the target intervals. This occurred when the target interval fell within core gaps of either of the first two holes or when the section was only partially cored.

SITE SUMMARIES

Site 1262

Latitude: 27°11.15′S
Longitude: 1°34.62′E
Water depth: 4755 m
Maximum depth of penetration: 213 meters below seafloor (mbsf)
Oldest formation: late Maastrichtian
Time on site: 4.69 days (1300 hr on 24 March–0530 hr on 29 March)

Site 1262 (proposed Site WALV-12A) is located at the northwestern end of the Walvis Ridge drilling transect and represents the deep end-member of the depth transect (Figs. F12, F13). At 4.75 km depth, Site 1262 is close to the level of the present-day lysocline and CCD, which in this sector of the eastern Atlantic Ocean are below 4.8 and 5.0 km, respectively. Close proximity to the CCD appears to be maintained for much of the Cenozoic as the rate of local subsidence has more or less kept pace with the long-term deepening of the CCD. As a result, Site 1262 is uniquely situated to record major changes in regional and/or global ocean carbon chemistry and/or circulation. As the deep end-member of the Walvis Ridge transect, Site 1262 was drilled with the objective of recovering sections suitable for detailing changes in bottom water chemistry and circulation at abyssal depths during several of the key paleoceanographic events of the Paleogene including the Eocene–Oligocene transition, the PETM, and the K/P boundary extinction. Initial results indicate that this objective was achieved.

Three holes, offset ~20 m from each other, were cored at Site 1262 using the APC coring system. A 213-m-thick section of upper Maastrichtian to Pleistocene nannofossil ooze and clay was recovered. Hole 1262A was started 6 m below the mudline and prematurely terminated at 150 mbsf because of a severed core barrel. Hole 1262B was cored from the mudline to 210 mbsf, and Hole 1262C was cored from 90 to 213 mbsf. Nominal recovery exceeded 100% in all three holes. Using magnetic susceptibility (MS) data, cores from the three holes were correlated by depth shifting and representative intervals were spliced together to create a single stratigraphic section with a total length of 236 meters composite depth (mcd).

Three lithologic units and five subunits were recognized (Fig. F14). Unit I (0–46 mcd) consists of upper Miocene to Pleistocene nannofossil ooze and foraminifer-bearing nannofossil ooze with sedimentation rates up to 10 m/m.y. Unit II (46–90 mcd) is divided into three distinct subunits based on the relative abundance of clay. Subunits IIA (46–68 mcd) and IIC (79–90 mcd) are upper Oligocene to upper Miocene and middle to upper Eocene clay units separated by a lower Oligocene nannofossil clay interval (68–79 mcd). Unit III (90–213 mcd) consists of upper Maastrichtian to upper Eocene clayey nannofossil ooze. Biostratigraphic results show the section to be stratigraphically complete in the Pleistocene and in the upper Paleocene–lower Eocene intervals with sedimentation rates up to 12 m/m.y. The middle to upper Eocene is highly condensed. Calcareous microfossils are generally well preserved at this site, particularly in the lower Eocene and upper Paleocene.

Sharp transitions between carbonate- and clay-rich facies at Site 1262 are an expression of the deepening of the CCD and related changes in ocean carbon chemistry and/or circulation. The carbonate-rich facies include the Pleistocene, Pliocene, lower Oligocene, Paleocene and lower–middle Eocene, and Maastrichtian intervals. The clay-rich facies include the Miocene and middle to upper Eocene sections as well as several discrete layers at the P/E and K/P boundaries. Preliminary age assignments indicate that each of the major facies changes at Site 1262 corresponds to a previously documented shift in the level of the CCD. The Pliocene and Pleistocene sedimentation rates of up to 10 m/m.y. are consistent with moderate rates of carbonate dissolution in this part of the Atlantic Ocean (Fig. F15). Dissolution occurred primarily during the Pleistocene glacial maxima, when the lower boundary of NADW shoaled and allowed more corrosive AABW to cross over into the Angola Basin through mid-ocean-ridge fracture zones. The facies transition between lithologic Units II and I reflects on a regional deepening of the CCD during the late Miocene and earliest Pliocene as has also been recorded in other cores from the abyssal Atlantic Ocean. Regional deepening of the CCD indicates that the Angola Basin would have been filled primarily with more corrosive AABW prior to the late Miocene, and the CCD would have shoaled. Similarly, the carbonate-rich lower Oligocene interval (lithologic Subunit IIB) implies a deep CCD, whereas the underlying upper Eocene clay (lithologic Subunit IIC) implies a shallow CCD. The contact between these two units is sharp, indicating that the CCD descent occurred rapidly, possibly in the span of two obliquity cycles as suggested by observations of Pacific cores recovered during Leg 199. The transition back into clay-rich facies in the mid-Oligocene does not imply a shoaling CCD but, rather, the local deepening of the seafloor via subsidence.

The most prominent clay layer at Site 1262 is a 60-cm-thick unit at the P/E boundary (base at 140.04 mcd) that is embedded within a thick and uniform sequence of upper Paleocene and lower Eocene foraminifer nannofossil ooze. The benthic foraminiferal extinction event occurs just below the base of this layer at 140.18 mcd, as does a major shift in nannofossil abundances from *Fasciculithus* to

Zygrhablithus. The basal color contact is relatively sharp, although magnetic susceptibility data indicate a more gradual, steplike increase in clay content over the lower 20 cm, with at least two brief reversals. The upper contact, although gradational, is relatively sharp compared to P/E boundary sections recovered at shallower water depths. Still, the overall pattern is consistent with other pelagic records and is inferred to result from seafloor carbonate dissolution because of the input of methane-derived CO_2. Overlying the clay layer is a sequence of nannofossil ooze, which is noticeably richer in carbonate than the unit immediately underlying the clay layer. This is an important feature of this boundary sequence as it confirms another prediction of the hydrate dissociation model (e.g., an overcompensation in global carbonate deposition driven by weathering feedbacks). In theory, such a feedback would be a natural response to rapid input of a large mass (2000 Gt) of carbon dioxide.

Another anomalous clay layer is present at the K/P boundary at 216.58 mcd. The basal contact of this layer is sharp, both in color and in MS. This clay layer gradually grades upward into clay nannofossil ooze over several meters. The lowest Danian biozones are well represented, if not expanded, in this section. The Pα and P1a zones are 0.4 and 1.0 m thick, respectively. Preservation of foraminifers and calcareous nannofossils is excellent, particularly in the clay-rich layers above the boundary. Many of the “dwarfed” foraminifer specimens exhibit “glassy” texture and should be particularly useful for geochemical and textural studies. The post-extinction flora is dominated by *Thoracosphaera* spp. Key marker species *Cruciplacolithus primus* and *Cruciplacolithus tenuis* first appear at 214.5 and 213.8 mcd, respectively. The boundary is present in the upper third of a reversed zone, Chron C29R, although postcruise analysis of discrete samples is required to confirm the chron boundaries. The combination of orbitally paced bedding cycles, stratigraphic continuity, and excellent fossil preservation will permit further refinement of key biostratigraphic datums, as well as testing of models concerning the rate of ecosystem recovery following mass extinction.

Pervasive bedding cycles are expressed in the MS, color reflectance, and other high-resolution core logging data at Site 1262. The lower Eocene and upper Paleocene cores, in particular, are characterized by pronounced decimeter- to meter-scale bedding cycles. The variance is concentrated in three frequency bands. The shorter cycles have a frequency close to that of the orbital precession, whereas the longer oscillations have frequencies similar to the 100- and 400-k.y. eccentricity cycles. Assuming pacing by precession, the total number of high frequency cycles in the upper Paleocene and lower Eocene would suggest that the sequence is stratigraphically continuous. The bedding cycles are even more pronounced in the Maastrichtian with power, again, mostly concentrated in the precession and eccentricity bands. Above the K/P boundary, the power shifts into the 100-k.y. eccentricity band. This phenomenon results from a 75% reduction in accumulation rates, primarily in the carbonate component. As previously recognized in most pelagic K/P boundary sequences, carbonate accumulation rates do not recover until much later in the Cenozoic. The presence of these orbitally paced cycles in stratigraphically complete sections provides a unique opportunity to astronomically calibrate the duration of Paleocene and lower Eocene chrons.

Site 1263

Latitude 28°31.98′S
Longitude: 02°46.77′E
Water depth: 2717 m
Maximum depth of penetration: 345.6 mbsf
Oldest formation: late Paleocene

Time on site: 6.79 days (1515 hr on 29 March–015 hr on 5 April)

Site 1263 (proposed Site WALV-8E) is located along the northwestern flank of Walvis Ridge just a few hundred meters beneath the summit (Figs. F16, F17). At 2.72 km water depth, this site represents the shallow end-member of the Leg 208 depth transect. Situated well above the level of the CCD throughout the Cenozoic, Site 1263 was expected to yield a stratigraphically continuous and expanded sequence of Paleogene pelagic nannofossil ooze. The primary objective was to recover sedimentary sections with sufficient resolution to detail orbital scale changes in bottom water chemistry and circulation at shallow bathyal depths during several of the key paleoceanographic events of the Paleogene including the Eocene–Oligocene transition, EECO, and the PETM. Ideally, this requires 100% recovery of the sedimentary section with minimal coring disturbance, a requirement that is best met by using APC coring. To this end, the site was positioned along a slope just beneath the ridge crest where the Neogene overburden is thin and the Paleogene target intervals are at subbottom depths of <300 m.

Four holes, offset ~20 m from each other, were cored at Site 1263 using the APC and XCB coring systems to recover a 346-m-thick section of upper Paleocene to Pleistocene nannofossil ooze and chalk. Hole 1263A was cored with the APC from the mudline to 284 mbsf and with the XCB to 346 mbsf. Hole 1263B was cored with the APC from 46 to 262 mbsf and with the XCB to 339 mbsf. Hole 1263C was cored with the APC from 90 to 119 mbsf and from 203 to 286 mbsf and with the XCB to 291 mbsf. Hole 1263D was cored with the APC from 272 to 287 mbsf. Nominal recovery averaged ~100% with the APC and ~60% with the XCB. Total nominal recovery for the site was 91%. Using MS data, cores from the four holes were aligned by depth shifting and representative intervals were spliced to create a continuous stratigraphic section for the Eocene and uppermost Paleocene extending from 48 to 340 mcd. The sections above and below were not completely recovered. Cores in those intervals were depth shifted, assuming a constant growth rate of 18% in the composite section. The total length of the composite is 401 mcd.

The sediments recovered at Site 1263 are comprised predominantly of calcareous nannofossil ooze and chalk with relatively little downhole variability (Fig. F18). Calcium carbonate contents are typically 90–95 wt% (except for the P/E boundary interval). As a result, only one lithologic unit and three subunits were recognized. Subunit IA (0–99.1 mcd) is upper Eocene to Pleistocene foraminifer-bearing nannofossil ooze and nannofossil ooze. The Pliocene–Pleistocene interval (0–26 mcd) has sedimentation rates of 1–6 m/m.y. The upper Oligocene to upper Miocene section (26–48 mcd) is condensed, shows evidence of extensive winnowing as well as reworking and downslope transport (slumps and turbidites), and possibly contains one or more hiatuses. The upper Eocene to lower Oligocene section (48–99 mcd) appears to be complete, although reworking is indicated by calcareous microfossils. Subunit IB (99.1–318.0 mcd) is a nannofossil ooze, clay-bearing nannofossil ooze, and chalky nannofossil ooze with occasional layers of volcanic ash and disseminated chert or chert stringers, most of which were easily penetrated by the APC. Eocene Subunit IB has sedimentation rates of 5–15 m/m.y. (Fig. F19). The Paleocene to lowermost Eocene Subunit IC (318.0–400.7 mcd) is composed of nannofossil ooze and chalky nannofossil ooze. Several chert horizons are present in the upper Paleocene section. The P/E boundary interval is represented by a 100-cm-thick “clay” layer at ~335 mcd. The basal contact is sharp with MS rising rapidly and carbonate content decreasing from ~90 wt% to <1 wt% over the first 5 cm of the transition. The upper contact is gradational with carbonate content increasing to >90 wt% over 100 cm. Sedimentation rates in Subunit IC are generally 10–20 m/m.y. and reach 30 m/m.y. near the top of the subunit in the lowermost Eocene.

The P/E boundary clay layer proved to be an exceptionally challenging target to recover at this site. At the level of the clay layer in Hole 1263A (285 mbsf), the APC took only a partial stroke but still penetrated into the top of the layer, 40 cm of which was captured in the core catcher. Switching to the XCB in the next core, we were able to recover another 50 cm of the clay layer. However, the contact with underlying Paleocene ooze, which was softer, appeared unconformable. In Hole 1263B, we elected to use the XCB to penetrate the boundary layer. This time, ~30 cm of the upper portion of the partially silicified clay unit lodged in the core catcher, apparently as the core was being cut. As a result, the remaining portion of the clay layer and uppermost Paleocene were washed away. In Hole 1263C, we again elected to use the APC, this time backing off a few meters to allow the core barrel to attain maximum velocity before striking the critical sediment interval. Although the stroke was only partial, the core barrel penetrated the entire clay layer plus 50 cm of the underlying Paleocene ooze. Because this represented the only copy of the entire P/E clay layer at this site, we decided to drill a fourth hole. In Hole 1263D we applied the same strategy as in the previous hole, firing the APC from a point 2 m above the bottom of the hole. This time the core barrel penetrated just the upper 30 cm of the clay layer. The second APC attempt, again fired from 2 m above the bottom of the hole, penetrated the remaining 50 cm of the clay layer as well as 150 cm of the upper Paleocene. As a result, the basal contact was recovered intact, providing the second complete copy of the critical interval for this site.

The moderate sedimentation rates and generally high carbonate content of the Site 1263 sediments are consistent with the relatively shallow depth of the site. During the Paleogene, the site remained well above the lysocline depth (<2 km). This is most evident with the presence of carbonate-rich upper Eocene and Oligocene sections, which are largely represented by condensed clay units in deeper segments of the ridge and surrounding seafloor. The lone exception is the 1-m-thick P/E boundary interval at 335 mcd, which is present within a thick and uniform sequence of upper Paleocene and lower Eocene foraminifer nannofossil ooze. The benthic foraminiferal extinction event occurs just below the base of this layer at 335.4 to 335.7 mcd. This coincides with a major shift in nannofossil abundances from *Fasciculithus* to *Zygrhablithus*. The overall pattern of the P/E boundary interval is consistent with other pelagic records and is inferred to result from seafloor carbonate dissolution resulting from the input of methane-derived CO_2 during the event. The fact that this site was at a paleodepth of 1400 m, ~2000 m shallower than Site 1262, attests to the scale of seafloor carbonate dissolution during this event.

The Site 1263 sediment record displays pervasive bedding cycles as expressed in the MS, color reflectance, and other high-resolution core logging data. The middle and lower Eocene, in particular, are characterized by pronounced decimeter- to meter-scale bedding cycles. The variance is concentrated in three frequency bands. The shorter cycles have a frequency close to that of the orbital precession, whereas the longer oscillations have a frequency similar to the 100- and 400-k.y. eccentricity cycles. Both the frequency and amplitude of the bedding cycles are similar to those observed at Site 1262 and should permit high-resolution correlation of units.

Site 1264

Latitude: 28°31.95′S
Longitude: 2°50.73′E
Water depth: 2505 m
Maximum depth of penetration: 282.8 mbsf
Oldest formation: early Oligocene
Time on site: 2.9 days (1310 hr on 5 April–1140 hr on 8 April)

Site 1264 (proposed Site WALV-8A) is located at a water depth of 2505 m at the crest of a north–south trending segment of Walvis Ridge in the uppermost segment of the Leg 208 Walvis Ridge depth transect

(Figs. F16, F20). At 2.5 km depth, the site is well above the level of the present day lysocline and CCD, which in this sector of the eastern Atlantic Ocean are below 4.8 and 5.0 km, respectively. As a result, Site 1264 is uniquely situated to record major changes in regional and/or global ocean carbon chemistry, ocean circulation, and the thermal evolution of the regional surface waters. Site 1264 was drilled as part of a two-site approach to the shallow water depth end-member of the Walvis Ridge transect. With a relatively expanded Oligocene to Neogene sediment sequence, Site 1264 was drilled with the objective to recover sections suitable for detailing changes in intermediate bottom water chemistry and circulation during key paleoceanographic events such as the Oligocene–Miocene transition, the MCO, and the late Pliocene–Pleistocene cooling in association with accelerated ice growth in the Arctic. Initial results indicate that this objective was achieved.

We recovered a ~273-m-thick sequence of lower Oligocene to Pleistocene nannofossil ooze at Site 1264. Three holes, offset ~20 m from each other, were cored by using the APC coring system. Hole 1264A was started few meters below the mudline and was terminated at 280.7 mbsf. Hole 1264B was cored from the mudline to 282.8 mbsf. One core was taken in Hole 1264C to confirm the mudline and recover the topmost sediments. A total of 566.5 m was cored and 563.8 m of sediment were recovered (average nominal recovery = 99.5%). Using color reflectance and MS core logging data, cores from Holes 1264A and 1264B were correlated by depth-shifting to create a mcd scale. Representative intervals were spliced together to create a single, nearly complete stratigraphic section for Site 1264.

The Site 1264 sediment sequence is divided into two lithologic units, with the lower unit divided into two subunits (Fig. F21). Unit I (0–29.4 mcd) consists of middle Pliocene–Pleistocene nannofossil foraminifer ooze, foraminifer nannofossil ooze, and foraminifer-bearing nannofossil ooze. Unit II (29.4–316.5 mcd) is divided into two subunits. Subunit IIA (29.4–117.0 mcd) consists of white upper Miocene to middle Pliocene nannofossil ooze and foraminifer-bearing nannofossil ooze. Subunit IIB (117.0–316.5 mcd) includes brown lower Oligocene to upper Miocene nannofossil ooze and foraminifer-bearing nannofossil ooze. Unit II sediments contain volcanic ashes and abundant oxides. Interstitial waters show high concentrations of iron in Subunit IIA, whereas Subunit IIB interstitial waters include high levels of manganese ions. Color reflectance and MS records from the recovered sequence at Site 1264 show centimeter- to meter-scale bedding cycles throughout. Centimeter-scale light bluish gray bands in Subunit IIB may represent orbital or even suborbital cycles.

Biostratigraphic results show that a nearly complete Neogene and upper Oligocene section is present, although a hiatus representing ~0.6 m.y. occurs in the upper Miocene (Fig. F22). The middle Miocene interval is condensed relative to the other parts of the record. In general, calcareous microfossils are reasonably well preserved at this site, although preservation deteriorates in the lower part of the record. Oligocene benthic foraminifers reveal downslope transport and reworking at Site 1264. Because of a pervasive overprint, only a few paleomagnetic reversals could be recognized. Sedimentation rates range from 5 to 10 m/m.y. in the Oligocene to middle Miocene, with the highest rates in the lower Miocene. Sedimentation rates are highly variable in the upper Miocene and Pliocene, ranging from 10 to 30 m/m.y.

Site 1265

Latitude 28°50.10′S
Longitude: 02°38.35′E
Water depth: 3060 m
Maximum depth of penetration: 321 mbsf
Oldest formation: late Paleocene

Time on site: 6.9 days (1410 hr on 08 April–1130 hr on 15 April)

Site 1265 (proposed Site WALV-9B) is located along the northwestern flank of Walvis Ridge just a few hundred meters beneath the summit (Figs. F16, F23). At 3.08 km water depth, this site represents the shallow middepth site of the Leg 208 depth transect. Situated above the level of the CCD throughout the Cenozoic, Site 1265 was expected to yield a stratigraphically continuous and expanded sequence of upper Paleocene and lower Eocene pelagic nannofossil ooze. The primary objective was to recover sedimentary sections with sufficient resolution to characterize high-frequency changes in bottom water chemistry and circulation at shallow bathyal depths during several of the key climatic events of the Paleogene including the Eocene–Oligocene transition, the EECO, and the PETM. Ideally, this requires complete recovery of the sedimentary section with minimal coring disturbance, a requirement that is best met by using the APC. To this end, the site was located in a broad channel at the base of a slope extending down from the ridge crest. Because the Neogene is relatively condensed here, the key Paleogene target intervals are at subbottom depths of <300 mbsf.

Four holes, offset ~20–30 m from each other, were cored at Site 1265 using the APC and XCB coring systems to recover a 321-m-thick section of upper Paleocene to Pleistocene nannofossil ooze and chalk. Hole 1265A was cored with the APC from the mudline to 286 mbsf and with the XCB to 321 mbsf. Hole 1265B was cored with the APC from the mudline to 252 mbsf, where mechanical problems prevented further penetration and required the recovery of the drill string. Hole 1265C was cored with the APC from 185 to 204 mbsf, where the same problem as in Hole 1265A occurred and the drill string had to be recovered again. Hole 1265D was cored with the XCB from 248 to 270 mbsf and by the APC to 275 mbsf to recover the P/E boundary. Total nominal core recovery for the site was 95%. Using MS and color reflectance (red/blue) data, cores from the four holes were aligned by depth shifting and representative intervals were spliced to create a nearly continuous stratigraphic section for the uppermost Paleocene to Pleistocene, extending from 0 to 316 mcd. Two small (<1 m) gaps exist in the lower Eocene interval. Cores from the upper Paleocene, where recovery was low, were depth shifted by extrapolating a constant growth rate of 14% from the correlated interval. The total length of the composite is 359 mcd.

The sediments recovered at Site 1265 are predominantly composed of nannofossil ooze, foraminifer-bearing nannofossil ooze, foraminifer-nannofossil ooze, nannofossil-foraminifer ooze, clay-bearing nannofossil ooze, and a foraminifer- and clay-bearing nannofossil ooze (Fig. F24). The sequence has been divided into two lithologic units and several subunits. Lithologic Unit I (0–55.8 mcd) is composed of upper Miocene to Pleistocene foraminifer-bearing nannofossil ooze and nannofossil ooze. Lithologic Unit II (55.8–359.1 mcd) is composed of upper Paleocene to middle Miocene nannofossil ooze with rare intervals of foraminifer-bearing nannofossil ooze and clay. Unit II is further subdivided into three subunits. Subunit IIA (55.8–192.7 mcd) consists of lower Oligocene to upper Miocene nannofossil ooze and foraminifer-bearing nannofossil ooze. Subunit IIB (192.7–248.5 mcd) is lower to upper Eocene nannofossil ooze, with occasional intervals of foraminifer-bearing nannofossil ooze. The contact between Subunits IIA and IIB represents the E/O boundary and is marked by a step increase in MS and step decrease in color lightness. Subunit IIC (248.5 – 359.1 mcd) is a Paleocene to lower Eocene nannofossil ooze and foraminifer-bearing nannofossil ooze.

The P/E boundary clay layer was recovered with mixed success. In Hole 1265A, the entire clay layer was recovered intact in Core 208-1265A-29H (317 mcd), the last full-stroke APC of the hole. In Hole 1265B, the APC became stuck in the core barrel at 251.7 mbsf (~288.7 mcd), just ~30 m above the target interval. In Hole 1265C, during our attempt to spot core the lower Eocene and upper Paleocene sediment, the core barrel again became stuck, this time at 204 mbsf (~229.7 mcd). After several XCB cores were taken in Hole

1265D, we returned to APC to core the boundary interval. A partial stroke (4.8 m) penetrated the top of the clay layer and recovered 50 cm in the core catcher. A second APC, fired from 2 m above the bottom of the hole, advanced <1 m and recovered an additional 10 cm of the clay layer.

Based on biostratigraphy, the sequence appears to be relatively complete over the upper Paleocene and lower Eocene, upper Oligocene and lower Miocene, and upper Pliocene. The middle Eocene is condensed, and unconformities spanning ~7 and ~3 m.y., respectively, are present at the lower/middle and middle/upper Eocene boundaries (Fig. F25). An unconformity spanning ~2–3 m.y. is present at the Miocene/Pliocene boundary. Sedimentation rates range from 10 to 25 m/m.y. in the upper Paleocene and lower Eocene, from 4 to 12 m/m.y. in the upper Eocene to middle Miocene, and from 8 to 14 m/m.y. in the Pliocene–Pleistocene. Downslope reworking of microfossils, particularly foraminifers, is common in the middle Eocene through Pliocene sequences.

A number of "bioevents" is recorded in Site 1265 that are also recorded at the other Leg 208 Sites. These include an early Miocene Bolivinid abundance acme at 85–87 mcd, an event recorded elsewhere in the Atlantic and Indian Oceans. Several discrete *Braarudosphaera* layers are also present in the upper Oligocene between 154 and 161 mcd. These layers, which are prominent throughout the south Atlantic Ocean, particularly at sites along the margins, are recorded at precisely the same stratigraphic level in each of the Leg 208 sites.

The moderate sedimentation rates and generally high carbonate content of the Site 1265 sediments are consistent with the relatively shallow depth of the site. During the Paleogene, the site apparently remained above the lysocline depth with the exception of several brief periods in the latest Paleocene and early Eocene, including the P/E boundary. The latter is marked by an abrupt contact between upper Paleocene nannofossil ooze and lower Eocene dusky red, zeolite- and nannofossil-bearing clay that grades upcore into nannofossil ooze. The minimum carbonate concentration at this "intermediate" depth site is ~30 wt%, whereas minimum values near 0 wt% characterize the deeper and shallower Sites 1262 and 1263, respectively. Either carbonate was bioturbated into the first centimeters above the contact at Site 1265 or the earliest Eocene is not represented at Site 1265. Moreover, the P/E boundary interval is marked by sharp increases in MS and a decrease in color lightness. The benthic foraminiferal extinction event occurs just below the base of this layer at 318.81 to 318.86 mcd. This coincides with the brief appearance of excursion planktonic foraminifer taxa and slightly precedes an abundance shift in nannofossils from *Fasciculithus* to *Zygrhablithus*.

Site 1265 sediments record pervasive bedding cycles as expressed in the MS, color reflectance, and other high-resolution core logging data. The lower Eocene, in particular, is characterized by pronounced decimeter- to meter-scale bedding cycles. The variance is concentrated in three frequency bands. The shorter cycles have a frequency close to that of the orbital precession, whereas the longer oscillations have a frequency close to the 100- and 400-k.y. eccentricity cycles. Both the frequency and amplitude of the bedding cycles are similar to those observed at Sites 1262 and 1263, which should permit high-resolution correlation of units.

Site 1266

Latitude: 28°32.55′S
Longitude: 2°20.61′E
Water depth: 3798 m
Maximum depth of penetration: 334.2 mbsf
Oldest formation: late Paleocene

Time on site: 5.6 days (1405 hr on 15 April–0445 hr on 21 April)

Site 1266 (proposed Site WALV-10F) is located along the northwestern flank of Walvis Ridge (Figs. F16, F26). At 3.8 km water depth, this site represents one of the middepth sites of the Leg 208 depth transect. Situated near the level of the CCD throughout the Cenozoic, Site 1266 was expected to yield a stratigraphically continuous and expanded sequence of upper Paleocene and lower Eocene pelagic nannofossil ooze. The primary objective was to recover sedimentary sections with sufficient resolution to characterize high-frequency changes in bottom water chemistry and circulation at shallow bathyal depths during several of the key climatic events of the Paleogene including the Eocene–Oligocene transition, the EECO, and the PETM. Ideally, this requires recovery of the complete sedimentary section with minimal coring disturbance; a requirement that is best met with the APC. To this end, the site was located in a broad channel at the base of a slope extending down from the ridge crest. Because the Neogene is relatively condensed here, the key Paleogene target intervals are at subbottom depths of <300 mbsf.

Three holes, offset ~20–30 m from each other, were cored at Site 1266 using the APC and the XCB coring systems to recover a 334.2-m-thick section of upper Paleocene to Pleistocene nannofossil ooze and chalk. Hole 1266A was cored with the APC to 217.1 mbsf and with the XCB to 298.6 mbsf. Hole 1266B was cored with the APC from the mudline to 7.6 mbsf. The hole was then drilled ahead to 220 mbsf without coring to save time, and the remainder of the hole (220–321 mbsf) was cored with the XCB. Hole 1266C was washed down to 62 mbsf and cored with the APC from 62 to 192 mbsf. From 192 to 245 mbsf the hole was washed again, and a single XCB core was taken from 245 to 254.5 mbsf, followed by three APC cores from 254.5 to 282.7 mbsf, which recovered the P/E critical boundary interval. Finally, the hole was completed with the XCB to 334.2 mbsf. Total nominal core recovery for the site was 98%.

Using MS and color reflectance (red/blue) data, cores from the three holes were aligned by depth shifting. A splice of representative intervals was created for the uppermost Paleocene to lowermost Eocene, the interval that contains the P/E boundary. Because the strategic decision not to double core the Pliocene–Pleistocene and upper Eocene and because of poor overlap between cores from Holes 1266A and 1266C in the Oligocene to Miocene interval, recovery of a complete section was not achieved in those intervals and cores from the Pleistocene down to lowermost Eocene were depth shifted, assuming a constant mcd growth rate of 15%.

The sediments recovered at Site 1266 are comprised predominantly of nannofossil ooze, foraminifer-bearing nannofossil ooze, foraminifer-nannofossil ooze, nannofossil-foraminifer ooze, clay-bearing nannofossil ooze, and foraminifer- and clay-bearing nannofossil ooze (Fig. F27). The sequence has been divided into three lithologic units. Lithologic Unit I (0–76.8 mcd) is composed of uppermost Miocene to Pleistocene foraminifer-bearing nannofossil ooze and nannofossil ooze. The unit yields frequent turbidites marked by distinctive light brown layers of coarse-grained foraminifer ooze that have sharp boundaries and gradational tops. Lithologic Unit II (76.7 to 214.7 mcd) is composed of Oligocene to uppermost Miocene clay-bearing nannofossil ooze and nannofossil ooze and clay. Lithologic Unit II shows clay horizons that are a function of carbonate dissolution, and inclined and folded layers are indicative of synsedimentary slumping. Unit III includes upper Paleocene to Oligocene clay-bearing nannofossil ooze, nannofossil ooze, nannofossil chalk, and nannofossil clay. The chalky intervals are in the lower part of Unit III, mainly below the P/E boundary. Volcanic ash is a minor component throughout the sequence.

As at Sites 1263 and 1265, recovery of the P/E boundary clay layer met with mixed success. The XCB recovered only a partial clay layer in Hole 1266A (Core 208-1266A-31X), presumably because the cutting shoe rotation tends to grind away sediment at the interface of stiff clay and soft calcareous ooze. Therefore, the APC was used in the subsequent two holes. In Hole 1265B, the APC core catcher got stuck in the clay layer (Section 208-1266B-6H-CC). In Hole 1265C, the APC achieved a full stroke and recovered the entire clay layer in Section 208-1266C-17H-3.

Biostratigraphy indicates that the calcareous microfossils generally show moderate preservation. All microfossil groups indicate extensive reworking throughout the section except for the interval surrounding the P/E boundary, the prime target of Site 1266. Despite all the reworked specimens, two unconformities were recognized, one with a duration of 1.2 m.y. in the upper Miocene and the second one spanning ~37 to ~47 Ma, a large part of the middle Eocene. Sedimentation rates range from 6 to 24 m/m.y. in the upper Paleocene to lower Eocene, <4 m/m.y. in the middle Eocene, and from 4 to 8 m/m.y. in the upper Eocene to Pleistocene, not including the upper Miocene unconformity (Fig. F28).

At the approximate middepth of the Leg 208 transect, Site 1266 is critical for constraining the timing of shifts in ocean carbonate chemistry. The moderate sedimentation rates and generally high carbonate content of the upper Paleocene–lower Eocene sediments are consistent with the results at Sites 1262 and 1267. During the Paleogene, the site apparently remained above the lysocline depth with the exception of at least two brief periods. The first "pink" clay-rich layer is present in the upper Eocene interval at ~293 mcd (carbonate content = ~40 wt%). The lower Eocene "pink" layer falls in zone NP11, and has now been identified in each of the lower Eocene sequences recovered on Walvis Ridge. This ~10-cm-thick layer clearly represents a regional bedding horizon and exhibits several lithologic characteristics of the P/E boundary layer. The second prominent clay layer is the P/E boundary clay at 306.4 mcd. The P/E boundary is marked by an abrupt contact between upper Paleocene nannofossil ooze and lower Eocene dusky red zeolite- and nannofossil-bearing clay that grades upwards into nannofossil ooze. The carbonate content is 0 wt% at this "intermediate" depth site. Moreover, the P/E boundary interval is marked by sharp increases in MS and a decrease in color lightness. The benthic foraminiferal extinction event occurs just below the base of the clay layer (306.8 mcd). This coincides with a major shift in nannofossil abundances from *Fasciculithus* to *Zygrhablithus*.

The Site 1266 sediment record displays pervasive bedding cycles as expressed in the MS, color reflectance, and other high-resolution core logging data. The entire Site 1266 sequence shows cycles with different wavelengths. The Miocene sequence exhibits light gray to brown foraminifer-bearing nannofossil ooze that alternates with medium brown foraminifer-bearing nannofossil ooze on a meter scale. The lightness record shows cycles on a decimeter to meter scale. The lower Eocene, in particular, is characterized by pronounced decimeter- to meter-scale bedding cycles. The variance is concentrated in three frequency bands. The shorter cycles have a frequency close to that of the orbital precession, whereas the longer oscillations have a frequency close to the 100- and 400-k.y. eccentricity cycles. Both the frequency and amplitude of the bedding cycles are similar to those observed at Sites1262, 1263, and 1265 and should permit high-resolution correlation of units.

Site 1267

Latitude: 28°5.88′S
Longitude: 1°42.66′E
Water depth: 4355 m
Maximum depth of penetration: 329.0 mbsf
Oldest formation: late Maastrichtian
Time on site: 5.3 days (0940 hr on 21 April–1648 hr on 26 April)

Site 1267 (proposed Site WALV-11B) is located on the lower northwestern flank of Walvis Ridge, just to the southwest of DSDP Site 527 (Figs. F29, F30). At 4.35 km, it is the second deepest site of the Leg 208 depth transect. Site 1267 is above the level of the present-day lysocline and CCD, which in this sector of the eastern Atlantic Ocean are below 4.8 and 5.0 km, respectively. Close proximity to the CCD appears to be maintained for much of the Cenozoic, as the rate of local subsidence has more or less kept pace with the long-term deepening of the CCD. As a result, Site 1267 is well situated to record major changes in regional carbon chemistry and/or circulation. Site 1267 was drilled with the objective of recovering sections suitable for detailing changes in bottom water chemistry and circulation at abyssal depths during several of the key paleoceanographic events of the Paleogene including the Eocene–Oligocene transition, the PETM, and the K/P boundary extinction. Initial results indicate that this objective was achieved.

Two holes offset ~20 m from each other were cored at Site 1267 using the APC and XCB coring systems. A 329-m-thick section of upper Maastrichtian to Pleistocene nannofossil ooze and clay was recovered. Hole 1267A was drilled from the mudline to 312 mbsf. Hole 1267B was cored from the mudline to 329 mbsf. Nominal recovery exceeded 99% in both holes. Using MS and color reflectance data, cores from the two holes were correlated by depth shifting and representative intervals were spliced together to create a single stratigraphic section with a total length of 368 mcd. At least five small recovery gaps remain in the interval from 267 to 368 mcd.

The Site 1267 lithologic units are nearly identical to those identified at Site 1262 (4.76 km water depth) but thicker and with slightly higher average carbonate contents (Fig. F31). Three lithologic units and five subunits were recognized. Unit I (0–102.3 mcd) consists of upper Miocene to Pleistocene nannofossil ooze and foraminifer-bearing nannofossil ooze. Unit II (102.3–157.8 mcd) is divided into three distinct subunits based on the relative abundance of clay. Subunits IIA (102.3–124 mcd) and IIC (143–157.8 mcd) are upper Oligocene to upper Miocene and middle to upper Eocene clay layers separated by a lower Oligocene nannofossil clay interval. Unit III (157.8–368 mcd) consists of upper Maastrichtian to middle Eocene clayey nannofossil ooze and chalk.

Biostratigraphic results show the section to be stratigraphically complete, at shipboard resolution, in the Pleistocene to uppermost Miocene and in the lower Eocene through upper Maastrichtian intervals (including the P/E and K/P boundaries), with sedimentation rates typically ranging 5–15 m/m.y. (Fig. F32). Two condensed intervals (sedimentation rates <1.5 m/m.y.) span the lowermost upper Miocene through lower Oligocene (~10.4–30.0 Ma; 108–124 mcd) and a large part of the upper and middle Eocene (34.0–42.3 Ma; 146–151 mcd), respectively.

As at Site 1262, sharp transitions between carbonate- and clay-rich facies at Site 1267 are an expression of the long-term deepening of the CCD and related changes in ocean carbon chemistry and/or circulation. The carbonate-rich facies include the Pleistocene, Pliocene, lower Oligocene, Paleocene and lower–middle Eocene, and Maastrichtian intervals. The clay-rich facies include the Miocene and middle to upper Eocene sections, as well as several discrete layers at the P/E and K/P boundaries. Preliminary age assignments indicate that each of the major facies changes at Site 1267 corresponds to a previously documented shift in the level of the CCD. The Pliocene and Pleistocene sedimentation rates of up to 26 m/m.y. are consistent with moderate rates of carbonate dissolution in this part of the Atlantic Ocean but with noticeably less dissolution than that at Site 1262, which is ~400 m deeper. The facies transition between lithologic Units II and I reflects on a regional deepening of the CCD during the late Miocene and earliest Pliocene, as has also been recorded in other cores in the abyssal Atlantic Ocean. Similarly, the carbonate-rich lower Oligocene interval (lithologic Subunit IIB) implies a deep CCD, whereas the underlying upper Eocene clay (lithologic Subunit IIC) implies a shallow CCD. The contact between these two units is sharp, indicating that the CCD descent occurred rapidly. The transition back into clay-rich facies in the mid-Oligocene does not imply a shoaling CCD but, rather, local deepening of the seafloor via subsidence.

The other clay-rich layers are relatively thin but pronounced as they are imbedded within relatively carbonate rich units. They include the P/E boundary (base at 231.53 mcd) that is present within a thick and uniform sequence of upper Paleocene and lower Eocene foraminifer nannofossil ooze. The benthic foraminiferal extinction event, including the uppermost appearance of *Stensioeina beccariiformis,* occurs just below the base of this layer at 231.53–231.62 mcd. This is followed by a shift in nannofossil abundance from *Fasciculithus* to *Zygrhablithus* between 230.3 and 230.8 mcd. Planktonic foraminifers are heavily dissolved in the clay layer with only extremely rare specimens of *Acarinina soldadoensis, Acarinina coalingensis, Acarinina "chascanona,"* and *Morozovella subbotinae*. The basal color contact is relatively sharp, although MS data show a more gradual, steplike increase over the lower 20 cm. The upper contact, although gradational, is relatively sharp compared to P/E boundary sections recovered at shallower water depths. In essence, the overall pattern is consistent with other pelagic records and is inferred to result from seafloor carbonate dissolution because of the input of methane-derived CO_2. Overlying the clay layer is a sequence of nannofossil ooze, which is slightly richer in carbonate than the unit immediately underlying the clay layer.

The K/P boundary was recovered at 320.4 mcd. The basal contact of this layer is sharp, both in color and in MS. This grades upward into clay nannofossil ooze over several meters. The lowest Danian biozones, the Pα and P1a zones, are ~0.2 and 0.8 m thick, respectively. Preservation of foraminifers and calcareous nannofossils is not as good as that observed at Site 1262. Many of the "dwarfed" foraminifer specimens are dissolved and slightly overgrown. The post-extinction flora is dominated by *Thoracosphaera* spp. Key marker species *C. primus* and *C. tenuis* first appear at 314.8 and 319.3 mcd, respectively. The boundary is present in the upper third of a reversed zone, Chron C29r, although postcruise analysis of discrete samples is required to confirm the chron boundaries.

Bedding cycles as expressed in the MS, color reflectance, and other high-resolution core logging data are common at Site 1267. The lower Eocene and upper Paleocene cores, in particular, are characterized by pronounced decimeter- to meter-scale bedding cycles. The shorter cycles have a frequency close to that of the orbital precession, whereas the longer oscillations have frequencies similar to the 100- and 400-k.y. eccentricity cycles. The bedding cycles are even more pronounced in the Maastrichtian with power again mostly concentrated in the precession and eccentricity bands. Above the K/P boundary, the power shifts primarily into the 100-k.y. eccentricity band. This appears to be an artifact of a reduction in accumulation rates, primarily in the carbonate component. As previously recognized in most pelagic K/P boundary sequences, carbonate accumulation rates do not recover until much later in the Cenozoic.

LEG 208 SYNTHESIS

The sediments recovered during Leg 208 have shed new light on the nature of short-term paleoceanographic events of the last 70 m.y., while also improving upon our understanding of the general long-term trends as established by earlier cruises. DSDP Leg 74, in particular, provided the essential groundwork for Leg 208 by defining the long-term depositional history of Walvis Ridge and surrounding basins and also by identifying the presence of critical intervals, including the P/E boundary (Moore, Rabinowitz, et al., 1984). This body of work, along with new multichannel seismic profiles (Spieß et al., 2003), was essential in developing the drilling strategy employed by Leg 208.

Despite its numerous seminal contributions, the critical deficiency of Leg 74 was a technological one, the inability to continuously core sedimentary sections with minimal disturbance. The consequences of this deficiency became increasingly evident as Leg 208 progressed. Because of the exceptional core recovery in multiple holes, we were able to resolve the complete spectrum of lithologic variability down to the centimeter scale, including the orbitally paced oscillations. As a consequence, Leg 208 documented the occurrence of a number of "critical" events of the Paleogene, several either previously undocumented or poorly constrained. These include the well-known events that served as the primary targets for this cruise, the P/E and K/P boundaries, but also several heretofore unrecognized events in the early Eocene and Paleocene. Finally, Leg 208, with the depth-transect approach, was also able to establish the character of both the long- and short-term changes in the vertical dimension, a constraint that is essential to understanding both the causes and consequences of change.

In the following section, we summarize the major findings of this leg, focusing primarily on those contributions that are novel, or represent a significant improvement upon previous findings. We start with a brief summary of the chronostratigraphy, followed by an overview of the depositional history of Walvis Ridge and its relation to paleoceanographic change, and then focus on specific critical events that were documented at multiple holes.

Chronostratigraphy

Leg 208 scientists cored a total of six sites between 2.5 and 4.8 km on Walvis Ridge. Upper Maastrichtian through Pleistocene sediments were recovered at Sites 1262 (4759 m) and 1267 (4354 m), upper Paleocene through Pleistocene sediments at Sites 1266 (3797 m), 1265 (3059 m), and 1263 (2717 m), and lower Oligocene through Pleistocene sediments at Site 1264 (2507 m) (Fig. F33).

Biostratigraphy

Overall, the Pleistocene through upper Miocene section is well represented at all sites and most expanded at Site 1264. The middle through lower Miocene is relatively condensed at Sites 1264 and 1265 and highly condensed and/or interrupted by unconformities at all other sites. The upper Oligocene is present at Sites 1263 and 1265 and condensed at Site 1264. At least part of the lower Oligocene has been identified at all sites. The E/O boundary is not recovered at Site 1262 and 1267 and is present in intervals of intense reworking and dissolution at Sites 1265 and 1266. The upper and middle Eocene is highly condensed or unconformable at all sites except Site 1263. Microfossil assemblages in the middle Miocene through middle Eocene are affected to varying degrees by dissolution, reworking, and downslope transport, especially at Sites 1265–1267.

In sharp contrast, the primary drilling target, the lower Eocene through upper Paleocene, is well represented at all sites where drilled, with generally good preservation of calcareous microflora and fauna except for dissolution in the clay layer just above the P/E boundary. The lower Paleocene and upper Maastrichtian are well represented at Sites 1267 and 1262. Preservation of microflora and fauna is generally good to moderate, with some reworking and dissolution in the lower upper Paleocene and dissolution in the Maastrichtian at Site 1267.

Pleistocene

Pleistocene sediments were recovered at all sites, with the most expanded sections (~20 m) at Sites 1266 and 1267. Calcareous nannofossils are abundant and have good preservation at all sites, except within slumps at Site 1262. A complete succession of nannofossil events is present at Sites 1264, 1266, and 1267. Pleistocene assemblages of planktonic foraminifers are a mixture of well-preserved subtropical to temperate planktonic foraminifers, with good preservation at Sites 1264 and 1265 and common reworking in the basal Pleistocene at Sites 1262 and 1265–1267. Benthic foraminifers are rare and well preserved at all sites and resemble faunas presently living in the Walvis Ridge region with depth-dependent assemblage composition.

Pliocene

The most expanded Pliocene sections were recovered at Sites 1264, 1266, and 1267. The lower Pliocene is missing at Site 1263 and the uppermost upper Pliocene at Site 1265. Pliocene calcareous nannofloras consist of abundant nannofossils with good preservation. The midlatitude discoasterid markers *Discoaster asymmetricus* and *Discoaster tamalis* are common to abundant, and the occurrence of common *Scyphosphaera* spp. characterizes the lower Pliocene.

Planktonic foraminiferal biostratigraphic resolution through the upper Pliocene is limited by the scarcity of key tropical/subtropical age-diagnostic taxa (e.g., the absence of all menardellids and *Globigerinoides fistulosus*), probably because of the presence of cool temperate waters. Assemblages at Site 1264 are best preserved. Reworking is common at Sites 1262 and 1267, and there are numerous turbidites at Sites 1262 and 1266. Benthic foraminifers are generally rare but well preserved, resembling faunas presently living in the Walvis Ridge region. Downhole fluctuations in relative species abundance probably reflect variability in deepwater circulation and productivity.

Miocene

At no site was a complete Miocene sequence recovered, but the upper Miocene is present at most sites. There are unconformities across the Miocene/Pliocene boundary at Sites 1263–1265, in the upper Miocene at Site 1266, and in the lower to middle Miocene at Site 1267. The Miocene is condensed at Sites 1263, 1262, and 1267 and at several sites interrupted by turbidites. At Site 1264, most of the upper Miocene is expanded but the middle and lower Miocene is complete and relatively condensed. Calcareous nannofossil assemblages of uppermost and/or lowermost Miocene (including the Oligocene/Miocene [O/M] boundary) are rich and moderately well preserved at Sites 1264–1266. The upper Miocene markers *Discoaster quinqueramus, Discoaster berggrenii,* and *Discoaster hamatus,* the middle Miocene *Helicosphaera ampliaperta* and most of the helicoliths, and the lower Miocene *Triquetrorhabdulus carinatus* are absent at all sites. All Miocene assemblages are dominated by small and medium sized placoliths (*Reticulofenestra* spp. and *Cyclicargolithus* spp.). Miocene planktonic foraminifer assemblages have generally good preservation at Site 1264 but have been affected by dissolution at all other sites. The subdivision of the upper–middle Miocene was hampered by the general absence of the *Fohsella* clade, probably because of temperate-water conditions, although their absence may also reflect evolution toward a more stenothermal ecology.

Middle–lower Miocene benthic foraminiferal assemblages are affected by downslope transport and reworking at all sites except Site 1264. The middle Miocene benthic foraminiferal turnover could be recognized at all sites but not documented in detail because of the unconformities and condensed sections. The lower Miocene bolivinid event (defined as the HAB event; ~18 Ma) was documented at Sites 1264 and 1265.

Oligocene

There are unconformities corresponding to part of the Oligocene at Sites 1262, 1263, 1266, and 1267. The upper Oligocene is present at Sites 1263 and 1265 and condensed at Site 1264, and at least part of the lower Oligocene has been identified at all sites. Oligocene assemblages at all sites are affected by dissolution and/or reworking. Oligocene calcareous nannofossils are generally abundant and moderately preserved and show slight dissolution and low diversity. Reworked Eocene specimens are most common at

Sites 1262 and 1265. Sphenoliths vary in abundance and are rare or have a discontinuous distribution at all sites, but the marker species *S. distentus* and *S. ciperoensis* provide biostratigraphic control. Rich "*Braarudosphaera* layers" occur in Zone NP23 (CP18) at Sites 1264 and 1265. *Helicosphaera* are always rare and absent in some intervals. The succession of lowermost Oligocene events could be identified at Sites 1263, 1265, 1266, and 1267, but the lowermost Oligocene biostratigraphic marker *Isthmolithus recurvus,* a "cool-water taxon," has a discontinuous distribution. Intense dissolution and extensive reworking of planktonic foraminifers made identification of the O/M boundary problematic at Sites 1262, 1263, 1266, and 1267. This interval contains well-preserved assemblages at Site 1265, but the record is interrupted by a slump. Lower Oligocene planktonic foraminiferal assemblages were recovered at all sites but were affected by intense dissolution.

Benthic foraminiferal assemblages are affected by dissolution, reworking of older material, and severe downslope transport at all sites, least at Site 1264. In situ components are mainly long-lived common uppermost Eocene through lower Miocene bathyal through abyssal species. Transported components reflect middle bathyal or greater depths.

Eocene/Oligocene Boundary Interval

Sections spanning the E/O boundary interval are incomplete or condensed. Sites 1263 and 1265 contain the most complete records, but even these are affected by dissolution and reworking. Calcareous nannofossil events marking this critical interval could be recognized at Sites 1263, 1265, and 1266. Preservation is moderate and specimens show dissolution, etching, and reworking. The uppermost Eocene, characterized by the uppermost occurrences of the representatives of the rosette-shaped discoasters, contains reworked Paleocene and Eocene forms. Planktonic foraminiferal assemblages show severe dissolution and reworking even at Sites 1263 and 1265, and the scarcity of key marker taxa (e.g., *Turborotalia cerroazulensis, Cribrohantkenina inflata*) hindered evaluation of stratigraphic completeness. A winnowed well-sorted assemblage of thick-shelled *Globigerinatheka* spp. is present within the uppermost Eocene at Sites 1263, 1265, 1266, and 1267 and intercalated in lower Oligocene sediments at Site 1266.

Eocene

The upper Eocene sections are condensed or interrupted by unconformities at all sites, and reworking is common. The upper part of the middle Eocene is incomplete at all sites except Site 1263. At Sites 1265 and 1266 the lower boundary of the middle Eocene is also marked by unconformities. Preservation of all calcareous microfossil groups improves in the lower Eocene at all sites but deteriorates because of dissolution just above the P/E boundary. Calcareous nannofossils are diverse but moderately preserved, and discoasters show strong overgrowth. Reworking is common in the middle and upper Eocene at Sites 1265 and 1266. The upper Eocene marker species *Cribrocentrum reticulatum* is absent at all sites. The absence of several key tropical-marker species of planktonic foraminifers reduced the level to which the Eocene could be subdivided. Specifically, upper through middle Eocene sections typically lack such marker species such as *Orbulinoides beckmanni, Morozovella lehneri,* and *Hantkenina nuttalli.* The scarcity of these biostratigraphically useful species is the result of strong carbonate dissolution and/or sub-optimal environmental conditions. Biostratigraphic subdivisions of lower Eocene sediments was hindered by the absence of as *Planorotalites palmerae* and general scarcity of *Morozovella formosa,* which likely reflects unfavorable ecological conditions.

Because of condensed sections, unconformities and reworking the upper Eocene–lower Oligocene benthic foraminiferal faunal turnover marked by the uppermost occurrence of *Nuttallides truempyi* could not be documented in detail. The presence of abundant *Plectofrondicularia paucicostata* indicates unusually intensive downslope transport in the upper Eocene at Sites 1265–1267. In contrast, lower Eocene benthic foraminiferal faunas are generally well preserved and show fluctuating species richness and relative abundance of abyssaminids and small smooth-walled bolivinids.

The Paleocene/Eocene Boundary Interval

The P/E boundary was recovered at all sites except Site 1264 and is marked by a prominent clay layer, the lowermost few centimeters of which is barren or contains very few calcareous microfossils. Preservation of all microfossil groups deteriorates in the clayey layer just above the boundary as defined by the uppermost occurrence of the benthic foraminifer *S. beccariiformis* in the benthic extinction event (BEE).

Calcareous nannofossil assemblages are abundant to sparse close to the boundary. Discoasters increase in abundance and *Rhomboaster* spp. show their lowermost occurrence in the clay level. Specimens belonging to the *Rhomboaster-Tribrachiatus* plexus are poorly preserved because of recrystallization, which prevents the identification of the boundaries between Zones NP11/NP10/NP9 at most sites. *Fasciculithus* and *Zygrhablithus* show a reversal in relative abundance just above the BEE. The clay layer contains few planktonic foraminifers. The *Morozovella velascoensis* clade is poorly represented in the Walvis Ridge region, and no "excursion" taxa were present in the P/E boundary interval. The overall scarcity of *M. velascoensis* made identification of the P5/P6a zonal boundary problematic.

The benthic foraminiferal extinction event was identified at all sites at the base of the clay layer. *S. beccariiformis* is present in the uppermost Paleocene sample just below the clay layer at all sites over the full depth transect. The lowermost few centimeters of the clay layer were barren at Sites 1262, 1267, and 1266 and contained a few small specimens at Sites 1265 and 1263. Postextinction faunas are dominated by minute *N. truempyi,* abyssaminids, clinapertinids, quadrimorphinids, small species of *Bulimina, Aragonia aragonensis,* and *Tappanina selmensis*. Abyssaminids and clinapertinids are more abundant at Sites 1262 and 1267 and buliminids, *T. selmensis,* and *A. aragonensis* at the other sites.

Paleocene

There is no evidence for unconformities in the Paleocene, but there is some dissolution, reworking, and downslope transport in the lower upper Paleocene at Sites 1262 and 1267. Diverse assemblages of calcareous nannofossils with good to moderate preservation show characteristics of midlatitude assemblages. Reworked Cretaceous specimens are rare between the lower part of Zone NP8 and the K/P boundary at Sites 1262, 1266, and 1267. The "mid-Paleocene biotic event" is recognized by the lowermost occurrence of *Heliolithus kleinpellii* at the base of Zone NP6 (CP5) at Sites 1262 and 1267. The rarity of *Ellipsolithus macellus* in the lower part of its range prevents the recognition of the NP3/NP4 zonal boundary.

Abundant large planktonic foraminifers are present through much of the Paleocene. Upper Paleocene assemblages are dominated by the genera *Acarinina, Morozovella, Subbotina,* and *Globanomalina.* The "mid-Paleocene biotic event" occurs in the lower part of the upper Paleocene (basal Subzone P4a) in a clayey interval at Sites 1262 and 1267 and is marked by a short-lived increase in the abundance of small igorinid taxa (Bralower, Premoli Silva, Malone, et al., 2002; Bralower et al., 2002). Lower Paleocene (Zone P2) assemblages are dominated by the praemuricate taxa.

Benthic foraminiferal assemblages are highly diverse in the upper Paleocene, but at the three deepest sites there are strong fluctuations in the relative abundance of *Siphogenerinoides brevispinosa* and *Bulimina thanetensis.* The lowermost occurrence of the latter may mark the benthic foraminiferal expression of the "mid-Paleocene biotic event."

Upper Cretaceous/Lower Paleocene Boundary Interval

The Maastrichtian/Danian boundary was recovered at Sites 1262 and 1267 and appears to be complete at both sites, although the planktonic foraminiferal Zone P0 could not be identified. Danian calcareous nannofossil assemblages are abundant and moderately well preserved. Just above the K/P boundary, assemblages contain reworked Cretaceous specimens and are dominated by *Thoracosphaera* spp., *Biantholithus sparsus,* and *Cyclagelosphaera reinhardtii.* Calcareous nannofossils are abundant in the upper Maastrichtian. Preservation varies from good to moderate with strong dissolution and fragmentation in the uppermost Maastrichtian where the assemblages are mainly composed of solution-resistant species such as *Micula staurophora, Micula murus, Watznaueria barnesae, Lithraphidites carniolensis,* and *Lithraphidites quadratus. Nephrolithus frequens,* a "cool-water marker species," is rare.

The Danian planktonic foraminiferal assemblages contain some reworked Cretaceous specimens and abundant but diminutive planktonic foraminifers (e.g., *Woodringina hornerstownensis, Parasubbotina* spp., *Globoconusa daubjergensis*) with highly variable preservation at Site 1267 and excellent preservation at Site 1262, particularly in the clay-rich sediments just above the K/P boundary. The Maastrichtian assemblages at both sites are moderately preserved and exhibit varying degrees of etching and dissolution. As observed elsewhere, benthic foraminifer assemblages across the K/P boundary at both sites do not exhibit any evidence of significant extinction.

Magnetostratigraphy

The soft, weakly magnetized carbonate sediments recovered on Leg 208 frequently produced erratic or seemingly biased inclination records, making magnetostratigraphic interpretations difficult or impossible over many intervals. Despite this, several polarity sequences were identifiable, including most of the major boundaries in the Pliocene–Pleistocene, a good upper Miocene through Oligocene sequence at Sites 1265 and 1266, and an excellent Paleocene through Upper Cretaceous sequence at Sites 1262 and 1267.

Whereas the inclination record from the Pliocene–Pleistocene is not very clean at most sites, we were frequently able to identify major reversal boundaries. However, assignment to a particular boundary was often aided in this interval by biostratigraphic datums or cyclostratigraphy. Of particular note, Chron C2n at the Pliocene/Pleistocene boundary is identified at all sites except Site 1262.

Sites 1265 and 1266 combined to produce a good upper Miocene through Oligocene sequence. This includes the excellent resolution at Site 1265 of chron C6Cn across the O/M boundary. This chron consists of three very distinctive short normal events which, combined with the biostratigraphic data and cyclostratigraphy, should allow for the refinement of the timescale across the Oligocene/Miocene boundary.

The Eocene was generally not well resolved at any of the sites, but an excellent Paleocene to Upper Cretaceous polarity sequence was recovered at Sites 1262 and 1267 (Fig. F34). At these two sites, the Paleocene cores were recovered either by APC coring or by XBC coring in well-lithified sediments, both of which served to recover relatively undisturbed sediments over this interval.

Identification of the upper and lower boundaries of Chron C24r will be important to help constrain the placement of the P/E boundary within the chron. Unfortunately, the top of Chron C24r is not well defined in the pass-through inclination data at most sites. Data from the lower Eocene is characterized by a large amount of scatter, as well as a frequent bias in the data toward negative values. At Sites 1262 and 1266, we believe the boundary is resolved in at least one hole, but we do not place a high degree of confidence in either of these boundary assignments. It is hoped that discrete sample analysis will provide cleaner data and allow for the precise constraint of this boundary. The base of Chron C24r is clearly defined at several sites, although high-frequency discrete sampling should help to place the boundary more precisely than is possible with the pass-through archive-half data.

The boundaries of Chron C29r have also been targeted for special attention to better constrain the reversal boundary ages around the K/P boundary. The inclination record in this interval at Site 1262 is characterized by high-frequency oscillations in both inclination and intensity. It is likely that the pass-through magnetometer maps these intensity oscillations into directional changes and that discrete sample data will provide a clean record of the reversal boundaries. This problem is not seen at Site 1267, however, where the top of Chron C29r is relatively well defined. Unfortunately, the base of the chron falls in a core break in both holes.

Cycle Stratigraphy and Orbital Rhythms

Marked cyclic variations are observed in MS and color reflectance data throughout the Maastrichtian to Holocene section at all the sites. These variations are expressed as more or less strong lithologic cycles that have frequencies at the decimeter to meter scale. This cyclic variability was used to correlate between parallel holes drilled at all sites and to define a composite section for each site. About 300 major cycles (peaks) in MS correlate very well between all Leg 208 sites (Fig. F35). They were calibrated using biostratigraphic datums and used to construct a refined initial-cycle-tuned age model for the complete Leg 208 ~74-m.y.-long record (Table T2). The distinct record of cyclic alternations in sediment physical properties (Figs. F36, F37, F38) offers potential for refining the Neogene astronomical timescale and the development of an astronomically tuned timescale of the Paleogene as far back as the Late Cretaceous.

The detailed investigation of the sedimentary cycles will be the objective of intense postcruise studies. Nevertheless, initial time-series analysis on selected time series representative for distinct intervals (late Maastrichtian, early Eocene, early to early late Miocene) were already done during the cruise. Continuous wavelet analysis allows rapid localization of repetitive patterns (e.g., Torrence and Compo, 1998). The 100-k.y. cyclicity is very strong in the Miocene, whereas a 40-k.y. periodicity is less pronounced (Fig. F39). Oscillations in the composition of the pelagic sediments at frequencies to that of the Earth's precessional (~20 k.y.) cycle of insolation occur through most of the time intervals drilled during Leg 208. Also the modulation by the shorter (~100 k.y.) eccentricity cycle is nicely documented. Figures F40 and F41 show examples for the Eocene and Maastrichtian. The bedding cycle patterns in Leg 208 sites were sufficiently distinct that they could easily be correlated between sites, allowing for the development of a detailed cycle stratigraphy for nearly the entire Cenozoic.

Depositional History of Walvis Ridge and Cenozoic Paleoceanography

A key aspect of the Leg 208 drilling strategy was the depth-transect approach, the basic objective of which is to constrain time-dependent changes in sediment properties as a function of depth. In principle, this strategy provides a number of advantages for paleoceanographic studies including the ability to (1) reconstruct changes in sediment production rates, (2) contour changes in the CCD and lysocline depths, (3) establish deepwater circulation patterns, and (4) splice stratigraphic gaps in high-resolution time series. For the Leg 208 transect, the benefits of each of these advantages were clearly evident, particularly for establishing the long-term sediment accumulation history of the ridge. With the lithostratigraphic and biomagnetostratigraphic data, we were able to construct relatively coarse-scale sediment accumulation curves for each site (Figs. F42, F43, F44), distinguishing noncarbonate from carbonate accumulation. The accumulation curves were then combined with the subsidence curves to contour the depth-dependent changes in accumulation rates as a function of time (Fig. F45). The curves are based on a simple thermal subsidence model which derives ~1.8–2.0 km of subsidence over the last 65 m.y. Although the absolute ages are coarse, the relative correlations are precise as a result of the application of cycle stratigraphic tie points to the Leg 208 sites, a first for a group of sites arrayed in a depth transect. Using the MS records, a total of 286 common points of correlation were identified over the Cenozoic and Maastrichtian. These points serve as the primary tie points for site-to-site correlation.

In general, carbonate accumulation rates are highest in the Maastrichtian, Paleocene and early Eocene, and Pleistocene, and lowest in the middle and late Eocene and early–middle Miocene (Fig. F45). These time-dependant changes become much more pronounced with depth, indicating that changes in the level of the CCD and lysocline contributed to the observed patterns. The large magnitude CCD events have been previously recognized and closely correspond in time to similar changes observed in other basins (Peterson and Backman, 1990; Lyle, Wilson, Janecek, et al., 2002).

The Leg 208 records show that from the K/P boundary to the early middle Eocene, the CCD appears to have maintained a position below the deepest Site 1262 (~3.5 km at 55 Ma), with one brief exception during the PETM. During the early middle Eocene, the CCD began to rise and carbonate accumulation began to collapse, initially at Site 1262 at ~50 Ma then at Site 1267 at ~49 Ma. The CCD continued to ascend, eventually rising above Site 1266 to its shallowest level between 2.5 and 3.0 km at 44 Ma. During the late Eocene, the CCD deepened significantly in two steps, with the first at ~42 Ma and the second at ~36 Ma. The latter descent, which is global in extent, was relatively rapid and extreme. It appears that the CCD settled at depth well below Site 1262, but only briefly before gradually shoaling again within a few million years. From the mid-Oligocene to middle Miocene, the CCD fluctuated at a middepth level, roughly between 3.2 and 4.5 km, deepening briefly in the early Miocene. In the late middle Miocene, the CCD began a slow descent, eventually reaching a depth close to modern by the earliest Pliocene.

Critical Events

A major achievement of Leg 208 was the recovery of continuous undisturbed cores spanning over a half-dozen "critical" intervals or events. All the events were recovered in at least two sites, and at least three of the early Cenozoic events were recovered in five sites. The Leg 208 cores allow each to be observed in the context of orbitally paced oscillations in climate. These events are unique as they stand out against the normal background variability of environmental change. They generally coincide with biotic events such as extinctions or abundance acmes indicative of unusual environmental stress. The most prominent, the P/E and K/P boundaries, are characterized by relatively rapid and extreme change. The other events, although less extreme, show characteristics that indicate brief extremes in climate and/or ocean carbon chemistry. This includes the mid-Paleocene biotic event at 58.2 Ma, the EOGM at 33.5 Ma, the early Oligocene *Braarudosphaera* layers at 28.5–30 Ma, and the early Miocene Bolivina Acme at ~18 Ma. In addition, several previously unrecognized events characterized by P/E boundarylike clay layers, but of a smaller scale, were identified in the upper Paleocene and lower Eocene of all sites. The most distinct of these smaller events includes what is affectionately referred to as the Eocene layer of mysterious origin, or "ELMO," event at 53 Ma. The assertion that these dissolution layers are linked to global events, and not regional, is based on their presence in other ocean basins, primarily the Pacific, where they are documented in cores recovered from Shatsky Rise (Bralower, Premoli Silva, Malone, et al., 2002). The documentation of such events is of importance, as their occurrence was predicted on the basis of anomalous excursions in benthic foraminiferal assemblages (Thomas et al., 1999).

The Cretaceous/Paleogene Boundary

A remarkably well-preserved complete K/P boundary was recovered at Walvis Ridge. The boundary was cored at two Sites 1262 and 1267. Double coring at these sites resulted in a total of four separate K/P records. In Hole 1267A, the boundary was biscuited because of XCB coring, whereas the record in Holes 1262B and 1262C was APC cored. The lithologic sequence in the K/P boundary interval is similar at both sites, as they differ in water depth by only 400 m today and had the same paleodepth during the K/P interval. At Site 1267, the boundary interval was more lithified and, to a higher degree, orangish Maastrichtian chalks were recovered below the boundary.

The boundary succession is marked by an irregular boundary between the light reddish brown and brown clay-bearing nannofossil ooze with foraminifers of uppermost Maastrichtian age (nannofossil Zone CC26). Color cyclicity is recorded in both color lightness and chromaticity. Within the darker lithology, bioturbation is preserved. Two prominent ash layers were identified just below the K/P boundary at Site 1267. At the boundary, this lithology is abruptly overlain by a 2- to 3-cm-thick dark red to reddish brown clay- and Fe oxide–bearing nonbioturbated foraminifer nannofossil ooze/chalk. Microtectites are present within this reddish transition zone directly at the boundary at Site 1262. The sediment grades upward into a moderately bioturbated brown nannofossil- and foraminifer-bearing clay (foraminiferal zones Pα and P1a). The K/P boundary is marked by decreased carbonate deposition/preservation and increased clay, iron oxide, and volcanic ash accumulation, both of which produce distinctive increases in MS and lightness (Fig. F46).

Preliminary biostratigraphy at all of the K/P boundary sequences shows the well-established abrupt change in plankton assemblages across the boundary (Luterbacher and Premoli-Silva, 1964; Thierstein, 1982; Monechi, 1985). The white nannofossil ooze below the boundary yields diverse assemblages of the uppermost Maastrichtian *Abathomphalus mayaroensis* planktonic foraminifer zone and *Micula prinsii* nannofossil zone (CC26). The brown nannofossil- and foraminifer-bearing clay contains high abundance of *W. hornerstownensis, Chilobuembelina midwayensis,* and *Chilobuembelina morsei* as well as increasing abundance of *Parvularugoglobigerina eugubina* through the basal Paleocene (Pα). Based on this preliminary analysis, Zone P0 is not present at Walvis Ridge. Remarkably well preserved planktonic foraminifers of zone Pα dominate the lowermost 20 cm of the Paleocene at Site 1262 (Fig. F46), whereas at Site 1267 the preservation within the similarly thick sequence is highly variable. At this site the "dwarfed" assemblages from within subzones Pα to P1b show fragmentation and some specimen overgrowth. Large reworked specimens of Maastrichtian foraminifers are present within zone Pα at both sites, although to a lesser degree at Site 1267. The benthic foraminifer fauna just above the boundary in Hole 1267A is distinctly different from samples above and below, since *Bulimina kugleri* becomes common and *Praebulimina reussi* becomes extinct. This opportunistic species is assumed to reflect high food conditions just above the boundary.

Nannofossils in the basal Danian sediments include survivor species such as *Thoracosphaera* spp., plus the first occurrence of *B. sparsus, Markalius inversus,* and *C. reinhardtii*. Both nannofossils and planktonic foraminifers show a complete succession typical for the Danian (Luterbacher and Premoli-Silva, 1964; Monechi, 1985). The uppermost Maastrichtian at all sites shows signs of dissolution in both nannofossils and foraminifers. The planktonic foraminifers display etching and fragmentation. The minute thin-walled earliest Paleocene faunas, however, are remarkably well preserved at Site 1262, suggesting that a latest Maastrichtian lysocline shoaling resulted in samples barren of foraminifers, just prior to the K/P boundary, followed by subsequent deepening in the earliest Paleocene. A significant feature of the K/P boundaries at Site 1262 is the presence of greenish unaltered ovoid spherules that are concentrated in the first few centimeter of the basal Paleocene. No spherules have been found higher up in the sediments.

The K/P boundary is similar to records from Blake Nose (western North Atlantic Ocean) and Shatsky Rise (Pacific Ocean). The Site 1262 record shows a microtectite layer (ejecta fallout) capped by a reddish to brown iron oxide layer. This layer is overlain by a dark brown to red clay that contains planktonic foraminifers diagnostic for Zone Pα. At Walvis Ridge, in contrast to the other records, the entire early Danian is recovered in brown nannofossil and foraminifer-bearing clay, whereas at Blake Nose and Shatsky Rise the increasing carbonate content results in white foraminifer-nannofossil ooze. The ultrafine micrite at Blake Nose and Shatsky Rise is assumed to be related to the collapse of the marine biosphere that resulted in a drop in the CCD. Although Zone Pα is normally unrecovered or poorly preserved in most sites, the substantial thickness of the uppermost Maastrichtian *M. prinsii* Zone and the lowermost Danian *P. eugubina* Zone indicate the K/P boundary is paleontologically complete. Moreover, the cycle stratigraphy is very robust with distinct spectral peaks in the precession and eccentricity bands. Thus, the Walvis Ridge sections provide a well-preserved and relatively detailed record of this major extinction event and the subsequent biotic recovery.

Mid-Paleocene Biotic Event

A prominent 10- to 30-cm-thick dark brown clay-rich calcareous nannofossil ooze was found at Sites 1262 and 1267, and a 10-cm-thick brown nannofossil chalk was found at Site 1266. This layer shows a pronounced peak in MS that reflects an increase in clay content (Fig. F47). Preliminary micropaleontological investigations suggest that this interval represents a short-lived event of considerable evolutionary significance. The event has also been identified at ODP Leg 198 Sites 1209–1212 (Bralower, T.J., Premoli Silva, I., Malone, M.J., et al., 2002). This interval corresponds to the P4 *Globanomalina pseudomenardii* planktonic foraminiferal zone and coincides with the evolutionary first occurrence of the nannofossil *H. kleinpellii,* an important component of late Paleocene assemblages and a marker for the base of Zone CP5 (NP6) (early late Paleocene; ~58.2 Ma).

Fundamental changes in faunal populations occur before, during, and after the deposition of the clay-rich ooze. Planktonic foraminifers in the clay-rich layer are characterized by a low-diversity largely dissolved assemblage, dominated by representatives of the genus *Igorina* (mainly *Igorina tadjikistanensis*). This low-diversity assemblage suggests some kind of oceanic perturbation of unknown origin. Together with the documented severe dissolution in this interval, the observed lithologic changes are likely to represent a response to increased seafloor carbonate dissolution owing to a transient shoaling of the lysocline and CCD. Regardless of origin, it is now clear from the high-resolution stratigraphy of the Leg 208 sites that this is a global event. Shore-based isotopic investigations should shed light on the nature of this event.

Paleocene–Eocene Thermal Maximum

The primary objective of Leg 208 was the recovery of a South Atlantic depth transect to reconstruct the tempo and mode of regional carbonate saturation response to the global carbon-cycle perturbation during the PETM. We successfully drilled the PETM interval in multiple holes at five drill sites (e.g., Sites 1262, 1263, 1265, 1266, 1267) that covered a modern depth range of 2717 to 4755 m and an estimated paleodepth range of ~1500 to ~3500 m (Fig. F48). Shipboard physical property, lithologic, and biostratigraphic data indicate complete recovery of the Paleocene–Eocene transition interval at all sites except Site 1265, where drilling difficulties prevented recovery of the entire ooze–clay transition or the

P/E transition interval had never been fully deposited. Major patterns within and between these sites are summarized and interpreted below in the depth domain; subsequent shore-based stable-isotope and cyclostratigraphic analyses will serve to test and refine these interpretations in the time domain.

In the uppermost Paleocene, nannofossil ooze predominates across the entire depth transect. Deeper sites have slightly lower carbonate content and markedly higher MS values, whereas intrasite variance in both parameters is minimal. Microfossil preservation varies between excellent and moderate both within and between sites. These patterns are consistent with a relatively stable latest Paleocene carbonate saturation profile of increasing undersaturation at greater paleodepth and a paleo-CCD well below the deepest site (~3500 m). Notably, at the deeper Sites 1267 and 1262, the uppermost centimeters of nannofossil ooze immediately underlying the PETM clay show slightly decreasing carbonate content, increasing MS, increasing planktonic foraminifer fragmentation, and unusually small pre-extinction benthic foraminifer species. These latest Paleocene changes likely represent some combination of syndepositional shoaling of the carbonate saturation profile and postdepositional carbonate dissolution "burndown."

At the onset of the PETM, carbonate content plummets to ~0 wt%, producing a pronounced lithologic shift from nannofossil ooze to a clay interval that roughly doubles in thickness from ~10 to ~20 cm down the depth transect. This general pattern of decreased carbonate content is present throughout marine PETM records (e.g., Bralower et al., 1997; Thomas and Shackleton, 1996; Thomas, 1998; Thomas et al., 1999), and is consistent with a massive methane flux to the ocean-atmosphere inorganic carbon reservoir that elevated pCO_2 levels, decreased carbonate ion concentrations, and shoaled the carbonate saturation profile (Dickens et al., 1995, 1997). Commensurately increasing MS values show progressively more structure in the thicker clay layers of deeper sites, whereas the maximum values at each site coincide with the uppermost clay interval where carbonate content begins to recover. These complex patterns represent some combination of time-transgressive shoaling of the paleo-CCD, differential burndown of previously deposited carbonate, and increased terrigenous input from enhanced chemical weathering and erosion. Most importantly, these new data clearly demonstrate that the South Atlantic paleo-CCD shoaled much more (more than 2000 m) than predicted by current models (~400 m) (Dickens et al., 1997), suggesting the release of a much larger volume of less isotopically negative methane or an incomplete understanding of carbon cycle dynamics.

Biostratigraphically, the onset of clay deposition coincides with the highest occurrence of the benthic foraminifer *S. beccariiformis* and other typical upper Paleocene taxa (Fig. F48A). Calcareous microfossils are absent to extremely rare and generally poorly preserved in the lowermost clay, reflecting some combination of deleterious benthic conditions, decreased carbonate export production, and intensified carbonate dissolution. Lowermost Eocene benthic foraminifer assemblages occur near the base of the clay layer (Fig. F48B) and are extremely low in abundance and minute in size. *A. aragonensis, T. selmensis,* and *Bulimina* spp. predominate at shallower Sites 1263, 1265, and 1266, whereas abyssaminids and clinapertinids predominate at deeper Sites 1262 and 1267 and in the lowermost sample at the shallower sites. Nannofossils are common and show only slight dissolution. The last appearance of the planktonic foraminifer *M. velascoensis* roughly coincides with the onset of the PETM, and no related "excursion" taxa (e.g., *Morozovella allisonensis, Acarinina sibaiyaensis, Acarinina africana*) occur within the PETM—a biogeographic pattern that stands in stark contrast to those documented at lower and higher paleolatitudes (Kelly et al., 1998; Kelly, 2002). Planktonic foraminifers within the clay layer primarily consist of extremely rare and poorly preserved specimens of *A. soldadoensis*. Nannofossil assemblages within the PETM clay are markedly poorer in preservation, lower in abundance and richness, and predominated by discoasters.

The start of the PETM recovery interval may be defined as the onset of increasing carbonate content, which produced a gradational upsection lithologic sequence at each site of nannofossil-bearing clay, nannofossil clay, clay-bearing nannofossil ooze, and finally nannofossil ooze. Recovery intervals are thicker at shallower sites, likely reflecting higher overall mass accumulation rates coupled with the time-transgressive deepening of the carbonate saturation profile and commensurately earlier increases in carbonate mass accumulation rates. Magnetic susceptibility values are consistent with this scenario, with shallower sites showing more oscillations within the generally decreasing trends.

As carbonate content increased through the PETM recovery interval, planktonic foraminifer preservation improved and faunal abundance and richness increased to include morozovellids, acarininids, subbotinids, and rare globanomalinids. The first occurrences of the nannofossils *Rhomboaster cuspis* and *Rhomboaster calcitrapa,* basal members of the *Rhomboaster-Tribrachiatus* lineage, are within the recovery interval (Fig. F48C) and provide potentially isochronous biomarkers for intersite correlation. Above these nannofossil first occurrences, three prominent bioevents occur in varying stratigraphic order at all five sites: Benthic foraminifer compositions shift from earliest Eocene low-diversity diminutive assemblages to early Eocene moderate-diversity assemblages (Fig. F48D, F48E), and nannofossil assemblages show a marked relative decrease in *Fasciculithus* spp. and increase in *Zygrhablithus bijugatus* (Fig. F48C). This relative increase in *Z. bijugatus* typically coincides with the BEE in other regions (e.g., Shatsky Rise and central Pacific), but occurs much later at Walvis Ridge and may be correlative with the *Fasciculithus–Rhomboaster* abundance reversal reported at equatorial Pacific Sites 1220 and 1221 (Lyle, Wilson, Janecek, et al., 2002). These intersite differences in bioevent ordination may represent incomplete sampling coverage or real paleoenvironmental differences between sites.

A subtle, but potentially important, final lithologic feature of the PETM recovery interval is the restabilization of carbonate content and magnetic susceptibility values at slightly higher and lower values, respectively, than their pre-PETM values. This pattern is present at other PETM sites (e.g., Southern Ocean Site 690) and is consistent with numerical simulations by Dickens et al. (1997), which predict a transient lysocline overdeepening to result from the oceanic mass-balancing of increased bicarbonate, carbonate, and Ca^{++} concentrations (via enhanced chemical weathering and runoff) as concurrent carbonate dissolution decreased CO_2-derived H+ concentrations and increased Ca^{++} concentrations (Broecker and Peng, 1982; Walker and Kasting, 1992).

Chron C24N "ELMO" Event

At ~20 to 35 m above the P/E boundary, a red-colored 5- to 15-cm carbonate-depleted layer was found at all sites covering the early Eocene (Figure F49). This layer, tentatively called the "ELMO" event, was a faithful indicator point for estimating the depth to the underlying P/E boundary in the parallel holes of each site. The ELMO event shows similar color characteristics as the P/E boundary layer as well as a drop in the MS values and calcium carbonate content of the sediment and an increase in natural gamma radiation values but not as intense. The ELMO event is characterized by a split drop in the 1-cm point MS records of all sites, which are marked by events A and B in Figure F49. At the shallowest sites (1263 to 1266), events A and B are most distinctly developed, whereas in the deepest sites (1267 and 1262) they are merged together. At the latter sites, an additional drop in MS values is observed slightly above the ELMO event. At the middepth Site 1266, a thin white-colored layer is found immediately above the red-colored layer.

This layer, which appears to be present in the MS records of sites drilled on Shatsky Rise, is associated with benthic foraminifer assemblages similar in character to those of the PETM. This implies a transient shift of paleoenvironmental conditions toward those documented for the PETM.

Eocene/Oligocene Boundary and Early Oligocene Glacial Maximum

Sediment recording the response of tropical South Atlantic sediment to global cooling and CCD deepening at the Eocene–Oligocene transition was recovered across a broad depth range on the northeastern flank of Walvis Ridge (Sites 1262, 1263, 1265, 1266, and 1267 in a total of nine holes). Reworking, downslope transport, and dissolution of microfossils prevent a detailed stratigraphy from being established across the E/O boundary. Nonetheless, the available nannofossil and planktonic foraminiferal data, combined with magnetostratigraphy, suggests that the boundary interval is relatively complete at the shallowest Site 1263 but highly condensed or unconformable at the deeper Sites 1262 and 1267. At the middepth Sites 1265 and 1266, the upper Eocene and lower Oligocene sediments show extensive reworking and dissolution (Fig. F50). Despite the extensive reworking, systematic pronounced lithostratigraphic changes are observed at all sites across this transition. That they are clearly correlatable on a coarse scale suggests these changes reflect on regional and global events.

The deep Sites 1262 and 1267 record abrupt lithologic changes over a ~0.5-m interval in the uppermost Eocene and lowermost Oligocene, from brown clay below to light brown to gray nannofossil ooze or foraminifer-bearing nannofossil ooze above. This transition is associated with a distinct decrease in MS and a corresponding increase in color reflectance lightness (L*); gamma ray attenuation (GRA) bulk density exhibits no uniform trend across these two sites. Carbonate content increases from <20 wt% to >80 wt% at the deeper sites. In comparison to the condensed deep sites, the E/O transition interval is greatly expanded at the two shallow sites. Here, decreases in MS and GRA bulk density and an increase in L* occur gradually over a 2- to 5-m petrographic shift from light brown clay-bearing nannofossil ooze to very pale brown nannofossil ooze.

The E/O boundary is associated with a marked increase in sedimentation rates and a general improvement in microfossil preservation at all sites. Whereas late Eocene nannofossils in most sections show a high degree of etching, early Oligocene assemblages show less dissolution and slightly more overgrowth. At the deepest site in the transect, planktonic foraminifers are largely absent because of intense carbonate dissolution; the Site 1262 transition interval is defined by nannofossil zones. Comparatively, the succession of nannofossil events that characterize the Eocene–Oligocene transition, including the distinctive boundary between Subzones CP16c and CP16b (NP22/NP21), first occurrence of *Ericsonia formosa,* have been recognized at the shallowest Site 1263. Planktonic foraminifers generally show better preservation, but are much more fragmented across the Eocene–Oligocene transition in this site as well. At all sites, the lithologic transition appears to be accompanied by a significant increase in carbonate accumulation rates as well (Fig. F50).

Increased carbonate content and improved microfossil preservation across the boundary interval indicate that the lysocline and CCD deepened substantially and rapidly along this transect during the Eocene–Oligocene transition. In the latest Eocene, the CCD on Walvis Ridge was between the paleodepths of Sites 1266 and 1267; based on the highly condensed upper Eocene sequence of Site 1267, we infer that it was likely nearer the paleodepth of Site 1266. After the Eocene shoaling, the CCD returned to a depth well below Site 1262. The “Oi-1” is estimated mainly from color reflectance L* (Fig. F50) and magnetostratigraphy, which places C13N at this level. At all sites, the carbonate values peak for a short interval that corresponds to this normal. These events suggest that this CCD migration may be related to the first widely accepted sustained glaciation of Antarctica. This shift is also observed in other ocean basins (e.g., Zachos et al., 1996) including the Pacific where the timing is tightly constrained by cores recovered by Legs 198 and 199 (Bralower, T.J., Premoli Silva, I., Malone, M.J., et al., 2002; Lyle, Wilson, Janecek, et al., 2002). By tightly constraining the timing and magnitude on a global scale, it should be possible to determine what role, if any, climate change played in driving this unique transition in ocean chemistry.

Early Oligocene *Braarudosphaera* Blooms

ODP Leg 208 recovered several intervals from the early Oligocene that contain nannofloras highly enriched in calcareous debris derived from *Braarudosphaera* dinocysts. Although still poorly understood, the recurrence of *Braarudosphaera* layers is thought to reflect unusual paleoceanographic conditions. This inference is supported by the global occurrence of braarudosphaerids among survivor assemblages preserved immediately following the K/P mass extinction. The exotic character of *Braarudosphaera* assemblages is further enhanced by the scarcity of other contemporaneous nannofossil taxa.

Braarudosphaera layers were recovered from all sites except the two deepest, Sites 1262 (4759 m) and 1267 (4378 m). Cursory examination revealed that two separate braarudosphaerid-rich layers were recovered at Site 1263 (Fig. F51). The upper braarudosphaerid layer is preserved within Section 208-1263A-6H-2 (~50 mcd) and is assigned to nannofossil Zone NP23 and planktonic foraminiferal Zone P20, whereas the lower braarudosphaerid layer from Sample 208-1263A-9H-3, 27 cm (83.84 mcd), is assigned to nannofossil Zone NP21 and planktonic foraminiferal Zone P18. Only one prominent *Braarudosphaera* layer was recovered at Sites 1264 (Core 208-1264A-29H) and 1265 (Core 208-1265A-15H). Much like the upper braarudosphaerid layer from Site 1263, these layers are from sediments belonging to nannofossil Zone NP23 and may represent a single *Braarudosphaera* depositional event that blanketed Walvis Ridge. The exact thicknesses of these braarudosphaerid layers is presently unknown.

Previous drilling throughout the South Atlantic Ocean has documented the presence of multiple *Braarudosphaera*-enriched layers in lower Oligocene sequences on both the Rio Grande Rise and Walvis Ridge. In the southwestern Atlantic Ocean atop the Rio Grande Rise, early Oligocene *Braarudosphaera* deposits have been recovered at DSDP Site 22 (Maxwell, Von Herzen, et al., 1970), and Site 516. One of the braarudosphaerid layers from DSDP Site 22, termed the "Maxwell Marker" for its distinctive acoustic properties, was described as an indurated chalk containing a nannoflora composed of 100% braarudosphaerid fragments (Maxwell, Von Herzen, et al., 1970).

In the southeastern Atlantic Ocean along Walvis Ridge, numerous *Braarudosphaera* layers from the early Oligocene have been recovered from Sites 362, 363, 522, 526 (Bolli et al., 1978; Hsü et al., 1984; Moore, Rabinowitz, et al., 1984). *Braarudosphaera* deposits around the Walvis Ridge region exhibit a strong spatial pattern, being most common and prominent closer to shore. Despite having been discontinuously cored, a lower Oligocene section drilled off the coast of Africa (Site 362) yielded at least 34 separate *Braarudosphaera* layers (Bukry, 1978).

Modern braarudosphaerids are most common in high-nutrient, low-salinity coastal waters and are extremely rare in today's open ocean. Moreover, the paleobiogeographic distribution of fossil braarudosphaerids, which extends from the Early Cretaceous to the Holocene, is strongly biased toward neritic coastal plain deposits (Perch-Nielsen, 1985). Thus, the temporal and spatial focusing of *Braarudosphaera* deposits in lower Oligocene sequences from the subtropical South Atlantic Ocean has been the source of much speculation among paleoceanographers.

Most hypotheses advanced to account for this glaring biogeographical anomaly have invoked reduced sea-surface salinities (e.g., Bukry, 1978). It has been proposed that pulses of deglacial meltwater decreased sea-surface salinities throughout the subtropics, thereby fostering the *Braarudosphaera* blooms (Bukry, 1978). Other proposed mechanisms have speculated that upwelling of low-salinity nutrient-laden waters triggered *Braarudosphaera* blooms (Siesser, 1978; Melguen, 1978; Peleo-Alampay et al., 1999). Another suite of hypotheses invokes taphonomic redepositional processes such as submarine slumps and/or surface-water current transport to explain the presence of "nearshore" braarudosphaerids in open-ocean, pelagic sediments (e.g., Maxwell, Von Herzen, et al., 1970; Maxwell, 1970).

Recent study of stable isotope data derived from assemblages of well-preserved depth-stratified foraminiferal species indicates that enhanced upwelling over glacial/interglacial timescales fueled the recurrence of massive *Braarudosphaera* blooms at Site 363 (Kelly et al., in press). The coherent structure of these stable isotope stratigraphies argue against large-scale redepositional mechanisms. This interpretation is corroborated by the presence of *Braarudosphaera* layers draped atop topographic highs along Walvis Ridge as those at Site 526. Hence, open-ocean *Braarudosphaera* layers recovered by ODP Leg 208 at Sites 1263–1265 may reflect exceptionally large blooms that extended far offshore. These enigmatic deposits represent a wealth of untapped information about rhythmic changes to the ocean/climate system throughout the subtropical South Atlantic region.

Early Miocene High Abundance of Bolivinids

Deep-sea benthic foraminifers show a gradual but profound faunal overturn in the middle Miocene, which started in the late early Miocene before the middle Miocene cooling (e.g., Thomas and Vincent, 1987). Before these gradual faunal changes, however, a highly unusual event occurred in benthic foraminiferal faunas in the western Atlantic and eastern Indian Oceans. Small, smooth species of the genus *Bolivina* reached extremely high relative abundances (>60%) at bathyal to abyssal open-ocean locations (Thomas, 1986; Smart, 1992; Smart and Murray, 1994; Smart and Ramsay, 1995). The bolivinids are very small and recognized only in studies of the small size fraction (>63 µm).

The event was called the HAB event (Smart and Ramsay, 1995) and can not be explained by observations on recent benthic foraminifers: high relative abundances of bolivinids occur within oxygen minimum zones under zones of upwelling along continental margins and in the silled basins off California (e.g., Bernhard and Sen Gupta, 1999). It is not clear whether such bolivinid-rich assemblages form in response to the high organic flux, the lack of oxygen, or the combination of both. The HAB event is recognized throughout the eastern Atlantic Ocean, northwest Indian Ocean, and Mediterranean Sea (Smart and Ramsay, 1995) but not in the eastern equatorial Pacific (Sites 573, 574, and 575) (Thomas, 1985) and eastern Indian Ocean (Site 758) (C.W. Smart, unpubl. data). Because of the spatial extent of the event, Smart and Ramsay (1995) speculated that the bolivinids outcompeted other species in locations bathed by low-oxygen waters derived from Tethyan sources that reached into the western Indian and eastern Atlantic Oceans. However, these explanations of the HAB event are unsatisfactory because there is no evidence in the sedimentary record for low-oxygen conditions or extremely high organic productivity during the event.

Pagani et al. (1999) identified a pronounced increase in the carbon isotopic composition of alkenones coeval with the HAB event at DSDP Site 608 in the North Atlantic Ocean. The carbon isotopic composition of alkenones is strongly controlled by nutrient concentrations in the modern ocean, therefore, these authors suggested that increased algal growth rates (responding to increased local availability of nutrients) and export productivity could have affected the benthic faunas. A linkage between the HAB event and primary producers in the surface waters is also suggested by the fact that the beginning of the HAB event is coeval with the lowermost occurrence followed by strong increase in abundance of the nannofossil taxon *Sphenolithus belemnos* at DSDP Site 608 (Olafsson, 1991).

A scenario involving regional changes in surface water nutrients precludes a Tethyan role for the HAB event and supports the hypothesis that a nutrient-rich water mass (possibly similar to Antarctic Intermediate Water) was introduced into the ocean basins where the HAB occurred or the hypothesis that the water-column stratification changed regionally. The timing of the end of the HAB event closely coincides with the termination of the early Miocene Climatic Optimum and possibly the rapid expansion of the East Antarctic ice sheet, and the oceanographic conditions responsible for the HAB event may have been due to changes in ocean heat transport that forced early to middle Miocene cooling.

Smart and Murray (1995) identified the HAB event at Walvis Ridge Site 529. During Leg 208, we identified the HAB event at Sites 1264 and 1265, where its lower boundary is coeval (at shipboard sample resolution) with the lowermost occurrence of *S. belemnos* at Site 608 in the northeastern Atlantic Ocean. The time interval in which the event occurred (range of *S. belemnos*) is present, although very thin, in the sediments at Site 1266 and may also yield these aberrant faunas. Preliminary shipboard cyclostratigraphy places the HAB event at Sites 1264 and 1265 in a very similar section of the record (Fig. F52), suggesting that detailed comparison of the timing and intensity of the HAB event over a depth range of >1000 m will be possible.

REFERENCES

Axelrod, D.I., 1984. An interpretation of Cretaceous and Tertiary biota in polar regions. *Palaeogeogr., Palaeoclimatol., Palaeoecol.,* 45:105–147.

Barrera, E., and Huber, B.T., 1991. Paleogene and early Neogene oceanography of the southern Indian Ocean: Leg 119 foraminifer stable isotope results. *In* Barron, J., Larsen, B., et al., *Proc. ODP, Sci. Results,* 119: College Station, TX (Ocean Drilling Program), 693–717.

Barrera, E., and Huber, B.T., 1993. Eocene to Oligocene oceanography and temperatures in the Antarctic Indian Ocean. *In* Kennett, J.P., Warnke, D.A., (Ed.), *The Antarctic Paleoenvironment: A Perspective on Global Change.* Antarct. Res. Ser., 49–65.

Barron, E.J., 1985. Explanations of the Tertiary global cooling trend. *Palaeogeogr., Palaeoclimatol., Palaeoecol.,* 50:45–61.

Berger, W.H., Lange, C.B., and Wefer, G., 2002. Upwelling history of the Benguela-Namibia system: a synthesis of Leg 175 results. *In* Wefer, G., Berger, W.H., and Richter, C. (Eds.), *Proc. ODP, Sci. Results,* 175: College Station TX (Ocean Drilling Program), 1–103 [CD-ROM]. Available from: Ocean Drilling Program, Texas A&M University, College Station TX 77845-9547, USA.

Berner, R.A., 1991. A model for atmospheric CO_2 over Phanerozoic time. *Am. J. Sci.,* 291:339–376.

Berner, R.A., Lasaga, A.C., and Garrels, R.M., 1983. The carbonate-silicate geochemical cycle and its effect on atmospheric carbon dioxide over the past 100 million years. *Am. J. Sci.,* 283:641–683.

Bernhard, J.M., and Sen Gupta, B.K., 1999. Foraminifera of oxygen-depleted environments. *In* Sen Gupta, B.K., (Ed.), *Modern Foraminifera:* Dordrecht (Kluwer Academic Publishers) 141–160.

Bice, K.L., Scotese, C.R., Seidov, D., and Barron, E.J., 2000. Quantifying the role of geographic change in Cenozoic ocean heat transport using uncoupled atmosphere and ocean models. *Palaeogeogr., Palaeoclimatol., Palaeoecol.,* 161:295–310.

Bolli, H.M., Ryan, W.B.F., et al., 1978. *Init. Repts. DSDP,* 40: Washington (U.S. Govt. Printing Office).

Borella, P.E., 1984. Sedimentary petrology and cyclic sedimentation patterns, Walvis Ridge Transect, Leg 74, Deep Sea Drilling Project. *In* Moore, T.C., Jr., Rabinowitz, P.D., et al., *Init. Repts. DSDP,* 74: Washington (U.S. Govt. Printing Office), 645–662.

Bralower, T.J., 2002. Evidence of surface water oligotrophy during the Paleocene–Eocene Thermal Maximum: nannofossil assemblage data from Ocean Drilling Program Site 690, Maud Rise, Weddell Sea. *Paleoceanography,* 17:1023.

Bralower, T.J., Premoli Silva, I., and Malone, M.J., 2002. New evidence for abrupt climate change in the Cretaceous and Paleogene: an Ocean Drilling Program expedition to Shatsky Rise, Northwest Pacific. *Geol. Soc. Am. Today,* 12:4–10.

Bralower, T.J., Premoli Silva, I., Malone, M.J., et al., 2002. *Proc. ODP, Init. Repts.,* 198 [CD-ROM]. Available from: Ocean Drilling Program, Texas A&M University, College Station TX 77845-9547, USA.

Bralower, T.J., Thomas, D.J., Zachos, J.C., Hirschmann, M.M., Röhl, U., Sigurdsson, H., Thomas, E., and Whitney, D.L., 1997. High-resolution records of the late Paleocene thermal maximum and circum-Caribbean volcanism: is there a causal link? *Geology,* 25:963–966.

Bralower, T.J., Zachos, J.C., Thomas, E., Parrow, M., Paull, C.K., Kelly, D.C., Premoli Silva, I., Sliter, W.V., and Lohmann, K.C., 1995. Late Paleocene to Eocene paleoceanography of the equatorial Pacific Ocean: stable isotopes recorded at Ocean Drilling Program Site 865, Allison Guyot. *Paleoceanography,* 10:841–865.

Broecker, W.S., 1997. Thermohaline circulation, the Achilles heel of our climate system: will man-made CO_2 upset the current balance? *Science,* 278:1582–1588.

Broecker, W.S., and Peng, T.-H., 1982. *Tracers in the Sea:* Palisades, NY (Eldigio Press).

Browning, J.V., Miller, K.G., and Pak, D.K., 1996. Global implications of lower to middle Eocene sequence boundaries on the New Jersey Coastal Plain—the Icehouse cometh. *Geology,* 24:639–642.

Bukry, D., 1978. Cenozoic silicoflagellate and coccolith stratigraphy, southeastern Atlantic Ocean, Deep Sea Drilling Project Leg 40. *In* Bolli, H.M., Ryan, W.B.F., et al., *Init. Repts. DSDP,* 40: Washington (U.S. Govt. Printing Office), 635–649.

Cande, S.C., and Kent, D.V., 1992. A new geomagnetic polarity time scale for the Late Cretaceous and Cenozoic. *J. Geophys. Res.,* 97:13917–13951.

Chave, A.D., 1984. Lower Paleocene–Upper Cretaceous magnetostratigraphy, Sites 525, 527, 528, and 529, Deep Sea Drilling Project Leg 74. *In* Moore, T.C., Jr., Rabinowitz, P.D., et al., *Init. Repts. DSDP,* 74: Washington (U.S. Govt. Printing Office), 525–532.

Clyde, W.C., and Gingerich, P.D., 1998. Mammalian community response to the latest Paleocene thermal maximum: an isotaphonomic study in the northern Bighorn Basin, Wyoming. *Geology,* 26:1011–1014.

Corfield, R.M., 1994. Palaeocene oceans and climate: an isotope perspective. *Earth-Sci. Rev.,* 37:225–252.

Corfield, R.M., and Cartlidge, J.E., 1992. Oceanographic and climatic implications of the Paleocene carbon isotope maximum. *Terra Nova,* 4:443–455.

Corfield, R.M., and Norris, R.D., 1996. Deep water circulation in the Paleogene Ocean. *In* Knox, R.W., Corfield, R.M., and Dunay, R.E., (Eds.), *Correlation of the Early Paleogene in Northwest Europe*. Spec. Publ.—Geol. Soc. London, 443–456.

D'Hondt, S., Donaghay, P., Zachos, J.C., Luttenberg, D., and Lindinger, M., 1998. Organic carbon fluxes and ecological recovery from the Cretaceous-Tertiary mass extinction. *Science,* 282:276–279.

D'Hondt, S., and Keller, G., 1991. Some patterns of planktic foraminiferal assemblage turnover at the Cretaceous Tertiary boundary. *Mar. Micropaleontol.,* 17:77–118.

D'Hondt, S., King, J., and Gibson, C., 1996. Oscillatory marine response to the Cretaceous-Tertiary impact. *Geology,* 24:611–614.

Dickens, G.R., 2000. Methane oxidation during the late Palaeocene Thermal Maximum. *Bull. Soc. Geol. Fr.,* 171:37–49.

Dickens, G.R., Castillo, M.M., and Walker, J.G.C., 1997. A blast of gas in the latest Paleocene: simulating first-order effects of massive dissociation of oceanic methane hydrate. *Geology,* 25:259–262.

Dickens, G.R., O'Neil, J.R., Rea, D.K., and Owen, R.M., 1995. Dissociation of oceanic methane hydrate as a cause of the carbon isotope excursion at the end of the Paleocene. *Paleoceanography,* 10:965–971.

Diester-Haass, L., and Zahn, R., 1996. Eocene–Oligocene transition in the Southern Ocean: history of water mass circulation and biological productivity. *Geology,* 24:163–166.

Eldholm, O., and Thomas, E., 1993. Environmental impact of volcanic margin formation. *Earth Planet. Sci. Lett.,* 117:319–329.

Estes, R., and Hutchison, J.H., 1980. Eocene lower vertebrates from Ellesmere Island, Canadian Arctic Archipelago. *Palaeogeogr., Palaeoclimatol., Palaeoecol.,* 30:325–347.

Gibson, T.G., Bybell, L.M., and Owens, J.P., 1993. Latest Paleocene lithologic and biotic events in neritic deposits of southwestern New Jersey. *Paleoceanography,* 8:495–514.

Hambrey, M.J., Ehrmann, W.U., and Larsen, B., 1991. Cenozoic glacial record of the Prydz Bay continental shelf, East Antarctica. *In* Barron, J., Larsen, B., et al., *Proc. ODP, Sci. Results,* 119: College Station, TX (Ocean Drilling Program), 77–132.

Herbert, T.D., and D'Hondt, S.L., 1990. Precessional climate cyclicity in Late Cretaceous–early Tertiary marine sediments: a high resolution chronometer of Cretaceous/Tertiary boundary events. *Earth Planet. Sci. Lett.,* 99:263–275.

Herbert, T.D., Premoli Silva, I., Erba, E., Fischer, A.G., 1995. Orbital chronology of Cretaceous–Paleogene marine strata. *In* Kent, W.A.B. (Ed)., *Geochronology, Time Scales, and Global Stratigraphic Correlation.* Spec. Publ.—SEPM, 81–93.

Hsü, K.J., He, Q., McKenzie, J.A., Weissert, H., Perch-Nielsen, K., Oberhänsli, H., Kelts, K., LaBrecque, J., Tauxe, L., Krähenbühl, U., Percival, S.F., Wright, R., Karpoff, A.M., Petersen, N., Tucker, P., Poore, R.Z., Gombos, A.M., Pisciotto, K., Carman, M.F., and Schreiber, E., 1982. Mass mortality and its environmental and evolutionary consequences. *Science,* 216:249–256.

Hsü, K.J., LaBrecque, J.L., et al., 1984. *Init. Repts. DSDP,* 73: Washington (U.S. Govt. Printing Office).

Hsü, K.J., and Weissert, H.J. (Eds.), 1985. *South Atlantic Paleoceanography:* Cambridge (Cambridge Univ. Press).

Kaiho, K., Arinobu, T., Isihwatar, R., Morgans, H.E.G., Okada, H., Takeda, N., Tazaki, K., Zhou, G., Kajiwara, Y., Matsumoto, R., Hirai, A., Niitsuma, N., and Wada, H., 1996. Latest Paleocene benthic foraminiferal extinction and environmental changes at Tawanui, New Zealand. *Paleoceanography,* 11:447–465.

Kelly, D.C., 2002. Response of Antarctic (ODP Site 690) planktonic foraminifera to the Paleocene–Eocene Thermal Maximum: faunal evidence for ocean/climate change. *Paleoceanography,* 17:1071.

Kelly, D.C., Bralower, T.J., and Zachos, J.C., 1998. Evolutionary consequences of the latest Paleocene thermal maximum for tropical planktonic foraminifera. *Palaeogeogr., Palaeoclimatol., Palaeoecol.,* 141:139–161.

Kelly, D.C., Bralower, T.J., Zachos, J.C., Premoli Silva, I., and Thomas, E., 1996. Rapid diversification of planktonic foraminifera in the tropical Pacific (ODP Site 865) during the late Paleocene thermal maximum. *Geology,* 24:423–426.

Kelly, R.K., Morris, R.D., and Zachos, J.C., in press. Deciphering the paleoceanographic significance of early Oligocene *Braarudosphaera* chalks in the South Atlantic. *Mar. Micropaleontol.,* 43.

Kennett, J.P., and Shackleton, N.J., 1976. Oxygen isotopic evidence for the development of the psychrosphere 38 Myr ago. *Nature,* 260:513–515.

Kennett, J.P., and Stott, L.D., 1990. Proteus and Proto-oceanus: ancestral Paleogene oceans as revealed from Antarctic stable isotopic results: ODP Leg 113. *In* Barker, P.F., Kennett, J.P., et al., *Proc. ODP, Sci. Results,* 113: College Station, TX (Ocean Drilling Program), 865–880.

————, 1991. Abrupt deep-sea warming, paleoceanographic changes and benthic extinctions at the end of the Palaeocene. *Nature,* 353:225–229.

Koch, P.L., Zachos, J.C., and Dettman, D.L., 1995. Stable isotope stratigraphy and palaeoclimatology of the Palaeogene Bighorn Basin. *Palaeogeogr. Palaeoclimatol. Palaeoecol.,* 115:61–89.

Koch, P.L., Zachos, J.C., and Gingerich, P.D., 1992. Correlation between isotope records in marine and continental carbon reservoirs near the Palaeocene/Eocene boundary. *Nature,* 358:319–322.

Kroon, D., Dickens, G., Erbacher, J., Herbert, T., Jansa, L., Jenkyns, H., Kaiho, K., Kent, D., Leckie, M., Norris, R., Premoli-Silva, I., Zachos, J., and Bassinot, F., 2000. Excerpts from the Final Report of the JOIDES Extreme Climates Program. *JOIDES Journal,* 26:17–28.

Little, M.G., Schneider, R.R., Kroon, D., Price, B., Summerhayes, C.P., and Segl, M., 1997. Trade wind forcing of upwelling, seasonality, and Heinrich events as a response to sub-Milankovitch variability. *Paleoceanography,* 12:568–576.

Lourens, L.J., Hilgen, F.J., Laskar, J., Shackleton, N.J., and Wilson, D., in press. *The Neogene Period.*

Luterbacher, H.P., and Premoli Silva, I., 1964. Biostratigrafia del limite Cretaceo-terziario nell' Appennino centrale. *Riv. Ital. Paleontol.,* 70:67–117.

Lyle, M., Wilson, P.A., Janecek, T.R., et al., 2002. *Proc. ODP, Init. Repts.,* 199 [CD-ROM]. Available from: Ocean Drilling Program, Texas A&M University, College Station TX 77845-9547, USA.

Maxwell, A.E., Von Herzen, R.P., et al., 1970. *Init. Repts. DSDP,* 3: Washington (U.S. Govt. Printing Office).

Maxwell, A.E., Von Herzen, R.P., Hsü, K.J., Andrews, J.E., Saito, T., Percival, S.F., Jr., Milow, E.D., and Boyce, R.E., 1970. Deep sea drilling in the South Atlantic. *Science,* 168:1047–1059.

Melguen, M., 1978. Facies evolution, carbonate dissolution cycles in sediments from the eastern south Atlantic (DSDP Leg 40) since the early Cretaceous. *In* Bolli, H.M., Ryan, W.B.F., et al., *Init. Repts. DSDP,* 40: Washington (U.S. Govt. Printing Office), 981–1024.

Mikolajewicz, U., Maier-Reimer, E., Crowley, T.J., and Kim, K.-Y., 1993. Effect of Drake and Panamanian gateways on the circulation of an ocean model. *Paleoceanography,* 8:409–426.

Miller, K.G., Janecek, T.R., Katz, M.E., and Keil, D.J., 1987. Abyssal circulation and benthic foraminiferal changes near the Paleocene/Eocene boundary. *Paleoceanography,* 2:741–761.

Miller, K.G., and Katz, M.E., 1987. Oligocene to Miocene benthic foraminiferal and abyssal circulation changes in the North Atlantic. *Micropaleontology,* 33:97–149.

Miller, K.G., Mountain, G.S., Browning, J.V., Kominz, M., Sugarman, P.J., Christie-Blick, N., Katz, M.E., and Wright, J.D., 1998. Cenozoic global sea level, sequences, and the New Jersey transect: results from coastal plain and continental slope drilling. *Rev. Geophys.,* 36:569–601.

Miller, K.G., Wright, J.D., and Fairbanks, R.G., 1991. Unlocking the Ice House: Oligocene–Miocene oxygen isotopes, eustasy, and margin erosion. *J. Geophys. Res.,* 96:6829–6848.

Monechi, S., 1985. Campanian to Pleistocene calcareous nannofossil stratigraphy from the northwest Pacific Ocean, Deep Sea Drilling Project Leg 86. *In* Heath, G.R., Burckle, L.H., et al., *Init. Repts. DSDP,* 86: Washington (U.S. Govt. Printing Office), 301–336.

Moore, T.C., Jr., Rabinowitz, P.D., et al., 1984. *Init. Repts. DSDP,* 74: Washington (U.S. Govt. Printing Office).

Norris, R.D., and Röhl, U., 1999. Carbon cycling and chronology of climate warming during the Palaeocene/Eocene transition. *Nature,* 401:775–778.

Oglesby, R.J., 1991. Joining Australia to Antarctica: GCM implications for the Cenozoic record of Antarctic glaciation. *Clim. Dynam.,* 6:13–22.

Olafsson, G., 1991. Late Oligocene through Late Miocene calcareous nannofossil biostratigraphy and biochronology [thesis]. *Medd. Stockholm Univ. Inst. Geol. Geochem.,* 283.

Pagani, M., Arthur, M.A., and Freeman, K.H., 1999. Atmospheric carbon dioxide. *Paleoceanography,* 14:273–292.

Pak, D.K., and Miller, K.G., 1992. Paleocene to Eocene benthic foraminiferal isotopes and assemblages: implications for deepwater circulation. *Paleoceanography,* 7:405–422.

Paytan, A., Kastner, M., Campbell, D., and Thiemens, M.H., 1998. Sulfur isotopic composition of Cenozoic seawater sulfate. *Science,* 282:1459–1462.

Pearson, P.N., and Palmer, M.R., 2000. Atmospheric carbon dioxide concentrations over the past 60 million years. *Nature,* 406:695–699.

Peleo-Alampay, A.M., Mead, G.A., and Wei, W., 1999.Unusual Oligocene *Braarudosphaera*-rich layers of the South Atlantic and their paleoceanographic implications. *J. Nannoplankton Res.,* 21:17–26.

Perch-Nielsen, K., 1985. Cenozoic calcareous nannofossils. *In* Bolli, H.M., Saunders, J.B., and Perch-Nielsen, K. (Eds.), *Plankton Stratigraphy:* Cambridge (Cambridge Univ. Press), 427–554.

Peterson, L.C., and Backman, J., 1990. Late Cenozoic carbonate accumulation and the history of the carbonate compensation depth in the western equatorial Indian Ocean. *In* Duncan, R.A., Backman, J., Peterson, L.C., et al., *Proc. ODP, Sci. Results,* 115: College Station, TX (Ocean Drilling Program), 467–507.

Rabinowitz, P.D., and Simpson, E.S.W., 1984. Geophysical site survey results on the Walvis Ridge. *In* Moore, T.C., Jr., Rabinowitz, P.D., et al., *Init. Repts. DSDP,* 74: Washington (U.S. Government Printing Office), 795–825.

Raymo, M.E., Ruddiman, W.F., Shackleton, N.J., and Oppo, D.W., 1990. Evolution of Atlantic-Pacific $\delta^{13}C$ gradients over the last 2.5 m.y. *Earth Planet. Sci. Lett.,* 97:353–368.

Rea, D.K., Zachos, J.C., Owen, R.M., and Gingerich, P.D., 1990. Global change at the Paleocene-Eocene boundary: climatic and evolutionary consequences of tectonic events. *Palaeogeogr., Palaeoclimatol., Palaeoecol.,* 79:117–128.

Rind, D., and Chandler, M., 1991. Increased ocean heat transport and warmer climate. *J. Geophys. Res.,* 96:7437–7461.

Robert, C., and Kennett, J.P., 1994. Antarctic subtropical humid episode at the Paleocene-Eocene boundary: clay mineral evidence. *Geology,* 22:211–214.

————, 1997. Antarctic continental weathering changes during Eocene–Oligocene cryosphere expansion: clay mineral and oxygen isotope evidence. *Geology,* 25:587–590.

Röhl, U., Bralower, T.J., Norris, R.D., and Wefer, G., 2000. New chronology for the late Paleocene thermal maximum and its environmental implications. *Geology,* 28:927–930.

Röhl, U., Norris, R.D., and Ogg., J.G., 2003. Cyclostratigraphy of upper Paleocene and late Eocene sediments at Blake Nose Site 1051 (western North Atlantic). *In* Gingerich, P., Schmitz, B., and Thomas, E., (Eds.), *Causes and Conseqeunces of Globally Warm Climates in the Early Paleogene*. Spec. Pap.—Geol. Soc. Am., 369:567–589.

Röhl, U., Ogg, J.G., Geib, T.L., and Wefer, G., 2001. Astronomical calibration of the Danian timescale. *In* Kroon, D., Norris, R.D., and Klaus, A. (Eds.), *Western North Atlantic Paleogene and Cretaceous Paleoceanography.* Spec. Publ.—Geol. Soc. London, 183:163–184.

Salamy, K.A., and Zachos, J.C., 1999. Latest Eocene–early Oligocene climate change and Southern Ocean fertility: inferences from sediment accumulation and stable isotope data. *Palaeogeogr., Palaeoclimatol., Palaeoecol.,* 145:61–77.

Schmitz, B., Charisi, S.D., Thompson, E.I., and Speijer, R.P., 1997. Barium, SiO_2 (excess), and P_2O_5 as proxies of biological productivity in the Middle East during the Palaeocene and the latest Palaeocene benthic extinction event. *Terra Nova,* 9:95–99.

Schrag, D.P., 2002. Control of atmospheric CO2 and climate through Earth history. *Geochim. Cosmochim. Acta,* 66:A688.

Shackleton, N., and Boersma, A., 1981. The climate of the Eocene ocean. *J. Geol. Soc. London,* 138:153–157.

Shackleton, N.J., 1987. The carbon isotope record of the Cenozoic: history of organic carbon burial and of oxygen in the ocean and atmosphere. *In* Brooks, J., and Fleet, A.J. (Eds.), *Marine Petroleum Source Rocks*. Spec. Publ.—Geol. Soc. London, 26:423–434.

Shackleton, N.J., and Hall, M.A., 1984. Carbon isotope data from Leg 74 sediments. *In* Moore, T.C., Jr., Rabinowitz, P.D., et al., *Init. Repts. DSDP,* 74: Washington (U.S. Govt. Printing Office), 613–619.

Shackleton, N.J., Hall, M.A., and Boersma, A., 1984. Oxygen and carbon isotope data from Leg 74 foraminifers. *In* Moore, T.C., Jr., Rabinowitz, P.D., et al., *Init. Repts. DSDP,* 74: Washington (U.S. Govt. Printing Office), 599–612.

Shipboard Scientific Party, 1998. Synthesis. *In* Norris, R.D., Kroon, D., Klaus, A., et al., *Proc. ODP, Init. Repts.,* 171B: College Station, TX (Ocean Drilling Program), 351–360.

Siesser, W.G., 1978. Leg 40 results in relation to continental shelf and onshore geology. *In* Bolli, H.M., Ryan, W.B.F., et al., *Init. Repts. DSDP,* 40: Washington (U.S. Govt. Printing Office), 965–979.

Sloan, L.C., and Barron, E.J., 1992. A comparison of Eocene climate model results to quantified paleoclimatic interpretations. *Palaeogeogr., Palaeoclimatol., Palaeoecol.,* 93:183–202.

Sloan, L.C., and Rea, D.K., 1996. Atmospheric carbon dioxide and early Eocene climate—a general circulation modeling sensitivity study. *Palaeogeogr., Palaeoclimatol., Palaeoecol.,* 119:275–292.

Sloan, L.C., Walker, J.C.G., and Moore, T.C., Jr., 1995. Possible role of oceanic heat transport in early Eocene climate. *Paleoceanography,* 10:347–356.

Sloan, L.C., Walker, J.C.G., Moore, T.C., Rea, D.K., and Zachos, J.C., 1992. Possible methane-induced polar warming in the early Eocene. *Nature,* 357:320–322.

Smart, C.W., 1992. Early to middle Miocene benthic foraminiferal faunas from DSDP Sites 518 and 529, South Atlantic: preliminary investigations. *In* Takayanagi, Y., and Saito, T. (Eds.), *Studies in Benthic Foraminifera: Proc. 4th Int. Symp. Benthic Foraminifera:* Sendai, Japan (Tokai Univ. Press), 245–248.

Smart, C.W., and Murray, J.W., 1994. An early Miocene Atlantic-wide foraminiferal/palaeoceanographic event. *Palaeogeogr., Palaeoclimatol., Palaeoecol.,* 108:139–148.

————, 1995. Miocene deep-sea benthic foraminifera from the Atlantic and Indian Oceans: diversity patterns and palaeoceanography. *Rev. Esp. Paleontol. Dr. Guillermo Colom,* 59–68.

Smart, C.W., and Ramsay, A.T.S., 1995. Benthic foraminiferal evidence for the existence of an early Miocene oxygen-depleted oceanic water mass? *J. Geol. Soc. (London, UK),* 152:735–738.

Spieß, V., Krastel, S., Beitler, B., Böke, W., Gerriets, A., Heidersdorf, F., Leupold, J., Salem, M., Schruöter, F., Schwenk, T., Zahn-Knoll, R., and Zuhisdorff, L., 2003. Report and preliminary results of *Meteor* Cruise M49/1 Cape Town (South Africa)–Montevideo (Uruguay) 04.01.2000–10.02.2000. *Ber., Fachbereich Geowiss., Univ. Bremen,* 205:57.

Stott, L.D., and Kennett, J.P., 1989. New constraints on early Tertiary palaeoproductivity from carbon isotopes in foraminifera. *Nature,* 342:526–529.

Stott, L.D., Kennett, J.P., Shackleton, N.J., and Corfield, R.M., 1990. The evolution of Antarctic surface waters during the Paleogene: inferences from the stable isotopic composition of planktonic foraminifers, ODP Leg 113. *In* Barker, P.F., Kennett, J.P., et al., *Proc. ODP, Sci. Results,* 113: College Station, TX (Ocean Drilling Program), 849–863.

Thierstein, H.R., 1982. Terminal Cretaceous plankton extinctions: a critical assessment. *In* Silver, L.T., and Schultz, P.H. (Eds.), *Geological Implications of Impacts of Large Asteroids and Comets on the Earth.* Spec. Pap.—Geol. Soc. Am., 190:385–399.

Thomas, D.J., Bralower, T.J., and Zachos, J.C., 1999. New evidence for subtropical warming during the late Paleocene thermal maximum: Stable isotopes from Deep Sea Drilling Project Site 527, Walvis Ridge. *Paleoceanography,* 14:561–570.

Thomas, E., 1985. Late Eocene to Recent deep-sea benthic foraminifers from the central equatorial Pacific Ocean. *In* Mayer, L., Theyer, F., Thomas, E., et al., *Init. Repts. DSDP,* 85: Washington (U.S. Govt. Printing Office), 655–694.

————, 1986. Early to middle Miocene benthic foraminiferal faunas from DSDP Sites 608 and 610, North Atlantic. *In* Summerhayes, C.P., and Shackleton, N.J. (Eds.), *North Atlantic Palaeoceanography.* Spec. Publ.—Geol. Soc. London, 21:205–218.

————, 1990. Late Cretaceous–early Eocene mass extinctions in the deep sea. *In* Sharpton, V.L., and Ward, P.D. (Eds.), *Global Catastrophes in Earth History: An Interdisciplinary Conference on Impacts, Volcanism, and Mass Mortality.* Spec. Pap.—Geol. Soc. Am., 247:481–495.

————, 1998. Biogeography of the late Paleocene benthic foraminiferal extinction. *In* Aubry, M.-P., Lucas, S.G., and Berggren, W.A. (Eds.), *Late Paleocene–Early Eocene: Climatic and Biotic Events in the Marine and Terrestrial Records:* New York (Columbia Univ. Press), 214–235.

Thomas, E., and Gooday, A.J., 1996. Cenozoic deep-sea benthic foraminifers: tracers for changes in oceanic productivity? *Geology,* 24:355–358.

Thomas, E., and Shackleton, N., 1996. The Palaeocene–Eocene benthic foraminiferal extinction and stable isotope anomalies. *In* Knox, R.W.O'B., Corfield, R.M., and Dunay, R.E. (Eds.), *Correlation of the Early Paleogene in Northwest Europe.* Spec. Publ.—Geol. Soc. London, 101:401–441.

Thomas, E., and Vincent, E., 1987. Equatorial Pacific deep-sea benthic foraminifera: faunal changes before the middle Miocene polar cooling. *Geology,* 15:1035–1039.

Thomas, E., and Zachos, J.C., 2000. Was the late Paleocene Thermal Maximum a unique event? *GFF,* 122:169–170.

Thomas, E., Zachos, J.C., Bralower, T.J., 2000. Deep-sea environments on a warm earth: latest Paleocene–early Eocene. *In* Huber, B.T., MacLeod, K.G.E., and Wing, S.L.E. (Eds.), *Warm Climates in Earth History:* Cambridge (Cambridge Univ. Press), 132–160.

Thunell, R.C., and Corliss, B.H., 1986. Late Eocene–early Oligocene carbonate sedimentation in the deep sea. *In* Pomerol, C., and Premoli Silva, I. (Eds.), *Terminal Eocene Events.* Dev. Palaeontol. Stratigr., 9:363–380.

Torrence, C., and Compo, G.P., 1998. A practical guide to wavelet analysis. *Bull. Am. Meteorol. Soc.,* 79:61–78.

van Andel, T.H., 1975. Mesozoic/Cenozoic calcite compensation depth and the global distribution of calcareous sediments. *Earth Planet. Sci. Lett.,* 26:187–194.

Volbers, A.N.A., and Henrich, R., 2002. Present water mass calcium carbonate corrosiveness in the eastern South Atlantic inferred from ultrastructural breakdown of *Globigerina bulloides* in surface sediments. *Mar. Geol.,* 186:471–486.

Wade, B.S., and Kroon, D., 2002. Middle Eocene regional climate instability: evidence from the western North Atlantic. *Geology,* 30:1011–1014.

Walker, J.C.G., Hays, P.B., and Kasting, J.F., 1981. A negative feedback mechanism for the long-term stabilization of Earth's surface temperature. *J. Geophys. Res., [Oceans],* 86:9776–9782.

Walker, J.C.G., and Kasting, J.F., 1992. Effects of fuel and forest conservation on future levels of atmospheric carbon dioxide. *Global Planet. Change,* 5:151–189.

Wing, S.L., 1998. Late Paleocene–early Eocene floral and climatic change in the Bighorn Basin, Wyoming. *In* Berggren, W.A., Aubrey, M.-P., and Lucas, S.G. (Eds.), *Late Paleocene–Early Eocene Biotic and Climatic Events:* New York (Columbia Univ. Press), 371–391.

Wolfe, J.A., 1980. Tertiary climates and fioristic relationships at high latitudes in the northern hemisphere. *Palaeogeogr., Palaeoclimatol., Palaeoecol.,* 30:313–323.

Zachos, J.C., and Arthur, M.A., 1986. Paleoceanography of the Cretaceous/Tertiary boundary event: inferences from stable isotopic and other data. *Paleoceanography,* 1:5–26.

Zachos, J.C., Arthur, M.A., and Dean, W.E., 1989. Geochemical evidence for suppression of pelagic marine productivity at the Cretaceous/Tertiary boundary. *Nature,* 337:61–64.

Zachos, J.C., Breza, J.R., and Wise, S.W., 1992. Early Oligocene ice-sheet expansion on Antarctica: stable isotope and sedimentological evidence from Kerguelen Plateau, southern Indian Ocean. *Geology,* 20:569–573.

Zachos, J.C., Lohmann, K.C., Walker, J.C.G., and Wise, S.W., Jr., 1993. Abrupt climate changes and transient climates during the Paleogene: a marine perspective. *J. Geol.,* 101:191–213.

Zachos, J.C., Pagani, M., Sloan, L., Thomas, E. and Billups, K., 2001. Trends, rhythms, and aberrations in global climate 65 Ma to present. *Science,* 292:686–693.

Zachos, J.C., Quinn, R.M., and Salamy, K., 1996. High resolution (10^4 yr) deep-sea foraminiferal stable isotope records of the Eocene–Oligocene climate transition. *Paleoceanography,* 11:251–266.

Zachos, J.C., Stott, L.D., and Lohmann, K.C., 1994. Evolution of early Cenozoic marine temperatures. *Paleoceanography,* 9:353–387.

TABLE CAPTIONS

Table T1. Operations summary, Leg 208.

Table T2. Common age tie points for the Leg 208 sites.

FIGURE CAPTIONS

Figure F1. Bathymetric chart of Walvis Ridge, the South African margin, DSDP sites (black circles), ODP drill sites (white circles with green centers), and proposed Leg 208 sites (white circles).

Figure F2. Bathymetric chart of Walvis Ridge, *Meteor* Cruise M49/1 tracklines, DSDP sites (black circles), ODP drill sites (white circles with green centers), and proposed Leg 208 sites (white circles).

Figure F3. A three-dimensional diagram of the Leg 208 drill site locations.

Figure F4. Multichannel seismic line GeoB 01-030 (*Meteor* Cruise M49/1) with DSDP Leg 74 sites and proposed Sites WALV-10A and WALV-11A. w.d. = water depth. GI = generated injection.

Figure F5. Cenozoic deep-sea stable isotope record based on a compilation of benthic foraminifer data from several dozen pelagic cores (modified from Zachos et al., 2001). The oxygen isotope record primarily reflects on changes in deepwater temperature and ice volume. Mi-1 and Oi-1 represent transient large-scale glaciations of Antarctica.

Figure F6. Cenozoic pCO_2 as estimated by the B isotope method (Pearson and Palmer, 2000) and by alkenone carbon isotope method (Pagani et al., 1999).

Figure F7. Benthic foraminifer isotope records across the P/E boundary from Sites 525, 527, 690, and 865 (Thomas and Shackleton, 1996; Zachos et al., 2001). The Paleocene–Eocene Thermal Maximum is characterized by a 5°C warming of the deep sea.

Figure F8. Box model simulated response of oceanic carbon isotopes and lysocline depth to gradual (10 k.y.) input of 1200 Gt of methane-derived CO_2 into the ocean (Dickens, 2000).

Figure F9. DSDP Site 527 planktonic foraminiferal stable isotope records plotted against depth for the three size fractions of *Acarinina soldadoensis*. The arrows indicate the three size fractions (90–150, 150–250, and 300–355 µm). The gray band indicates the position of the clay interval within Core 527-24. The $CaCO_3$ record reveals the low carbonate layer coincident with the Paleocene–Eocene Thermal Maximum (Thomas et al., 1999).

Figure F10. A composite of the *Cibicidoides* spp. stable carbon and oxygen isotope records for Sites 522, 744, and 689 plotted as a function of age for the period from 31 to 35 Ma (Zachos et al., 1996; Diester-Haas and Zahn, 1996). The earliest Oligocene Glacial Maximum (EOGM) spans the interval 33.0–33.4 Ma. The age model is based on the geomagnetic polarity timescale of Cande and Kent (1992). The lower scale shows the bottom water temperature for an ice-free world (pre-EOGM) assuming calcite formation in oxygen isotope equilibrium (Zachos et al., 1996). PDB = Peedee belemnite. S.W. = seawater, SMOW = standard mean ocean water.

Figure F11. Latest Cretaceous through earliest Paleogene $\delta^{13}C$ records from DSDP Site 528 (after D'Hondt et al., 1998). Magnetostrat. = magnetostratigraphy. K/P = Cretaceous/Paleogene boundary. Open symbols = $\delta^{13}C$ differences between near-surface planktonic foraminifers and benthic foraminifers. Solid symbols = $\delta^{13}C$ differences between deeper-dwelling planktonic and benthic foraminifers. The benthic foraminifers are *Gavelinella* and *Nuttallides*. The planktonic foraminifers are *Morozovella angulata* (open triangles), *Praemurica taurica* (open circles), *Eoglobigerina eobulloides* (solid circles), *Rugoglobigerina rotundata* (open squares), *Pseudotextularia elegans* (solid squares), and *Heterohelix rajagopalani* (solid triangles). **A.** $\delta^{13}C$ differences between fine (ff; <25 µm) carbonate and benthic foraminifers (bf). **B.** $\delta^{13}C$ differences between planktonic (pf) and benthic foraminifers. **C.** $\delta^{13}C$ differences between near-surface planktonic foraminiferal species and the deepest dwelling (thermocline) planktonic species (calculated by subtracting $\delta^{13}C$ values of the latter from those of the former). The deepest dwelling planktonic species are *H. rajagopalani* (Cretaceous) and *E. eobulloides* (Paleogene).

Figure F12. *Meteor* Cruise M49/1 track chart showing the location of Site 1262 (proposed Site WALV-12A) and alternate sites (WALV-12B and WALV-12C) along line GeoB 01-035.

Figure F13. Line GeoB 01-035 and Site 1262 plotted along with age estimates of prominent reflectors. R_1 is a regional reflector that marks a local unconformity. Although time transgressive, sediments below the reflector tend to be Paleogene, above Neogene. The P/E boundary reflector ($R_{P/E}$) is at ~127 mbsf, and the K/P boundary ($R_{K/P}$) is at ~189 mbsf. Both reflectors can be traced over most of the ridge. CDP = common depth point. V.E. = vertical exaggeration.

Figure F14. Site 1262 lithostratigraphic composite illustrating downhole variation in magnetic susceptibility (MS), natural gamma radiation (NGR), carbonate content, and color reflectance (L*, lightness). Major lithologic unit boundaries coincide with step changes in these parameters. MS and NGR variations largely correlate with clay and volcaniclastic content. The P/E and K/P boundaries are distinct from adjacent sediments in their MS and NGR values as they represent intervals of decreased carbonate deposition/preservation and increased clay and volcanic ash accumulation, both of which produce distinctive increases in MS and NGR. A single value reached 625 on the MS scale as indicated in the figure.

Figure F15. Site 1262 (**A**) core recovery, (**B**) age-depth model, and (**C**) linear sedimentation rate (LSR) and mass accumulation rate (MAR) sampled at 1-m.y. intervals. Rectangles in (B) = condensed intervals and/or unconformities as constrained by biostratigraphic data. Horizontal lines and roman numerals in (B) = lithologic units and subunits. The highest MAR values in (C) are the total MARs; the lowest values are the "background" noncarbonate (noncarb) MARs (typically <0.1 g/cm²/k.y.), illustrating that mass accumulation at this site is controlled by carbonate deposition. Gaps in MAR estimates exist where no dry density and/or carbonate data were available for the 1-m.y. sampling interval (typically in condensed intervals). FO = first occurrence, LO = last occurrence.

Figure F16. *Meteor* Cruise M49/1 track chart showing the location of Site 1263 (proposed Site WALV-8E), Site 1264 (proposed Site WALV-8A), alternate sites (WALV-8B, WALV-8C, and WALV-8D) on lines GeoB 01-046 and GeoB 01-031, and other proposed sites.

Figure F17. Line GeoB 01-046 and Sites 1263 and 1264 plotted with age estimates of prominent reflectors. R_1 is a regional reflector associated with an erosional unconformity. The P/E boundary reflector ($R_{P/E}$) is estimated to be at 280 mbsf and the K/P boundary reflector ($R_{K/P}$) at 360 mbsf. $R_{O/M}$ = Oligocene/Miocene boundary reflector. CDP = common depth point. V.E. = vertical exaggeration.

Figure F18. Stratigraphic variation in parameters used to define Site 1263 lithostratigraphic units. Foraminifer percentages (triangles) are smoothed with a 3-point moving average (line). Natural gamma radiation (NGR) is smoothed with a 5-point moving average. MS = magnetic susceptibility. cps = counts per second.

Figure F19. Site 1263 (**A**) core recovery, (**B**) age-depth model, and (**C**) linear sedimentation rate (LSR) and mass accumulation rate (MAR) sampled at 1-m.y. intervals. Rectangle in (B) = condensed interval and/or unconformity as constrained by biostratigraphic data. Horizontal lines and roman numerals in (B) = lithologic subunits. The highest MAR values in (C) are the total MARs; the lowest values are the "background" noncarbonate (noncarb) MARs (typically <0.1 g/cm^2/k.y.), illustrating that mass accumulation at this site is controlled by carbonate deposition. Gaps in MAR estimates exist where no dry density and/or carbonate data were available for the 1-m.y. sampling interval (typically in condensed intervals). FO = first occurrence, LO = last occurrence.

Figure F20. Line GeoB 01-046 and Sites 1263 and 1264 plotted with age estimates of prominent reflectors. $R_{O/M}$ is the Oligocene/Miocene boundary. R_1 is a regional reflector associated with an erosional unconformity. The P/E boundary reflector ($R_{P/E}$) is estimated to be at 280 mbsf and the K/P boundary reflector ($R_{K/P}$) at 360 mbsf. CDP = common depth point. V.E. = vertical exaggeration.

Figure F21. Stratigraphic variation in parameters used to define Site 1264 lithostratigraphic units, including magnetic susceptibility (MS), nannofossil content, color reflectance (b*, blue-yellow chromaticity value), and *P*-wave velocity (V_P). MS and color reflectance data are smoothed with a 5-point moving average. Nannofossil content and V_P are smoothed with a 5% weighted average.

Figure F22. Site 1264 (**A**) core recovery, (**B**) age-depth model, and (**C**) linear sedimentation rate (LSR) and mass accumulation rate (MAR) sampled at 1-m.y. intervals. Rectangle in (B) = condensed interval and/or unconformity as constrained by biostratigraphic data. Horizontal lines and roman numerals = lithologic units and subunits. The highest MAR values in (C) are the total MARs; the lowest values are the "background" noncarbonate (noncarb) MARs (typically <0.1 g/cm^2/k.y.), illustrating that mass accumulation at this site is controlled by carbonate deposition. Gaps in MAR estimates exist where no dry density and/or carbonate data were available for the 1-m.y. sampling interval (typically in condensed intervals). FO = first occurrence, LO = last occurrence.

Figure F23. Line GeoB 01-048 and Site 1265 plotted with prominent reflectors. $R_{O/M}$ is just below the Oligocene/Miocene boundary at ~113 mbsf. The P/E boundary reflector ($R_{P/E}$) is at ~275 mbsf, and the K/P boundary reflector ($R_{K/P}$) is at ~330 mbsf. CDP = common depth point, V.E. = vertical exaggeration.

Figure F24. Downcore variations in parameters used to define Site 1265 lithologic units, including magnetic susceptibility (MS) (Site 1265 splice, 21-point moving average), color reflectance (L*, lightness) (Site 1265 splice, 21-point moving average), and smear slide percentage of foraminifers (open triangles = Hole 1265A and solid triangles = Hole 1265B; solid line is combined 3-point moving average).

Figure F25. Site 1265 (**A**) core recovery, (**B**) age-depth model, and (**C**) linear sedimentation rate (LSR) and mass accumulation rate (MAR) sampled at 1-m.y. intervals. Rectangles in (B) = condensed intervals and/or unconformities as constrained by biostratigraphic data. Horizontal lines and roman numerals in (B) = lithologic units and subunits. The highest MAR values in (C) are the total MARs; the lowest values are the "background" noncarbonate (noncarb) MARs (typically <0.1 $g/cm^2/k.y.$), illustrating that mass accumulation at this site is controlled by carbonate deposition. Gaps in MAR estimates exist where no dry density and/or carbonate data were available for the 1-m.y. sampling interval (typically in condensed intervals). FO = first occurrence, LO = last occurrence.

Figure F26. Line GeoB 01-030 with Site 1266 and DSDP Site 528 (proposed sites WALV-10F and WALV-10A, respectively) with age estimates of prominent reflectors. A middle–late Miocene reflector, R_{M1}, is at ~105 mbsf, and the Oligocene/Miocene boundary reflector, $R_{O/M}$, is at ~140 mbsf. The Paleocene/Eocene boundary reflector ($R_{P/E}$) is at ~275 mbsf, and the K/P boundary reflector ($R_{K/P}$) is at 350 mbsf. Both $R_{P/E}$ and $R_{K/P}$ can be identified over most of the surveyed area. CDP = common depth point. V.E. = vertical exaggeration.

Figure F27. Stratigraphic variation in parameters used to define Site 1266 lithostratigraphic units. The Unit I/II boundary was chosen at an abrupt step change in chromaticity value b*, lightness (L*), inflection in magnetic susceptibility (MS), and decrease in foraminifer abundance. The Unit II/III boundary was chosen at a decrease in lightness (L*) and increase in MS and natural gamma radiation (NGR). All data are smoothed with a 5-point moving average with the exception of NGR and smear slide components, which were smoothed with a 10-point and 3-point moving average, respectively.

Figure F28. Site 1266 (**A**) core recovery, (**B**) age-depth model, and (**C**) linear sedimentation rate (LSR) and mass accumulation rate (MAR) sampled at 1-m.y. intervals. Rectangles in (B) = condensed intervals and/or unconformities as constrained by biostratigraphic data. Horizontal lines and roman numerals in (B) = lithologic units. The highest MAR values in (C) are the total MARs; the lowest values are the "background" noncarbonate (noncarb) MARs (typically <0.1 $g/cm^2/k.y.$), illustrating that mass accumulation at this site is controlled by carbonate deposition. Gaps in MAR estimates exist where no dry density and/or carbonate data were available for the 1-m.y. sampling interval (typically in condensed intervals). FO = first occurrence, LO = last occurrence.

Figure F29. *Meteor* Cruise M49/1 track chart showing the location of Site 1267 (proposed Site WALV-11B) and alternate Site WALV-11A (DSDP Site 527) along line GeoB 01-039.

Figure F30. Locations of Site 1267 and DSDP Site 527 along Line GeoB 01-039. R_1 is a regional reflector that marks an unconformity or condensed interval. Although time transgressive, sediments below the reflector tend to be Paleogene and those above tend to be Neogene. The P/E boundary reflector ($R_{P/E}$) is estimated to be at 213 mbsf and the K/P boundary ($R_{K/P}$) at 279 mbsf. Both reflectors can be traced over most of the ridge. CDP = common depth point. V.E. = vertical exaggeration.

Figure F31. Site 1267 lithostratigraphic composite illustrating downhole variation in magnetic susceptibility (MS), natural gamma radiation (NGR), carbonate concentration, and color reflectance (L*, lightness). Major lithologic unit boundaries coincide with step changes in these parameters. MS and NGR variations largely correlate with clay and volcaniclastic content.

Figure F32. Site 1267 (**A**) core recovery, (**B**) age-depth model, and (**C**) linear sedimentation rate (LSR) and mass accumulation rate (MAR) sampled at 1-m.y. intervals. Rectangles in (B) = condensed intervals and/or unconformities as constrained by biostratigraphic data. Horizontal lines and roman numerals in (B) = lithologic units and subunits. The highest MAR values in (C) are the total MARs; the lowest values are the "background" noncarbonate (noncarb) MARs (typically <0.1 g/cm²/k.y.), illustrating that mass accumulation at this site is controlled by carbonate deposition. Gaps in MAR estimates exist where no dry density and/or carbonate data were available for the 1-m.y. sampling interval (typically in condensed intervals). FO = first occurrence, LO = last occurrence.

Figure F33. Sediment age distribution at Leg 208 sites.

Figure F34. Maastrichtian, Paleocene, and lower Eocene magnetic polarity reversal records for Sites 1262, 1266, and 1267. Arrows = Paleocene/Eocene (P/E) and Cretaceous/Paleogene (K/P) boundaries. The geomagnetic polarity timescale (Cande and Kent, 1992) is plotted on the left.

Figure F35. Magnetic susceptibility (MS) vs. age for the complete composite sections of all Leg 208 sites, except Site 1264.

Figure F36. Magnetic susceptibility (MS) vs. age for the 0- to 5-Ma time interval of all Leg 208 sites, except Site 1263.

Figure F37. Magnetic susceptibility (MS) vs. age for the 52- to 56-Ma time interval of all Leg 208 sites, except Site 1264. P/E = P/E boundary.

Figure F38. Magnetic susceptibility (MS) vs. age for the 52- to 66-Ma time interval of Sites 1262 and 1267. K/P = K/P boundary, P/E = P/E boundary.

Figure F39. Depth-scale representation of the magnetic susceptibility (MS) record at Site 1264 between 170 and 260 mcd (early to early late Miocene, 11 to 23 Ma). Assuming a sedimentation rate of ~0.9 cm/k.y., the energy bands centered on the 0.36- and 0.9-cm depth scale may be linked to obliquity and eccentricity forcing, respectively. Modulations in the energy bands are probably related to changes in sedimentation rates.

Figure F40. Depth-scale representation of the magnetic susceptibility (MS) record at Site 1265 between 278.9 and 294.8 mcd (early Eocene, 53.3 to 53.9 Ma). Assuming an average sedimentation rate of ~2.1 cm/k.y., the energy bands centered on the 0.5- and 2.5-m scale may be linked to precession and eccentricity forcing, respectively. The 1-m energy band might be linked to obliquity. Modulations in the energy bands are probably related to slight changes in sedimentation rates.

Figure F41. Depth-scale representation of the magnetic susceptibility (MS) record at Site 1267 between 320.9 and 367.5 mcd (Maastrichtian, 65 to 67.5 Ma). Assuming a sedimentation rate of ~2 cm/k.y., the energy bands centered on the 0.4- and 2.0-m depth scale may be linked to precession and eccentricity forcing, respectively. The 0.8-m energy band might be linked to obliquity but can also be related to changes in sedimentation rate.

Figure F42. Age-depth models for Leg 208 sites.

Figure F43. Linear sedimentation rates (LSRs) and total mass accumulation rates (MARs) at Leg 208 sites. The bulk of the MARs are due to carbonate deposition; noncarbonate accumulation rates are typically <0.1 g/cm^2/k.y. (see Figs. F15, F19, F22, F25, F28, F32). The shaded rectangles highlight time intervals of relatively increased accumulation rates across the sites: the late Paleocene to early Eocene at all sites, the early Oligocene at some sites, and the Pliocene at most sites.

Figure F44. Lithostratigraphy of Leg 208 sites with mass accumulation rates (MARs) vs. age.

Figure F45. Carbonate contours and accumulation contours. MAR = mass accumulation rate.

Figure F46. The Cretaceous/Paleocene boundary at Walvis Ridge Holes 1262B, 1262C, 1267A, and 1267B. A strong change in magnetic susceptibility (MS) and color reflectance (L*) indicate the Fe oxide–bearing nonbioturbated foraminifer nannofossil boundary layer. The interpolated bases of planktonic foraminifer zones are indicated by arrows and biostratigraphic sample locations by black squares. The records are all at the same scale.

Figure F47. Magnetic susceptibility (MS) and color reflectance (L*) data for Sections 208-1262B-18H-4, 208-1267B-27X-6 and 27X-CC (a small recovery gap between Sections 208-1267B-27X-6 and 27X-CC is possible), and 208-1266C-21X-1 exhibiting the mid-Paleocene biotic event on Walvis Ridge. Sites are ordered according to present water depths (from deep on the left to shallow on the right).

Figure F48. Magnetic susceptibility (MS) and $CaCO_3$ through the Paleocene–Eocene transition at the shallow to deep transect. The MS graphs represent both point magnetic susceptibility (PMS) data measured on the split core and loop sensor (MSL) data measured on the whole core. For correlation of these two methods, 1-cm resolution PMS data were linearly interpolated at 2.5-cm resolution, after which a linear expansion formula was calculated and PMS values were normalized to MSL values: MSL = 2.0683 × PMS + 7.8257 ($R^2 = 0.9885$). For Site 1263, MS data from Hole 1263C are spliced with data from Hole 1263D at 335.88 meters composite depth (mcd). Sample depths for Hole 1263D were normalized to Hole 1263C mcd using a linear expansion based on PMS correlation through the P/E transition: Hole 1263C mcd = Hole 1263D mcd × 1.383 – 128.45. For Site 1262, sample depths of $CaCO_3$ data from Hole 1262A (Core 208-1262A-13H) were normalized to Hole 1262B mcd using a linear expansion based on PMS correlation through the lower part of the P/E transition: Hole 1262B mcd = Hole 1262A mcd × 1.1343 – 18.785 ($R^2 = 0.996$; only for data below 139.95 mcd). At Site 1266, $CaCO_3$ data from Hole 1266B (Section 208-1266B-6H-7) give way to Hole 1266C values at 306.56 mcd. LO = last occurrence, FO = first occurrence.

Figure F49. Magnetic susceptibility (MS) records across the early Eocene C24N event at Leg 208 sites. The 1-cm and 2.5-cm MS records were obtained from point magnetic susceptibility (PMS) measurements and loop measurements (MSL), respectively. The PMS values were calibrated to the MSL values by multiplying each value with 2.0683 and adding 7.8257.

Figure F50. Composite digital images of the Eocene–Oligocene sequence at Leg 208 sites. Also shown are magnetic susceptibility (MS), color reflectance lightness (L*), and gamma ray attenuation (GRA) bulk density data. The lithologic change from clay or clay-bearing nannofossil ooze to nannofossil ooze is associated with decreasing MS and GRA bulk density and increasing L*. The dashed line approximates the E/O boundary, and arrows suggest the “Oi-1” (earliest Oligocene Glacial Maximum) event.

Figure F51. Photomicrograph of an early Oligocene nannofossil assemblage showing the super abundance of *Braarudosphaera* skeletal debris.

Figure F52. Magnetic susceptibility (MS) records from Sites 1264 and 1265 showing the approximate duration of the high abundance of bolivinids event interval in the early Miocene. FO = first occurrence.

Table T1. Operations summary, Leg 208.

Hole	Latitude	Longitude	Water depth (mbsl)	Interval cored (m)	Core recovered (m)	Core recovered (%)	Drilled without coring (m)	Penetration (m)	Number of APC cores	Number of XCB cores	Time on site (days)
1262A	27°11.160′S	1°34.620′E	4759.0	161.5	163.5	101		161.5	17	0	
1262B	27°11.150′S	1°34.620′E	4753.6	209.9	212.5	101		209.9	23	0	
1262C	27°11.139′S	1°34.619′E	4753.6	122.5	126.5	103	90.0	212.5	14	0	
Site 1262 averages:	27°11.15′S	1°34.62′E	4755	493.9	502.5	102	90.0	583.9	54	0	4.7
1263A	28°31.970′S	2°46.769′E	2717.1	345.6	295.8	86		345.6	33	7	
1263B	28°31.960′S	2°46.765′E	2717.1	291.4	275.8	95	47.1	338.5	25	8	
1263C	28°31.985′S	2°46.778′E	2717.1	126.3	122.1	97	164.5	290.8	15	1	
1263D	28°31.994′S	2°46.782′E	2717.1	14.6	15.9	109	272.0	286.6	4	0	
Site 1263 averages:	28°31.98′S	2°46.77′E	2717	777.9	709.5	91	483.6	1261.5	77	16	6.8
1264A	28°31.961′S	2°50.731′E	2507.0	280.7	270.8	97		280.7	30	0	
1264B	28°31.950′S	2°50.729′E	2504.0	282.8	290.1	103		282.8	30	0	
1264C	28°31.936′S	2°50.727′E	2504.3	3.0	3.0	100		3.0	1	0	
Site 1264 averages:	28°31.95′S	2°50.73′E	2505	566.5	563.8	100		566.5	61	0	2.9
1265A	28°50.101′S	2°38.360′E	3059.8	321.0	300.0	94		321.0	32	4	
1265B	28°50.101′S	2°38.347′E	3059.6	251.7	243.4	97		251.7	27	0	
1265C	28°50.101′S	2°38.336′E	3059.6	19.0	19.7	104	185.0	204.0	2	0	
1265D	28°50.101′S	2°38.372′E	3059.6	26.9	23.8	88	248.0	274.9	2	3	
Site 1265 averages:	28°50.10′S	2°38.35′E	3060	618.6	586.9	95	433.0	1051.6	63	7	6.9
1266A	28°32.561′S	2°20.610′E	3799.7	298.6	287.0	96		298.6	25	9	
1266B	28°32.550′S	2°20.610′E	3796.6	108.6	110.4	102	212.4	321.0	3	9	
1266C	28°32.539′S	2°20.609′E	3796.6	196.4	194.0	99	137.8	334.2	17	4	
Site 1266 averages:	28°32.55′S	2°20.61′E	3798	603.6	591.5	98	350.2	953.8	45	22	5.6
1267A	28°5.881′S	1°42.659′E	4354.3	312.1	308.3	99		312.1	25	8	
1267B	28°5.890′S	1°42.658′E	4355.1	329.0	328.4	100		329.0	25	11	
Site 1267 averages:	28°5.89′S	1°42.66′E	4355	641.1	636.6	99		641.1	50	19	5.3
Leg 208 averages:				3702	3591	97	1357	5058	350	64	32

Note: APC = advanced piston corer, XCB = extended core barrel.

Table T2. Leg 208 age control points. (Continued on the next four pages.)

	Site												
	1262		1263		1264		1265		1266		1267		Leg 208
Tie	Depth (mcd)	Age (Ma)	Depth (mcd)	Age (Ma)	Depth (mcd)	Age (Ma)	Depth (mcd)	Age (Ma)	Depth (mcd)	Age (Ma)	Depth (mcd)	Age (Ma)	Age (Ma)
1	0		0.00		0.00		0.00		0.00		0.00		0.000
2									0.25	0.026	0.28	0.091	0.091
3									0.52	0.054	0.60	0.195	0.195
4											1.28	0.300	0.300
5											1.60	0.327	0.327
6									1.90	0.199	2.22	0.379	0.379
7	3.49				2.31		2.32		2.82	0.295	3.21	0.462	0.462
8											4.21	0.546	0.546
9											4.63	0.582	0.582
10	5.02	0.641							5.40	0.594	5.65	0.667	0.634
11	5.48	0.696							5.92	0.663	6.41	0.731	0.697
12									6.39	0.726	6.68	0.754	0.740
13							3.92		6.79	0.780	6.98	0.779	0.779
14									7.42	0.867	7.61	0.859	0.863
15	6.82	0.879							7.72	0.908	7.93	0.899	0.895
16	7.89	1.043			5.31	1.047			9.26	1.038	9.25	1.044	1.043
17	8.46	1.116			5.81	1.144			10.16	1.105	10.15	1.123	1.122
18	9.14	1.197			6.31	1.241			11.02	1.223	11.19	1.215	1.219
19	9.39	1.225			6.61	1.286	5.67		11.56	1.316	11.57	1.255	1.270
20	9.72	1.261			6.88	1.326			12.24	1.433	12.05	1.306	1.332
21	9.96	1.288			7.16	1.367			12.49	1.475	12.42	1.346	1.369
22	10.34	1.330			7.51	1.419					12.92	1.400	1.383
23	10.76	1.377			7.84	1.468			14.19	1.607	13.39	1.450	1.475
24	11.04	1.408			8.16	1.515			14.62	1.618	13.89	1.504	1.511
25	11.29	1.436			8.41	1.552			15.50	1.640	14.35	1.553	1.545
26	11.66	1.477			8.68	1.588	7.22		15.65	1.643	14.77	1.591	1.575
27			8.80										1.690
28													1.950
29	20.63	2.267									26.24	2.324	2.295
30	21.41	2.334									27.61	2.403	2.368
31	22.31	2.411									28.63	2.462	2.437
32	22.76	2.450									29.19	2.494	2.472
33	23.19	2.487			16.43		12.40		26.79	2.531	29.69	2.523	2.514
34	24.53	2.603									31.19	2.614	2.608
35	25.21	2.661									31.93	2.665	2.663
36	26.09	2.736			18.23		13.48		29.91	2.798	33.06	2.743	2.759
37	27.04	2.818									34.23	2.823	2.820
38	27.39	2.848									34.73	2.857	2.853
39	27.94	2.895									35.46	2.907	2.901
40	28.67	2.958									36.09	2.951	2.954
41	29.71	3.047									37.72	3.062	3.055
42	31.03	3.161									39.14	3.160	3.160
43	33.13	3.341			23.76		16.08		39.13	3.292	41.12	3.296	3.309
44			17.70										3.350
45	34.06	3.421			24.69				40.36	3.356	42.42	3.397	3.391
46	36.01										44.67		3.588
47									45.00				3.600
48					29.00								3.660
49					30.60		20.50		48.40		47.94		3.820
50					34.10								4.184
51									50.50				4.200
52							26.00		52.50		54.00		4.560
53	41								55.50				4.805
54			29.00		64.62								4.940
55									61.80		82.90		5.100
56									68.41				5.236
57							32.20						5.330
58					76.79				71.74		87.99		5.370
59					77.24		33.20				95.53		6.000
60							35.00						6.500
61					83.22		36.51				100.78		6.840
62			32.50										7.000
63					111.22		37.00		76.69		103.03		7.390
64	47				116.00								7.910
65											103.76		8.430
66					121.65								8.790
67					123.37				78.00				8.910

Table T2 (continued).

	Site												
	1262		1263		1264		1265		1266		1267		Leg 208
Tie	Depth (mcd)	Age (Ma)	Depth (mcd)	Age (Ma)	Depth (mcd)	Age (Ma)	Depth (mcd)	Age (Ma)	Depth (mcd)	Age (Ma)	Depth (mcd)	Age (Ma)	Age (Ma)
68							39.88						8.940
69													9.000
70					133.00								9.300
71					142.00								9.630
72					144.20								9.640
73							42.50						9.700
74					145.00								9.754
75									79.70				9.890
76					148.99		46.20		87.66		107.00		10.480
77					161.54		52.10		93.50				10.790
78					169.69								11.020
79							54.50		94.00				11.043
80					177.26								11.600
81							57.13		94.10				11.640
82					184.77		61.23		94.50				12.810
83					187.40		65.30		98.95				13.550
84					190.00								14.020
85									104.00				15.500
86					198.51								15.600
87			39.00								110.00		16.000
88							77.67						16.160
89					205.63	16.961	80.77	16.759					16.860
90					206.11	17.053	81.12	16.826					16.939
91					206.79	17.183	81.57	16.913					17.048
92					207.24	17.269	82.07	17.010					17.139
93					207.69	17.355	82.67	17.125					17.240
94					208.24	17.460	83.22	17.232					17.346
95					208.97	17.599	83.97	17.376					17.488
96					209.49	17.699	84.62	17.502	114.25	18.376			17.859
97					210.07	17.810	85.42	17.656	114.85	18.445			17.970
98					210.51	17.893	85.77	17.724	115.13	18.477			18.031
99					210.81	17.944	86.07	17.782	115.37	18.505			18.077
100					211.37	18.040	86.77	17.912	115.77	18.550			18.167
101					211.81	18.114	87.27	17.991	116.20	18.600			18.235
102					212.51	18.233	87.97	18.101	116.63	18.649			18.328
103					213.39	18.383	88.77	18.227	117.25	18.720			18.443
104					213.94	18.476	89.42	18.329	117.63	18.763			18.523
105					214.82	18.626	90.32	18.471	118.35	18.846			18.648
106					215.57	18.753	91.07	18.589	118.90	18.909			18.750
107					216.50	18.912	91.92	18.723	119.90	19.078			18.904
108	57												19.000
109					217.97	19.058	93.47	18.966					19.012
110					219.15	19.172	94.77	19.167					19.170
111					219.87	19.242	95.47	19.275					19.259
112					221.50	19.401	97.17	19.538					19.469
113					222.47	19.495	97.77	19.631					19.563
114					223.29	19.575	98.57	19.754					19.664
115					225.05	19.745	100.12	19.994					19.870
116					226.25	19.862	100.97	20.111					19.986
117					227.25	19.959	101.82	20.221					20.090
118					228.69	20.099	102.87	20.356					20.228
119					229.99	20.225	103.87	20.486					20.355
120					232.22	20.442	106.07	20.762					20.602
121					233.09	20.526	106.92	20.858					20.692
122					234.82	20.694	108.52	21.038					20.866
123					235.95	20.804	109.47	21.145					20.974
124					239.22	21.121	112.37	21.471					21.296
125					240.16	21.213	113.70	21.621					21.417
126					242.44	21.434	115.32	21.799					21.617
127					243.52	21.544	116.42	21.909					21.727
128					244.57	21.651	117.52	22.020					21.835
129					245.52	21.747	118.50	22.118					21.932
130					249.19	22.121	121.95	22.443	139.50	22.645			22.282
131					250.60	22.264	122.61	22.502	140.22	22.758			22.383
132					252.10	22.417	123.91	22.618	141.28	22.924			22.517
133					252.78	22.486	124.54	22.674	141.98	23.033			22.580
134					254.03	22.613	125.31	22.743	142.85	23.169			22.678

Table T2 (continued).

	Site												
	1262		1263		1264		1265		1266		1267		Leg 208
Tie	Depth (mcd)	Age (Ma)	Depth (mcd)	Age (Ma)	Depth (mcd)	Age (Ma)	Depth (mcd)	Age (Ma)	Depth (mcd)	Age (Ma)	Depth (mcd)	Age (Ma)	Age (Ma)
135					255.50	22.762	126.38	22.839	143.29	23.238			22.801
136											114.50		22.820
137					256.93	22.908	127.51	22.940	144.61	23.478			22.924
138					259.06	23.125	128.91	23.066					23.095
139					260.30	23.251	129.86	23.200					23.225
140					262.16	23.481	131.51	23.438					23.460
141					263.50	23.669	133.50	23.725					23.697
142					264.57	23.819	134.35	23.848					23.833
143					265.25	23.915	134.88	23.924					23.919
144					270.20	24.683	138.65	24.468					24.576
145					276.07	25.668	141.97	24.948					25.308
146					277.81	25.960	142.85	25.075	158.58	25.596			25.544
147			46.00										26.000
148					280.65	26.370	145.22	25.418	162.25	26.692			26.160
149					282.58	26.647	146.20	25.560	163.15	26.878			26.362
150					287.27	27.320	148.99	25.963	166.18	27.505			26.929
151					288.92	27.557	149.82	26.083	167.71	27.743			27.128
152					290.17	27.729	150.55	26.190	168.76	27.898			27.272
153					291.80	27.953	151.47	26.326	169.94	28.072			27.450
154					293.30	28.160	152.39	26.461	170.68	28.181			27.601
155					294.22	28.286	153.19	26.579	171.58	28.314			27.726
156					295.04	28.399	153.95	26.691	172.18	28.403			27.831
157					295.65	28.483	154.75	26.808	172.68	28.476			27.923
158					296.30	28.572	155.15	26.867	173.60	28.612			28.017
159	66.24	28.157	48.87	27.636	298.11	28.821	156.41	27.053	174.50	28.745			28.082
160			51.15	28.168	301.01	29.221	157.90	27.272					28.220
161			51.33	28.210	301.76	29.324	158.47	27.356	176.11	28.982			28.468
162			52.75	28.542	302.39	29.410	159.21	27.465	176.94	29.105			28.630
163			57.46	29.512			159.86	27.574	177.88	29.243			28.777
164			59.03	29.741	311.21	30.537	164.28	29.091					29.416
165			60.11	29.898	313.36	30.748	166.01	29.650					29.774
166					315.16	30.924	167.03	29.980					29.980
167			62.79	30.288			169.32	30.454					30.371
168											124.27		30.479
169			64.23	30.492			170.72	30.604					30.548
170			65.39	30.616			172.02	30.744					30.680
171											125.12		30.939
172			68.73	30.971			174.22	30.998					30.985
173			72.53	31.343			176.97	31.457					31.400
174			75.09	31.593			178.05	31.637					31.615
175											129.00		31.700
176	74.34	32.355	79.76	32.137			180.83	32.122	203.41	32.231	131.42	32.115	32.192
177	75.71	32.872	81.94	32.404			182.53	32.421	206.78	32.757	135.48	32.811	32.653
178	76.01	32.932	82.56	32.480			182.88	32.483	207.51	32.870	136.21	32.920	32.737
179			85.92	32.891			185.58	32.949					32.920
180	77.52	33.201	90.17	33.389			188.55	33.389	211.90	33.321	139.55	33.251	33.310
181			93.49	33.639			190.78	33.744	215.98	33.730	142.37	33.537	33.663
182	79.02						192.78	34.131	221.10	34.243	143.43	33.671	34.015
183			108.56	34.789			196.86	35.248	225.40	34.674			34.904
184			110.09	35.192			197.71	35.481	226.22	34.757			35.143
185			111.49	35.542			198.61	35.727	226.98	34.833			35.367
186			128.46	37.556			211.62	38.667	239.68	36.034			37.419
187			129.58	37.677			212.62	38.970	240.63	36.081			37.576
188			138.07	39.217			217.43	40.618					39.918
189									254.60				40.300
190									257.20				43.600
191			202.99	46.715			225.00	46.850					46.783
192									259.60				47.200
193	85.24	42.554	204.29	46.849			226.05	47.838			150.10	41.200	47.343
194			205.42	46.964			226.85	48.438					47.701
195									260.80				47.800
196									262.20				48.000
197			207.87	47.215			228.15	49.319					48.267
198			208.73	47.303			228.55	49.368					48.336
199			214.74	47.918			230.73	49.638					48.778
200									265.00				49.000
201	96.66	50.969									179.66	51.025	50.997

Table T2 (continued).

	Site													
	1262		1263		1264		1265		1266		1267		Leg 208
Tie	Depth (mcd)	Age (Ma)	Depth (mcd)	Age (Ma)	Depth (mcd)	Age (Ma)	Depth (mcd)	Age (Ma)	Depth (mcd)	Age (Ma)	Depth (mcd)	Age (Ma)	Age (Ma)
202									269.00				51.000
203	97.26	51.033									180.43	51.076	51.055
204	97.81	51.104									181.20	51.126	51.115
205	98.16	51.149									181.66	51.156	51.153
206	98.43	51.184									181.97	51.176	51.180
207	99.2	51.283									183.15	51.253	51.268
208	99.56	51.329									183.65	51.286	51.307
209	100.03	51.390									184.35	51.331	51.360
210	100.56	51.458	260.83	51.656			245.88	51.353			185.07	51.378	51.461
211	101.53	51.582	262.90	51.757			248.26	51.555			186.37	51.463	51.589
212	102.2	51.669	264.65	51.843			249.06	51.623			187.12	51.512	51.661
213	102.66	51.728	265.93	51.905			249.94	51.697			187.70	51.550	51.720
214			267.40	51.977			251.06	51.793			188.34	51.592	51.787
215	104.56	51.972	269.31	52.070			253.14	51.969			189.94	51.696	51.927
216	105.53	52.097	270.33	52.120			254.78	52.109			191.14	51.789	52.029
217	106.49	52.220	273.85	52.292			256.04	52.216			192.22	51.873	52.150
218	107.24	52.316	275.18	52.357			257.34	52.326			192.99	51.933	52.233
219	107.76	52.383	276.51	52.427			258.37	52.409			193.69	51.987	52.302
220	108.32	52.445	277.91	52.509			259.41	52.466			194.29	52.034	52.363
221									282.20				52.400
222	109.06	52.523	279.93	52.627			260.94	52.550			195.53	52.130	52.458
223	109.69	52.589	280.91	52.684			262.24	52.622			196.21	52.183	52.520
224			283.93	52.861			264.41	52.741			197.71	52.300	52.634
225	110.99	52.726	284.21	52.878			265.44	52.798			198.08	52.328	52.682
226	112.16	52.849	284.90	52.918			267.07	52.888			198.94	52.395	52.762
227	112.43	52.877	285.37	52.946			267.57	52.915			199.22	52.438	52.794
228	112.67	52.902	285.94	52.979			268.11	52.945			199.52	52.490	52.829
229			286.34	53.004			268.44	52.963			199.76	52.532	52.833
230	113.15	52.953	286.92	53.058			269.07	52.998			200.06	52.583	52.898
231	113.53	52.993	287.77	53.138			270.01	53.038			200.52	52.663	52.958
232	116.27	53.157	292.98	53.356			275.59	53.276	291.38	52.845	203.99	53.264	53.179
233	116.93	53.196	294.88	53.386			277.40	53.323	292.68	52.908	205.05	53.324	53.227
234	122.14	53.477	300.45	53.470			283.56	53.488	295.05	53.175	209.70	53.512	53.425
235	124.09	53.629	305.43	53.544			289.01	53.723			212.80	53.696	53.648
236	126.31	53.812	309.76	53.608			292.65	53.879			215.37	53.848	53.787
237	129.53	54.087	314.79	53.683							218.67	54.075	53.948
238	132.37	54.330					302.30	54.344			222.63	54.360	54.345
239	133.91	54.462					305.27	54.488			224.51	54.496	54.482
240	136.41	54.676					309.21	54.678			227.35	54.701	54.685
241	137.24	54.747					310.84	54.757	301.92	54.450	228.20	54.762	54.755
242	138.82	54.882							304.65		230.18	54.905	54.893
243	140.02	54.985	335.59	54.998			315.81	54.998	306.75	54.990	231.48	54.999	54.994
244	144	55.263									236.28	55.246	55.255
245	144.87	55.323					319.18	55.163	313.17	55.434	237.60	55.314	55.309
246			345.00										55.600
247	151.58	55.788									246.55	55.776	55.782
248	155.34	56.215									251.14	56.133	56.174
249							340.43						56.200
250	156.41	56.262									252.43	56.356	56.309
251	161.14	56.592									259.28	56.721	56.657
252	162.27	56.718									261.23	56.801	56.760
253	165.94	57.026									265.63	56.981	57.004
254	168.74	57.242									271.91	57.239	57.240
255	169.54	57.306									273.30	57.295	57.301
256	170.79	57.484									274.77	57.459	57.472
257	171.51	57.551									275.57	57.553	57.552
258	173.24	57.887									277.37	57.887	57.887
259	173.71	57.986							371.06	58.198	277.99	58.189	58.124
260	175.11	58.286									278.51	58.312	58.299
261									372.64				58.400
262	177.91	58.652									281.75	58.849	58.750
263	178.54	58.722									282.28	58.870	58.796
264	181.04	58.876									285.22	58.989	58.932
265	181.64	58.901									285.79	59.012	58.957
266	184.57	59.025									287.92	59.098	59.062
267	185.64	59.070									289.72	59.171	59.121
268	186.24	59.096									290.70	59.210	59.153

Table T2 (continued).

	Site												
	1262		1263		1264		1265		1266		1267		Leg 208
Tie	Depth (mcd)	Age (Ma)	Depth (mcd)	Age (Ma)	Depth (mcd)	Age (Ma)	Depth (mcd)	Age (Ma)	Depth (mcd)	Age (Ma)	Depth (mcd)	Age (Ma)	Age (Ma)
269	186.94	59.125									291.52	59.243	59.184
270	194.61	60.672									297.16	60.768	60.720
271	195.38	60.880									298.24	60.894	60.887
272	196.84	61.109									299.94	61.106	61.107
273	198.62	61.390									301.66	61.356	61.373
274	201.7	61.954									304.89	62.051	62.003
275	210.73	63.883									313.63	63.900	63.892
276	214.15	64.661									317.32	64.653	64.657
277	216.72	65.009									320.38	64.995	65.002
278	218.04	65.108									321.78	65.081	65.095
279	223.16	65.493									326.25	65.347	65.420
280	225.86	66.037									330.64	65.988	66.013
281	226.8	66.312									331.32	66.075	66.193
282	230.87	67.502									334.66	66.317	66.909
283											360.60		67.610
284											362.45		67.735

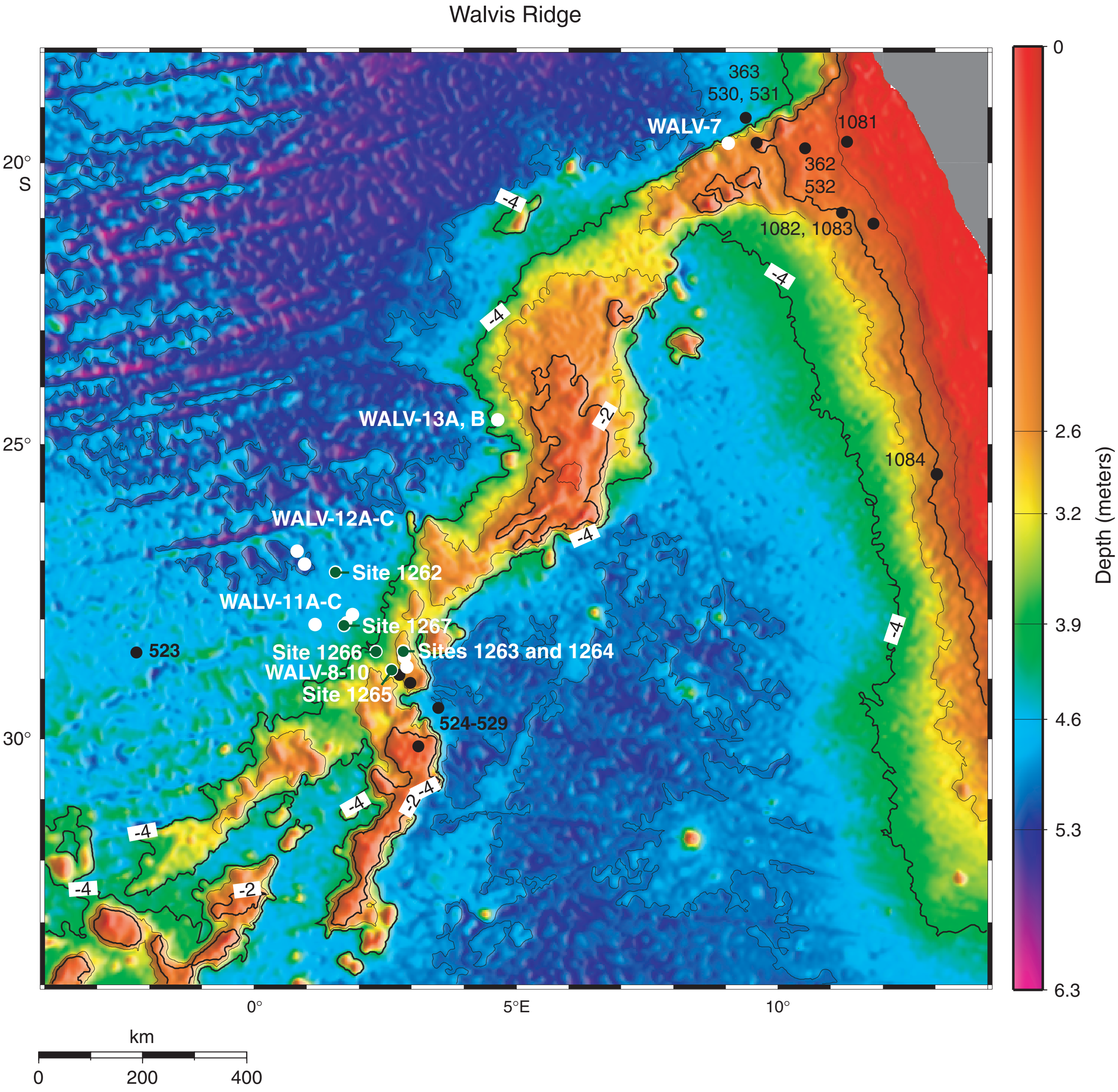
Walvis Ridge
363
530, 531
WALV-7
1081
362
532
1082, 1083
-4
-4
-4
-2
WALV-13A, B
1084
WALV-12A-C
-4
Site 1262
WALV-11A-C
Site 1267
523
Site 1266
Sites 1263 and 1264
WALV-8-10
Site 1265
524-529
-4
-4
-2 -4
-4
-4
-2
20°
S
25°
30°
0°
5°E
10°
km
0
200
400
Depth (meters)
0
2.6
3.2
3.9
4.6
5.3
6.3

Figure F1

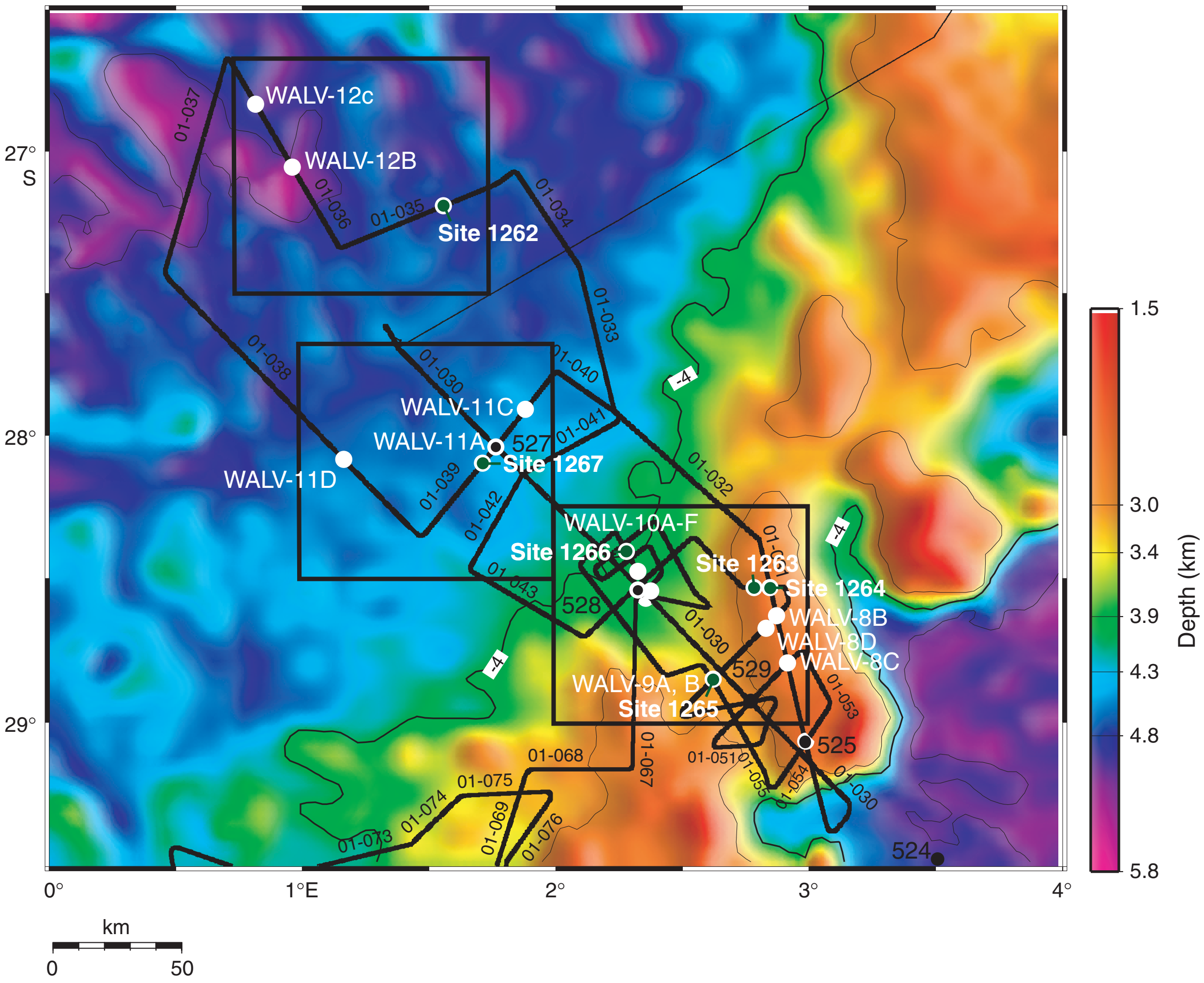
WALV-12c
WALV-12B
01-037
01-036
01-035
01-034
Site 1262
01-033
01-038
01-030
01-040
WALV-11C
WALV-11A
527
01-041
Site 1267
WALV-11D
01-039
01-042
01-032
-4
WALV-10A-F
Site 1266
Site 1263
Site 1264
01-043
528
WALV-8B
01-030
WALV-8D
WALV-8C
529
WALV-9A, B
Site 1265
01-053
525
01-068
01-067
01-051
01-055
01-054
01-030
01-075
01-074
01-073
01-069
01-076
524
27°
S
28°
29°
0°
1°E
2°
3°
4°
km
0
50
1.5
3.0
3.4
3.9
4.3
4.8
5.8
Depth (km)

Figure F2

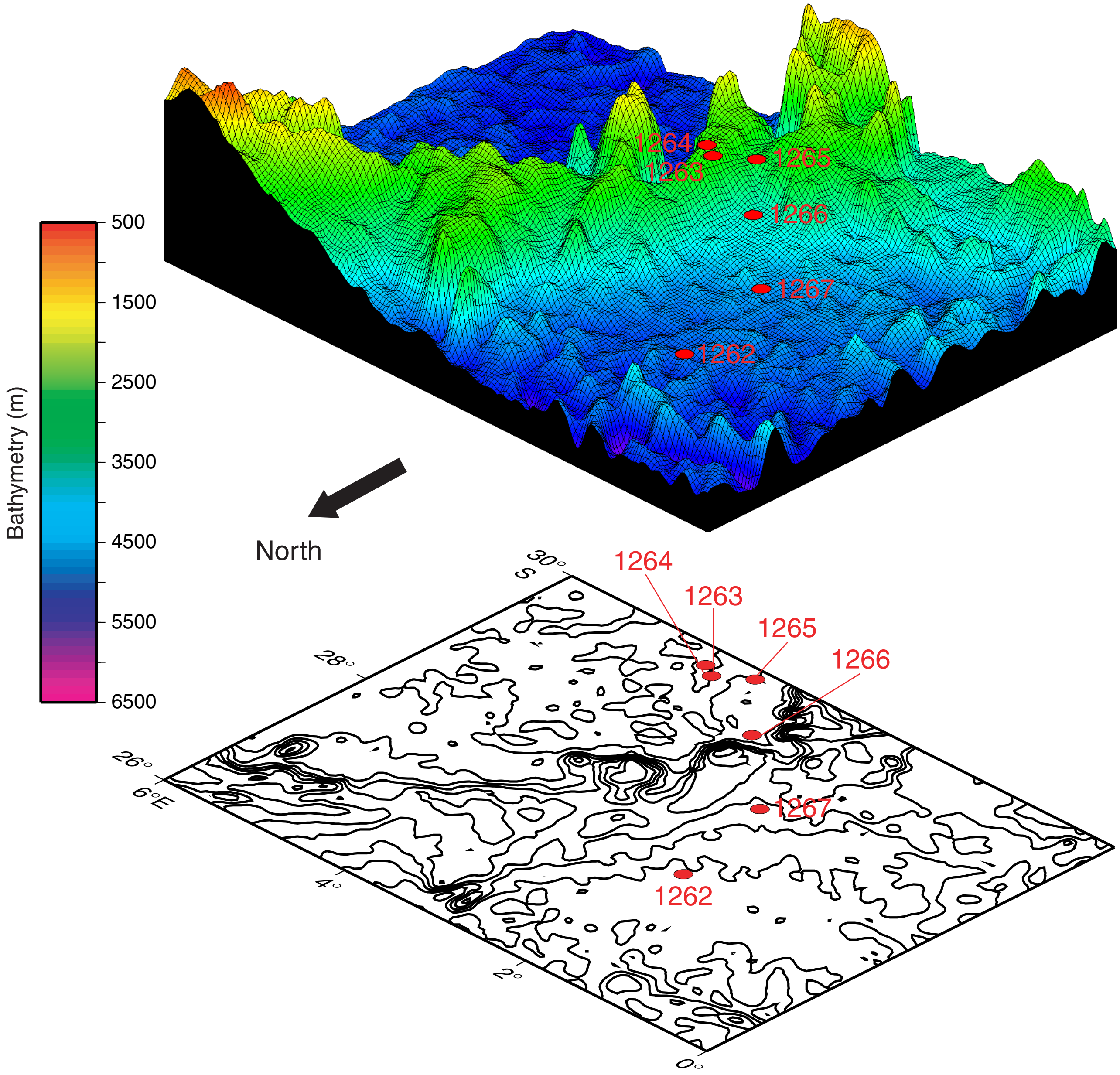
1264
1263
1265
1266
1267
1262
Bathymetry (m)
500
1500
2500
3500
4500
5500
6500
North
30° S
28°
26°
6°E
4°
2°
0°
1264
1263
1265
1266
1267
1262

Figure F3

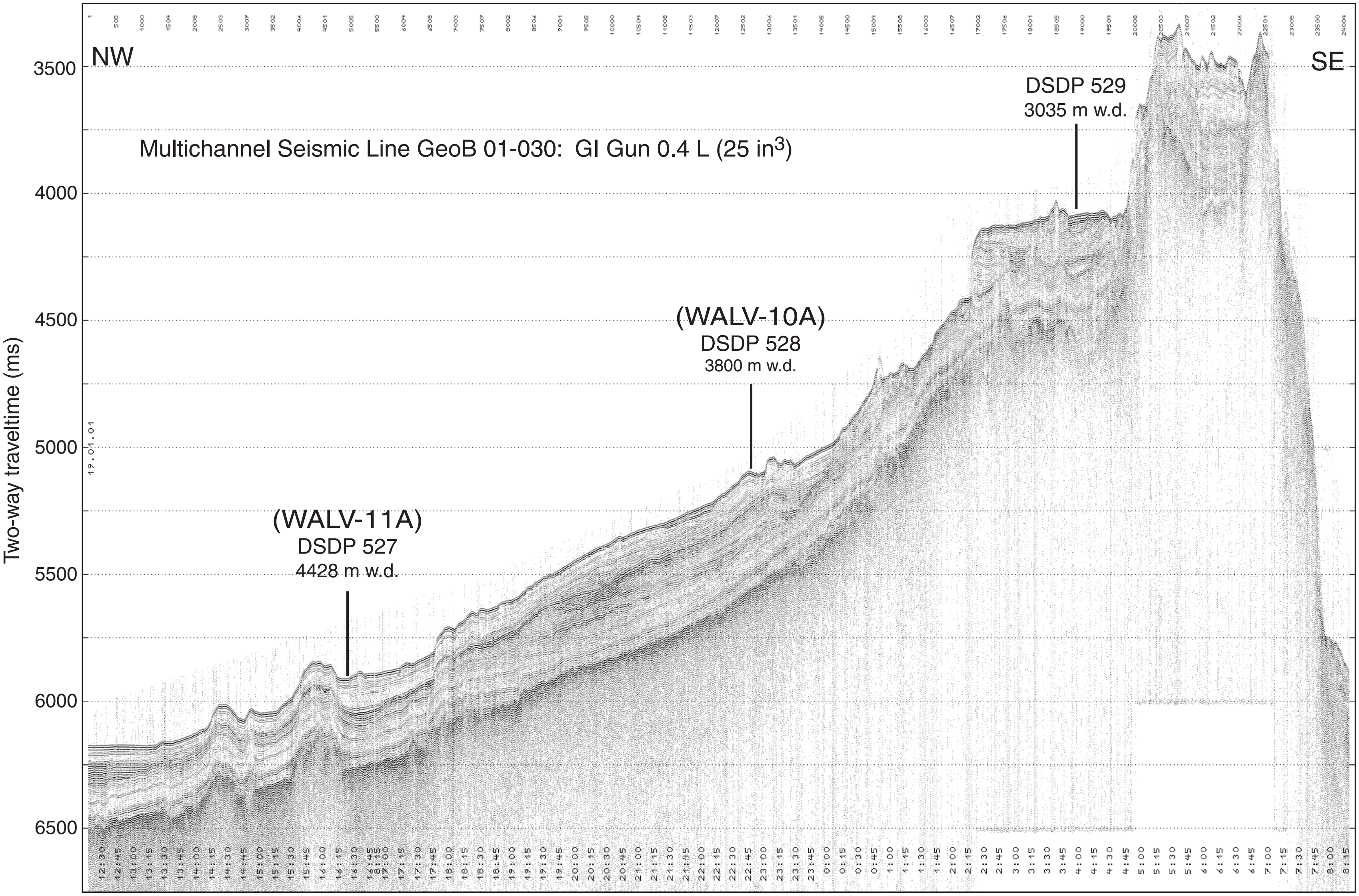
NW
SE
Multichannel Seismic Line GeoB 01-030: GI Gun 0.4 L (25 in³)
DSDP 529
3035 m w.d.
(WALV-10A)
DSDP 528
3800 m w.d.
(WALV-11A)
DSDP 527
4428 m w.d.
Two-way traveltime (ms)
3500
4000
4500
5000
5500
6000
6500
19.01.01

Figure F4

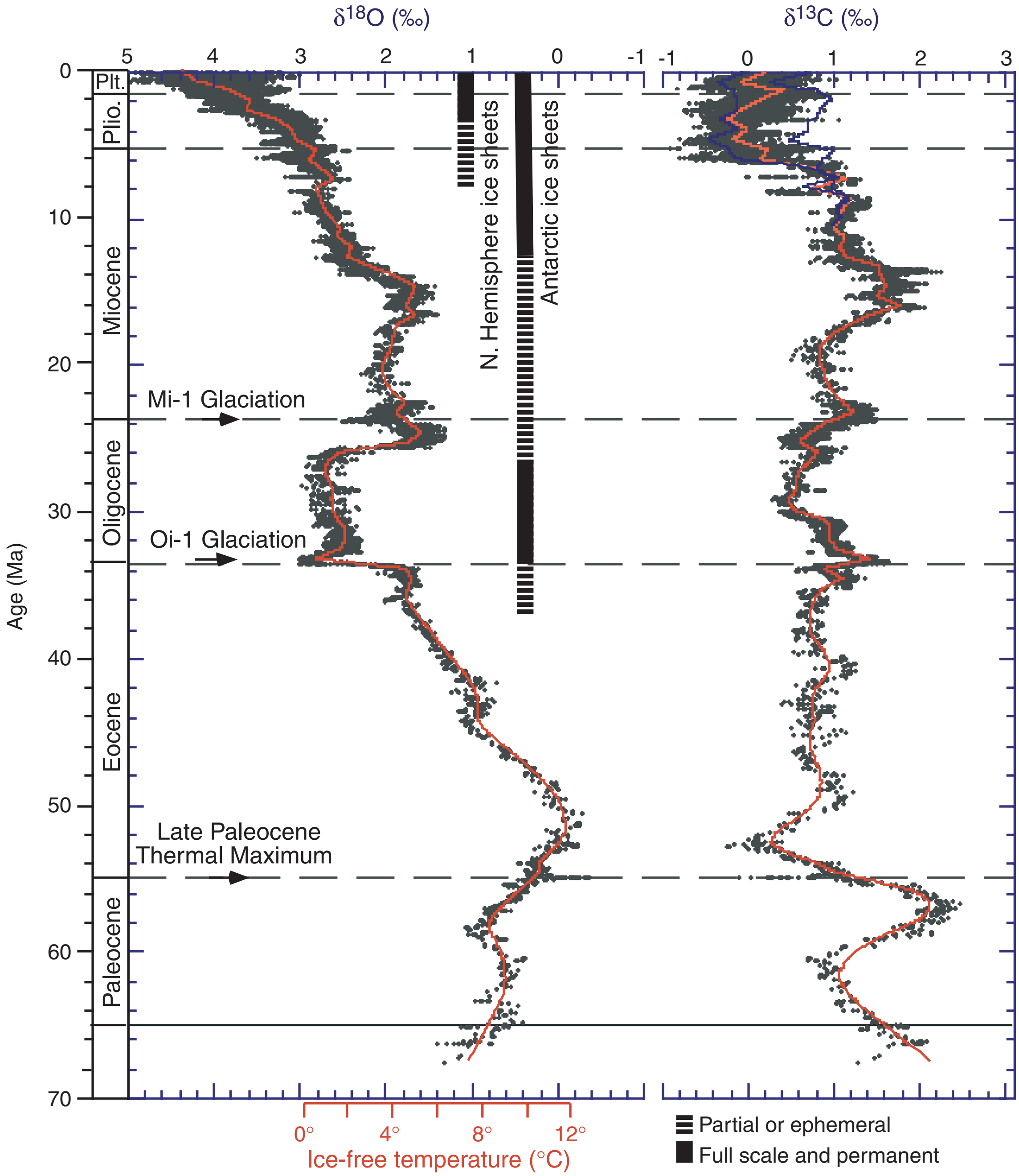
$\delta^{18}O$ (‰)
$\delta^{13}C$ (‰)
5
4
3
2
1
0
-1
-1
0
1
2
3
Age (Ma)
0
10
20
30
40
50
60
70
Plt.
Plio.
Miocene
Oligocene
Eocene
Paleocene
Mi-1 Glaciation
Oi-1 Glaciation
Late Paleocene
Thermal Maximum
N. Hemisphere ice sheets
Antarctic ice sheets
0°
4°
8°
12°
Ice-free temperature (°C)
Partial or ephemeral
Full scale and permanent

Figure F5

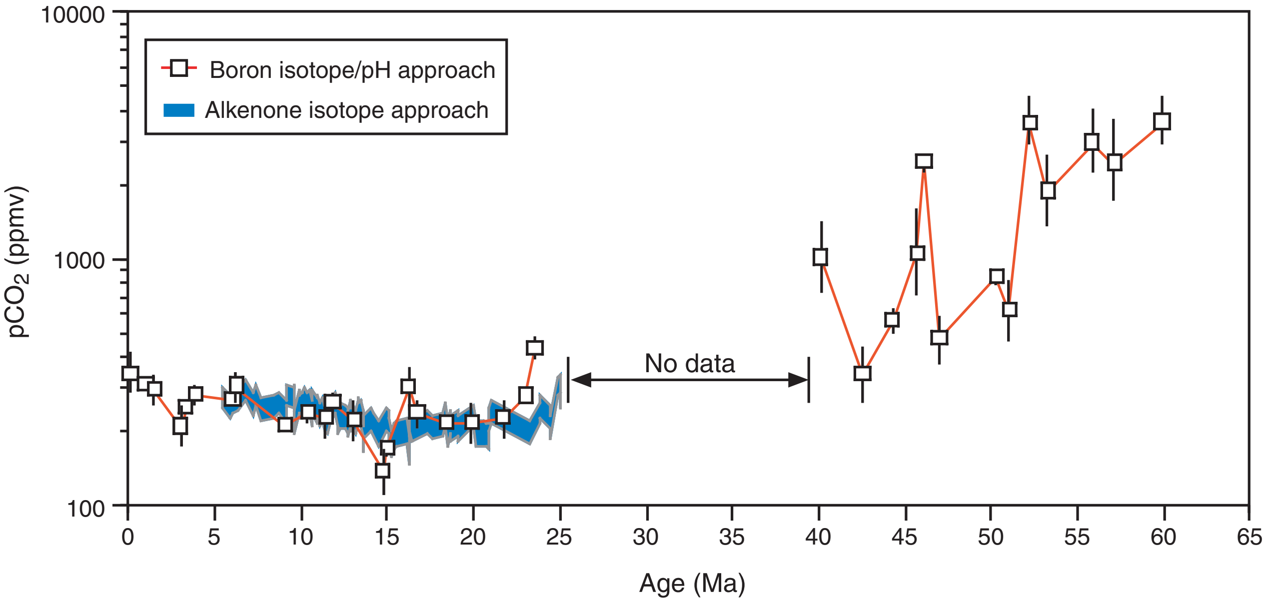
Boron isotope/pH approach
Alkenone isotope approach
pCO$_2$ (ppmv)
10000
1000
100
No data
0
5
10
15
20
25
30
35
40
45
50
55
60
65
Age (Ma)

Figure F6

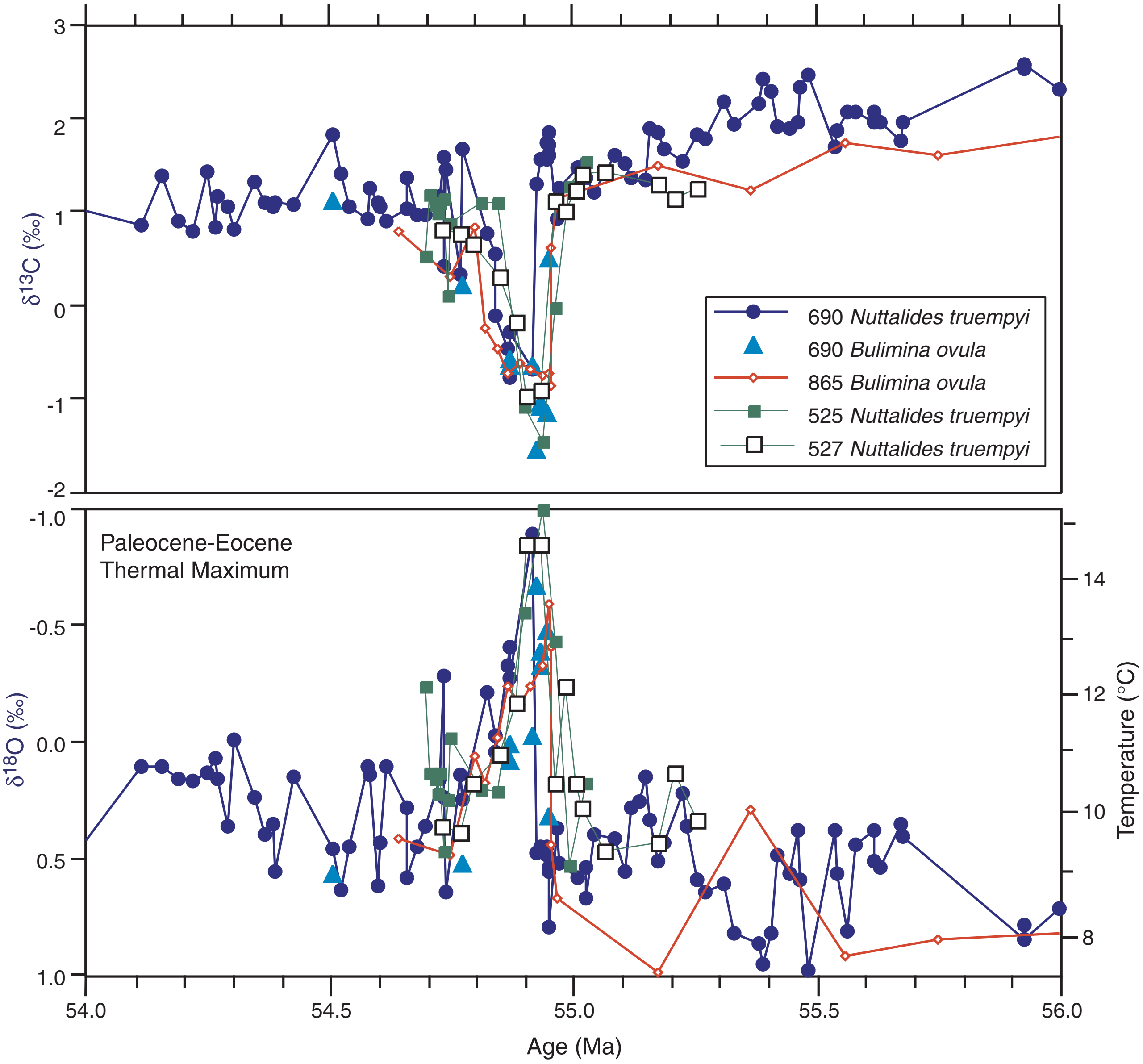
3
2
1
0
-1
-2
δ13C (‰)
690 Nuttalides truempyi
690 Bulimina ovula
865 Bulimina ovula
525 Nuttalides truempyi
527 Nuttalides truempyi
-1.0
-0.5
0.0
0.5
1.0
δ18O (‰)
Paleocene-Eocene
Thermal Maximum
14
12
10
8
Temperature (°C)
54.0
54.5
55.0
55.5
56.0
Age (Ma)

Figure F7

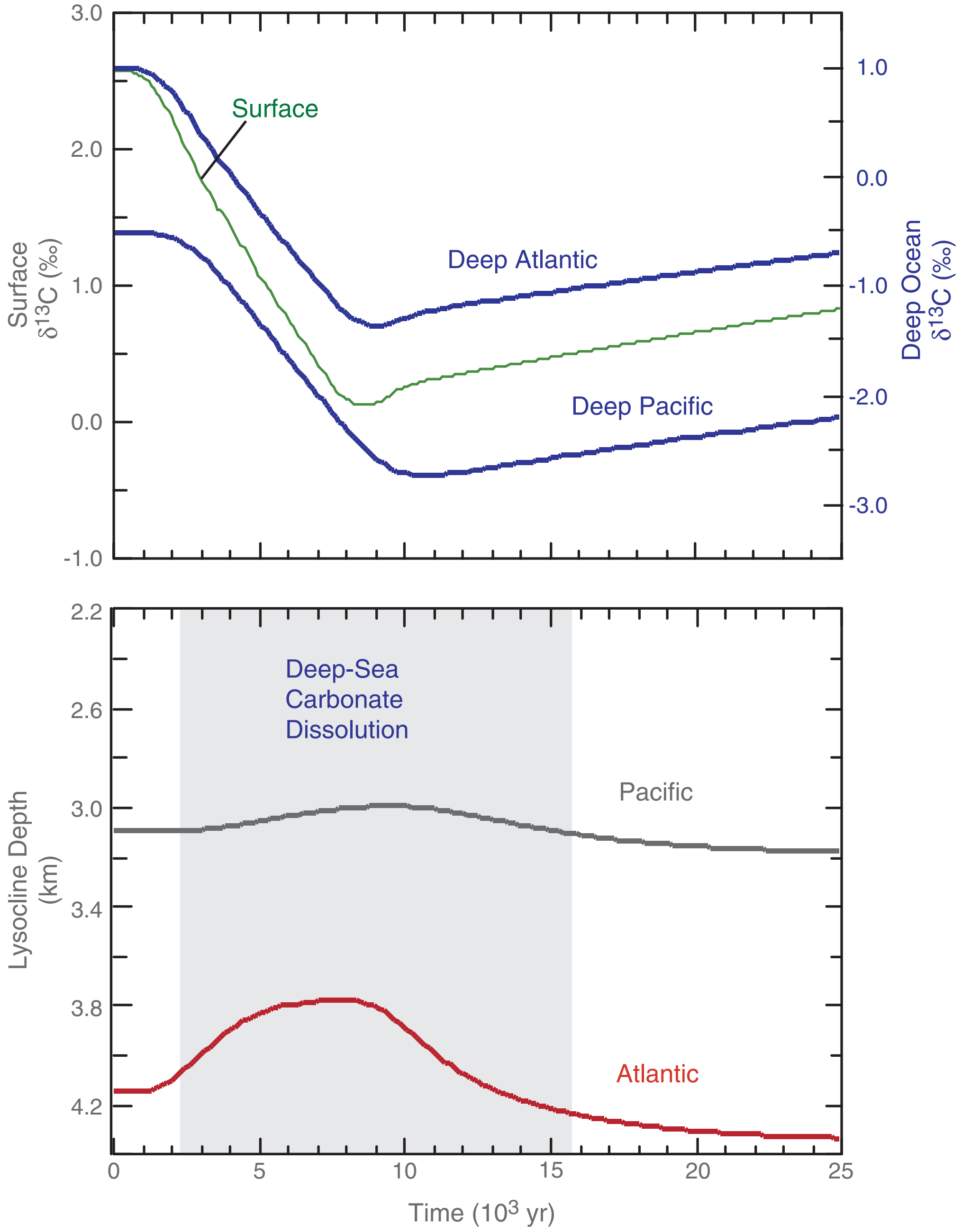
3.0
2.0
1.0
0.0
-1.0
Surface
δ13C (‰)
Surface
Deep Atlantic
Deep Pacific
1.0
0.0
-1.0
-2.0
-3.0
Deep Ocean
δ13C (‰)
2.2
2.6
3.0
3.4
3.8
4.2
Lysocline Depth
(km)
Deep-Sea
Carbonate
Dissolution
Pacific
Atlantic
0
5
10
15
20
25
Time (10³ yr)

Figure F8

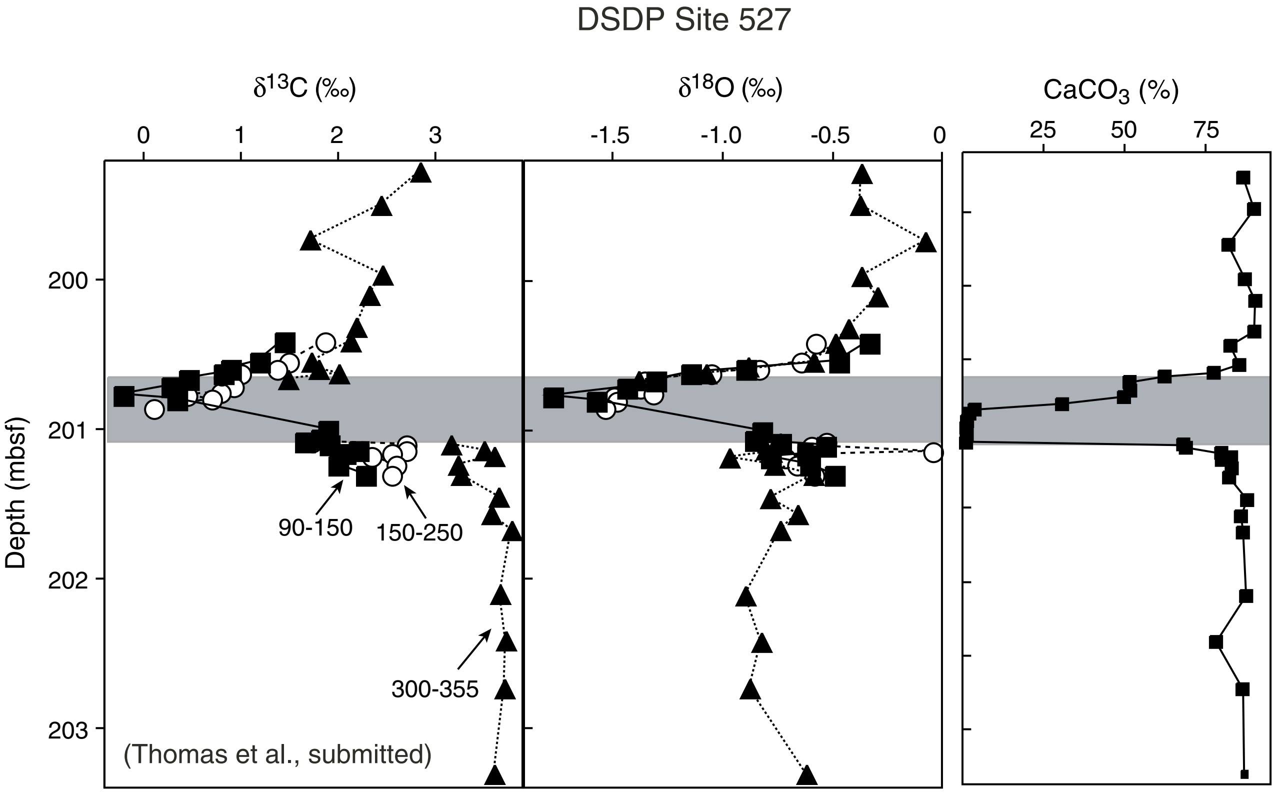
DSDP Site 527
δ13C (‰)
0
1
2
3
δ18O (‰)
-1.5
-1.0
-0.5
0
CaCO3 (%)
25
50
75
Depth (mbsf)
200
201
202
203
90-150
150-250
300-355
(Thomas et al., submitted)

Figure F9

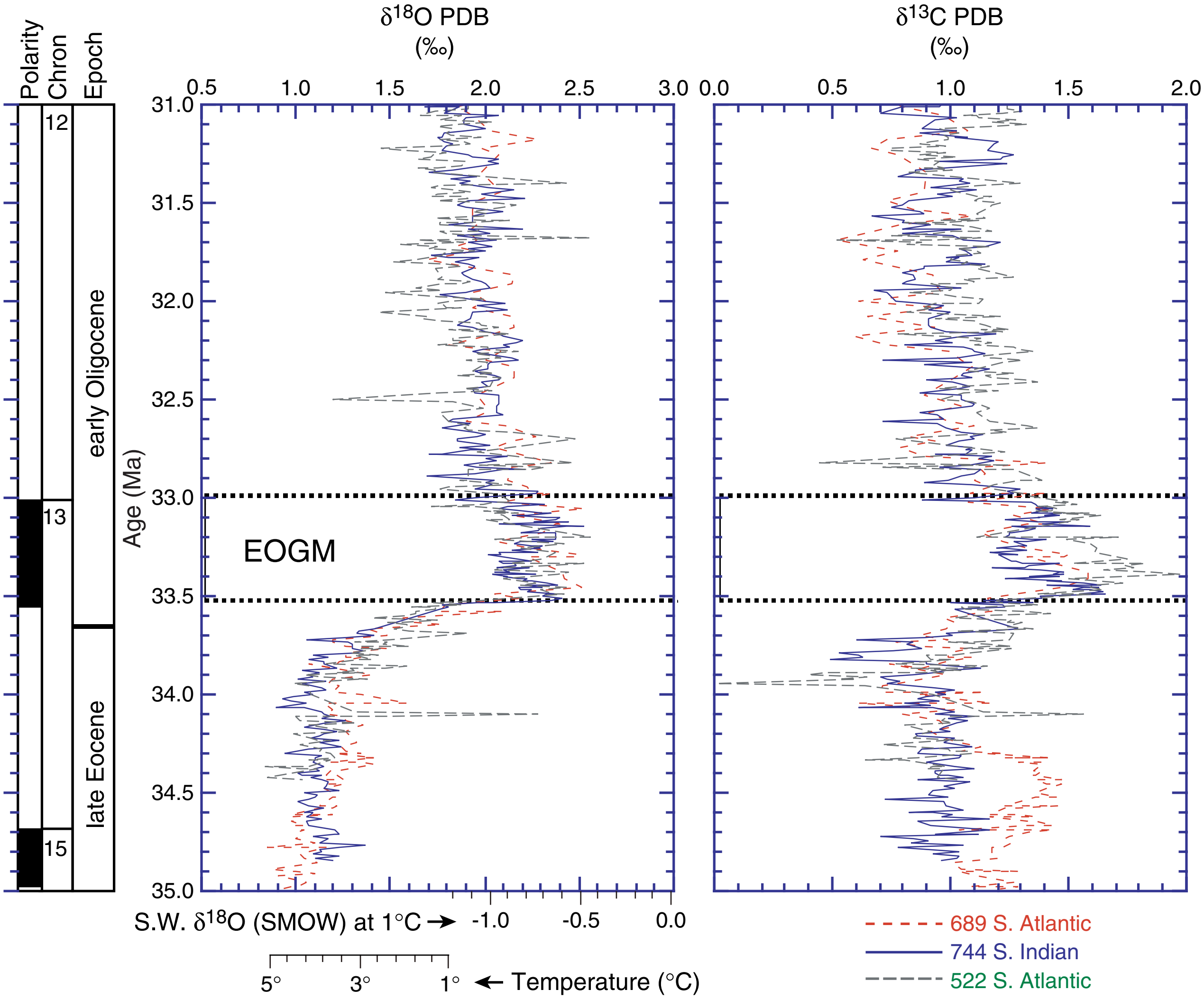
Polarity
Chron
Epoch
12
13
15
early Oligocene
late Eocene
Age (Ma)
31.0
31.5
32.0
32.5
33.0
33.5
34.0
34.5
35.0
δ^{18}O PDB
(‰)
0.5
1.0
1.5
2.0
2.5
3.0
δ^{13}C PDB
(‰)
0.0
0.5
1.0
1.5
2.0
EOGM
S.W. δ^{18}O (SMOW) at 1°C →
-1.0
-0.5
0.0
5°
3°
1°
← Temperature (°C)
689 S. Atlantic
744 S. Indian
522 S. Atlantic

Figure F10

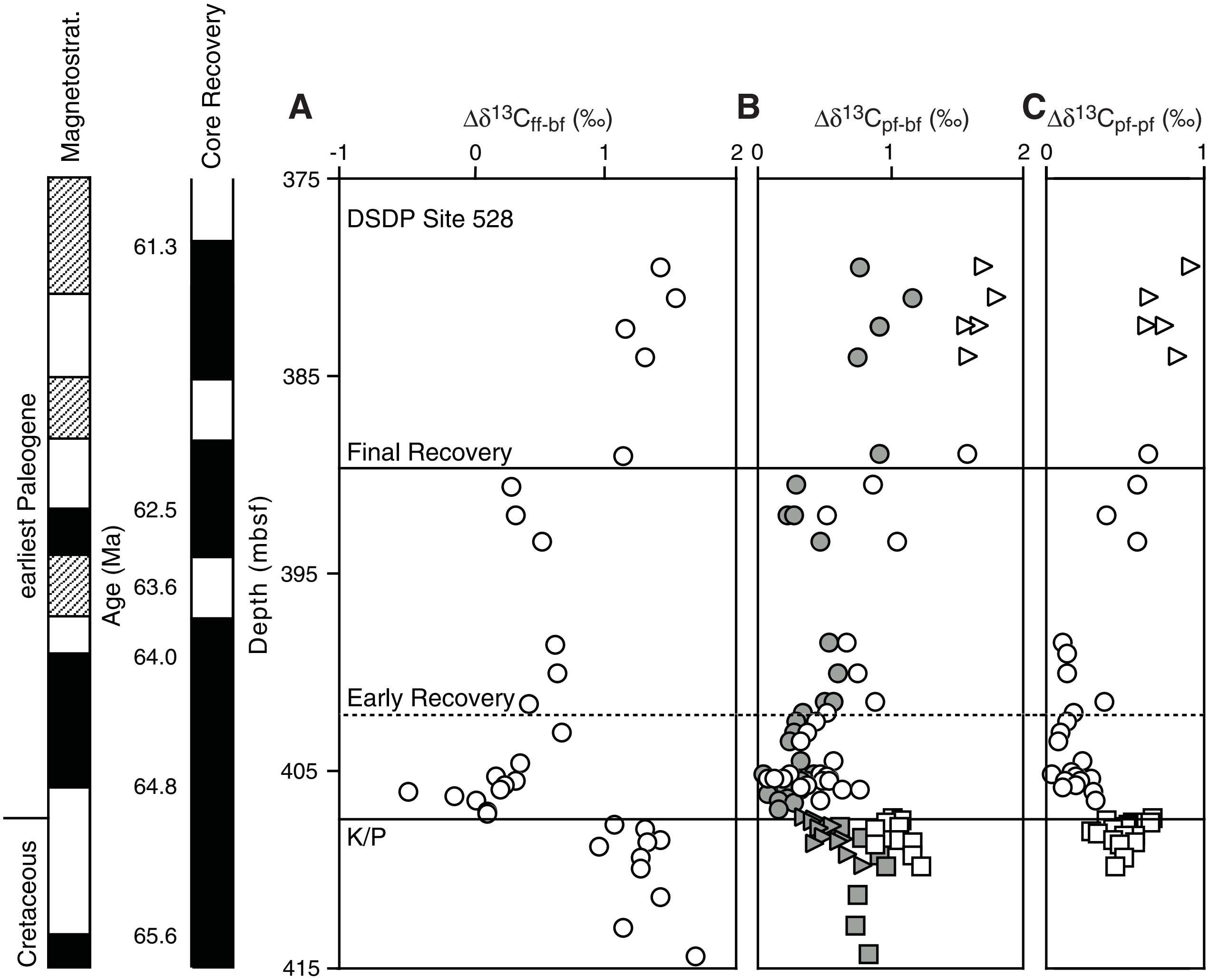
Magnetostrat.
Core Recovery
earliest Paleogene
Cretaceous
Age (Ma)
61.3
62.5
63.6
64.0
64.8
65.6
Depth (mbsf)
375
385
395
405
415
A
$\Delta\delta^{13}C_{ff\text{-}bf}$ (‰)
-1
0
1
2
B
$\Delta\delta^{13}C_{pf\text{-}bf}$ (‰)
0
1
2
C
$\Delta\delta^{13}C_{pf\text{-}pf}$ (‰)
0
1
DSDP Site 528
Final Recovery
Early Recovery
K/P

Figure F11

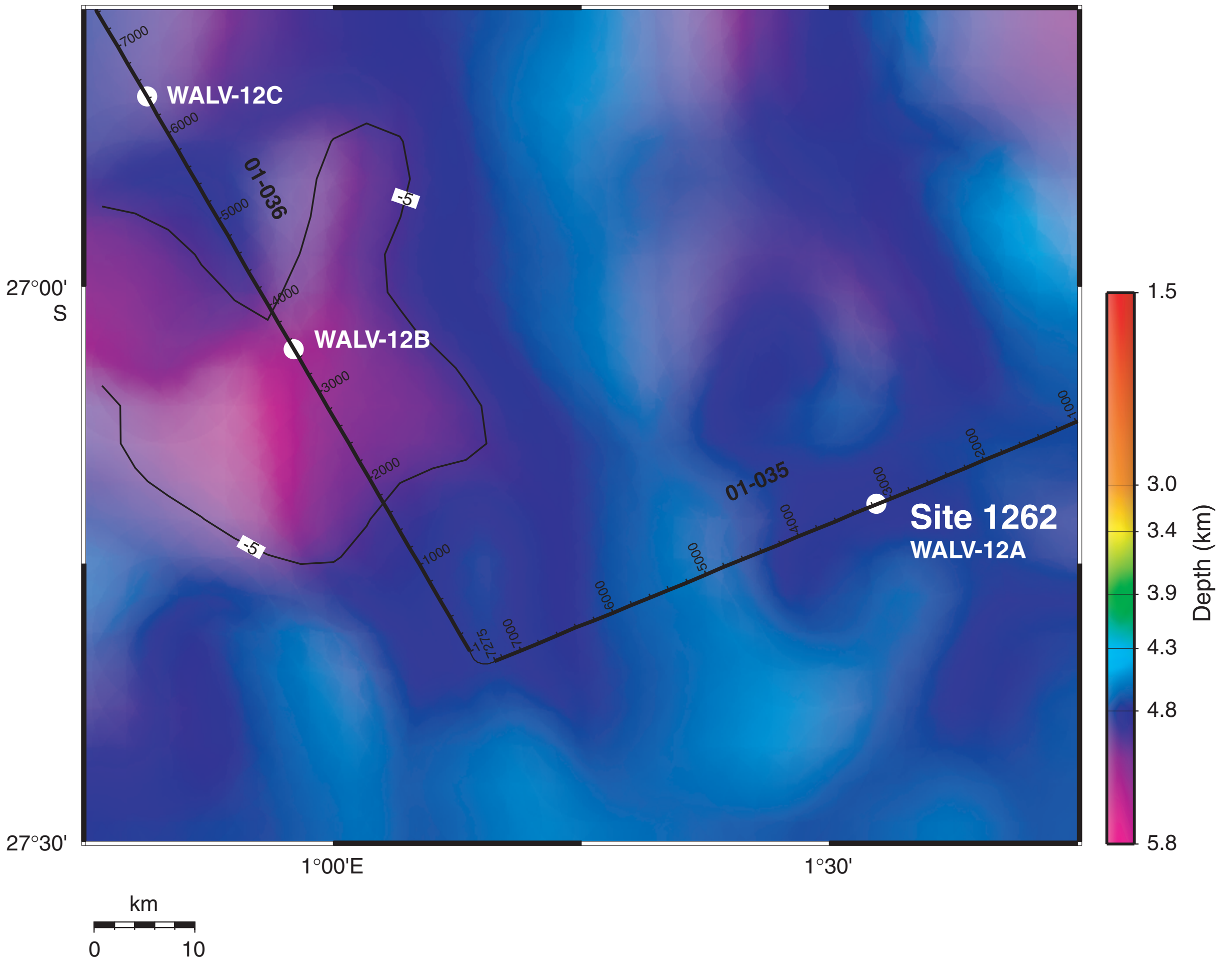
7000
WALV-12C
6000
01-036
5000
-5
4000
WALV-12B
3000
2000
-5
1000
1
7275
7000
6000
5000
01-035
4000
3000
Site 1262
WALV-12A
2000
1000
27°00'
S
27°30'
1°00'E
1°30'
1.5
3.0
3.4
3.9
4.3
4.8
5.8
Depth (km)
km
0
10

Figure F12

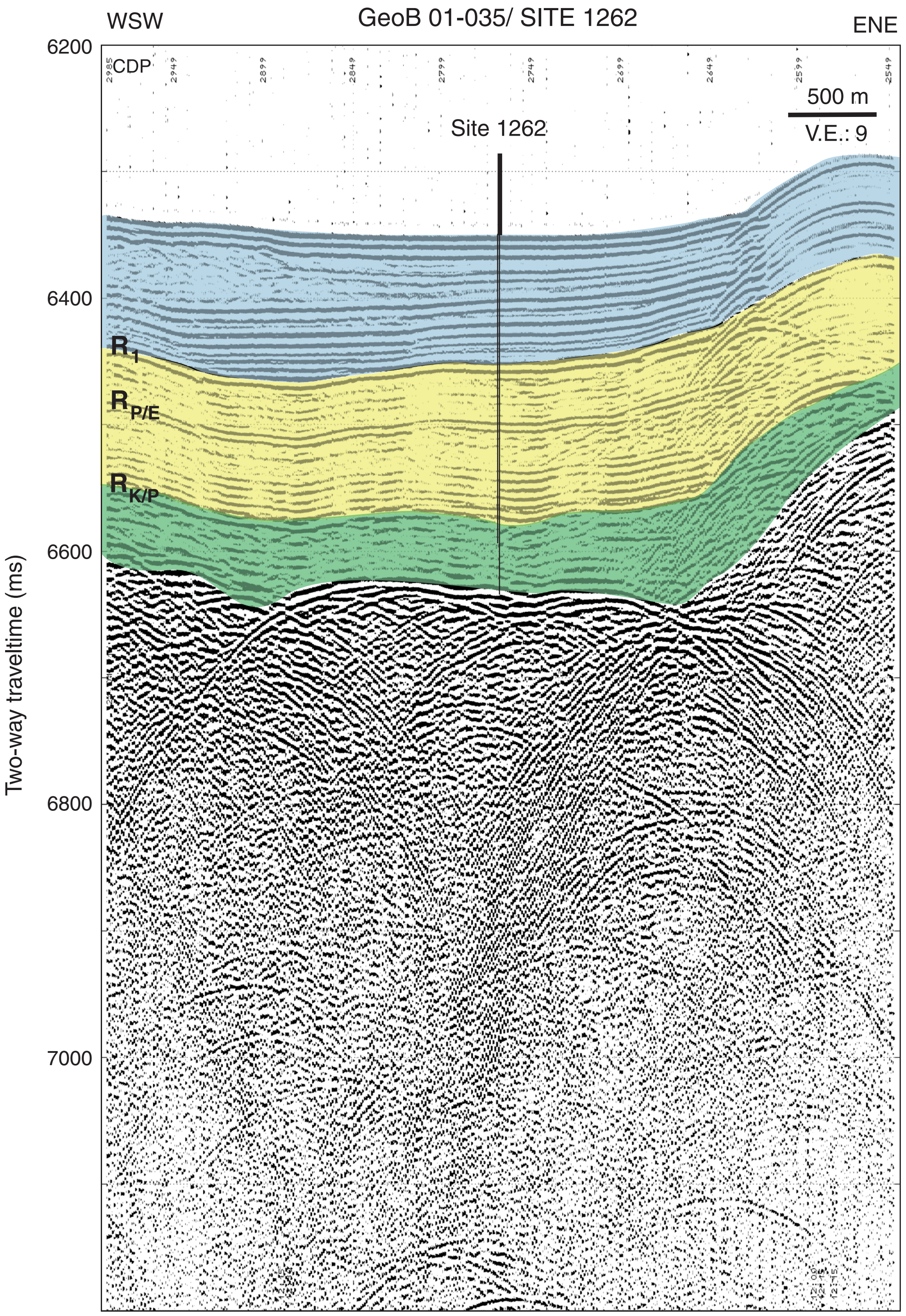
WSW
GeoB 01-035/ SITE 1262
ENE
CDP
2985
2949
2899
2849
2799
2749
2699
2649
2599
2549
Site 1262
500 m
V.E.: 9
R1
RP/E
RK/P
6200
6400
6600
6800
7000
Two-way traveltime (ms)

Figure F13

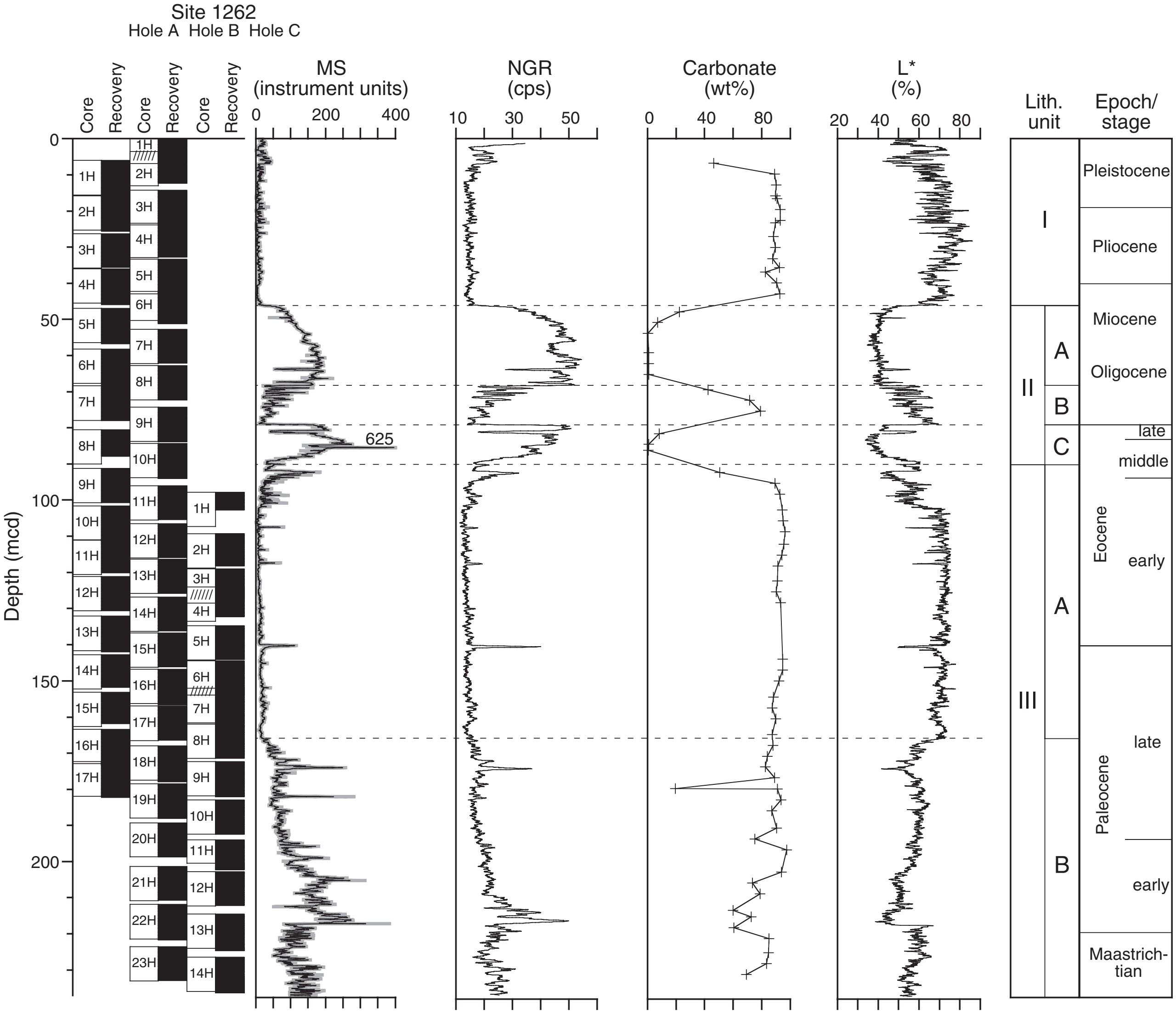
Site 1262
Hole A Hole B Hole C
Core
Recovery
Depth (mcd)
MS (instrument units)
0 200 400
625
NGR (cps)
10 30 50
Carbonate (wt%)
0 40 80
L* (%)
20 40 60 80
Lith. unit
Epoch/stage
I
II
III
A
B
C
Pleistocene
Pliocene
Miocene
Oligocene
Eocene
late
middle
early
Paleocene
Maastrichtian
0
50
100
150
200

Figure F14

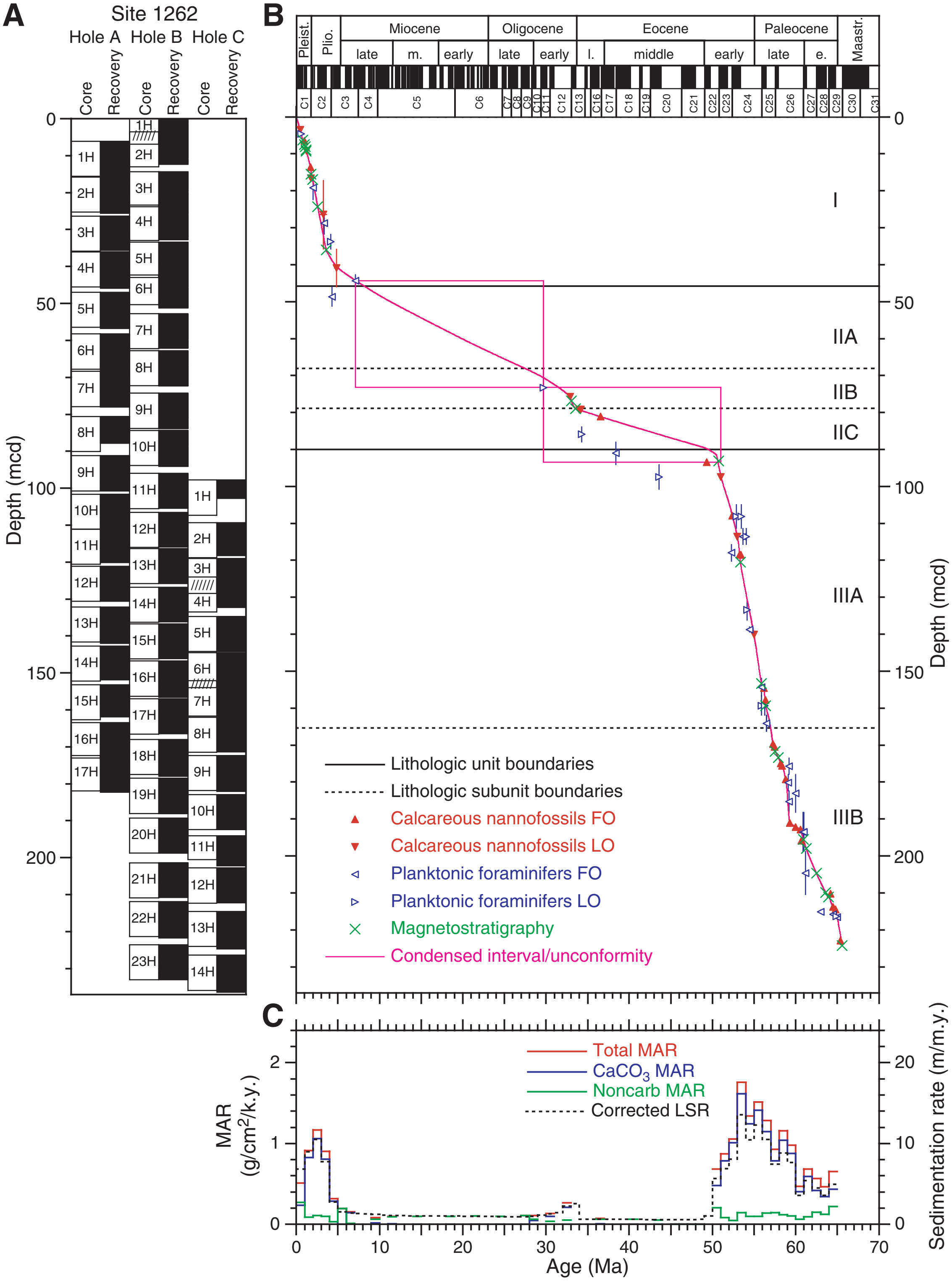
A
Site 1262
Hole A
Hole B
Hole C
Core
Recovery
Depth (mcd)
0
50
100
150
200
1H 2H 3H 4H 5H 6H 7H 8H 9H 10H 11H 12H 13H 14H 15H 16H 17H
1H 2H 3H 4H 5H 6H 7H 8H 9H 10H 11H 12H 13H 14H 15H 16H 17H 18H 19H 20H 21H 22H 23H
1H 2H 3H 4H 5H 6H 7H 8H 9H 10H 11H 12H 13H 14H
B
Pleist.
Plio.
Miocene
late
m.
early
Oligocene
late
early
Eocene
l.
middle
early
Paleocene
late
e.
Maastr.
C1 C2 C3 C4 C5 C6 C7 C8 C9 C10 C11 C12 C13 C16 C17 C18 C19 C20 C21 C22 C23 C24 C25 C26 C27 C28 C29 C30 C31
I
IIA
IIB
IIC
IIIA
IIIB
Lithologic unit boundaries
Lithologic subunit boundaries
Calcareous nannofossils FO
Calcareous nannofossils LO
Planktonic foraminifers FO
Planktonic foraminifers LO
Magnetostratigraphy
Condensed interval/unconformity
Depth (mcd)
C
Total MAR
$CaCO_3$ MAR
Noncarb MAR
Corrected LSR
MAR ($g/cm^2/k.y.$)
0
1
2
Sedimentation rate (m/m.y.)
0
10
20
Age (Ma)
0 10 20 30 40 50 60 70

Figure F15

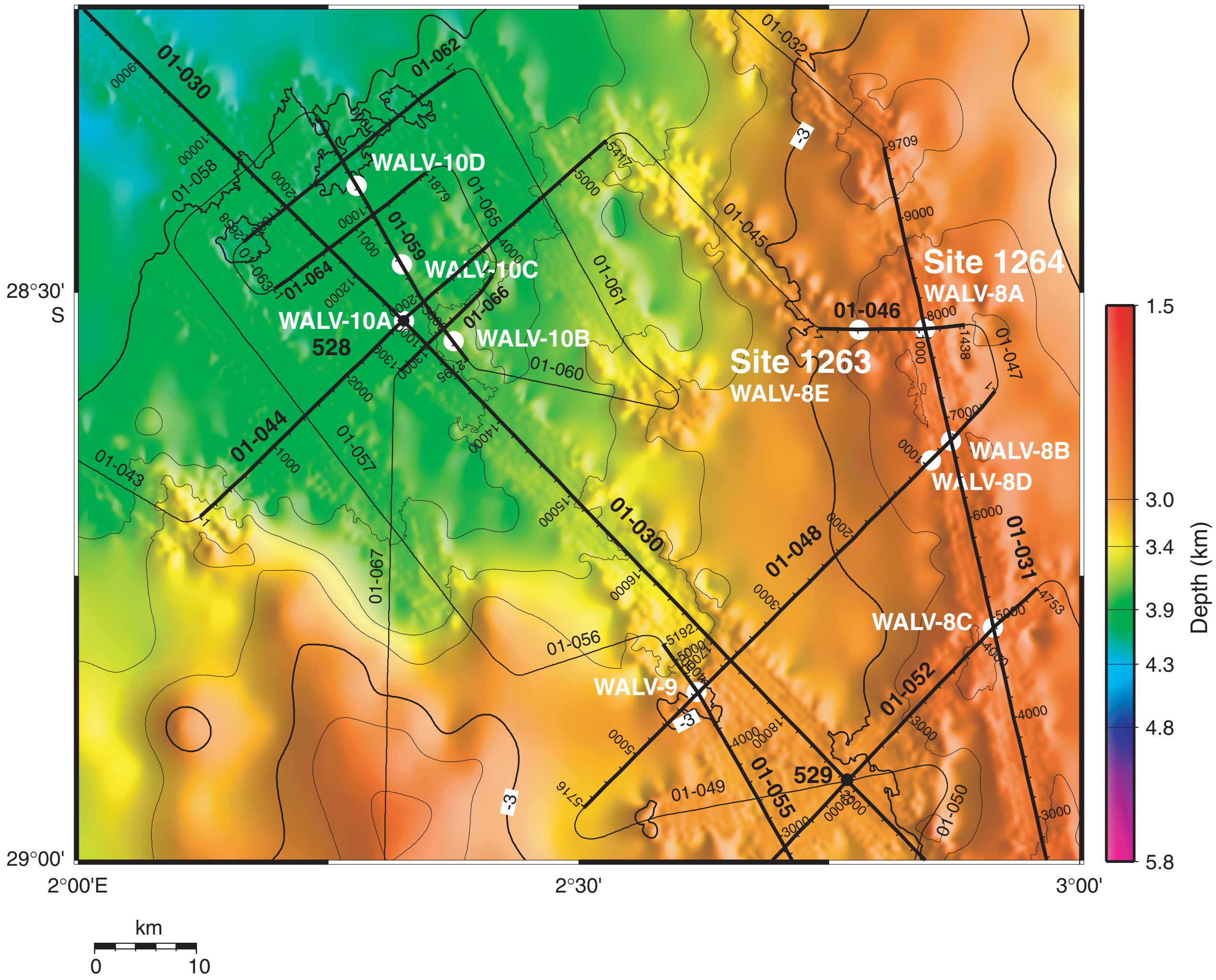
01-030
01-062
01-032
-3
9709
WALV-10D
01-058
01-065
01-045
9000
Site 1264
WALV-8A
01-059
WALV-10C
01-061
01-064
01-066
01-046
8000
1438
01-047
WALV-10A
528
WALV-10B
01-060
Site 1263
WALV-8E
7000
WALV-8B
WALV-8D
01-044
01-057
01-043
01-030
01-048
6000
01-031
4753
01-067
WALV-8C
5000
01-056
5192
WALV-9
01-052
-3
529
01-049
01-055
01-050
5716
4000
3000
-3
28°30' S
29°00'
2°00'E
2°30'
3°00'
1.5
3.0
3.4
3.9
4.3
4.8
5.8
Depth (km)
km
0
10

Figure F16

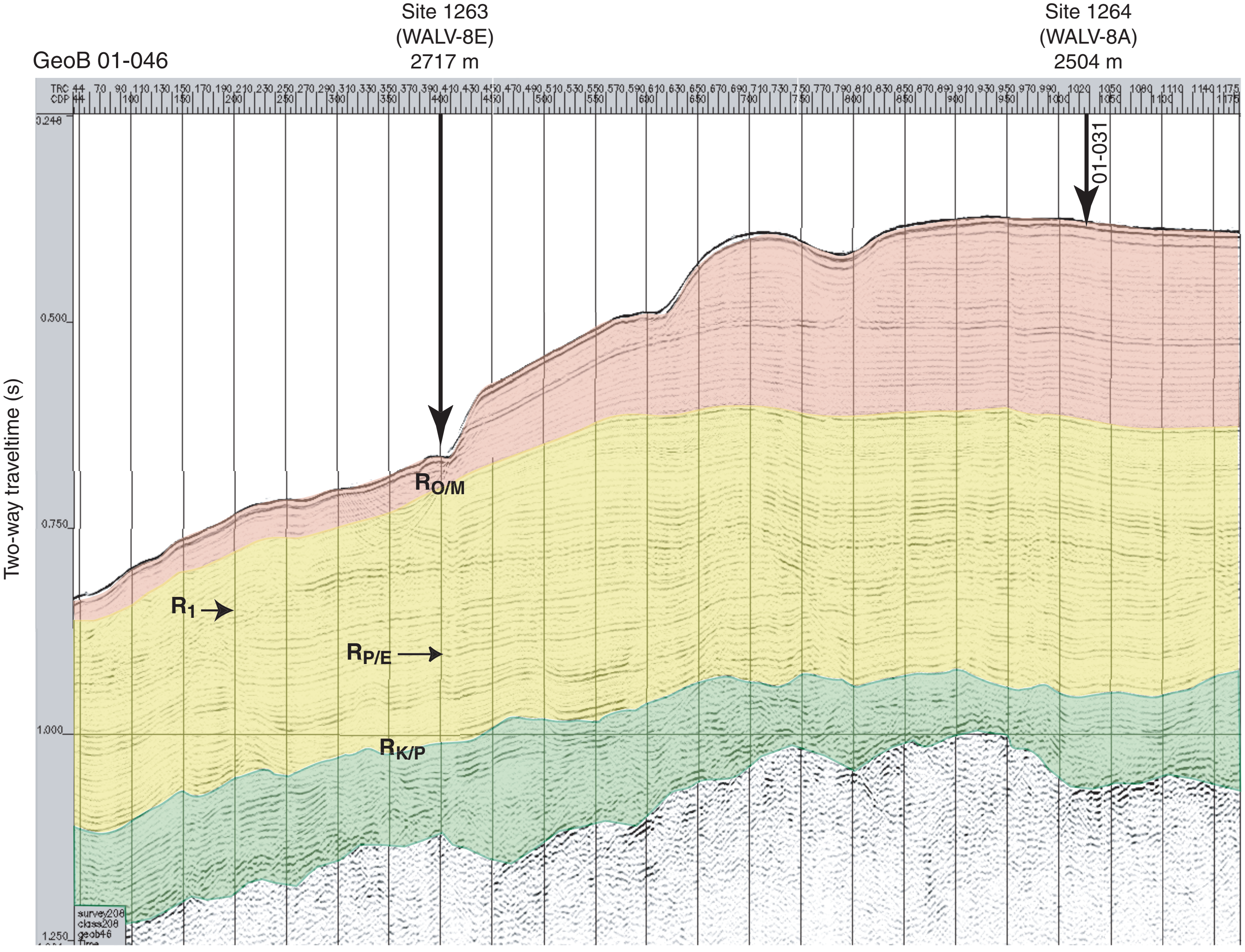
GeoB 01-046
Site 1263
(WALV-8E)
2717 m
Site 1264
(WALV-8A)
2504 m
TRC
CDP
01-031
Two-way traveltime (s)
0.248
0.500
0.750
1.000
1.250
R_O/M
R_1
R_P/E
R_K/P
survey208
class208
geob46

Figure F17

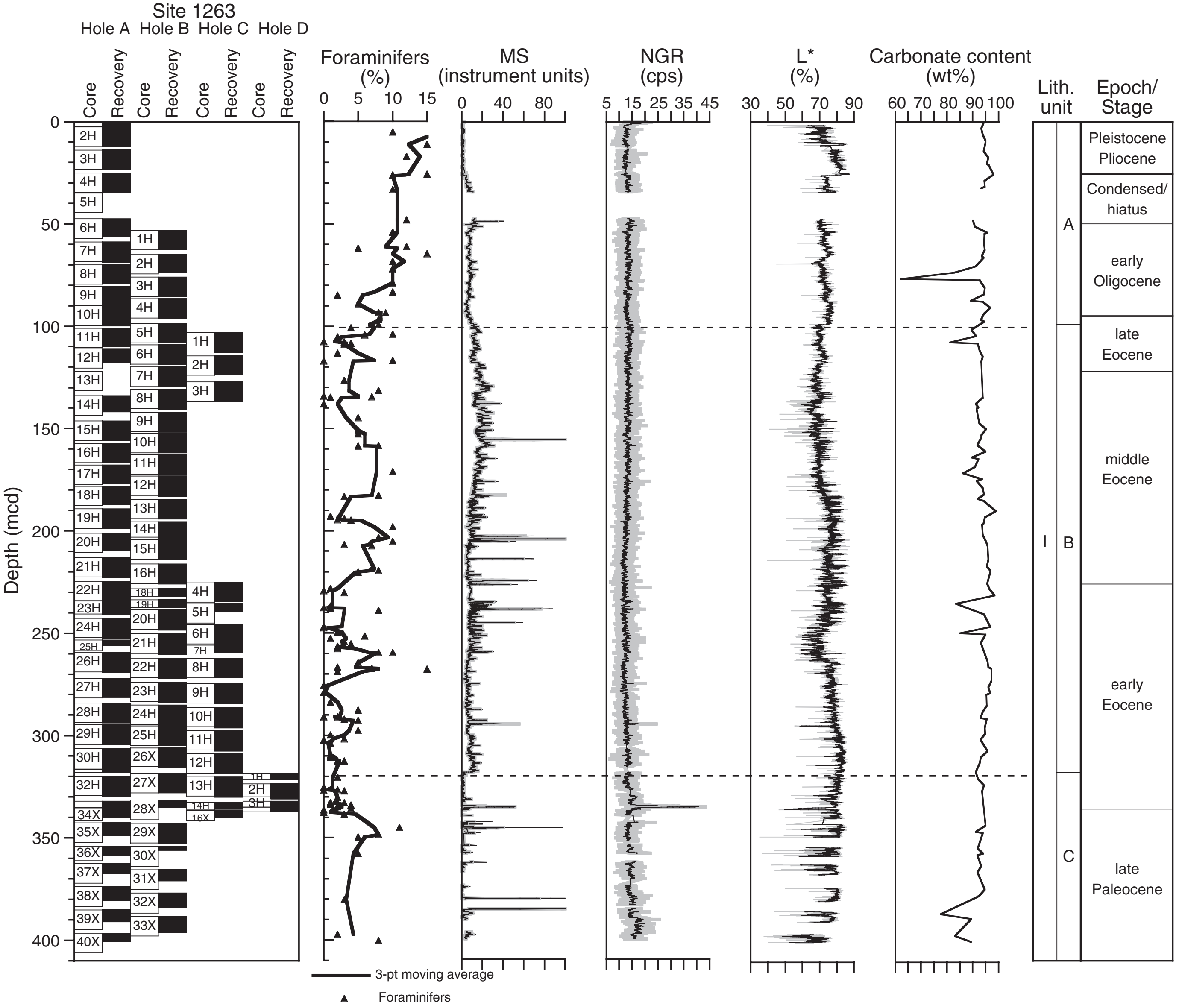
Site 1263
Hole A
Hole B
Hole C
Hole D
Core
Recovery
Depth (mcd)
Foraminifers (%)
MS (instrument units)
NGR (cps)
L* (%)
Carbonate content (wt%)
Lith. unit
Epoch/ Stage
Pleistocene Pliocene
Condensed/ hiatus
early Oligocene
late Eocene
middle Eocene
early Eocene
late Paleocene
I
A
B
C
3-pt moving average
Foraminifers

Figure F18

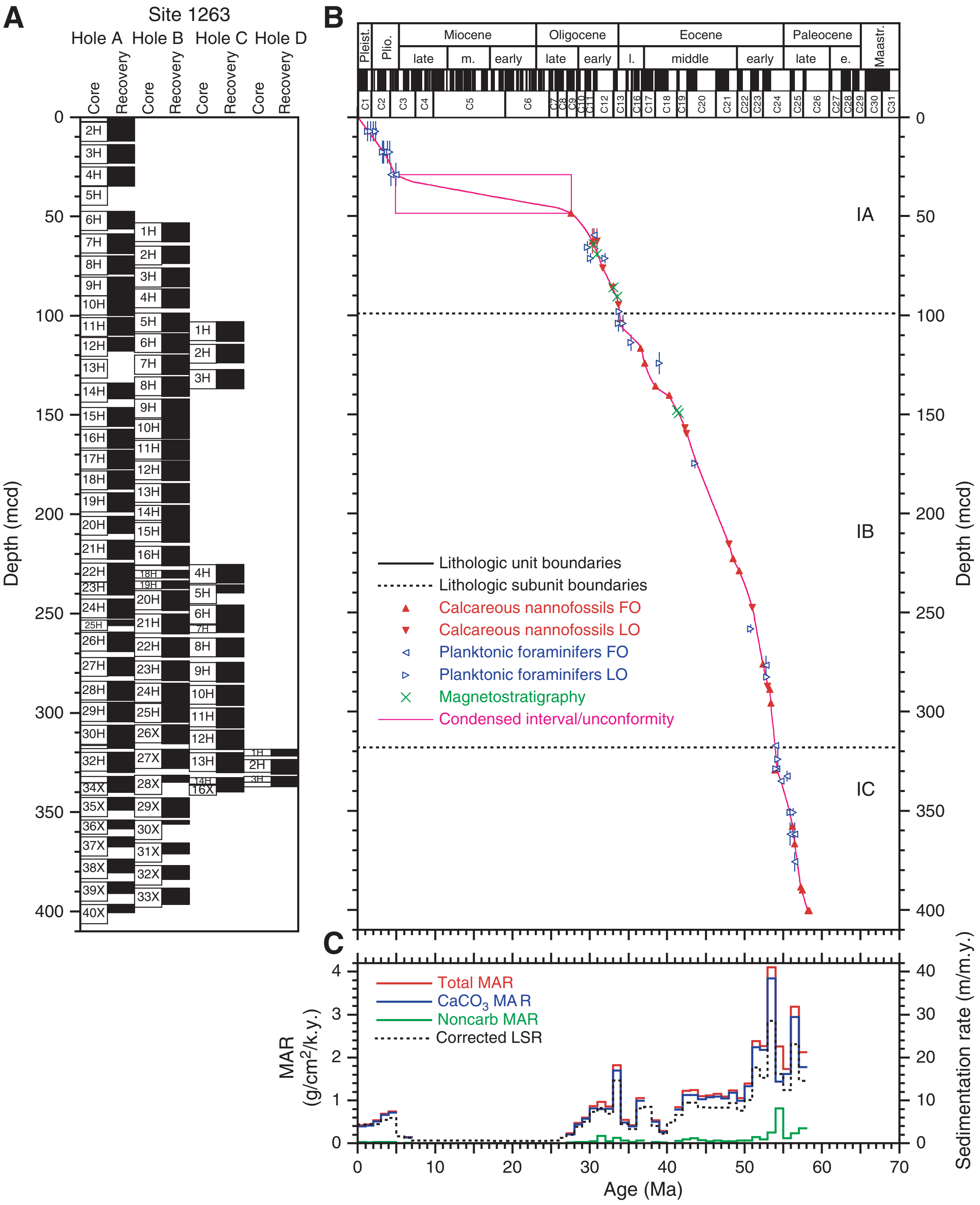
A
Site 1263
Hole A
Hole B
Hole C
Hole D
Core
Recovery
Depth (mcd)
B
Pleist.
Plio.
Miocene
late
m.
early
Oligocene
late
early
Eocene
l.
middle
early
Paleocene
late
e.
Maastr.
C1
C2
C3
C4
C5
C6
C12
C13
C16
C17
C18
C19
C20
C21
C22
C23
C24
C25
C26
C27
C28
C29
C30
C31
IA
IB
IC
Lithologic unit boundaries
Lithologic subunit boundaries
Calcareous nannofossils FO
Calcareous nannofossils LO
Planktonic foraminifers FO
Planktonic foraminifers LO
Magnetostratigraphy
Condensed interval/unconformity
C
Total MAR
$CaCO_3$ MAR
Noncarb MAR
Corrected LSR
MAR ($g/cm^2/k.y.$)
Sedimentation rate (m/m.y.)
Age (Ma)

Figure F19

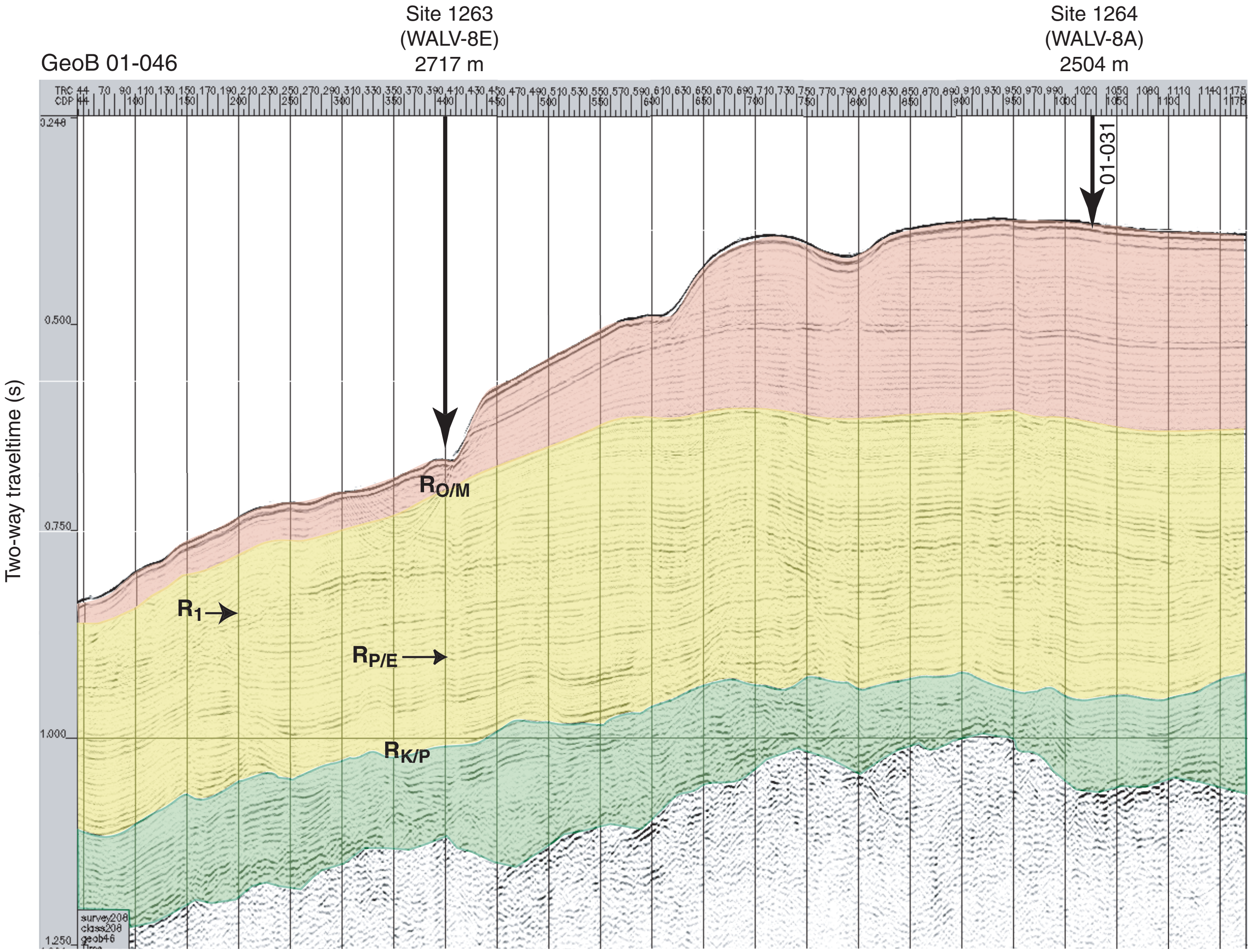
Site 1263
(WALV-8E)
2717 m
Site 1264
(WALV-8A)
2504 m
GeoB 01-046
01-031
Two-way traveltime (s)
0.248
0.500
0.750
1.000
1.250
$R_{O/M}$
R_1
$R_{P/E}$
$R_{K/P}$
survey208
class208
geob46

Figure F20

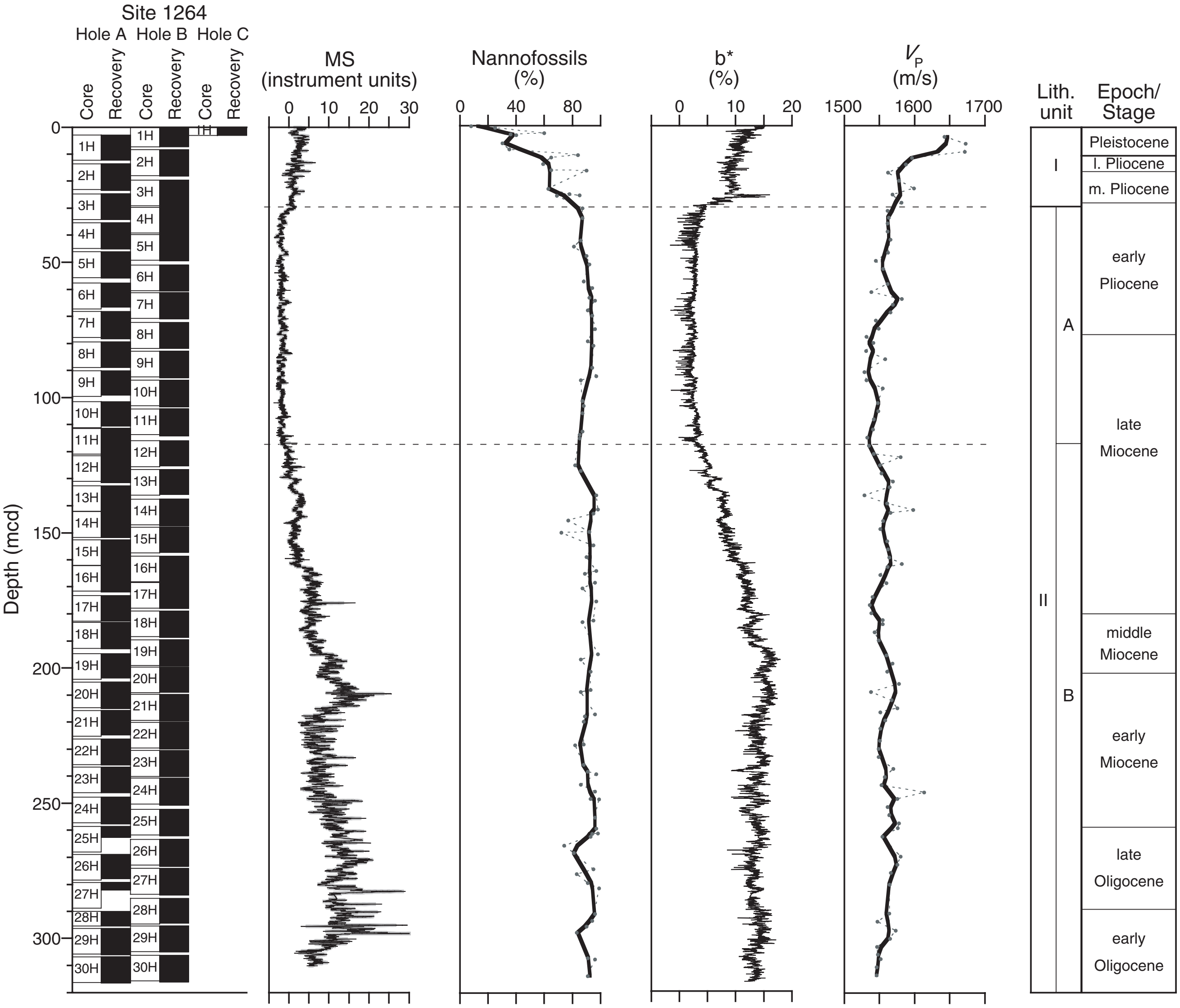
Site 1264
Hole A
Hole B
Hole C
Core
Recovery
MS (instrument units)
Nannofossils (%)
b* (%)
V_P (m/s)
Lith. unit
Epoch/ Stage
Depth (mcd)
0
50
100
150
200
250
300
10
20
30
40
80
1500
1600
1700
1H
2H
3H
4H
5H
6H
7H
8H
9H
10H
11H
12H
13H
14H
15H
16H
17H
18H
19H
20H
21H
22H
23H
24H
25H
26H
27H
28H
29H
30H
I
II
A
B
Pleistocene
l. Pliocene
m. Pliocene
early Pliocene
late Miocene
middle Miocene
early Miocene
late Oligocene
early Oligocene

Figure F21

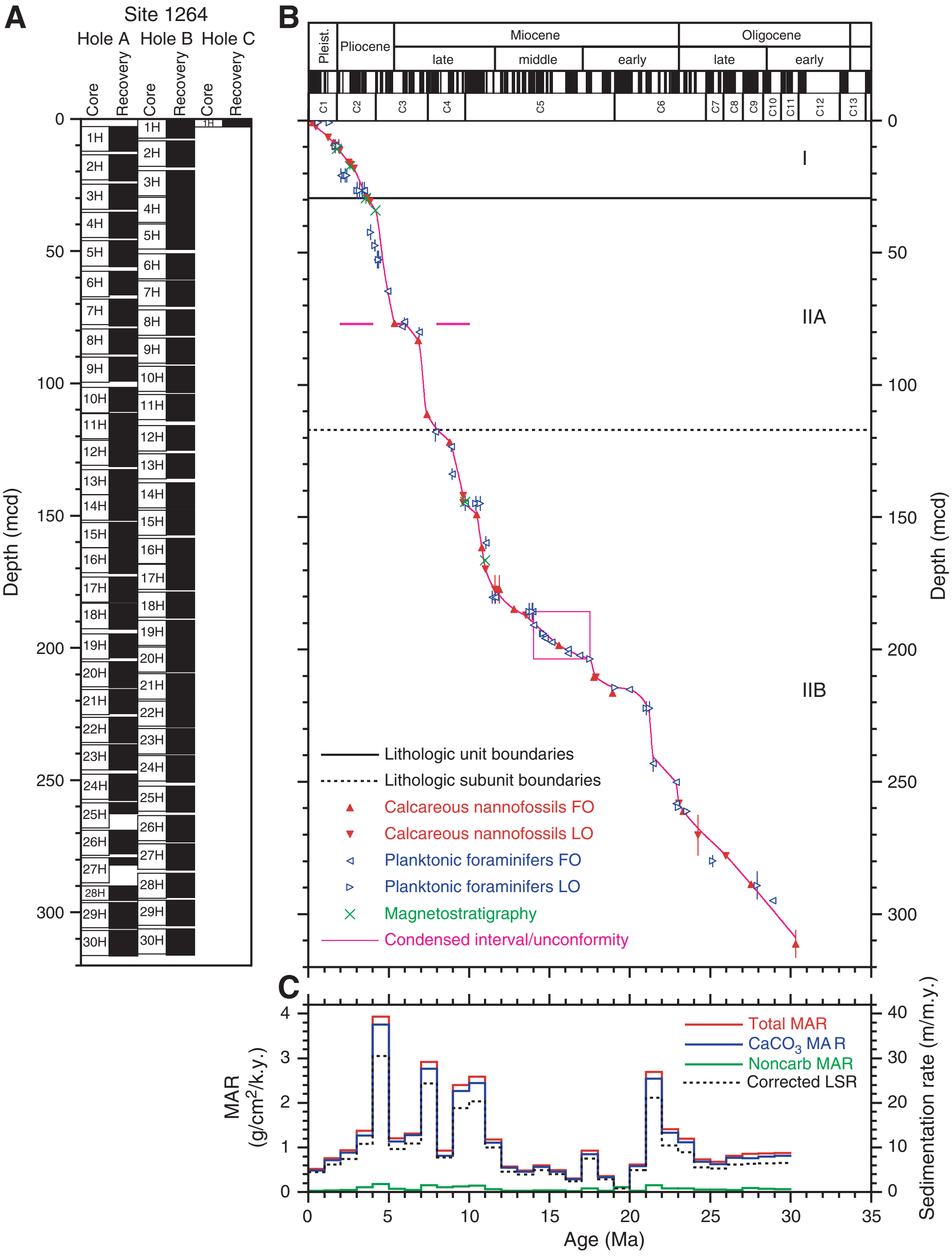
A
Site 1264
Hole A
Hole B
Hole C
Core
Recovery
Depth (mcd)
1H
2H
3H
4H
5H
6H
7H
8H
9H
10H
11H
12H
13H
14H
15H
16H
17H
18H
19H
20H
21H
22H
23H
24H
25H
26H
27H
28H
29H
30H
0
50
100
150
200
250
300
B
Pleist.
Pliocene
Miocene
Oligocene
late
middle
early
late
early
C1
C2
C3
C4
C5
C6
C7
C8
C9
C10
C11
C12
C13
I
IIA
IIB
Lithologic unit boundaries
Lithologic subunit boundaries
Calcareous nannofossils FO
Calcareous nannofossils LO
Planktonic foraminifers FO
Planktonic foraminifers LO
Magnetostratigraphy
Condensed interval/unconformity
C
MAR (g/cm²/k.y.)
Sedimentation rate (m/m.y.)
Total MAR
CaCO₃ MAR
Noncarb MAR
Corrected LSR
0
1
2
3
4
10
20
30
40
5
15
25
35
Age (Ma)

Figure F22

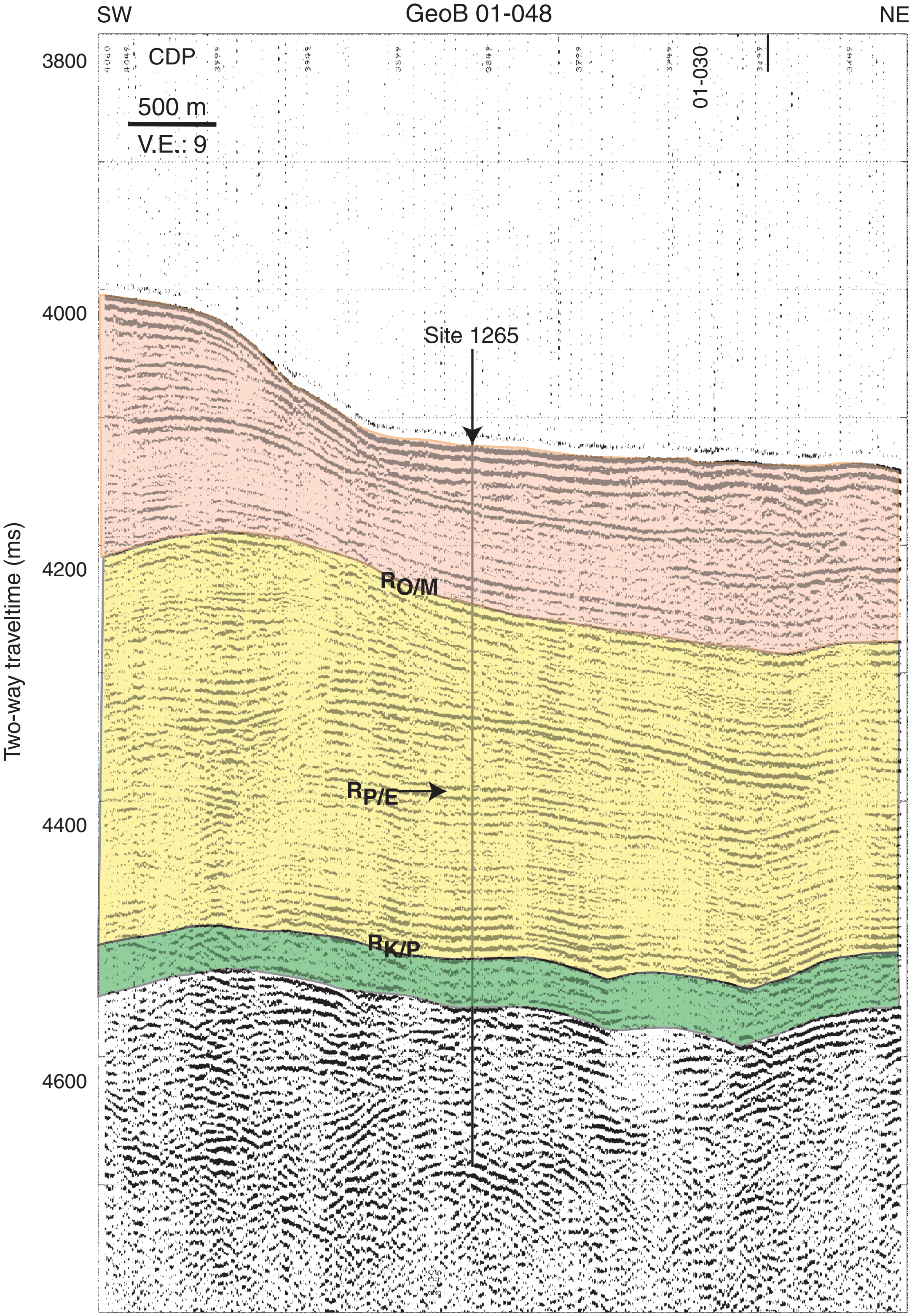
SW
GeoB 01-048
NE
CDP
500 m
V.E.: 9
01-030
Site 1265
$R_{O/M}$
$R_{P/E}$
$R_{K/P}$
Two-way traveltime (ms)
3800
4000
4200
4400
4600

Figure F23

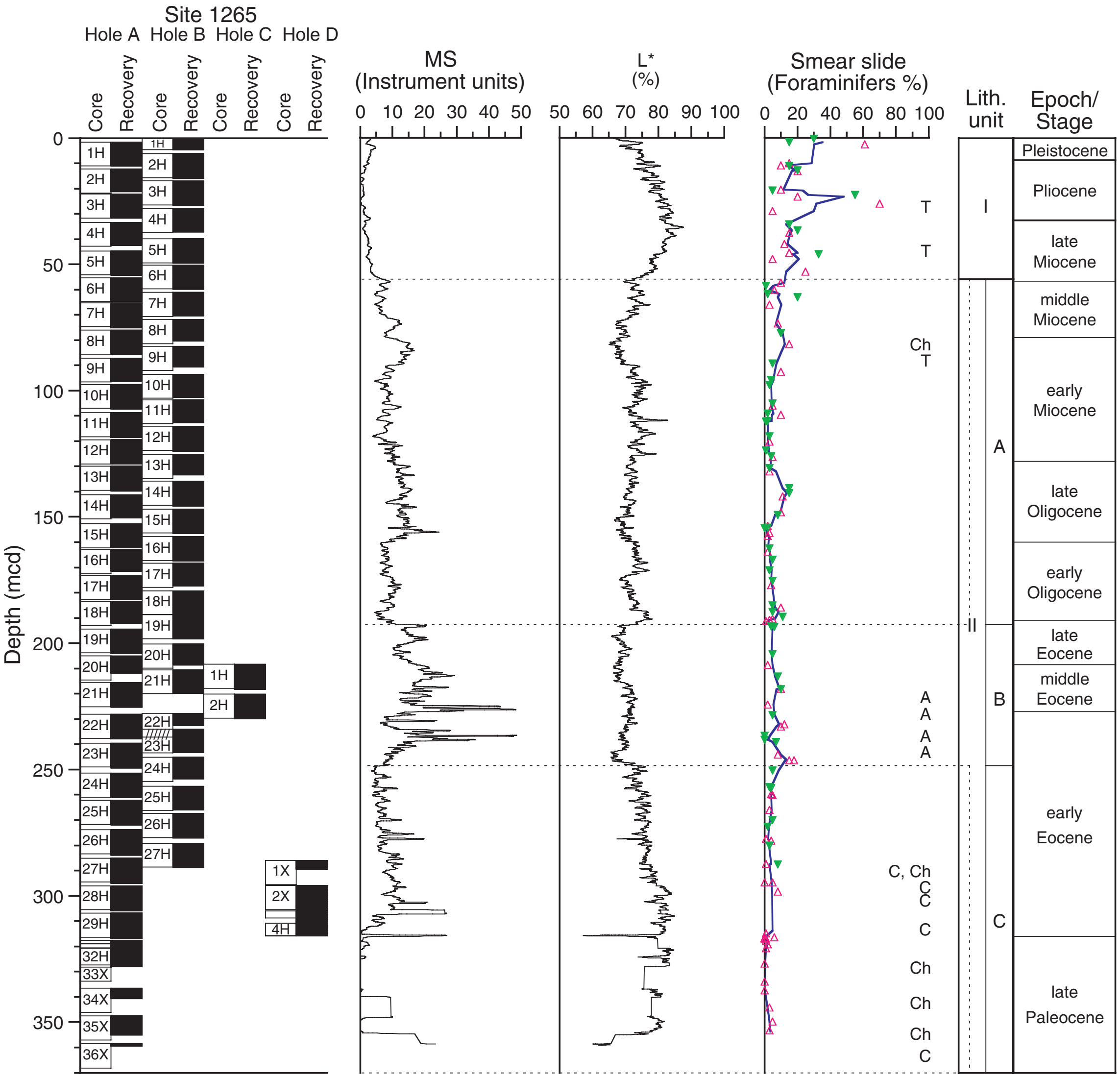
Site 1265
Hole A
Hole B
Hole C
Hole D
Core
Recovery
MS
(Instrument units)
L*
(%)
Smear slide
(Foraminifers %)
Lith. unit
Epoch/ Stage
Depth (mcd)
0
50
100
150
200
250
300
350
10
20
30
40
60
70
80
90
I
II
A
B
C
T
Ch
C, Ch
Pleistocene
Pliocene
late Miocene
middle Miocene
early Miocene
late Oligocene
early Oligocene
late Eocene
middle Eocene
early Eocene
late Paleocene

Figure F24

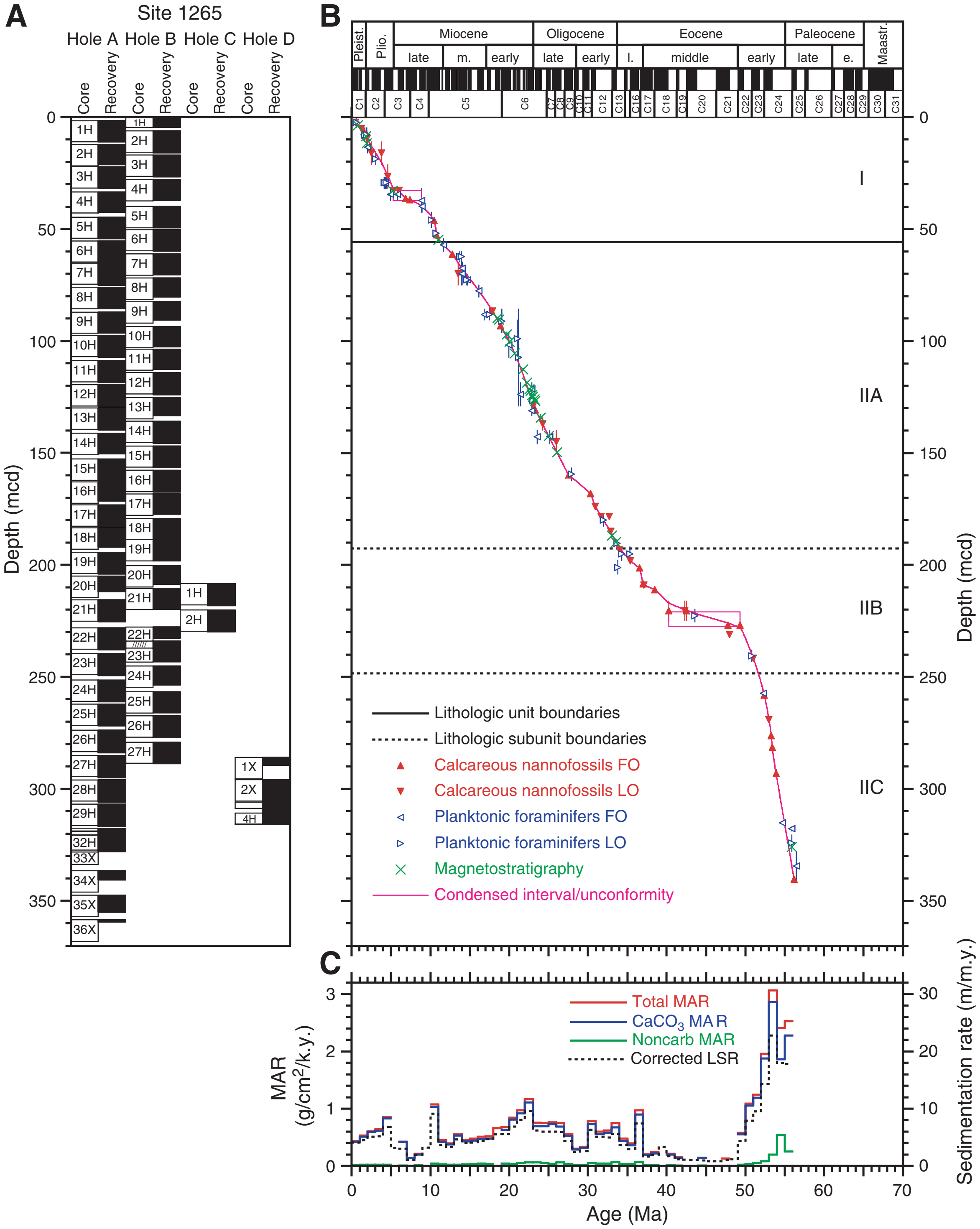
A
Site 1265
Hole A Hole B Hole C Hole D
Core Recovery Core Recovery Core Recovery Core Recovery
Depth (mcd)
B
Pleist. Plio. Miocene Oligocene Eocene Paleocene Maastr.
late m. early late early l. middle early late e.
C1 C2 C3 C4 C5 C6 C7 C8 C9 C10 C11 C12 C13 C16 C17 C18 C19 C20 C21 C22 C23 C24 C25 C26 C27 C28 C29 C30 C31
I
IIA
IIB
IIC
Lithologic unit boundaries
Lithologic subunit boundaries
Calcareous nannofossils FO
Calcareous nannofossils LO
Planktonic foraminifers FO
Planktonic foraminifers LO
Magnetostratigraphy
Condensed interval/unconformity
C
Total MAR
$CaCO_3$ MAR
Noncarb MAR
Corrected LSR
MAR (g/cm²/k.y.)
Sedimentation rate (m/m.y.)
Age (Ma)

Figure F25

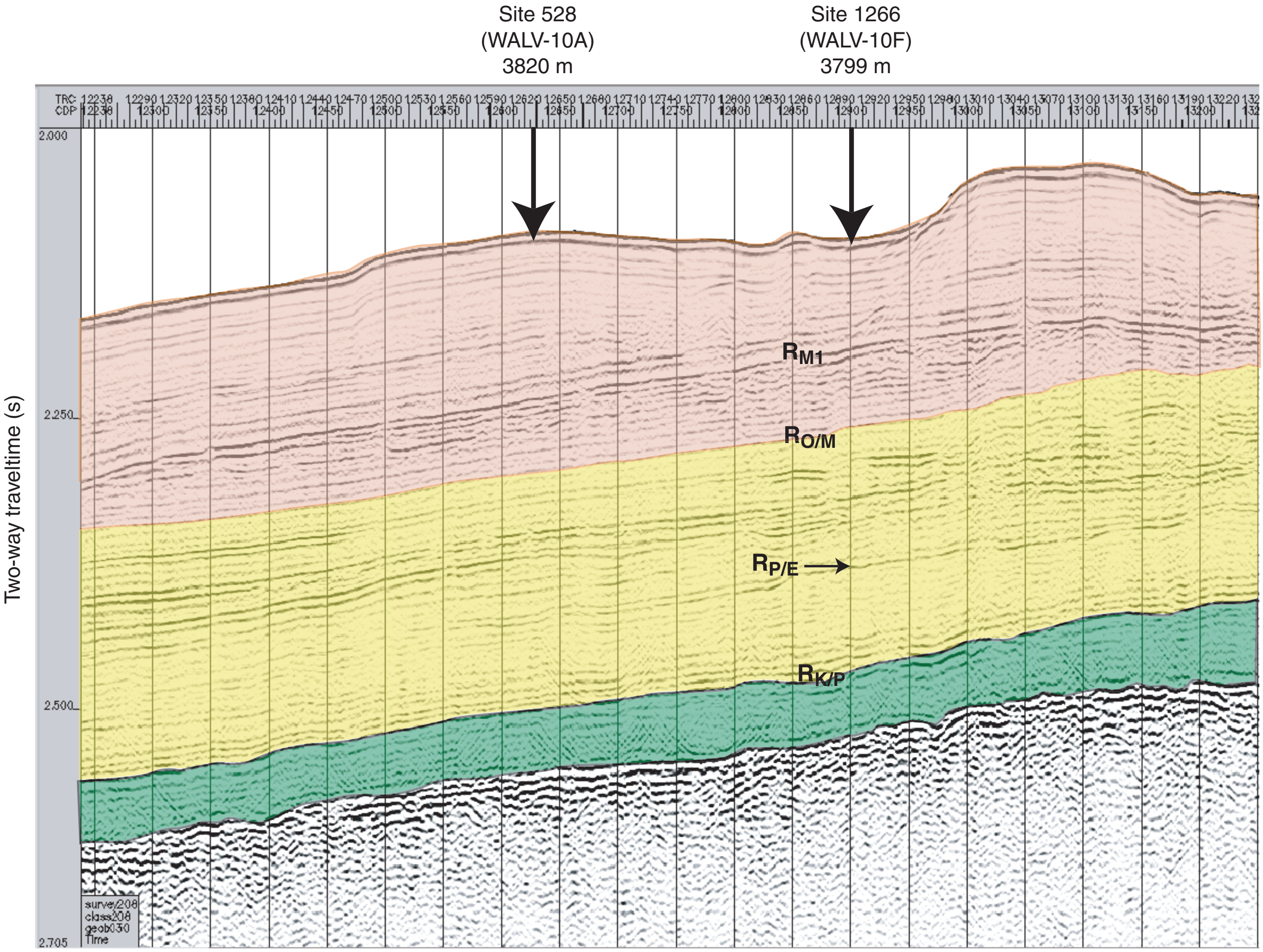
Site 528
(WALV-10A)
3820 m
Site 1266
(WALV-10F)
3799 m
TRC
CDP
2.000
2.250
2.500
2.705
Two-way traveltime (s)
R_{M1}
$R_{O/M}$
$R_{P/E}$
$R_{K/P}$
survey208
class208
geob030
Time

Figure F26

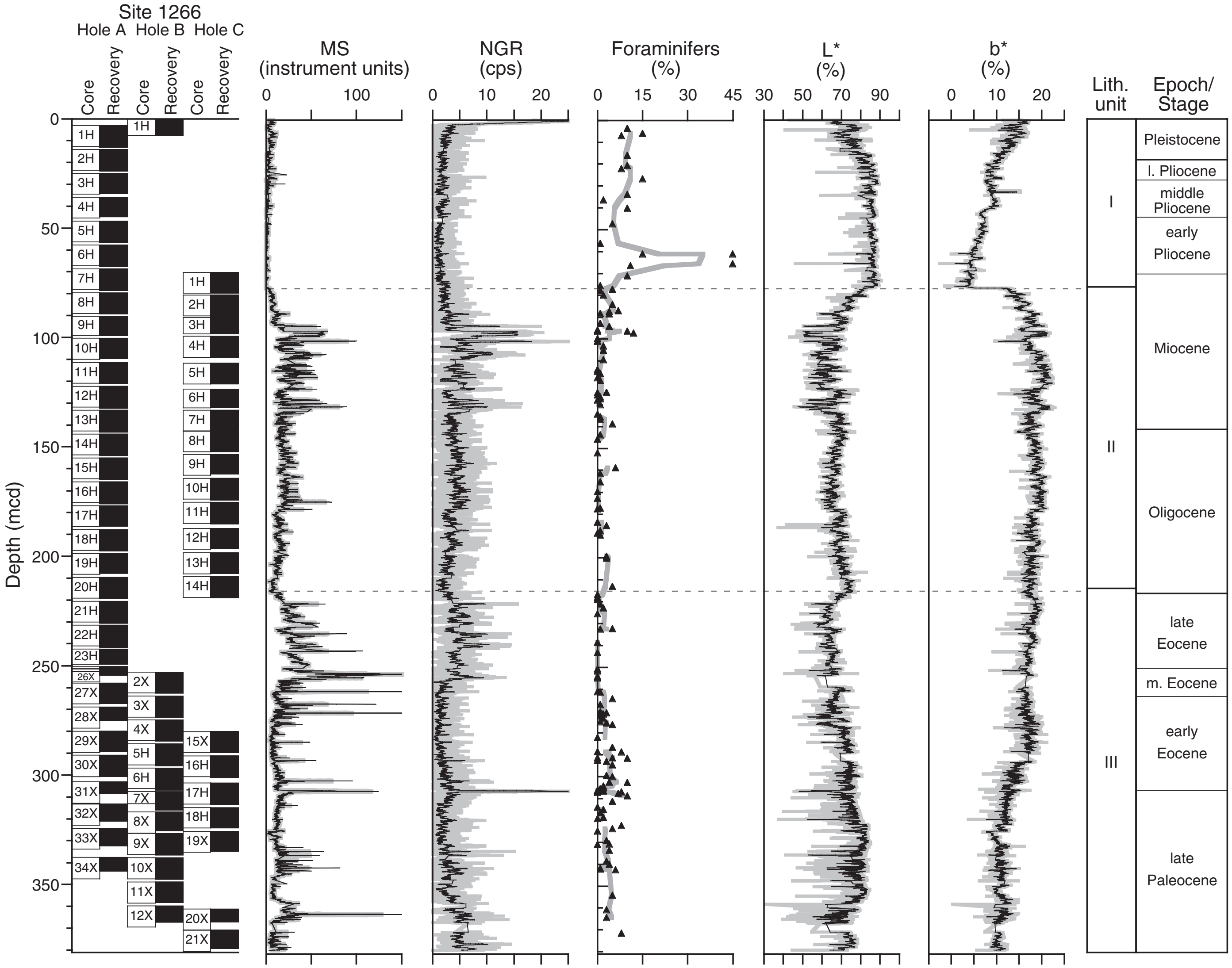
Site 1266
Hole A
Hole B
Hole C
Core
Recovery
Depth (mcd)
0
50
100
150
200
250
300
350
MS (instrument units)
NGR (cps)
Foraminifers (%)
L* (%)
b* (%)
Lith. unit
I
II
III
Epoch/ Stage
Pleistocene
l. Pliocene
middle Pliocene
early Pliocene
Miocene
Oligocene
late Eocene
m. Eocene
early Eocene
late Paleocene

Figure F27

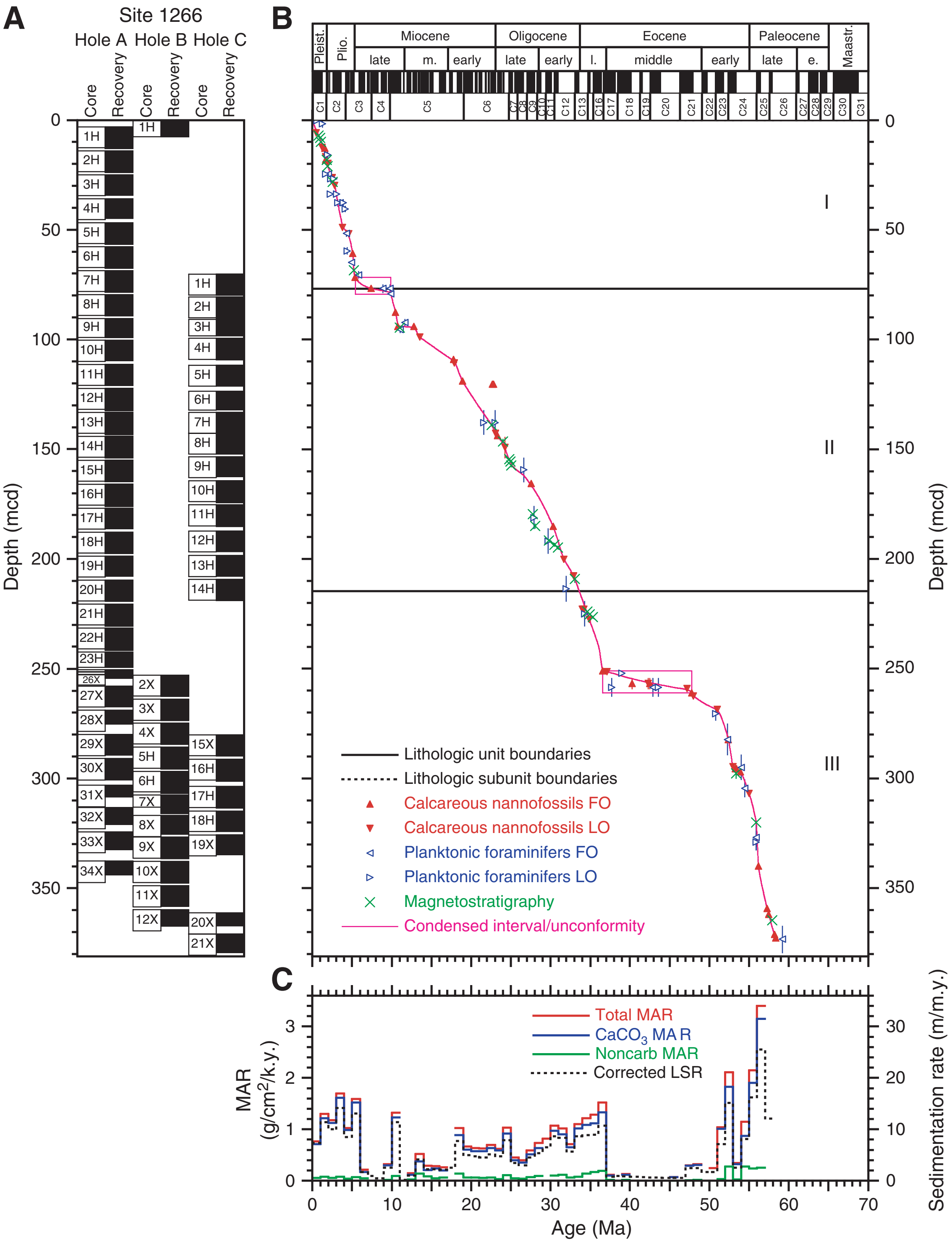
A
Site 1266
Hole A
Hole B
Hole C
Core
Recovery
Depth (mcd)
B
Pleist.
Plio.
Miocene
late
m.
early
Oligocene
late
early
Eocene
l.
middle
early
Paleocene
late
e.
Maastr.
I
II
III
Lithologic unit boundaries
Lithologic subunit boundaries
Calcareous nannofossils FO
Calcareous nannofossils LO
Planktonic foraminifers FO
Planktonic foraminifers LO
Magnetostratigraphy
Condensed interval/unconformity
C
Total MAR
$CaCO_3$ MAR
Noncarb MAR
Corrected LSR
MAR (g/cm^2/k.y.)
Sedimentation rate (m/m.y.)
Age (Ma)

Figure F28

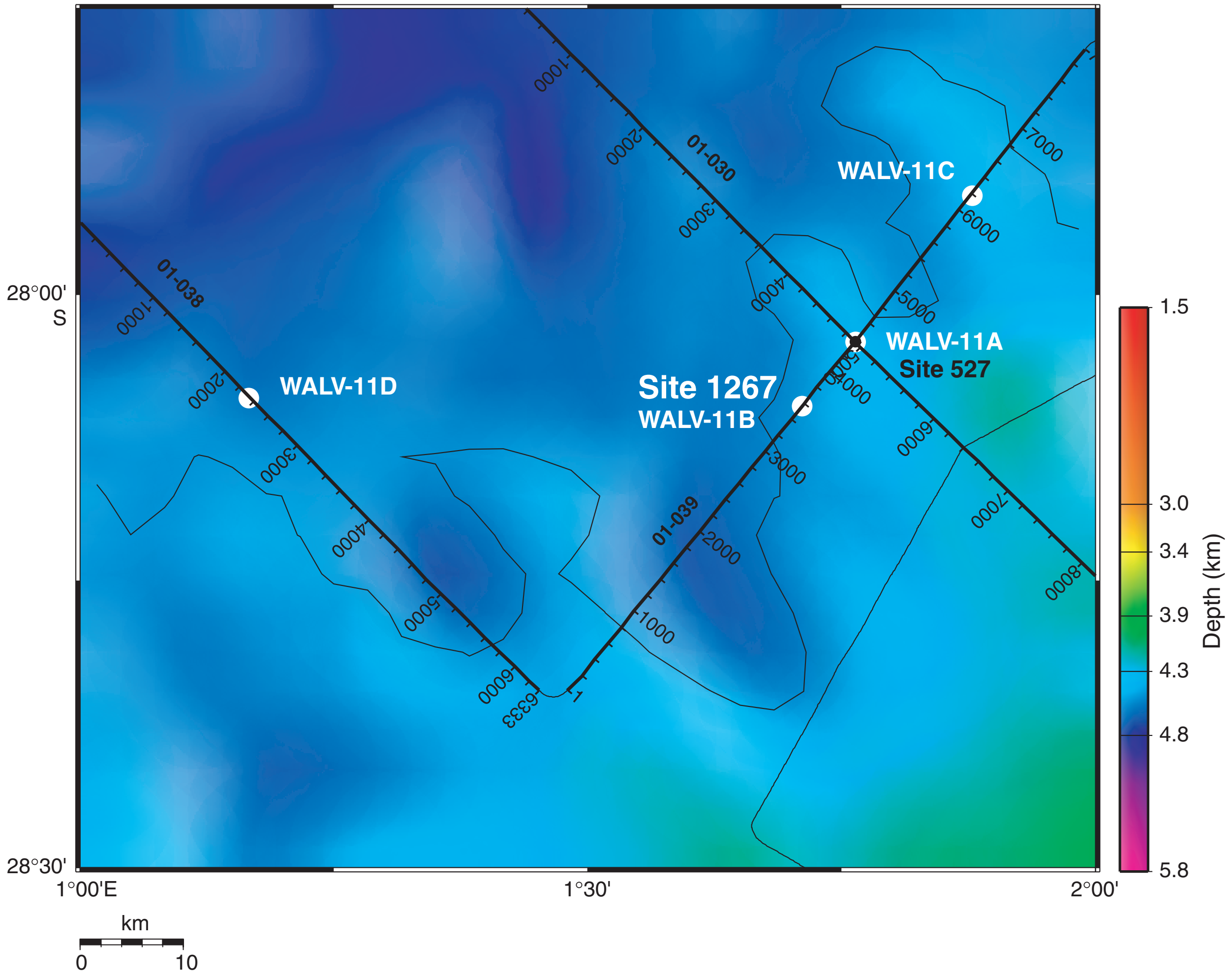
WALV-11C
WALV-11A
Site 527
Site 1267
WALV-11B
WALV-11D
01-030
01-038
01-039
28°00' S
28°30'
1°00'E
1°30'
2°00'
km
0
10
1.5
3.0
3.4
3.9
4.3
4.8
5.8
Depth (km)

Figure F29

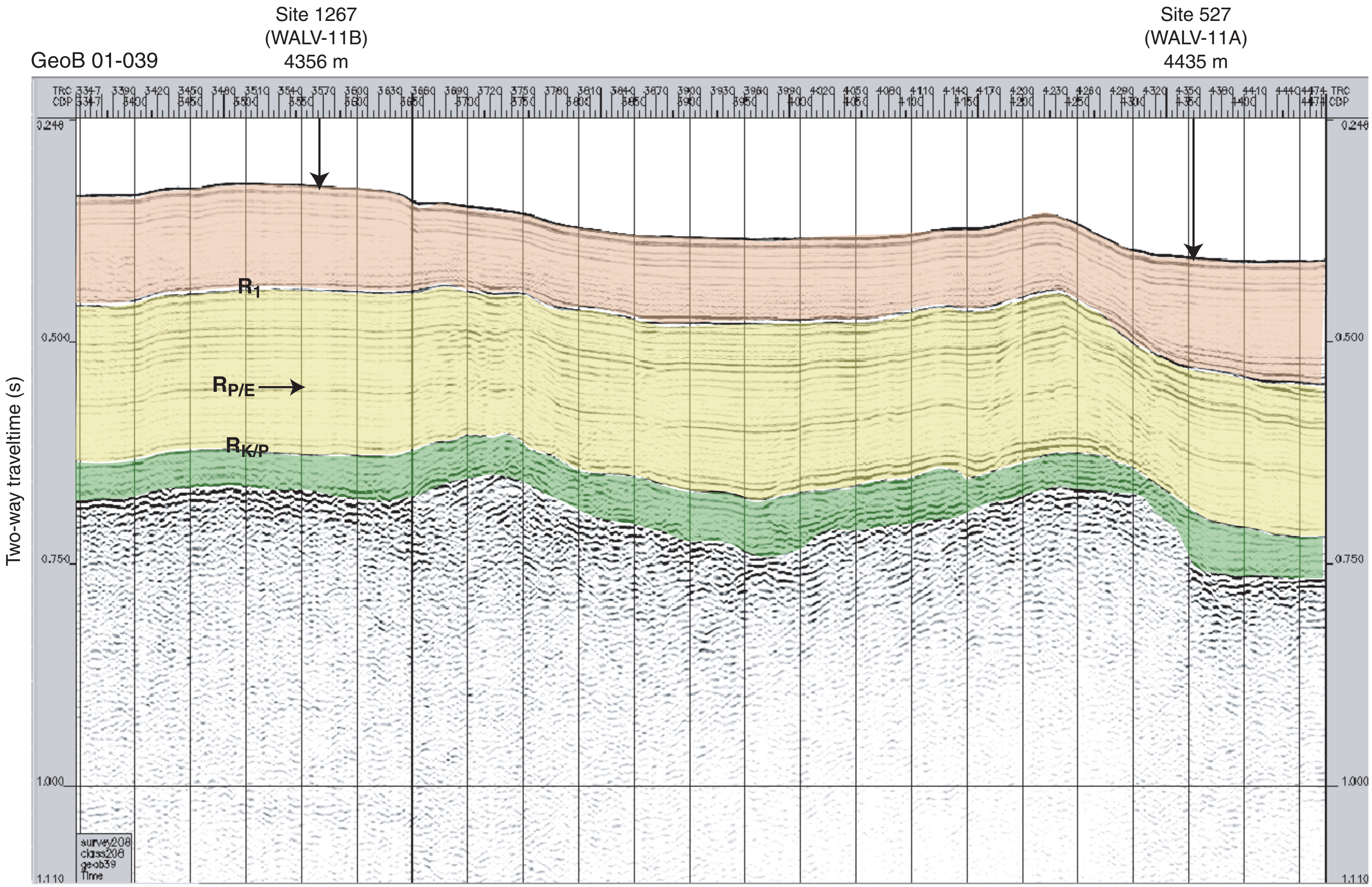
GeoB 01-039
Site 1267
(WALV-11B)
4356 m
Site 527
(WALV-11A)
4435 m
TRC
CDP
R1
RP/E
RK/P
Two-way traveltime (s)
0.248
0.500
0.750
1.000
1.110
survey208
class208
geob39
Time

Figure F30

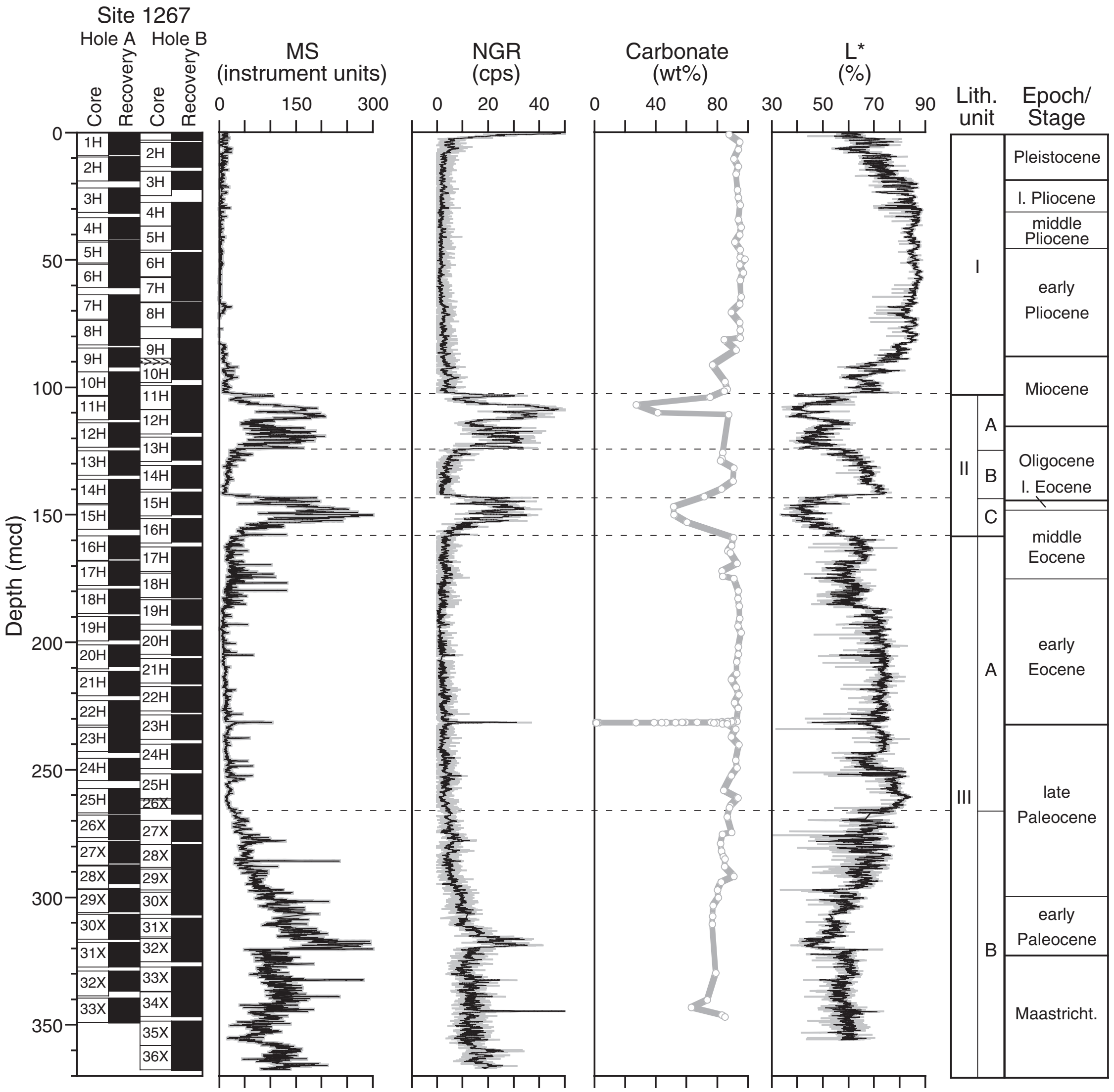
Site 1267
Hole A
Hole B
Core
Recovery
Core
Recovery
Depth (mcd)
0
50
100
150
200
250
300
350
MS
(instrument units)
0
150
300
NGR
(cps)
0
20
40
Carbonate
(wt%)
0
40
80
L*
(%)
30
50
70
90
Lith. unit
I
II
III
A
B
C
A
B
Epoch/ Stage
Pleistocene
l. Pliocene
middle Pliocene
early Pliocene
Miocene
Oligocene
l. Eocene
middle Eocene
early Eocene
late Paleocene
early Paleocene
Maastricht.
1H
2H
3H
4H
5H
6H
7H
8H
9H
10H
11H
12H
13H
14H
15H
16H
17H
18H
19H
20H
21H
22H
23H
24H
25H
26X
27X
28X
29X
30X
31X
32X
33X
34X
35X
36X

Figure F31

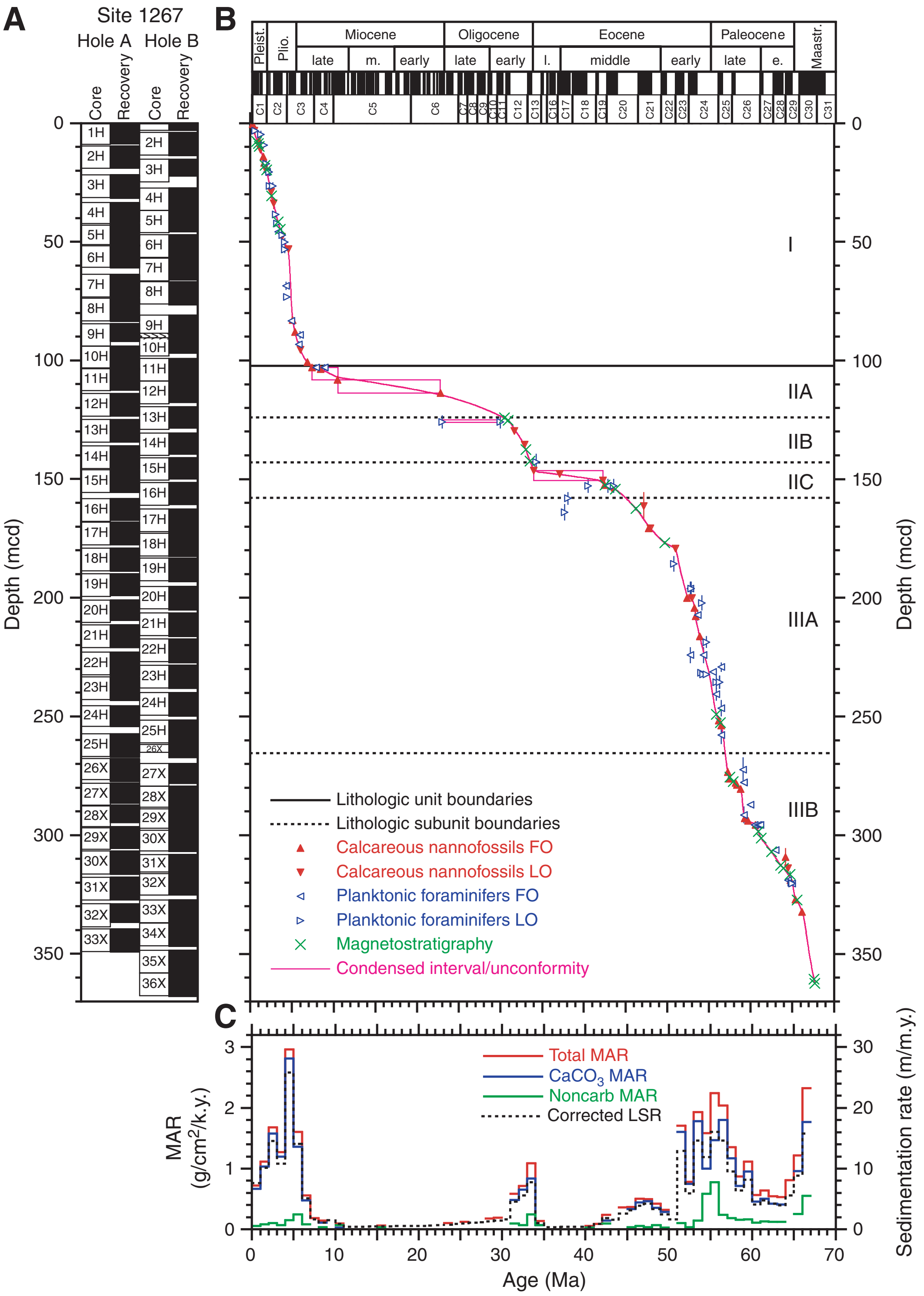
A
Site 1267
Hole A
Hole B
Core
Recovery
Depth (mcd)
B
Pleist.
Plio.
Miocene
Oligocene
Eocene
Paleocene
Maastr.
late
m.
early
late
early
l.
middle
early
late
e.
C1
C2
C3
C4
C5
C6
C12
C13
C16
C17
C18
C19
C20
C21
C22
C23
C24
C25
C26
C27
C28
C29
C30
C31
I
IIA
IIB
IIC
IIIA
IIIB
Lithologic unit boundaries
Lithologic subunit boundaries
▲ Calcareous nannofossils FO
▼ Calcareous nannofossils LO
◁ Planktonic foraminifers FO
▷ Planktonic foraminifers LO
× Magnetostratigraphy
Condensed interval/unconformity
C
Total MAR
CaCO$_3$ MAR
Noncarb MAR
Corrected LSR
MAR (g/cm^2/k.y.)
Sedimentation rate (m/m.y.)
Age (Ma)
0
10
20
30
40
50
60
70
0
50
100
150
200
250
300
350

Figure F32

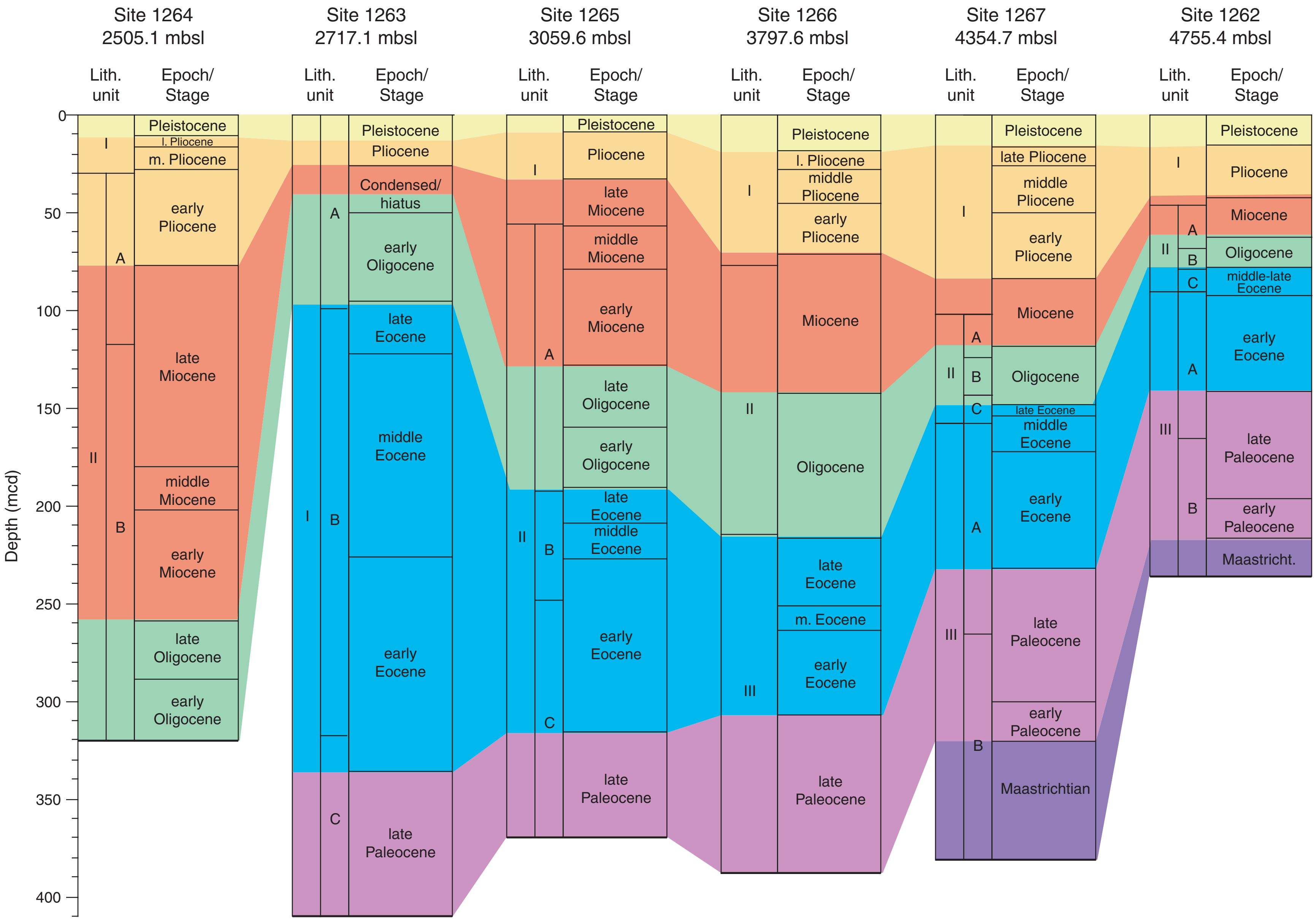
Site 1264
2505.1 mbsl
Site 1263
2717.1 mbsl
Site 1265
3059.6 mbsl
Site 1266
3797.6 mbsl
Site 1267
4354.7 mbsl
Site 1262
4755.4 mbsl
Lith. unit
Epoch/ Stage
Depth (mcd)
0
50
100
150
200
250
300
350
400
I
II
III
A
B
C
Pleistocene
l. Pliocene
m. Pliocene
early Pliocene
late Miocene
middle Miocene
early Miocene
late Oligocene
early Oligocene
Pliocene
Condensed/ hiatus
early Oligocene
late Eocene
middle Eocene
early Eocene
late Paleocene
late Miocene
middle Miocene
early Miocene
late Oligocene
early Oligocene
late Eocene
middle Eocene
early Eocene
late Paleocene
l. Pliocene
middle Pliocene
early Pliocene
Miocene
Oligocene
late Eocene
m. Eocene
early Eocene
late Paleocene
late Pliocene
middle Pliocene
early Pliocene
Miocene
Oligocene
late Eocene
middle Eocene
early Eocene
late Paleocene
early Paleocene
Maastrichtian
Pliocene
Miocene
Oligocene
middle-late Eocene
early Eocene
late Paleocene
early Paleocene
Maastricht.

Figure F33

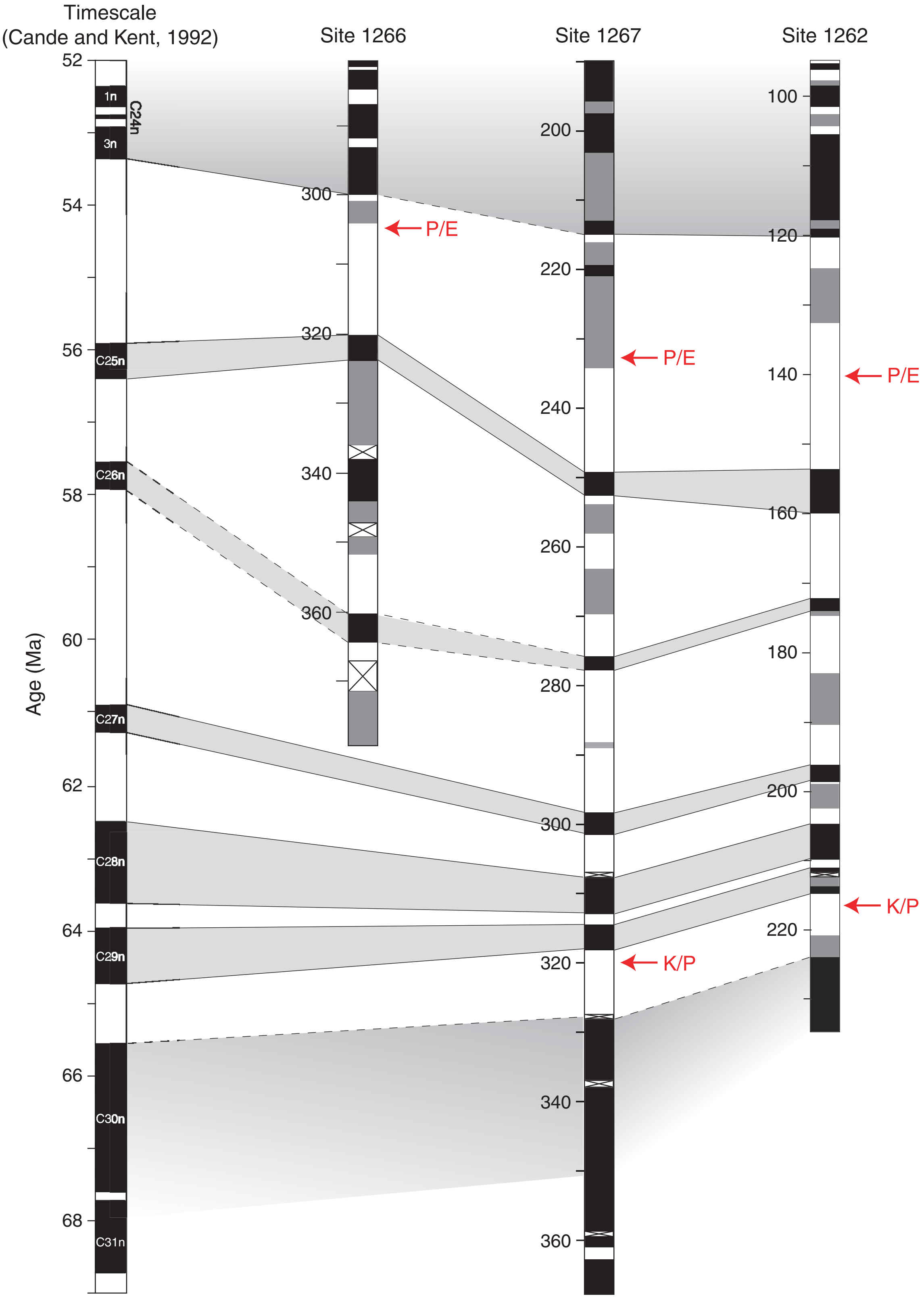
Timescale
(Cande and Kent, 1992)
Site 1266
Site 1267
Site 1262
Age (Ma)
52
54
56
58
60
62
64
66
68
1n
3n
C24n
C25n
C26n
C27n
C28n
C29n
C30n
C31n
300
320
340
360
200
220
240
260
280
300
320
340
360
100
120
140
160
180
200
220
P/E
P/E
P/E
K/P
K/P

Figure F34

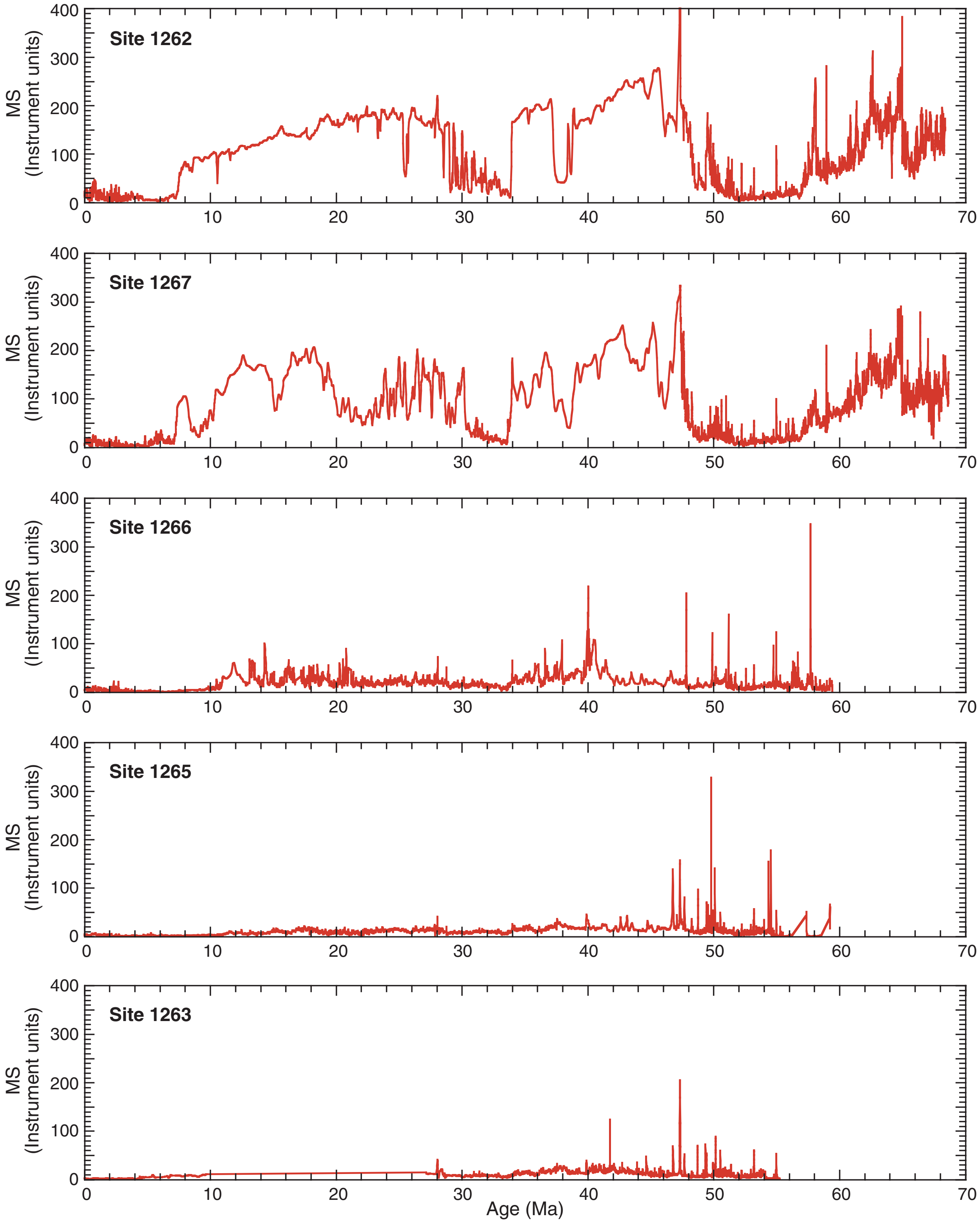
Site 1262
Site 1267
Site 1266
Site 1265
Site 1263
MS
(Instrument units)
0
100
200
300
400
0
10
20
30
40
50
60
70
Age (Ma)

Figure F35

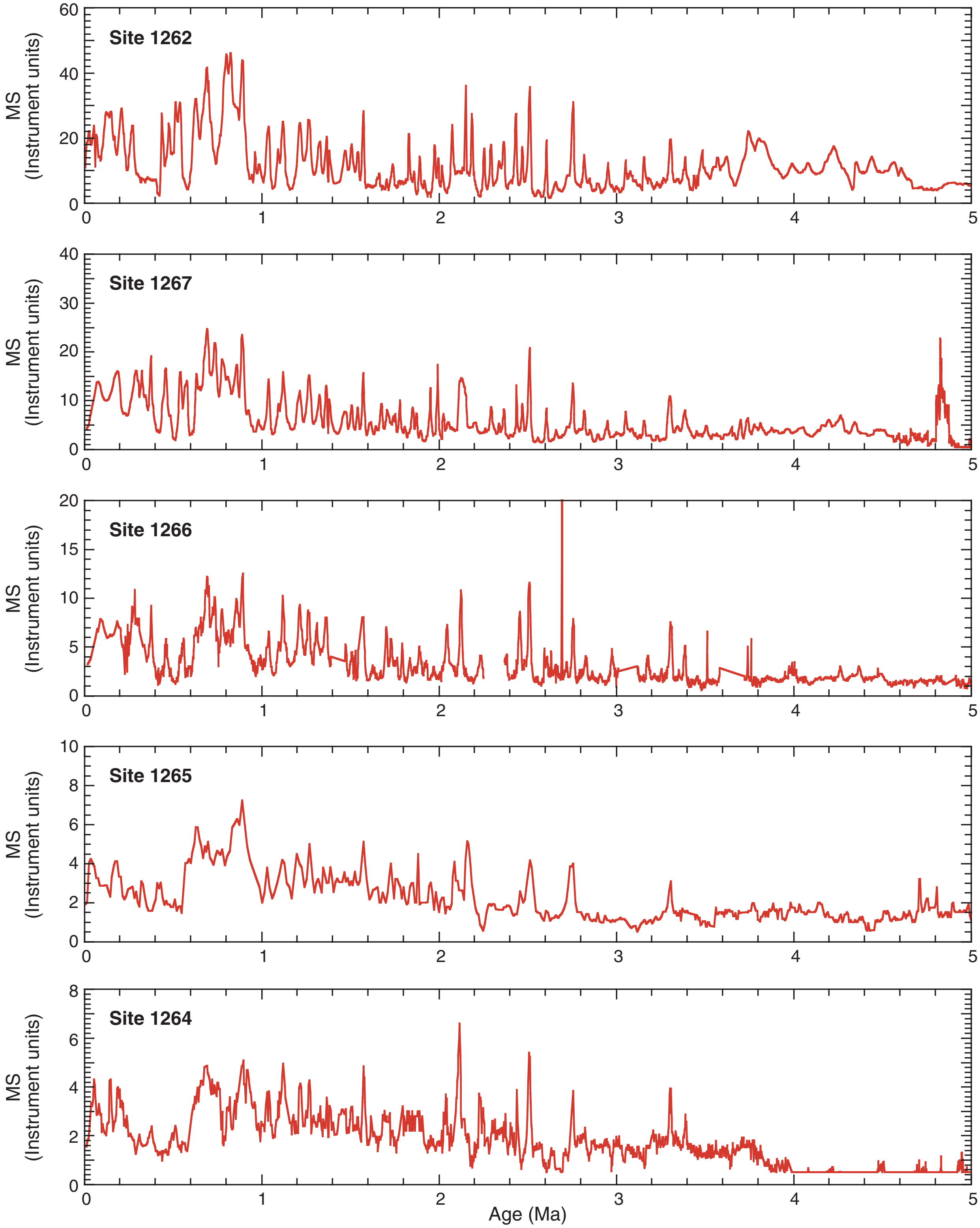
Site 1262
Site 1267
Site 1266
Site 1265
Site 1264
MS (Instrument units)
60
40
20
0
30
10
15
5
8
6
4
2
1
3
Age (Ma)

Figure F36

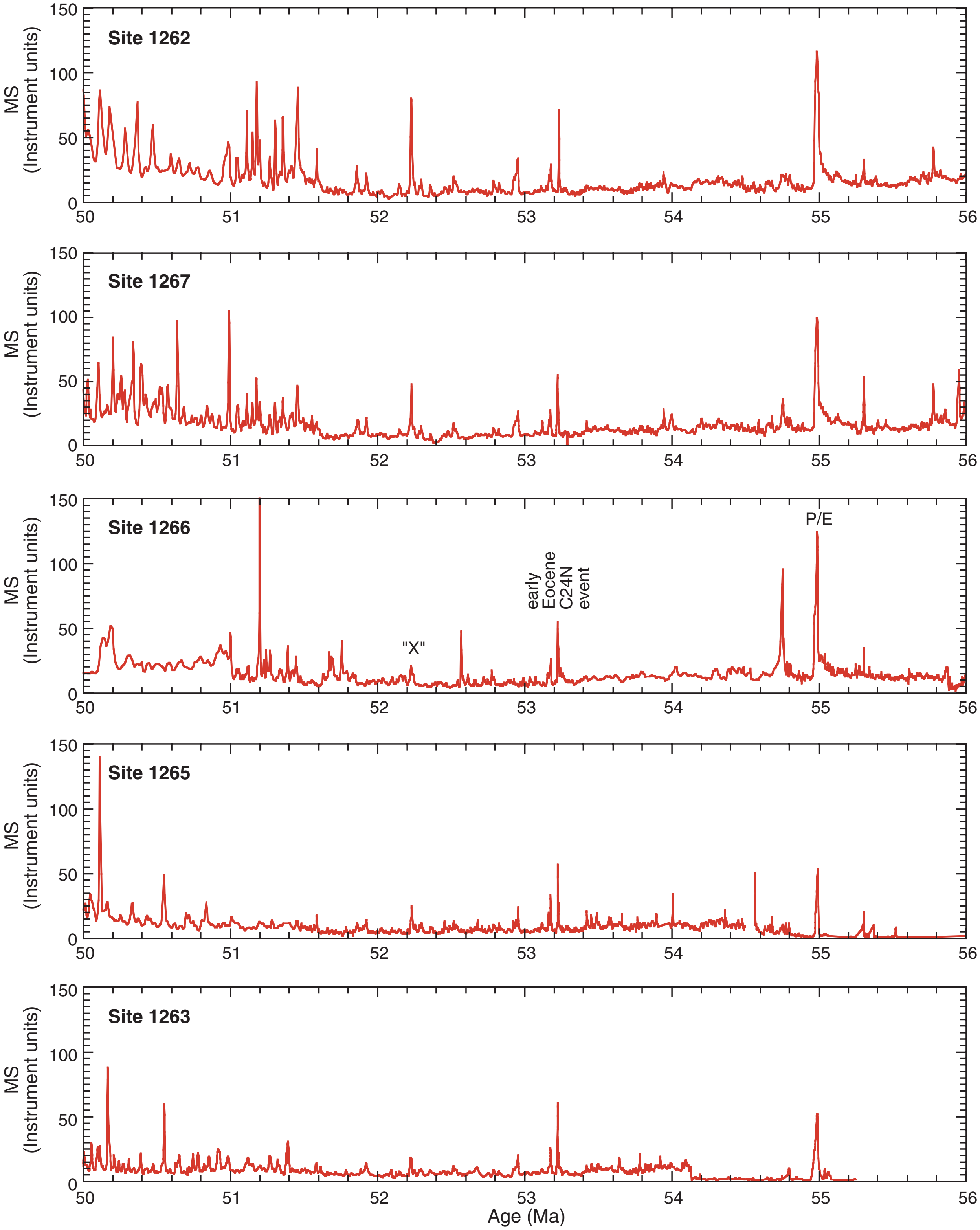
Site 1262
Site 1267
Site 1266
Site 1265
Site 1263
MS (Instrument units)
150
100
50
0
50
51
52
53
54
55
56
"X"
early Eocene C24N event
P/E
Age (Ma)

Figure F37

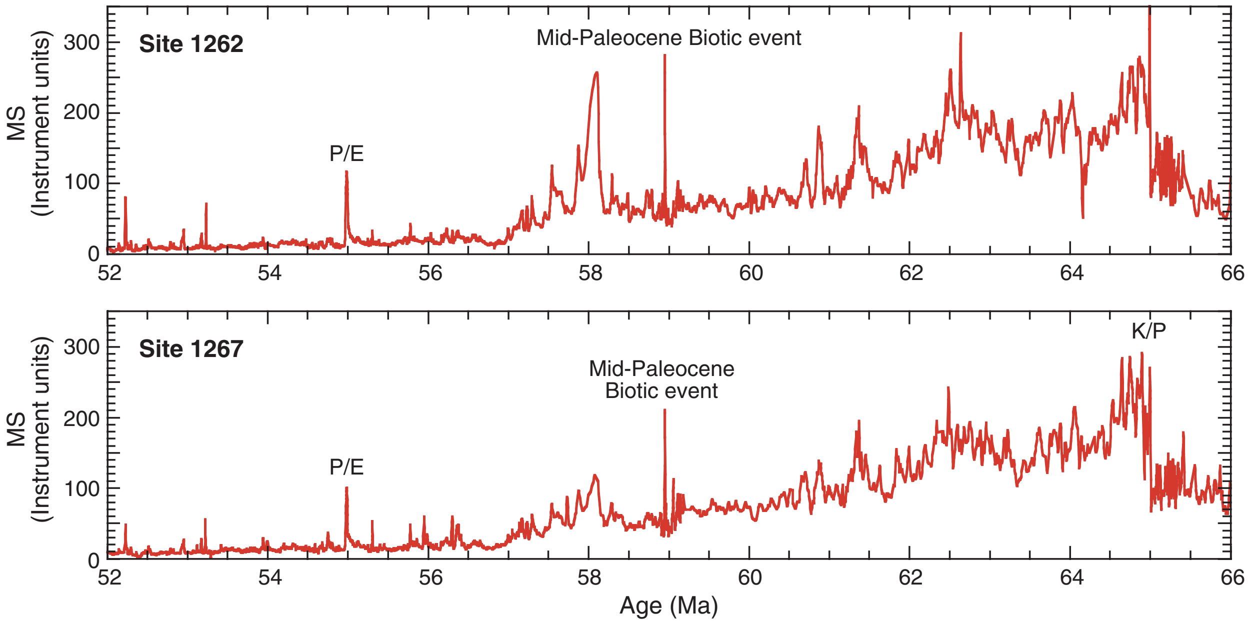
Site 1262
Mid-Paleocene Biotic event
P/E
MS (Instrument units)
0
100
200
300
52
54
56
58
60
62
64
66
Site 1267
Mid-Paleocene Biotic event
P/E
K/P
Age (Ma)

Figure F38

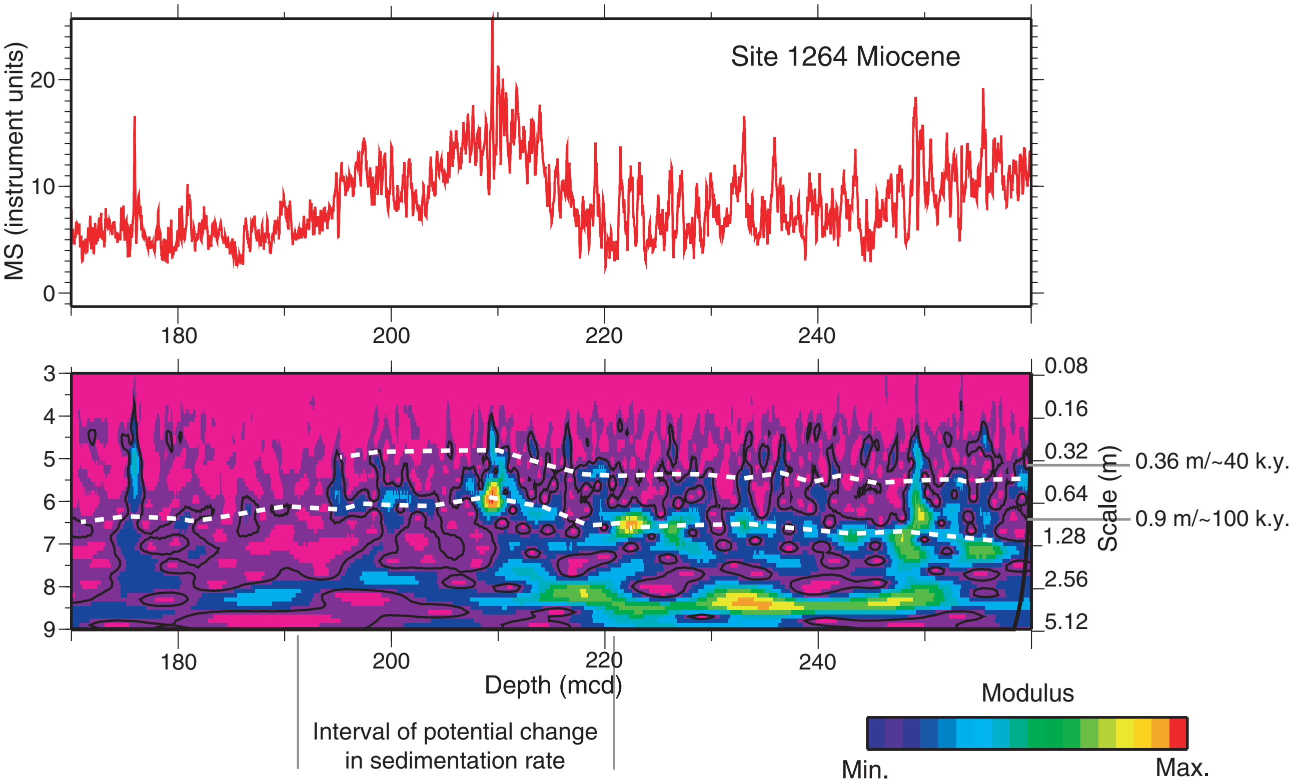
Site 1264 Miocene
MS (instrument units)
0
10
20
180
200
220
240
3
4
5
6
7
8
9
0.08
0.16
0.32
0.64
1.28
2.56
5.12
Scale (m)
0.36 m/~40 k.y.
0.9 m/~100 k.y.
Depth (mcd)
Interval of potential change in sedimentation rate
Modulus
Min.
Max.

Figure F39

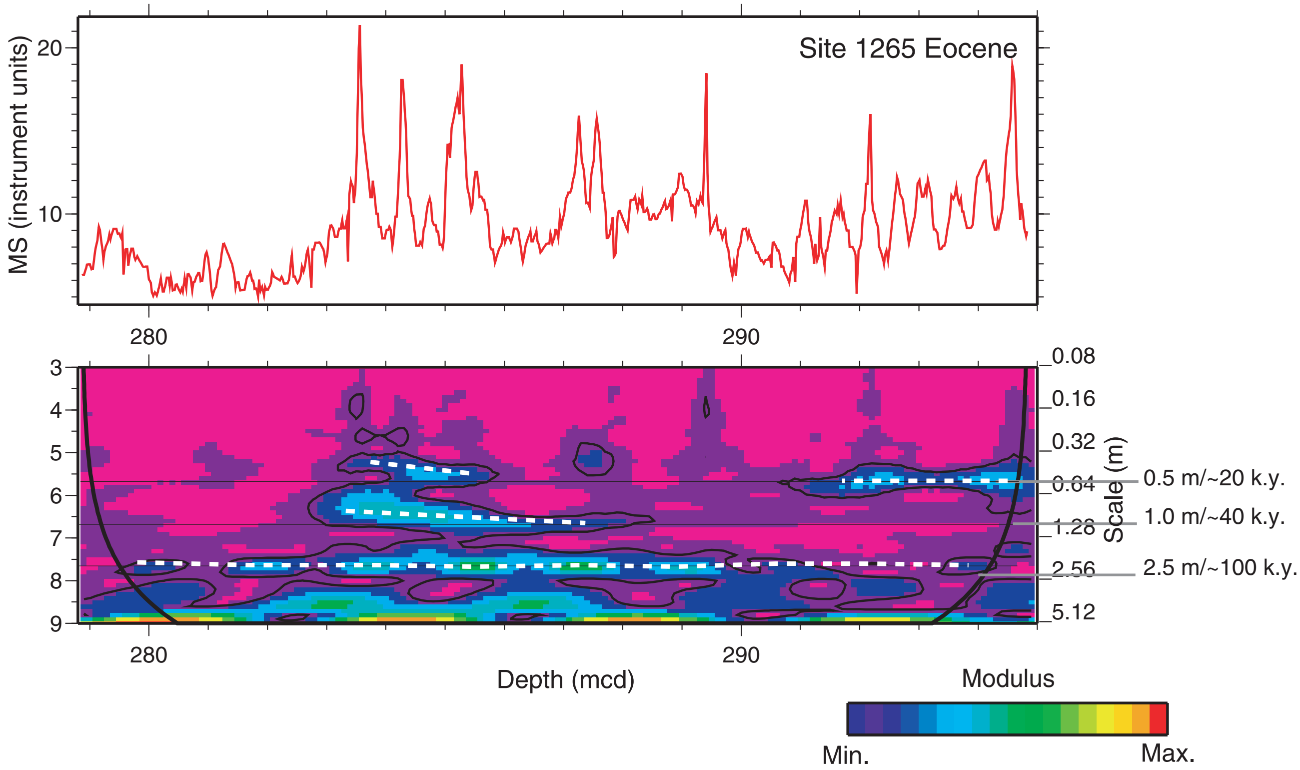
MS (instrument units)
20
10
Site 1265 Eocene
280
290
3
4
5
6
7
8
9
0.08
0.16
0.32
0.64
1.28
2.56
5.12
Scale (m)
0.5 m/~20 k.y.
1.0 m/~40 k.y.
2.5 m/~100 k.y.
280
290
Depth (mcd)
Modulus
Min.
Max.

Figure F40

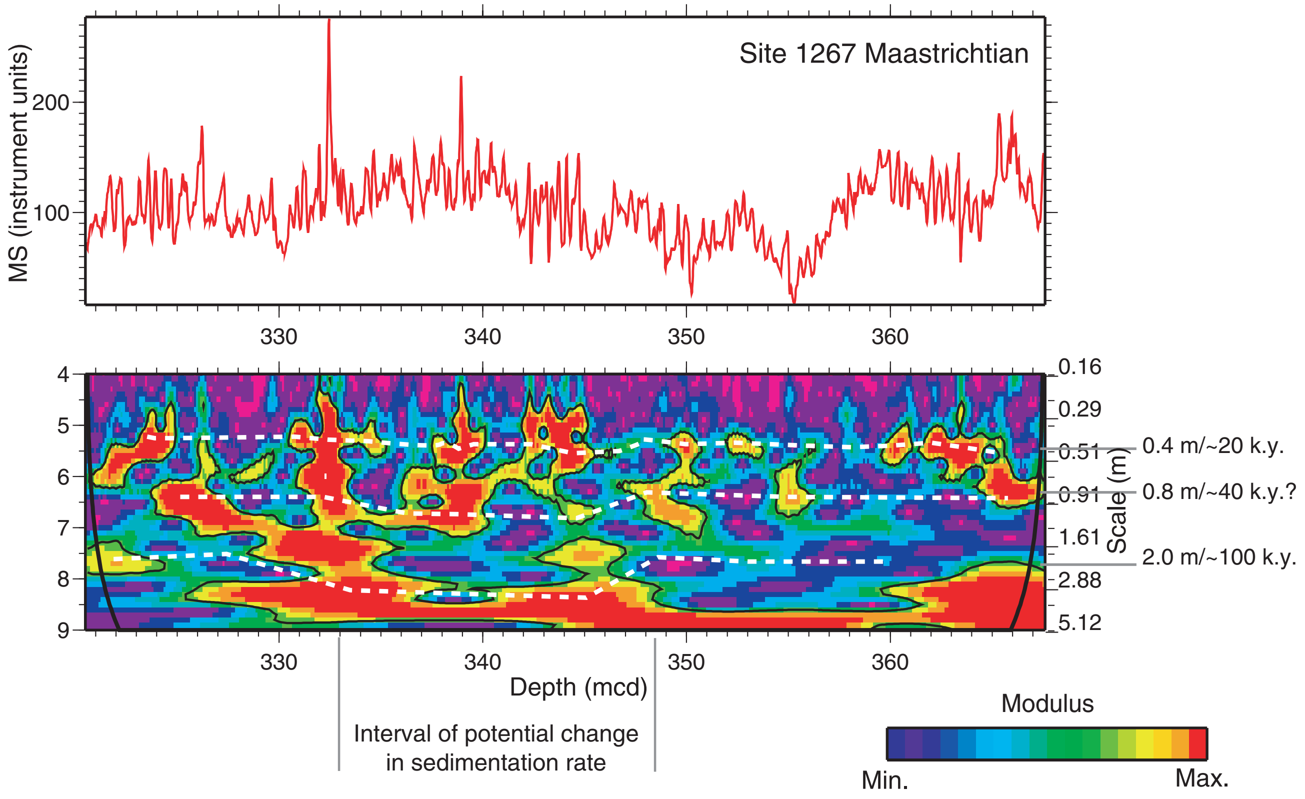
Site 1267 Maastrichtian
MS (instrument units)
200
100
330
340
350
360
4
5
6
7
8
9
0.16
0.29
0.51
0.91
1.61
2.88
5.12
Scale (m)
0.4 m/~20 k.y.
0.8 m/~40 k.y.?
2.0 m/~100 k.y.
Depth (mcd)
Interval of potential change in sedimentation rate
Modulus
Min.
Max.

Figure F41

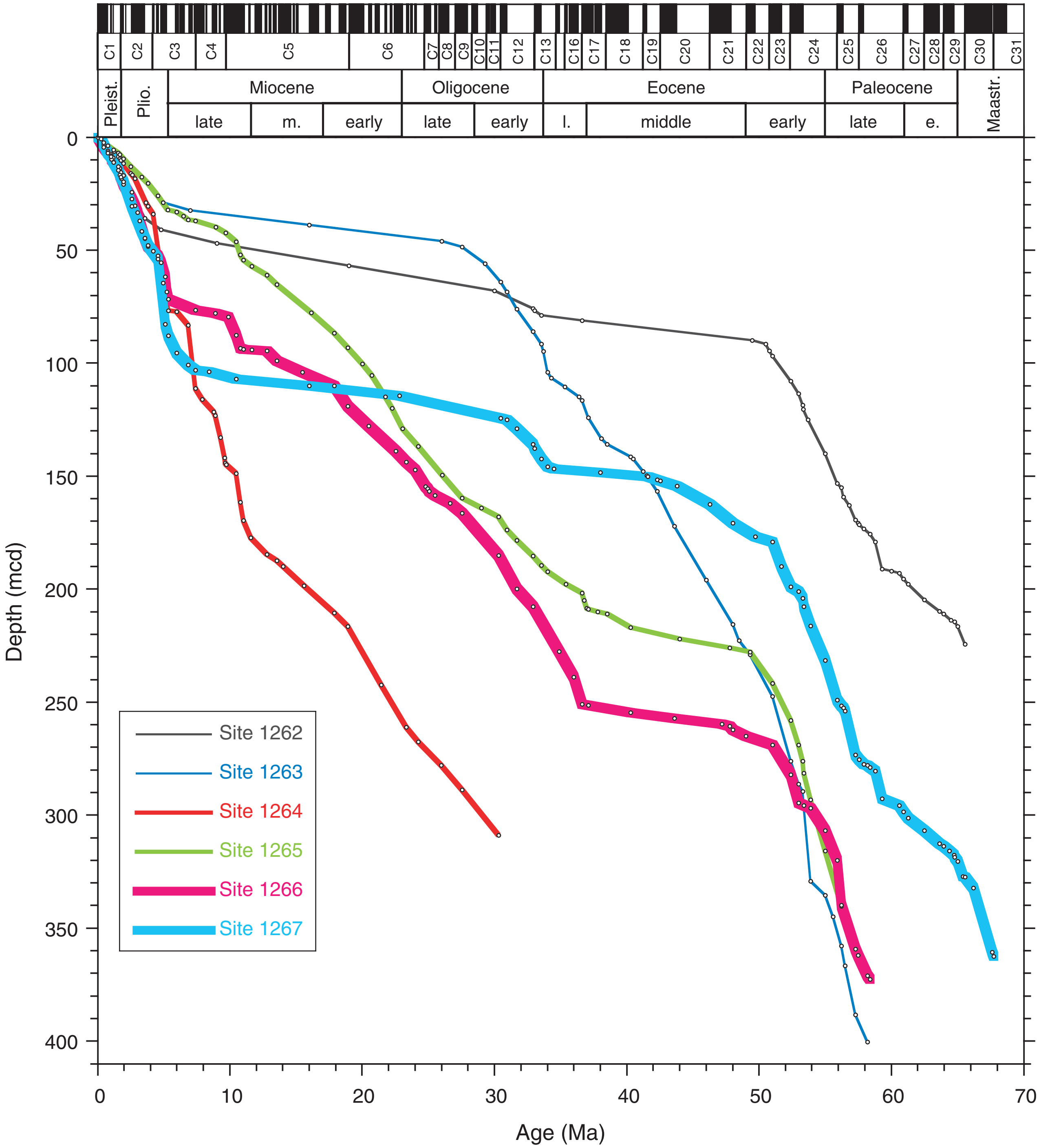
C1
C2
C3
C4
C5
C6
C7
C8
C9
C10
C11
C12
C13
C16
C17
C18
C19
C20
C21
C22
C23
C24
C25
C26
C27
C28
C29
C30
C31
Pleist.
Plio.
Miocene
late
m.
early
Oligocene
late
early
Eocene
l.
middle
early
Paleocene
late
e.
Maastr.
Depth (mcd)
0
50
100
150
200
250
300
350
400
Age (Ma)
0
10
20
30
40
50
60
70
Site 1262
Site 1263
Site 1264
Site 1265
Site 1266
Site 1267

Figure F42

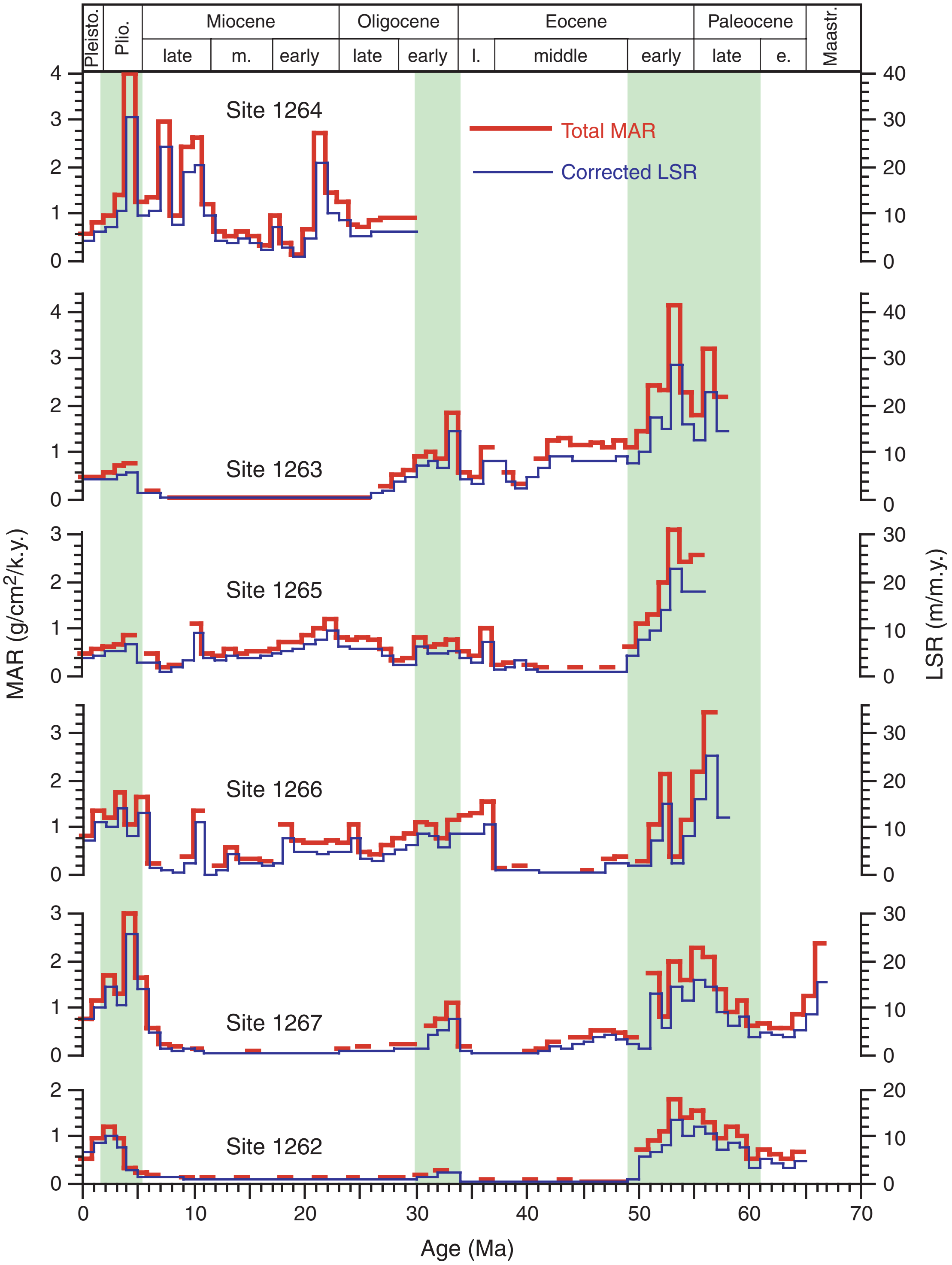
Pleisto.
Plio.
Miocene
late
m.
early
Oligocene
late
early
Eocene
l.
middle
early
Paleocene
late
e.
Maastr.
Site 1264
Total MAR
Corrected LSR
Site 1263
Site 1265
Site 1266
Site 1267
Site 1262
MAR (g/cm²/k.y.)
LSR (m/m.y.)
Age (Ma)
0
10
20
30
40
50
60
70

Figure F43

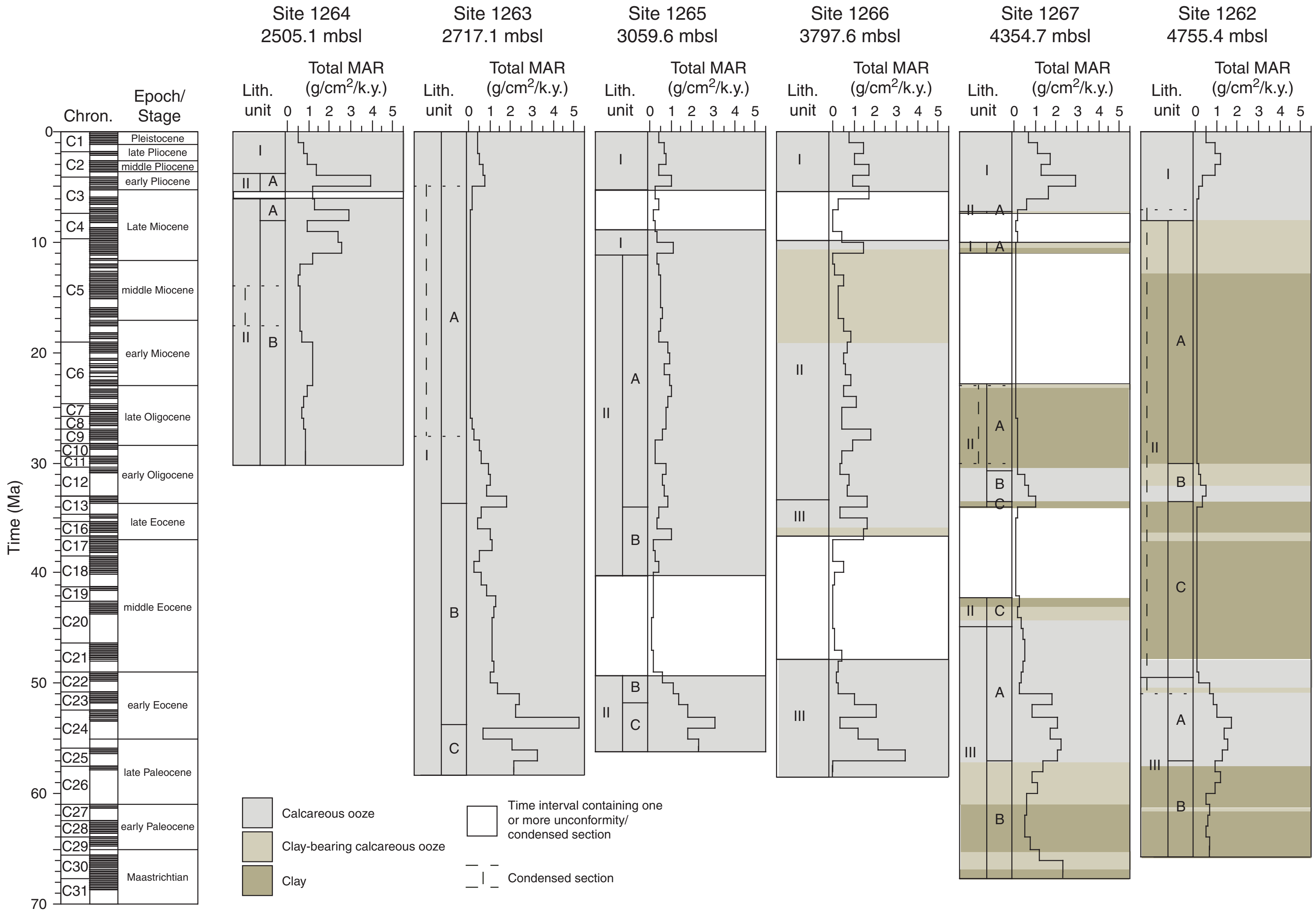
Site 1264
2505.1 mbsl
Site 1263
2717.1 mbsl
Site 1265
3059.6 mbsl
Site 1266
3797.6 mbsl
Site 1267
4354.7 mbsl
Site 1262
4755.4 mbsl
Lith. unit
Total MAR (g/cm2/k.y.)
0 1 2 3 4 5
Chron.
Epoch/ Stage
Time (Ma)
0
10
20
30
40
50
60
70
C1
C2
C3
C4
C5
C6
C7
C8
C9
C10
C11
C12
C13
C16
C17
C18
C19
C20
C21
C22
C23
C24
C25
C26
C27
C28
C29
C30
C31
Pleistocene
late Pliocene
middle Pliocene
early Pliocene
Late Miocene
middle Miocene
early Miocene
late Oligocene
early Oligocene
late Eocene
middle Eocene
early Eocene
late Paleocene
early Paleocene
Maastrichtian
I
II
III
A
B
C
Calcareous ooze
Clay-bearing calcareous ooze
Clay
Time interval containing one or more unconformity/ condensed section
Condensed section

Figure F44

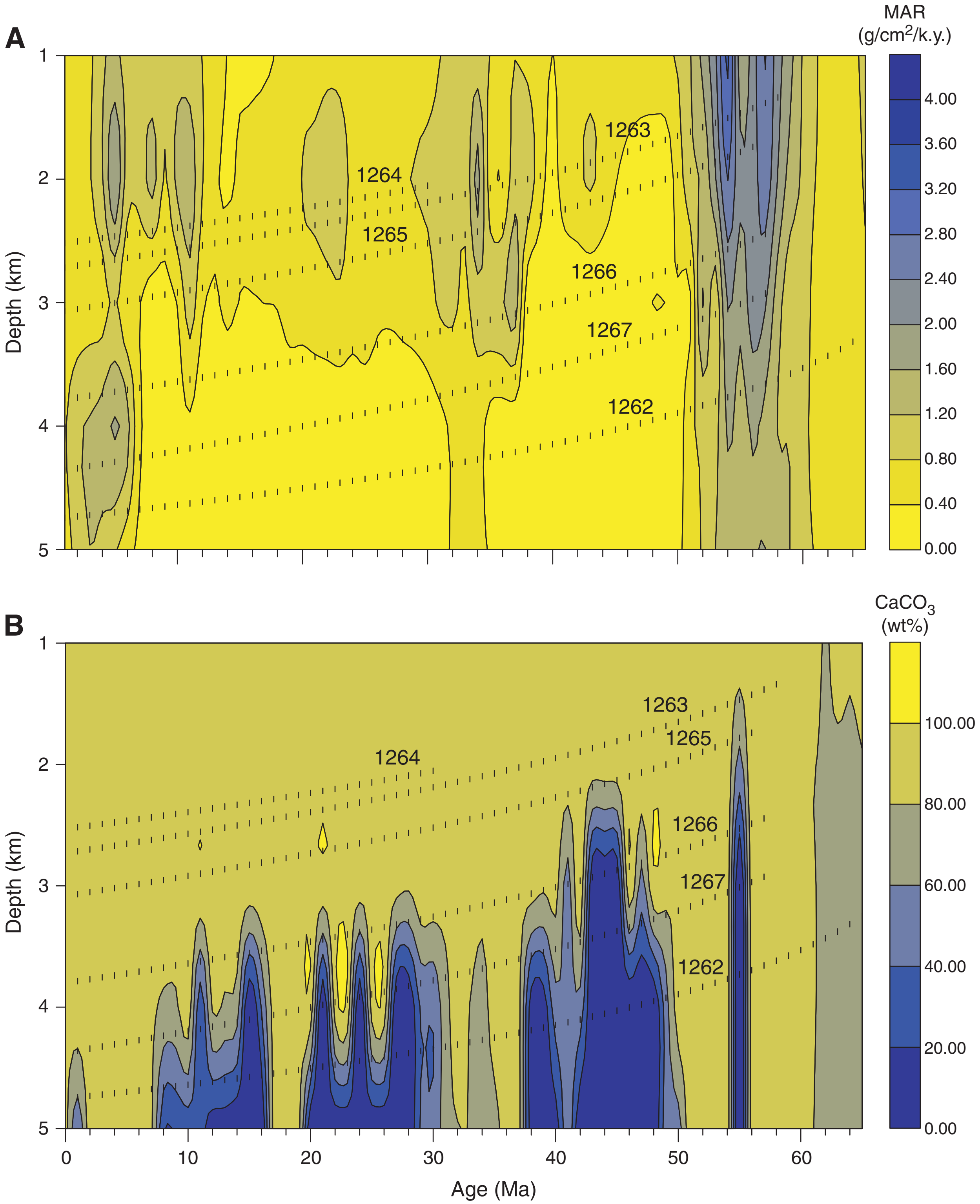
A
MAR
(g/cm²/k.y.)
4.00
3.60
3.20
2.80
2.40
2.00
1.60
1.20
0.80
0.40
0.00
Depth (km)
1
2
3
4
5
1263
1264
1265
1266
1267
1262
B
CaCO3
(wt%)
100.00
80.00
60.00
40.00
20.00
0.00
Depth (km)
1
2
3
4
5
1263
1265
1264
1266
1267
1262
0
10
20
30
40
50
60
Age (Ma)

Figure F45

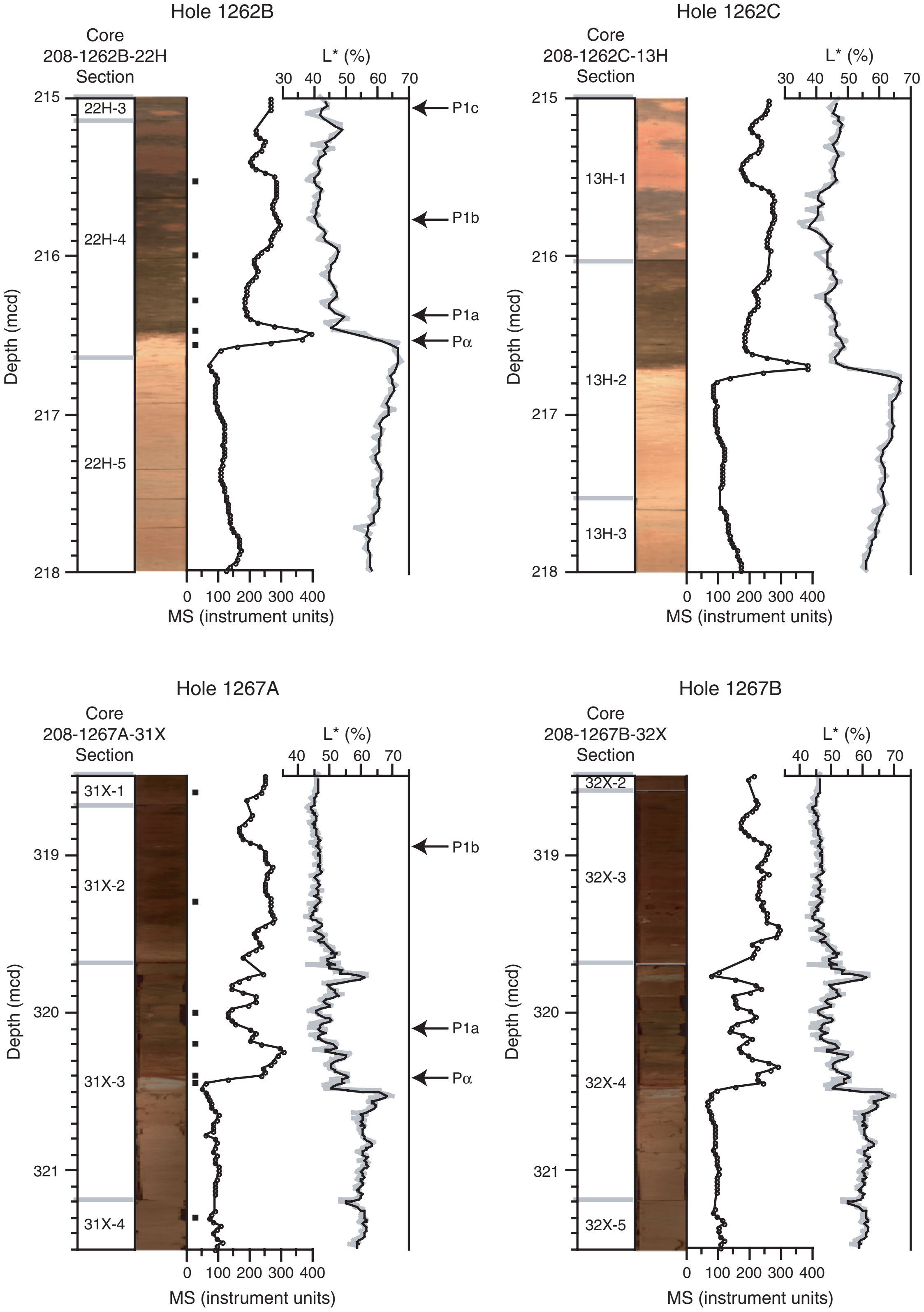
Hole 1262B
Core
208-1262B-22H
Section
L* (%)
30 40 50 60 70
215
216
217
218
22H-3
22H-4
22H-5
Depth (mcd)
P1c
P1b
P1a
Pα
0 100 200 300 400
MS (instrument units)
Hole 1262C
Core
208-1262C-13H
Section
13H-1
13H-2
13H-3
Hole 1267A
Core
208-1267A-31X
Section
L* (%)
40 50 60 70
319
320
321
31X-1
31X-2
31X-3
31X-4
Hole 1267B
Core
208-1267B-32X
Section
32X-2
32X-3
32X-4
32X-5

Figure F46

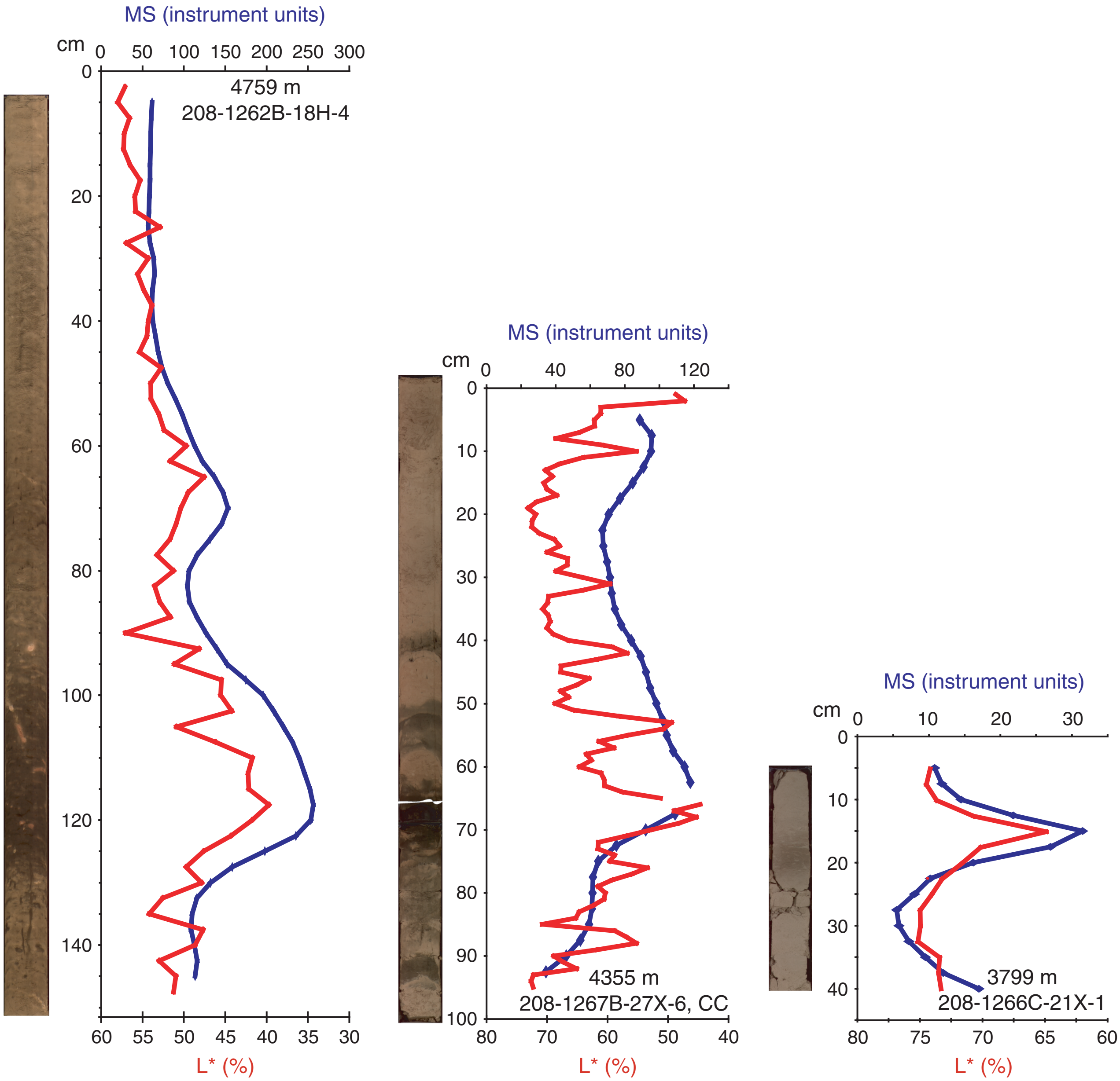
MS (instrument units)
cm
0
50
100
150
200
250
300
4759 m
208-1262B-18H-4
20
40
60
80
100
120
140
60
55
50
45
40
35
30
L* (%)
MS (instrument units)
40
80
120
4355 m
208-1267B-27X-6, CC
10
20
30
50
70
90
L* (%)
MS (instrument units)
3799 m
208-1266C-21X-1
75
65
L* (%)

Figure F47

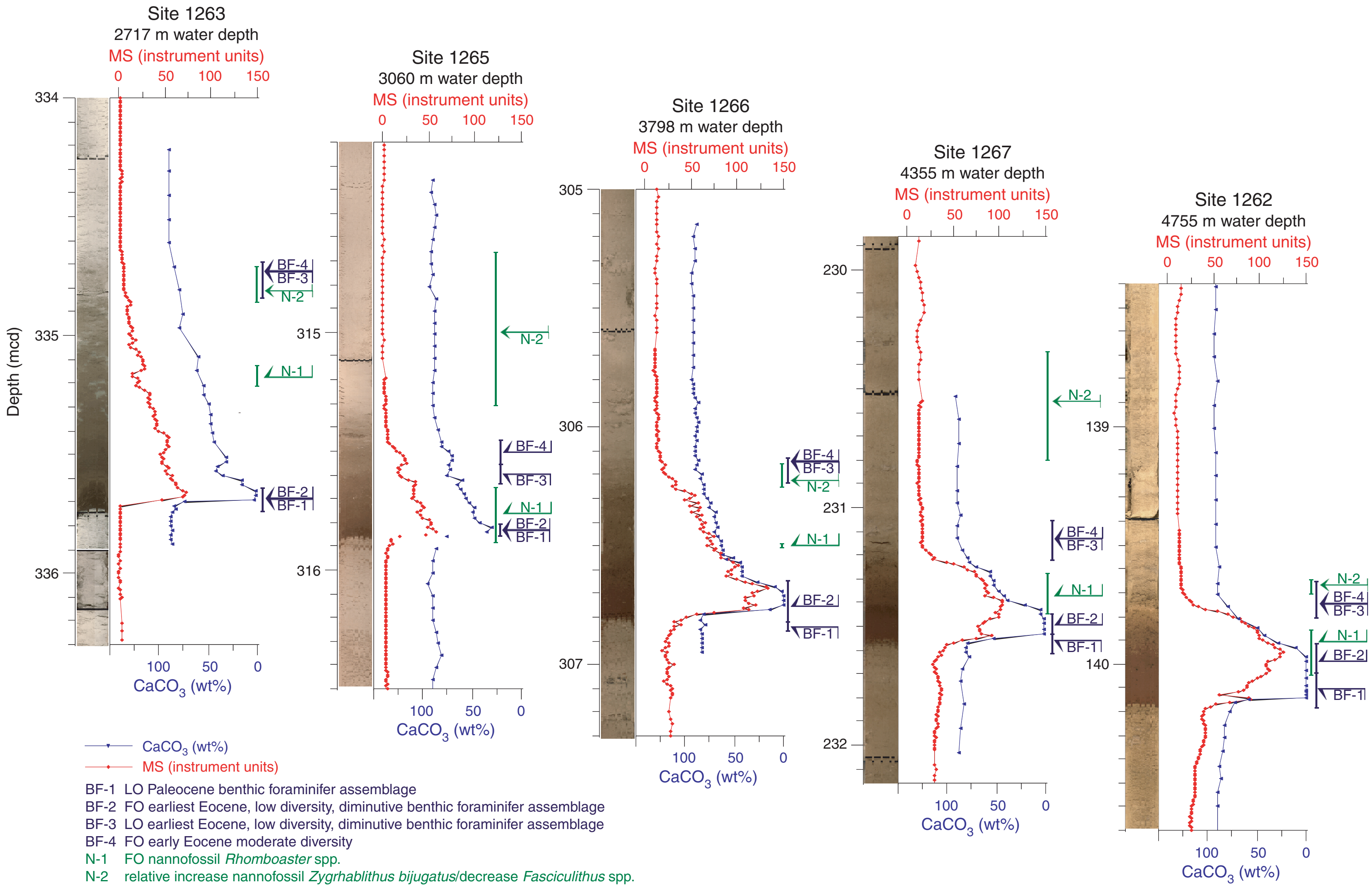

CaCO$_3$ (wt%)
MS (instrument units)
BF-1 LO Paleocene benthic foraminifer assemblage
BF-2 FO earliest Eocene, low diversity, diminutive benthic foraminifer assemblage
BF-3 LO earliest Eocene, low diversity, diminutive benthic foraminifer assemblage
BF-4 FO early Eocene moderate diversity
N-1 FO nannofossil *Rhomboaster* spp.
N-2 relative increase nannofossil *Zygrhablithus bijugatus*/decrease *Fasciculithus* spp.

Figure F48

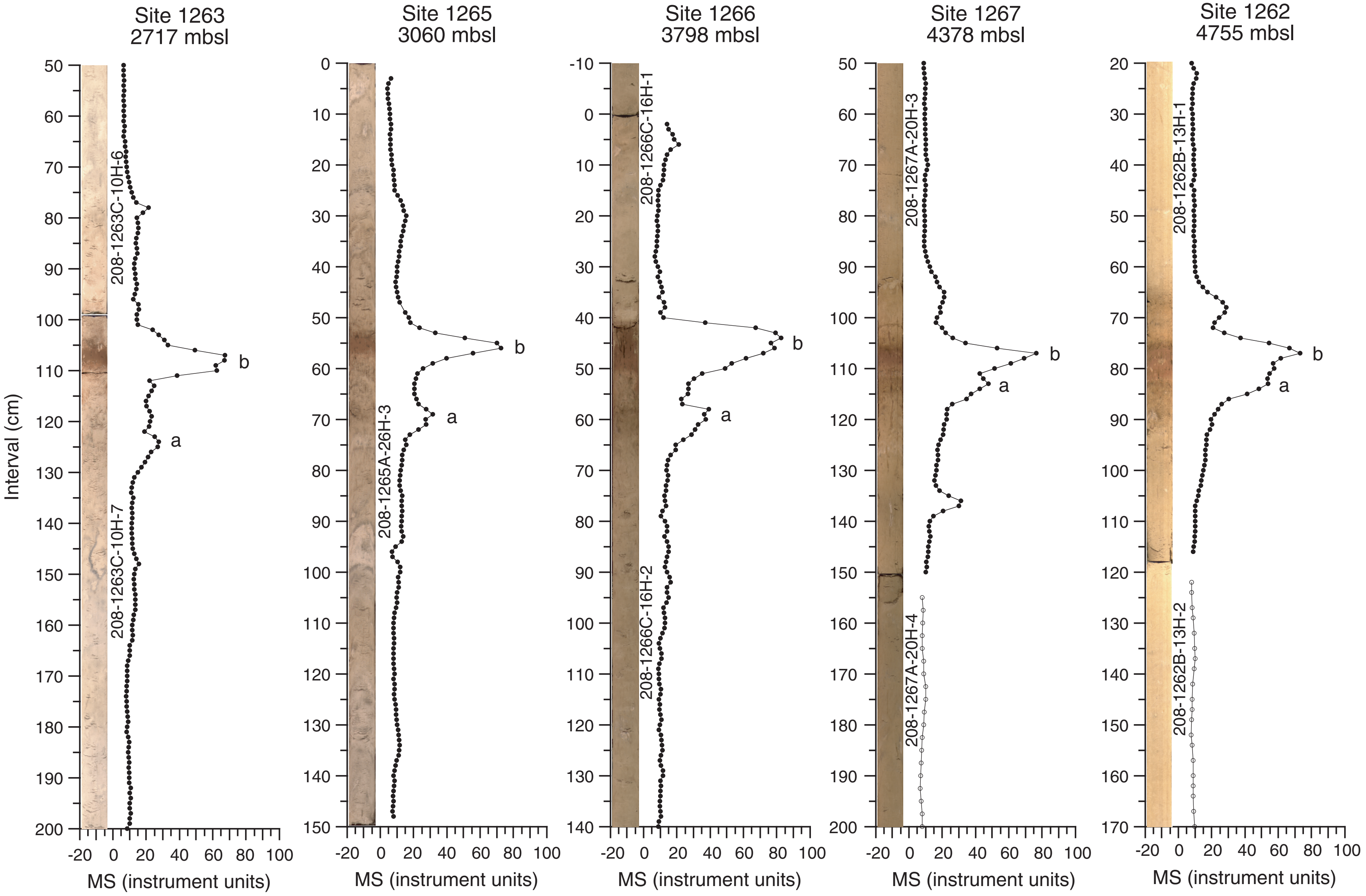
Site 1263
2717 mbsl
Site 1265
3060 mbsl
Site 1266
3798 mbsl
Site 1267
4378 mbsl
Site 1262
4755 mbsl
Interval (cm)
MS (instrument units)
-20
0
20
40
60
80
100
208-1263C-10H-6
208-1263C-10H-7
208-1265A-26H-3
208-1266C-16H-1
208-1266C-16H-2
208-1267A-20H-3
208-1267A-20H-4
208-1262B-13H-1
208-1262B-13H-2
a
b

Figure F49

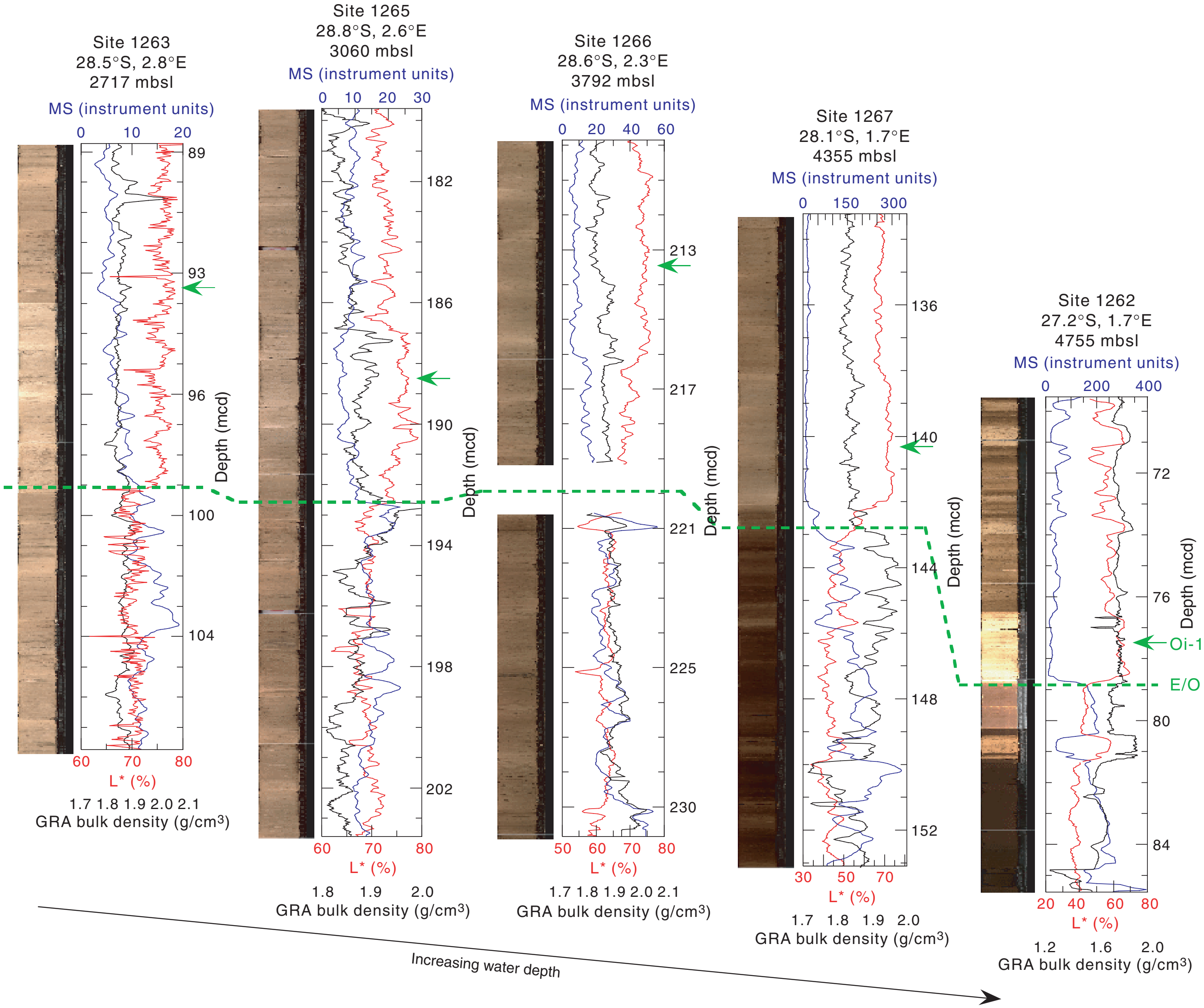
Site 1263
28.5°S, 2.8°E
2717 mbsl
MS (instrument units)
0 10 20
89
93
96
100
104
Depth (mcd)
60 70 80
L* (%)
1.7 1.8 1.9 2.0 2.1
GRA bulk density (g/cm3)
Site 1265
28.8°S, 2.6°E
3060 mbsl
MS (instrument units)
0 10 20 30
182
186
190
194
198
202
Depth (mcd)
60 70 80
L* (%)
1.8 1.9 2.0
GRA bulk density (g/cm3)
Site 1266
28.6°S, 2.3°E
3792 mbsl
MS (instrument units)
0 20 40 60
213
217
221
225
230
Depth (mcd)
50 60 70 80
L* (%)
1.7 1.8 1.9 2.0 2.1
GRA bulk density (g/cm3)
Site 1267
28.1°S, 1.7°E
4355 mbsl
MS (instrument units)
0 150 300
136
140
144
148
152
Depth (mcd)
30 50 70
L* (%)
1.7 1.8 1.9 2.0
GRA bulk density (g/cm3)
Site 1262
27.2°S, 1.7°E
4755 mbsl
MS (instrument units)
0 200 400
72
76
80
84
Depth (mcd)
Oi-1
E/O
20 40 60 80
L* (%)
1.2 1.6 2.0
GRA bulk density (g/cm3)
Increasing water depth

Figure F50

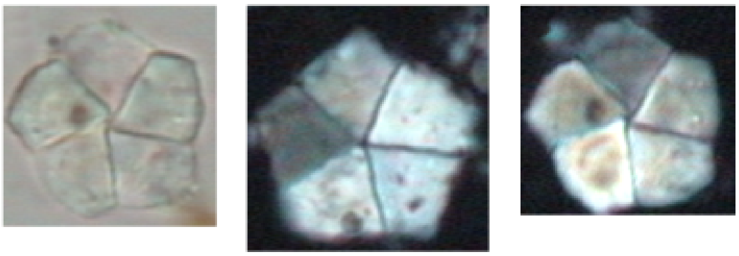

Figure F51

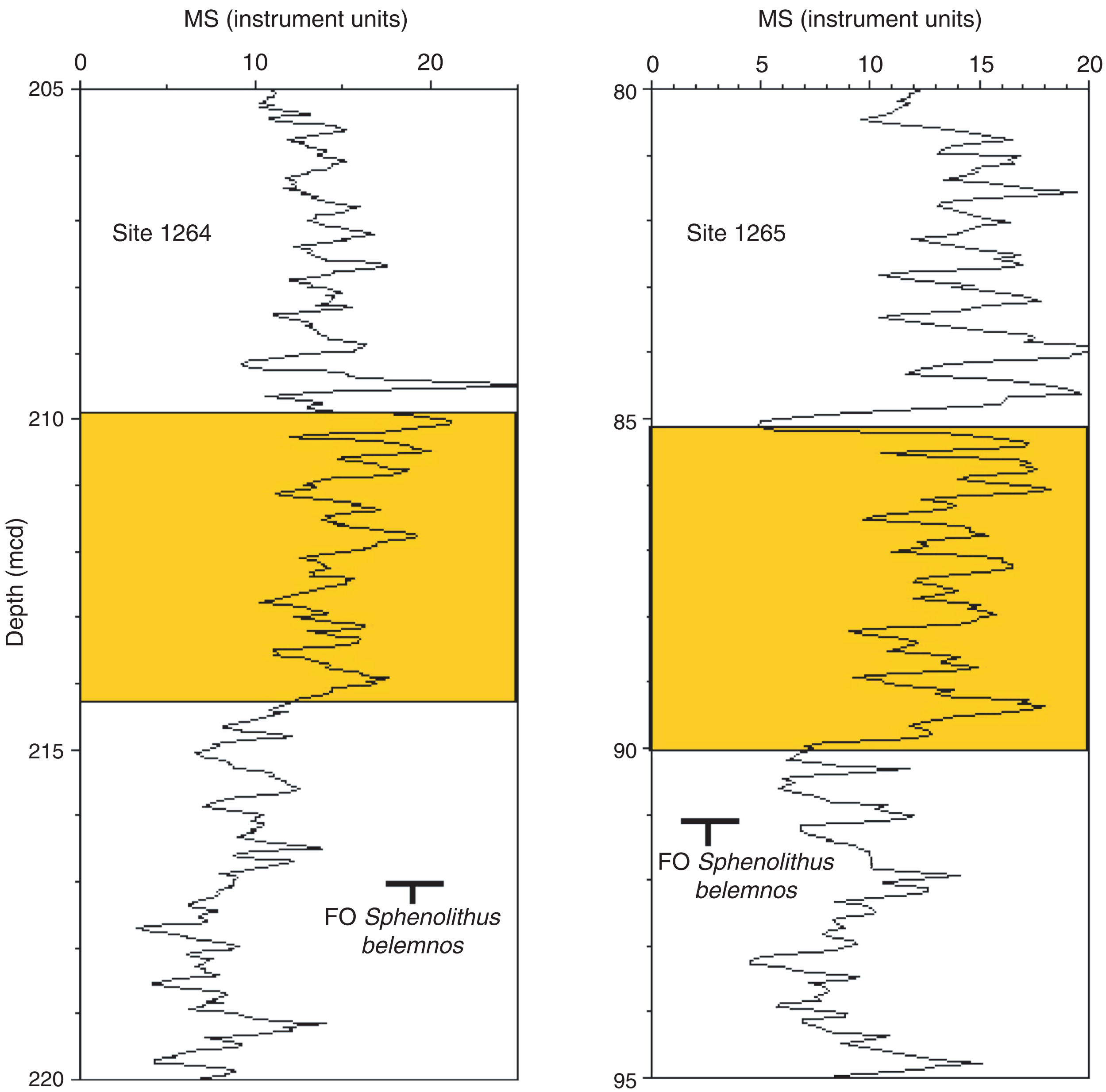
MS (instrument units)
0
10
20
205
210
215
220
Depth (mcd)
Site 1264
FO *Sphenolithus belemnos*
MS (instrument units)
0
5
10
15
20
80
85
90
95
Site 1265
FO *Sphenolithus belemnos*

Figure F52